# Ultrafast dynamics in multiferroic materials

Zixin Li

université PARIS-SACLAY

# Ultrafast Dynamics in Multiferroics

*Dynamique Ultrarapide dans les Matériaux Multiferroïques*

**Thèse de doctorat de l'université Paris-Saclay**

École doctorale n°564 Physique en Île-de-France (EDPIF)
Spécialité de doctorat: Physique
Graduate school: Physique. Référent : Faculté des Sciences d'Orsay

Thèse préparée dans l'unité de recherche **SPEC** (Université Paris-Saclay, CEA, CNRS), sous la direction de **Michel VIRET**, chercheur, et le co-encadrement de **Jean-Yves CHAULEAU**, chercheur

**Thèse soutenue à Paris-Saclay, le 10 Novembre 2023, par**

**Zixin LI**

## Composition du jury

Membres du jury avec voix délibérative

| | |
|---|---|
| **André THIAVILLE**<br>Directeur de recherche, Laboratoire de Physique des Solides, Université Paris-Saclay | Président |
| **Liliana BUDA-PREJBEANU**<br>Professeur, SPINTEC, Université Grenoble Alpes | Rapporteur & Examinatrice |
| **Bertrand DUPÉ**<br>Professeur Associé, Complex and Entangled Systems from Atoms to Materials (CESAM), Université de Liège | Rapporteur & Examinateur |
| **Hélène BÉA**<br>Professeur Associé, SPINTEC, Université Grenoble Alpes | Examinatrice |

THESE DE DOCTORAT

NNT : 2023UPASP141

université PARIS-SACLAY

ÉCOLE DOCTORALE
Physique en Île-de-France (PIF)

**Titre:** Dynamique ultrarapide dans les matériaux multiferroïques
**Mots clés:** Modelisation, Ferroïques, Magnetisme

**Résumé:** Les matériaux antiferromagnétiques (AF) possèdent des fréquences de résonance atteignant la gamme du THz, soit deux ordres de grandeur supérieurs à ceux des ferromagnétiques. De nombreux antiferromagnétiques, tels le prototype oxyde de nickel NiO, sont des oxydes isolants dans lesquels la dissipation d'énergie de la dynamique de spin est faible en raison de la nature localisée des électrons. Leur fréquence de résonance élevée et leur faible dissipation d'énergie ont récemment suscité un intérêt considérable alors que l'industrie électronique moderne se heurte à des limites dures en fréquence et dissipation et atteint aussi ses limites en taille. Aussi, en raison de leur disposition antiparallèle, les textures de spin dans les AF sont robustes et ne sont pas facilement affectées par les champs extérieurs. Parce qu'ils ne produisent pas de champs de fuite, ces matériaux magnétiques sont très difficiles à sonder et à manipuler, en particulier à ce stade précoce de leur développement. Par conséquent, la modélisation et les simulations numériques de leur dynamique de spin sont cruciales pour comprendre les processus microscopiques pertinents à l'échelle de la picoseconde et pour prédire les conditions critiques de certains phénomènes physiques intéressants. Outre leur ordre magnétique, certains de ces matériaux sont également multiferroïques, c'est-à-dire qu'ils possèdent simultanément plusieurs ordres ferroïques. La ferrite de bismuth $BiFeO_3$ (BFO) en est l'archétype, étant dans les conditions ambiantes, antiferromagnétique et ferroélectrique. L'orientation des spins AF dans le BFO est modulée par un ordre cycloïdal incommensurable, induit par l'interaction magnéto-électrique qui couple les deux ordres. Cette interaction offre ainsi un levier supplémentaire pour manipuler la structure de spin, ainsi que la possibilité de créer des entités topologiques.

Dans cette thèse, nous avons concentré notre étude sur NiO et $BiFeO_3$. Nous avons basé notre modélisation de la dynamique de spin sur les paramètres mesurés expérimentalement et mené des études théoriques et numériques. Nous avons étudié la propagation des ondes de spin dans NiO, dans des géométries variées, ainsi que l'interaction entre les ondes de spin dans une jonction. Afin de modéliser BFO, nous avons entièrement développé un nouveau code pour simuler efficacement sa dynamique en profitant d'une considérable accélération GPU. La vitesse de calcul largement amplifiée a rendu possible une série de simulations. Nous avons par exemple étudié la transition de phase de la texture de spin de BFO sous fort champ magnétique d'orientations différentes. Nous avons simulé sa dynamique de spin sous l'effet d'une impulsion de couple de transfert de spin. Nous avons également modélisé des textures de spin dans des parois de domaines ferroélectriques et des configurations de polarisation plus exotiques. Enfin, nous avons mis à jour les conditions critiques pour l'existence et la stabilité des skyrmions AF dans le BFO, étudié leurs propriétés dynamiques et les conditions possibles pour leur nucléation. Ce travail vise ainsi à fournir une référence utile pour de futures études expérimentales dans le nouveau domaine de la spintronique antiferromagnétique.

université PARIS-SACLAY | ÉCOLE DOCTORALE Physique en Île-de-France (PIF)

**Title:** Ultrafast dynamics in multiferroics
**Keywords:** Simulation, Ferroics, Magnetism

**Abstract:** Antiferromagnetic (AF) materials possess resonance frequencies reaching the THz range, which is two orders of magnitude higher than those of ferromagnets. Many antiferromagnets, such as the prototypical AF Nickel Oxide NiO, are insulating oxides in which the energy dissipation of the spin dynamics is low due to the localized nature of electrons. Their high resonance frequency and low energy dissipation have triggered considerable interest as the modern electronics industry is hitting the walls of frequency and dissipation, and is reaching size limits. Moreover, due to their antiparallel arrangement, the spin structures in AFs are robust and not easily affected by external fields. Because they do not produce stray fields outside the sample, these magnetic materials bring challenges to probe and manipulate, especially at this early stage of their development. Consequently, modelling and numerical simulations of their spin dynamics are crucial in understanding the relevant microscopic processes at the picosecond time scale and in predicting the critical conditions for some interesting physical phenomena. Besides their magnetic order, some materials are also multiferroic, i.e. they possess more than one ferroic order simultaneously. As an archetype of such materials, Bismuth Ferrite $BiFeO_3$ (BFO) is at ambient conditions a ferroelectric antiferromagnet. The AF spin orientation in BFO is modulated by an incommensurate cycloidal order, which is induced by the magneto-electric interaction. This interaction couples the magnetic and ferroelectric orders, providing an extra handle to manipulate the spin structure, as well as the possibility of creating topological entities.

In this dissertation, we focused our study on NiO and $BiFeO_3$. We based our modelling of the spin dynamics on the experimentally measured parameters and conducted theoretical and numerical studies. We studied the spin wave propagation in NiO starting from trivial geometries to more complex ones, as well as the interaction between spin waves in a junction. In order to model BFO, we developed a new code from scratch to efficiently simulate its spin dynamics with GPU acceleration. This code vastly boosted the computational speed and made possible a series of studies. We then addressed the phase transition of its spin texture under a strong magnetic field of different orientations. We simulated its spin dynamics under the effect of a spin-transfer torque pulse. We also modelled spin textures in ferroelectric domain walls and more exotic polarization configurations. In the end, we uncovered the critical conditions for the existence and stability of AF skyrmions in BFO, studied their dynamical properties, and the possible conditions for their nucleation. This work aims to provide a useful reference for future experimental studies in the new field of antiferromagnetic spintronics.

# Acknowledgements

I would like to thank Michel Viret and Jean-Yves Chauleau for their supervision and teaching in the last three years. All of the results presented in this dissertation would not have been possible without their countless effort. I would also like to express my gratitude for their help in other aspects of life and work.

I also want to thank my parents, especially my mother, who supported me during the last three years. I would like to thank Chenxi, who has helped me in many aspects of life.

I would like to thank all the people who have helped me in the SPEC laboratory and all the people I collaborated with or discussed with.

I would like to thank the scholarship program for my master's study at Paris-Saclay University, which has made my graduate study in France possible.

# Contents

# Chapter 1

# Introduction

Human has a long history of exploring and utilizing magnetism. It was as early as around 600 B.C. in ancient China and ancient Greece that people recorded magnetic phenomena and it was believed that the first direction pointer utilizing magnetic materials called "Sinan" was made a few centuries later during the Qin dynasty ( 221-207 B.C.) of China [1]. Since these early times and probably before, humans have been studying and making use of magnetism and the study continues until today. Compared with these ancient times, we now understand that these lodestones contain ferrimagnetic $Fe_3O_4$, with the origin of the magnetization stemming from the spin-level magnetic moment. The functionality of these compasses is due to the interaction of their magnetic moment with the Earth's magnetic field. Magnetism and magnetic materials are used for more purposes including data storage, energy converting, communication... Despite our deepened knowledge of the origin of magnetism and the functionality of magnetic materials since ancient times, the understanding and manipulation of many magnetic materials remain challenging. Interestingly, even today we are still searching for methods to manipulate the tiny "compasses" — the spin and orbital magnetic moments, using the functionality of their "navigation" — to record and process information in the micrometer or nanometer level by their magnetization direction with the handle of their interaction with fields. Among the materials studied for this purpose, antiferromagnetic materials have been demonstrated to be exotic with their robustness and high frequency. Yet, there are many properties remaining unknown and functionalities awaiting exploration. This dissertation focuses on understanding the ultrafast dynamics and spin structures with mainly theoretical and numerical analyses of the prototypical antiferromagnet NiO and archetypal multiferroic antiferromagnet $BiFeO_3$.

The arrangement of this dissertation is as follows: Chapter 1 is a general introduction to the basic concepts of magnetism and in particular antiferromagnetism. Chapter 2 explains the numerical methods used to obtain the results, particularly the software we developed. Chapter 3 is dedicated to an in-detailed introduction to the two materials that we study, and explains the microscopic models throughout the study. Chapters 4 to 8 present the results of our study; each chapter contains an independent study on a particular topic. Chapter 9 is a summary of this dissertation.

## 1.1 Basics of Magnetism

In this section, a few basic magnetic quantities will be recalled.

### 1.1.1 Magnetic Moment

It is known that the electron possesses spin angular momentum and magnetic moment. The direction of the magnetic moment is opposite to the direction of the angular momentum. We adopt a semi-classical description of the electron spin throughout this dissertation. An electron possesses spin angular momentum $\boldsymbol{S} = S\hat{\boldsymbol{s}}$, where, the value of the momentum is $S = \frac{\hbar}{2}$ and $\hat{\boldsymbol{s}}$ is a unit vector pointing to the direction of the spin angular momentum. If there are n electrons on a certain orbital of an atom with the same spin directions, the total spin angular momentum of these electrons is $\boldsymbol{S}_{tot} = nS\hat{\boldsymbol{s}}$. The vector defined by $\boldsymbol{s} = \frac{\boldsymbol{S}_{tot}}{\hbar} = \frac{n}{2}\hat{\boldsymbol{s}}$ is often used in studies to represent the spin directions and spin norm of these electrons [2]. It is also known that an electron possesses spin magnetic moment $\boldsymbol{\mu}$ which has a relation with its angular moment

$$\boldsymbol{\mu} = -\frac{g_s \mu_B \boldsymbol{S}}{\hbar} \tag{1.1}$$

where $g_s$ is the Lande factor (approximately taken to be 2 in this study), $\mu_B = \frac{e\hbar}{2m_e} = 5.7883818060(17) \times 10^{-5} eV/T$ is the Bohr magneton. Here $e$ is the absolute value of the charge of an electron. $\hbar$ is the reduced Planck constant. $m_e$ is the mass of the electron.

An electron in a central field in three-dimensional space, which is an approximation of real-world cases such as a hydrogen atom or an atom with only one valence electron, has its eigenstate on certain orbitals [3]. These orbitals possess orbital angular momentum. They can be classically described as "circling electrons". A circling electron possesses orbital angular momentum $\boldsymbol{L}$ and magnetic moment

$$\boldsymbol{\mu_l} = -\frac{g_l \mu_B \boldsymbol{L}}{\hbar} \tag{1.2}$$

Electrons in solids thus have both spin angular momentum and orbital angular momentum, and their corresponding magnetic moments. In this study however, we will focus mainly on the spin angular moment and magnetic moment because much of the orbital angular moment is quenched by crystal fields and the spin magnetic moment is the dominating one in the materials that we study.

### 1.1.2 Interaction Energy of Magnetic Moment

Magnetic moments interact at a distance via their magnetic field $\boldsymbol{H}(\boldsymbol{r})$. This is also called the dipole-dipole interaction. The magnetic moment radiates a magnetic field that reads [4]

$$\boldsymbol{H}(\boldsymbol{r}) = \frac{1}{4\pi}\left(\frac{3\boldsymbol{r}(\boldsymbol{\mu}\cdot\boldsymbol{r})}{|\boldsymbol{r}|^5} - \frac{\boldsymbol{\mu}}{|\boldsymbol{r}|^3}\right) \tag{1.3}$$

The magnetic induction $\boldsymbol{B}$ is another frequently used quantity to describe the magnetic interaction. In the vacuum, it is related to the magnetic field by [1]

$$\boldsymbol{B} = \mu_0 \boldsymbol{H} \tag{1.4}$$

where $\mu_0$ is the magnetic permeability of the vacuum.

The energy of a magnetic moment in a magnetic field is described by the Hamiltonian [5]

$$\mathcal{H} = -\boldsymbol{\mu} \cdot \boldsymbol{B} \tag{1.5}$$

A magnetic moment in a magnetic field undergoes a torque. The torque is described by [6]

$$\boldsymbol{\tau} = \boldsymbol{\mu} \times \boldsymbol{B} \tag{1.6}$$

A magnetic moment with some angular momentum such as an electron thus precesses in a magnetic field as described by

$$\frac{d\boldsymbol{\mu}}{dt} = \gamma_e(\boldsymbol{\mu} \times \boldsymbol{B}) \tag{1.7}$$

where $\gamma_e = -g_s\mu_B$ is the gyromagnetic ratio of an electron. The precession is called the Larmor precession with an angular frequency (Larmor frequency) of

$$\boldsymbol{\omega} = -\gamma_e \boldsymbol{B} \tag{1.8}$$

When the wavefunction of two electrons overlap, due to the symmetry requirement of Fermions (Pauli principles), there are certain states of the spin which are energetically favoured compared with the other [7, 8, 9, 10]. The energy difference is called the exchange energy [1]. The energy of the system can be simplified and mapped to the Hamiltonian that only involves spin. Such a Hamiltonian is called the Heisenberg Hamiltonian

$$\mathcal{H}_{ex} = J\boldsymbol{s_i} \cdot \boldsymbol{s_j} \tag{1.9}$$

In ferromagnetic materials, the spins tend to be parallel to each other. In some materials such as the transition metal oxides, the exchange is mediated by a nonmagnetic oxygen atom [11, 12]. In these materials, the nearest neighbour spins can be antiferromagnetically coupled. That is, the exchange energy between the two spins favours the antiparallel state. In Eq. 1.9, the $J$ is negative for the case of ferromagnetic materials and positive for antiferromagnetic materials.

Electrons moving in a field could be described by the Pauli equation. A term of energy arises from the Pauli equation due to relativistic effects that connect the orbital angular momentum with the spin angular momentum. This term has the form of Hamiltonian

$$\mathcal{H}_{so} = \xi \boldsymbol{s} \cdot \boldsymbol{l} \tag{1.10}$$

where $\xi$ is a factor describing the strength of the interaction. Such a term leads to an interaction between the spin and the crystal structure, and it is the only term in energy that breaks the isotropic symmetry of a system of spins with only exchange interaction when no external field is present. It leads to the magneto-crystalline anisotropy, which in its first-order approximation has the form

$$\mathcal{H}_{ani} = K(\boldsymbol{a} \cdot \boldsymbol{s})^2 \tag{1.11}$$

The $K$ factor is negative if the anisotropy is an easy-axis type, and positive for easy-plane anisotropy. The spin-orbit interaction also allows for a certain type of asymmetric exchange so-called Dzyaloshinskii–Moriya Interaction (DMI)

$$\mathcal{H}_{DMI} = \boldsymbol{D} \cdot (\boldsymbol{s_i} \times \boldsymbol{s_j}) \tag{1.12}$$

It favours a perpendicular arrangement of the two spins.

### 1.1.3 Time Evolution of the Magnetic Moment

The evolution of the spin direction is approximated by the Landau–Lifshitz–Gilbert (LLG) equation:

$$\frac{d\hat{\boldsymbol{s}}}{dt} = \boldsymbol{\omega}_\Sigma \times \hat{\boldsymbol{s}} - \alpha \frac{d\hat{\boldsymbol{s}}}{dt} \times \hat{\boldsymbol{s}} \tag{1.13}$$

where $\boldsymbol{\omega}_\Sigma$ is given by:

$$\boldsymbol{\omega}_\Sigma = \gamma\mu_0 \boldsymbol{H}_\Sigma + \hat{\boldsymbol{s}} \times \boldsymbol{\omega}_\tau = \frac{1}{\hbar|\boldsymbol{s}|}\frac{\partial \mathcal{H}}{\partial \hat{\boldsymbol{s}}} + \hat{\boldsymbol{s}} \times \boldsymbol{\omega}_\tau \tag{1.14}$$

where $\hat{\boldsymbol{s}} = \frac{\boldsymbol{s}}{|\boldsymbol{s}|}$ is the dimensionless unit vector, representing the spin vector of an atom $\boldsymbol{s}$ with spin $|\boldsymbol{s}|$ ( e.g. $|\boldsymbol{s}| = 2.5$ for BFO ), $\boldsymbol{H}_\Sigma$ is the effective field defined as the derivative of the Hamiltonian of the system, and $\alpha$ is the damping parameter. The $\boldsymbol{\omega}_\tau$ is the damping-like torque, which originates from the spin-transfer torque mechanism described in Chapter 1.3. Solving Eq. 1.13 gives a simpler equation:

$$\frac{d\hat{\boldsymbol{s}}}{dt} = \boldsymbol{\omega}_{eff} \times \hat{\boldsymbol{s}} \tag{1.15}$$

where the effective torque is

$$\boldsymbol{\omega}_{eff} = \frac{1}{1+\alpha^2}\left(\boldsymbol{\omega}_\Sigma - \alpha \boldsymbol{\omega}_\Sigma \times \hat{\boldsymbol{s}}\right) \tag{1.16}$$

## 1.2 Ferromagnetism and Antiferromagnetism

In this section, the basic properties of ferromagnetic and antiferromagnetic materials will be reviewed.

### 1.2.1 Ferromagnetic Materials and the Stoner Model

Transition metals Fe, Co, Ni and their alloys have been the most explored magnetic materials in history and still possess an important influence in today's magnetism. The electrons of these transition metals form the band structure. The magnetic moment almost entirely comes from the electrons in the 3d band and is mainly due to the spin magnetic moment as shown in Table 1.1. Their calculated band structure together with Cu for comparison is shown in Fig. 1.1. Due to exchange, the spins in these materials are polarized and the band structure of 3d-transition metals presents an energy split between the majority spins and minority spins. Despite the overall magnetization direction, the spin polarization of electrons at the Fermi surface $E_F$ is a central quantity for 'spintronics' as well as several experiments, such as the ultrafast demagnetization of a ferromagnetic film induced by a femtosecond laser pulse, which will be discussed in the section 1.3. As can be seen from Fig. 1.1, in Ni and Co the minority spins dominate at the Fermi surface whereas in Fe the majority spins tend to be more numerous at $E_F$.

| | $m_{sat}[\mu_B]$ | $m_o$ $[\mu_B]$ |
|---|---|---|
| Fe (bcc) | 2.216 | 0.0918 |
| Co (hcp) | 1.715 | 0.1472 |
| Ni (fcc) | 0.616 | 0.0507 |

Table 1.1: Experimental values for the total magnetic moments $m_{sat}$ and the orbital moments $m_o$ (which are included in $m_{sat}$ ) for the metals Fe, Co, and Ni taken from [1] P537

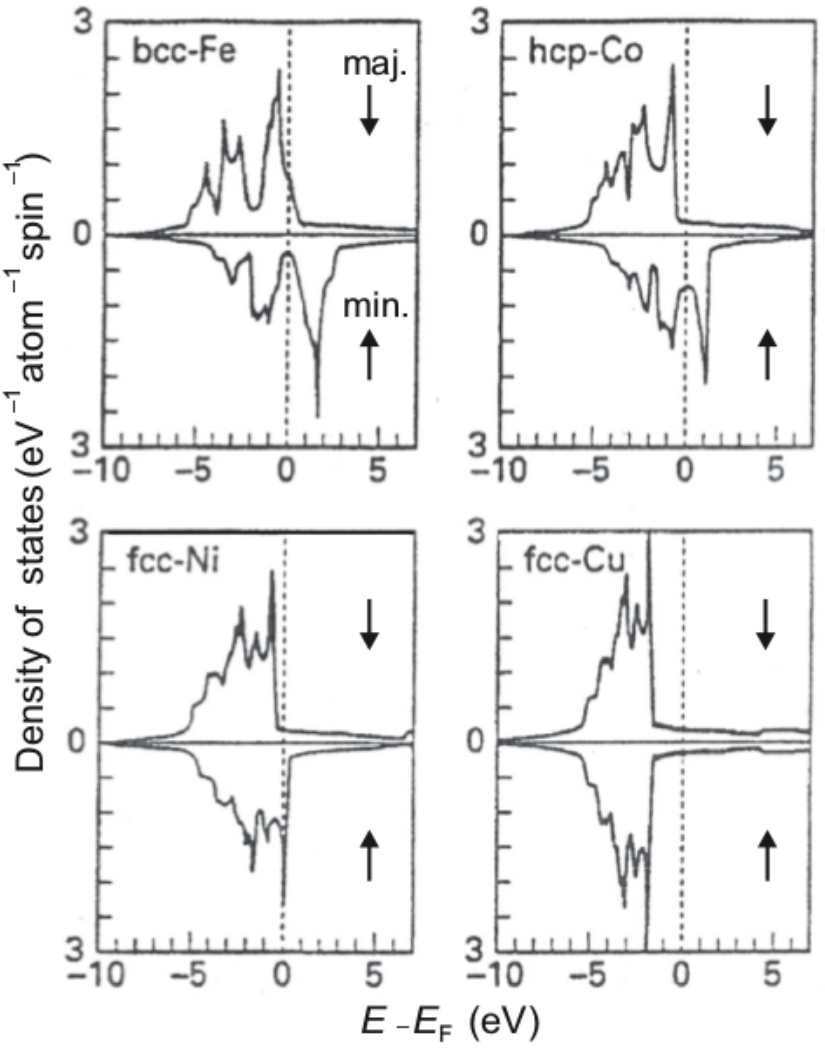


Figure 1.1: The band structure of Fe, Ni, Co, Cu obtained form first principle calculations [13, 1]

Magnetic domains usually form in ferromagnets due to the competition of short-range exchange interactions and long-range dipole-dipole interactions. These domains could be aligned by applying an external magnetic field. Due to the presence of dipole-dipole interactions, the spins in the system

endure a demagnetization field, which tends to anti-align the spins. The demagnetization field depends on the geometry of the magnetic material. In Chapter 4, we will see how this demagnetization field complicates the properties of ferromagnets and how the absence of this field in antiferromagnets brings advantages.

Assuming a homogeneous ferromagnetic system with external field $\boldsymbol{H_0}$ applied, which corresponds to the case where all the domains are aligned, an oscillating (weak) magnetic field perpendicular to the static field will induce a resonance of the spin dynamics, called the ferromagnetic resonance. The resonance frequency was derived by Charles Kittel [14] to explain some puzzling results of the earliest ferromagnetic resonance experiments [15]. This is also the $k = 0$ mode of the propagating spin dynamics, which are called spin waves or magnons. Demagnetization fields play a crucial role in the dynamics of ferromagnetic materials. In Chapter 4 we will discuss the difference between ferromagnetic spin waves and their antiferromagnetic counterparts.

### 1.2.2 Antiferromagnets

In antiferromagnetic (AF) materials, neighbouring spins are aligned in opposite directions. Such a structure is robust and not easily affected by external fields. Due to the antiparallel arrangement of spins, no dipolar stray field is produced outside the sample. These magnetic materials bring challenges to probe and manipulate their magnetic states compared with conventional magnetic materials which are sensitive to magnetic fields. Despite these difficulties, some specificities of antiferromagnets are of great interest like their resonance frequencies in the THz range, orders of magnitude higher than the GHZ range of ferromagnets [16, 17]. The high resonance frequency and the ultrafast spin dynamics generate a growing interest as the modern electronics industry is hitting the wall of frequency and dissipation, and is reaching size limits [18, 19]. Many antiferromagnets are insulating oxides, where the exchange coupling, called the superexchange[12], is mediated by nonmagnetic oxygen. This is different from ferromagnets which are usually conductors since the exchange relies on the delocalization of electrons [20]. The localized nature of electrons in insulators brings advantages in terms of energy dissipation. Based on these potentially useful properties, people start to envision the functionalities of ultrafast manipulation of spins with low dissipation [21, 22].

### 1.2.3 Spin Resonance in Antiferromagnets

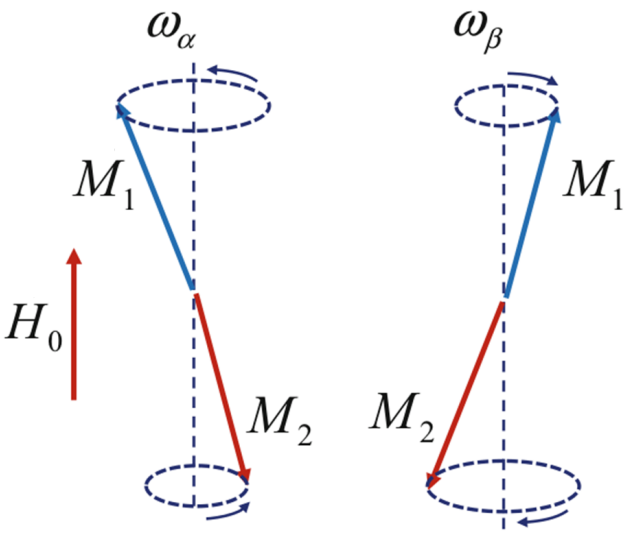


Figure 1.2: Illustration of the two resonance modes of an easy-axis AF ( figure taken from [23]).

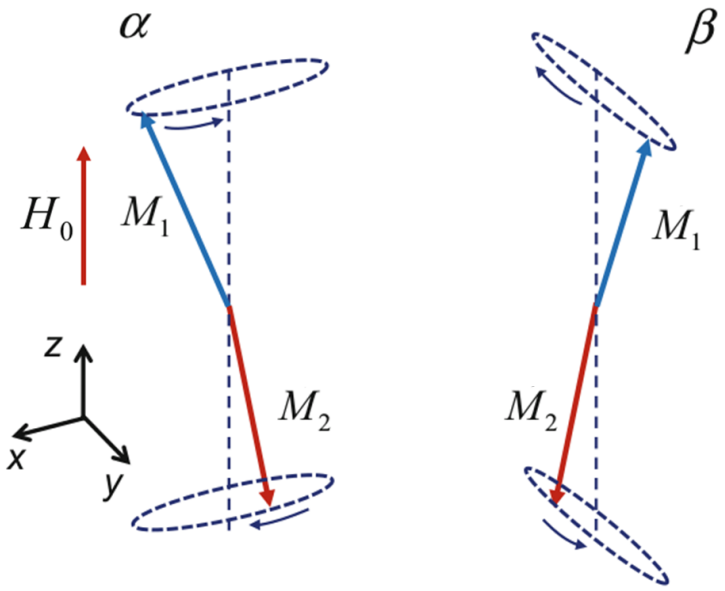


Figure 1.3: Illustration of the two resonance modes of an easy-plane AF ( figure taken from [23] ). The easy plane is perpendicular to the x-axis. The easy axis is z.

The simplest case of an AF insulator should be a spin system with antiferromagnetic exchange and some uniaxial anisotropy. In this system, the spins can be viewed as the discrete points of two sublattices on two continuous vector fields, usually represented by $\boldsymbol{M_1}$ and $\boldsymbol{M_2}$. Their resonance mode can be different depending on their anisotropy type. One class is the AF with easy-axis anisotropy, such as the fluorides $MnF_2$ and $FeF_2$. The other class is AF with easy-plane anisotropy, such as the oxides NiO and MnO.

The resonance frequency of an easy-axis AF is

$$\omega_0 = \gamma_e H_c \pm \gamma_e H_0 \tag{1.17}$$

where

$$H_c = (2H_E H_A + H_A^2)^{1/2} \tag{1.18}$$

The $\pm$ sign represents the two eigenmodes usually called $\alpha$ and $\beta$ mode shown in Fig. 1.2. $H_E$ is an effective field representing the exchange, $H_A$ represents the easy-axis anisotropy, $H_0$ is a magnetic field applied along the easy-axis. These two modes have circular motion and are degenerate in the absence of an external field.

Easy-plane AFs usually have an extra small easy-axis anisotropy that favours some direction in the easy-plane, and this anisotropy is orders of magnitude smaller than the easy-plane anisotropy. Assuming the easy-plane is perpendicular to x direction and the easy-axis is along z, then the resonance frequency of an easy-plane AF is

$$\omega_{\alpha 0}^2 = \gamma_e (2H_E H_{Ax} + 3H_0^2) \tag{1.19}$$

and

$$\omega_{\beta 0}^2 = \gamma_e (2H_E H_{Az} - H_0^2) \tag{1.20}$$

where $H_{Ax}$ represents the easy-plane anisotropy and $H_{Az}$ represents the easy-axis. $H_0$ is applied along the easy-axis direction. The $\alpha$ and $\beta$ modes are respectively out-of-plane and in-plane. They are shown in Fig. 1.3. These two modes have very elliptical trajectories. The ellipticity is defined as the ratio between the amplitude of the motion in the x and y directions. For NiO they have been calculated to be 55 for the $\alpha$ mode and 1/419 for the $\beta$ mode [23].

Antiferromagnets also have spin-waves. The property of the spin waves in antiferromagnets is different from their counterparts in ferromagnets. As can be seen from the spin resonance (k=0), the antiferromagnetic spin wave does not include demagnetization, since the net magnetization is zero. The spin dynamics are related to the exchange interaction. Spin waves in antiferromagnetic NiO will be discussed in more detail in Chapter 4.

## 1.3 Detection and Manipulation of the Antiferromagnetic Order

Antiferromagnetic orders can be detected by neutron diffraction, spin-polarized scanning tunnelling microscopy or electrical transport measurements. Optical detection of these magnetic orders includes second-harmonic generation [24, 25], linear bi-refrigerant [26], XPEEM-XMLD. These measurements of AF order have been a difficult task, making numerical simulations an important tool for

understanding spin textures and their dynamics in AFs. It is not our purpose in this dissertation to model the detection process; instead, we focus on the manipulation and evolution of the spin textures. Antiferromagnetic manipulation can be achieved by magnetic and electric fields, optics, and spin-torque [27]. In the following, these manipulations on AF will be briefly introduced.

Time-independent magnetic fields applied on easy-axis antiferromagnets could induce several transitions. A magnetic field applied perpendicular to the easy axis cants the two sublattices. The net magnetization builds up as the magnetic field increases and saturates when the field applied reaches the level of the stronger one amongst the exchange field and anisotropy field. We first consider an antiferromagnet with an exchange interaction much stronger than its anisotropy. If the magnetic field is applied along the easy axis, the spins flop to the plane perpendicular to the applied field (spin-flop transition [28] ) as the magnetic field is increased over a threshold. Different from the spin-flop case, an antiferromagnet with anisotropy stronger than exchange (which is rare) will experience a transition from the spin anti-aligned to spin aligned (spin-flip transition [29]). Typical spin-flop fields vary from several Tesla to tens of Tesla. Besides time-independent magnetic fields, time-dependent magnetic fields could also be used to manipulate antiferromagnetic order, and the fields required are much weaker. This can be understood from the sigma model, where a $\partial_t \boldsymbol{H}$ term exists in the dynamical equation of the antiferromagnetic vector[27, 30]. Such kind of fields are usually induced by optical methods. Electric fields could also couple to the magnetic order via the magneto-electric interaction. As introduced in Chapter 3.2, it is possible to alter the antiferromagnetic order by switching the ferroelectricity in multiferroic $BiFeO_3$ [31].

Antiferromagnetic orders could be manipulated by optical stimuli through several different mechanisms. Spin states in NiO and rare-earth orthoferrites such as $TmFeO_3$ can be re-oriented in the picosecond time scale[32, 33]. The re-orientation is induced by the switch of the favoured direction of anisotropy, which is altered by the thermal effect of the femtosecond laser. It is also demonstrated that in $HoFeO_3$ a short pulse (100fs) of magnetic field the order of 0.5T could trigger an inertial transition of two metastable phases. This magnetic field pulse is induced by a femtosecond laser pulse via the inverse Faraday effect [34].

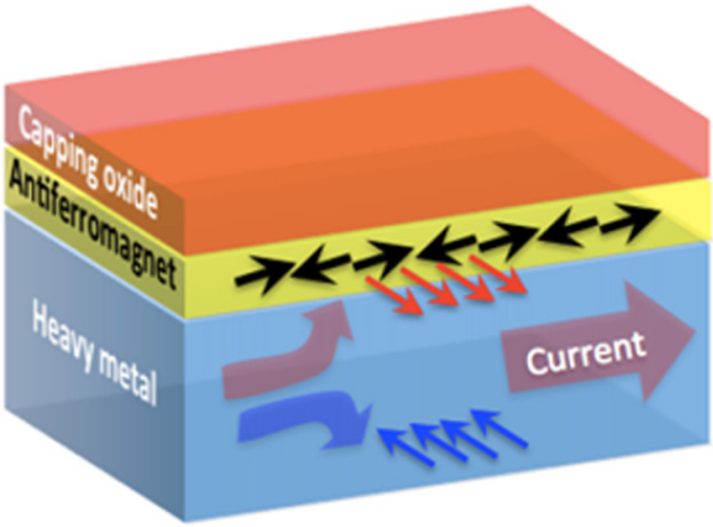


Figure 1.4: Illustration of the structure to inject SOT in an antiferromagnet from an adjacent Pt layer. A charge current is applied to the heavy metal ( represented by the wide brown arrow ). Electrons with the spin direction represented by the red arrows accumulate at the interface with AF, whilst electrons with opposite spin ( blue arrows ) accumulate at the bottom. This is due to the spin-orbit interaction, which induces a spin current represented by the wide arrows ( the wide red arrow represents the flux of red-colour spins and the wide blue arrow represents the blue-colour spins ). Figure is from [27]

Antiferromagnetic orders could also be switched by spin torque. The proper torques that could achieve switching are not magnetic fields ( the two sublattices cancel out ), but staggered magnetic fields ( the fields are opposite for the two sublattices ) including the damping-like term in the spin-transfer torque (STT) or spin-orbit torque (SOT). In this dissertation, we mainly consider spin-transfer torque and spin-orbit torque. In magnetic systems with broken inversion symmetry (globally or locally) and sizable spin-orbit coupling, the transfer of angular momentum between the orbital angular momentum of carriers and the spin angular moment of the localized electrons results in so-called spin-orbit torques. Several mechanisms including the spin Hall effect and the Rashba-Edelstein effect have been found and new emerging mechanisms have been discussed[35]. The main mechanism that will be mentioned in this dissertation is the spin Hall effect in heavy metals. By injecting a current in a heavy metal such as Pt, due to the spin-orbit coupling a spin current is induced that flows perpendicular to the electric current. As shown in Fig. 1.4, a heterostructure could inject spin-orbit torque into an antiferromagnetic layer. This spin-orbit torque is modelled by the formula

$$\tau = \tau_{||}\boldsymbol{\mu} \times [(\boldsymbol{u} \times \boldsymbol{j}_C) \times \boldsymbol{\mu}] + \tau_{\perp}\boldsymbol{\mu} \times (\boldsymbol{u} \times \boldsymbol{j}_C) \tag{1.21}$$

where $\boldsymbol{u}$ is a unit vector determined by the symmetry of the system and $\boldsymbol{j}_C$ is the current density. In the case of the spin Hall effect in Pt shown in Fig. 1.4, $\boldsymbol{u}$ is along the z-axis.

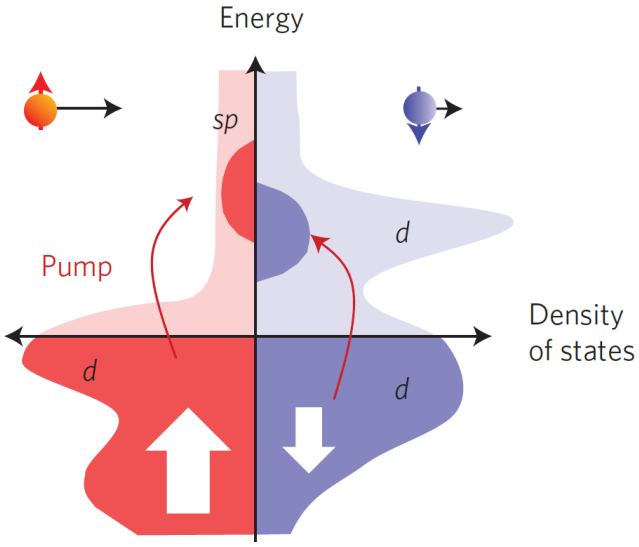


Figure 1.5: An illustration of the ultrafast laser-induced demagnetization. The material is a ferromagnet, with the majority of spins pointing up (denoted by red) and the minority pointing down ( denoted by blue). The electrons are excited to higher energy states. Figure taken from [36]

.

In our studies, we also consider spin-transfer torque generated from the ultrafast demagnetization process [36]. A femtosecond laser pulse shooting on a ferromagnetic metal excites electrons into higher energy states in the bands, as demonstrated by Fig. 1.5 . Due to the asymmetric band structure of up spins and down spins, these hot electrons carry net spin angular momentum. When they reach higher energy bands, the populations of up and down spins have to readapt and the material loses angular momentum through other degrees of freedom. The magnetization of the material is lost within hundreds of femtoseconds and recovers in the picosecond time scale. If the material is deposited in the vicinity of another metal or insulator, the hot electrons either dissipate into the other material or accumulate at the interface. In both cases, they transfer some spin angular momentum to a neighbouring material. Therefore, this mechanism provides a way of injecting very fast bursts of angular momentum in thin AF layers in contact. Spin-transfer torque in an antiferromagnet is modelled by a very similar formula as in the SOT case:

$$\tau = \tau_{||}\boldsymbol{\mu} \times (\boldsymbol{P} \times \boldsymbol{\mu}) + \tau_{\perp}(\boldsymbol{\mu} \times \boldsymbol{P}) \tag{1.22}$$

where $\boldsymbol{P}$ is the direction of the polarizing layer. $\tau_{||}$ ( $\tau_{\perp}$ ) is the magnitude of the so-called damping-like (field-like) torque component that lies in ( out of ) the ($\boldsymbol{\mu}$, $\boldsymbol{P}$) plane. In this dissertation, we will study the manipulation of AF states by SOT and STT. Since the field-like spin torque is much less efficient in the manipulation of the AF states, we consider only the damping-like spin torque in the modelling, as indicated in Eq. 1.14.

## 1.4 Skyrmions

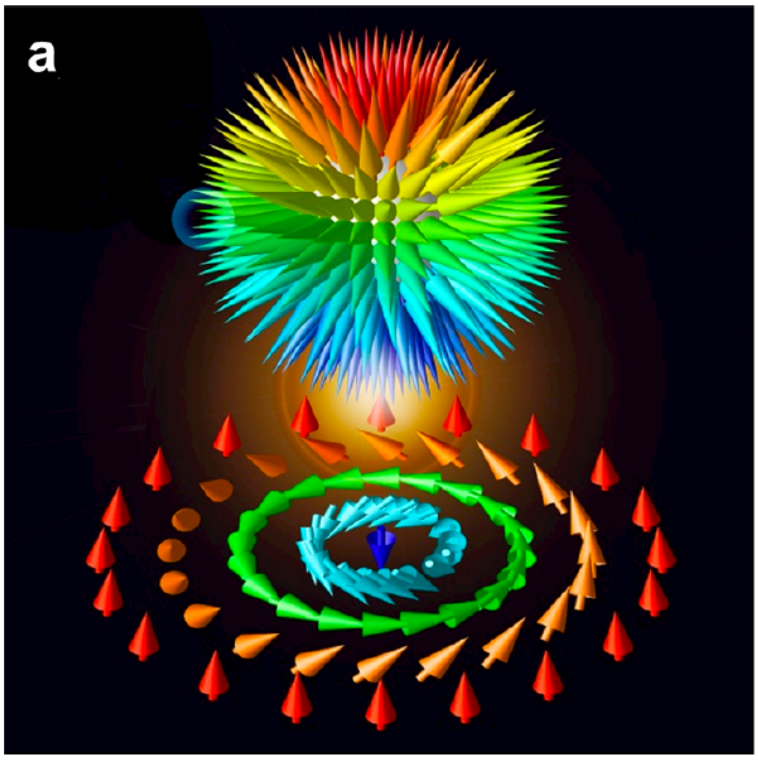


Figure 1.6: Schematic illustration of the mapping from spin vector field of a 2D skyrmion into to a 3D sphere [37]

In classical mechanics, particles are treated as point-like objects. In field theory, they are explained as wave-like excitations. To explain the stability of particles in field theory, Skyrme proposed that these wave-like excitations could be protected by topology, which prevents them from annihilation by a continuous transformation of the field configuration [38, 39]. This model has been applied in magnetic systems by Bogdanov and Yablonskii [40] to predict the possible existence of topologically protected wave-like excitations now called skyrmions. In 2009 this existence was experimentally verified [41] and in 2010 the topology was confirmed in real-space [42]. The topology of a skyrmion and a real-space experimental measurement can be seen as an example in Fig. 1.6.


Figure 1.7: Three types of skyrmion [37]

A skyrmion can be mathematically discribed by a set of two functions $\Phi(\phi)$ and $\Theta(r)$ that map the radius $r$ and azimuthal angle $\phi$ of the displacement vector in 2D into the polar angle $\Theta$ and the azimutal angle $\Phi$ in the sphere [43]. The swirling structure of a skyrmion is thus described by a vector field $\boldsymbol{n}(\boldsymbol{r})$ given by

$$\boldsymbol{n}(\boldsymbol{r}) = (\cos\Phi(\phi)\sin\Theta(r), \sin\Phi(\phi)\sin\Theta(r), \cos\Theta(r)) \tag{1.23}$$

in the continuous limit. Here $\boldsymbol{n}(\boldsymbol{r})$ is the direction of the moment $\boldsymbol{n}(\boldsymbol{r}) = \boldsymbol{m}(\boldsymbol{r})/|\boldsymbol{m}(\boldsymbol{r})|$ . The function $\Phi(\phi)$ is

$$\Phi(\phi) = m\phi + \gamma \tag{1.24}$$

where $m$ is the vorticity and $\gamma$ is the helicity. The topological charge is defined by

$$Q = \frac{1}{4\pi}\int\int d^2\boldsymbol{r}\boldsymbol{n}\cdot\left(\frac{\partial\boldsymbol{n}}{\partial x}\times\frac{\partial\boldsymbol{n}}{\partial y}\right) \tag{1.25}$$

Putting the Eq. 1.23 into this equation, we have

$$Q = -\frac{1}{4\pi}\left[\cos\Theta(r)\right]_{r=0}^{r=\infty}\left[\Phi(\phi)\right]_{\phi=0}^{\phi=2\pi} \tag{1.26}$$

Suppose spins point up at $r\to\infty$ and down at $r=0$. Then, $[\cos\Theta(r)]_{r=0}^{r=\infty} = 2$. In this case, $Q = -m$. For the three types of skyrmions shown in Fig. 1.7, $(Q, m, \gamma) = (-1, 1, -\pi/2), (-1, 1, 0), (1, -1, -\pi/2)$.

In conductors, these entities can interact with conduction electrons. If a conduction electron collects an additional phase over a closed travel path, this phase is called the geometrical phase or Berry phase [44]. An Electron going through a skyrmion in a close loop endures a Berry phase that is related to the integral of $\boldsymbol{n}\cdot\left(\frac{\partial\boldsymbol{n}}{\partial x}\times\frac{\partial\boldsymbol{n}}{\partial y}\right)$ over the path. Since the Berry phase affects electron transport in a similar way as an external magnetic flux, skyrmions in conductors can be regarded as sources of effective magnetic fields. These effective fields are a type of emergent electromagnetic field (EMF) [45], leading to the Hall effect of conducting electrons, called the Topological Hall Effect (THE).

Skyrmions can also be driven by spin-polarized currents via the spin-transfer torque mechanism. However, such a current in ferromagnetic conductors cannot drive skyrmions to move in a straight line. This is a direct result of the spin precessions described by the LLG equation[46]. The fact that skyrmions can not move in a straight line is problematic for their electrical manipulation in devices.

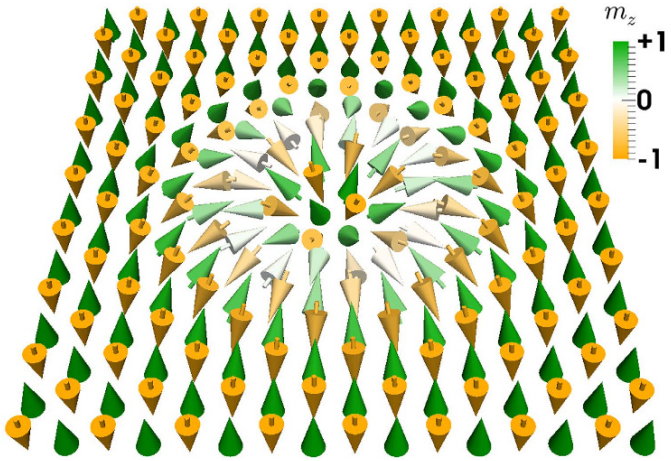


Figure 1.8: An illustration of an antiferromagnetic skyrmion spin texture [47]

Our discussion so far has been constrained to ferromagnetic materials. Skyrmions in antiferromagnetic materials have been theoretically studied in a general sense [47]. A typical spin texture is shown in Fig. 1.8 and it can be viewed as two ferromagnetic skyrmions, one for each sublattice, that are antiferromagnetically coupled and anti-aligned at the atomic scale. Antiferromagnetic skyrmions have been predicted to be able to move in a straight line and at higher velocities than their ferromagnetic counterparts. However, they have not been observed in any experiments hitherto. Part of this Ph.D. work is to simulate BFO based on the generally accepted parameters that are measured from experiments and uncover the condition to stabilize an antiferromagnetic skyrmion. The details of this study will be discussed in Chapter 8.

# Chapter 2

# Methods

Thanks to the rapid advancement of computing devices, we are capable of simulating systems that are much larger than before. Large-scale simulations such as spin dynamics usually require parallel computing. We have used two software for our study: LAMMPS and a homemade code that we developed. LAMMPS can be used as a spin dynamics simulation code for any material. Since it could only parallelize on CPUs, we could only use it to simulate smaller spin textures at the atomic scale ( a few ten thousand atoms ). We have only used LAMMPS in our study in NiO. On usual computers, LAMMPS will take an unacceptably long time to simulate larger spin systems such as the 2-dimensional skyrmion textures in BFO where millions of atoms are simulated. In order to simulate these spin textures without the assistance of supercomputers, we chose to develop a new code which parallelizes the computation on GPUs. This homemade code has been delicately designed to optimize the performance on GPUs and its algorithm is specially designed to simulate the spin textures with the $BiFeO_3$ lattice structure. With the aid of the newest GPU, its performance is more than 100 times faster than LAMMPS and it has been the main boost to our study in BFO. In this chapter, we will introduce the main principle, the algorithm of these two software, and the packages on which the homemade code depends. In the end, we will show some verification results of our newly developed homemade code which ensures the accuracy of our results.

## 2.1 General Methods for Simulating Spin Dynamics

### 2.1.1 Numerical Implementation of the LLG Equation

In the LLG equation, the unit vector $\hat{\boldsymbol{s}}$ is required to keep its norm to be 1. In order to achieve this in numerical implementations, the differential equation is solved by [2]

$$\boldsymbol{s}_{t+\Delta t} = \frac{\boldsymbol{s}_t + \Delta t(\boldsymbol{\omega}_{eff} \times \boldsymbol{s}_t) + \frac{1}{4}(\Delta t)^2 \left(2(\boldsymbol{\omega}_{eff} \cdot \boldsymbol{s}_t)\boldsymbol{\omega}_{eff} - \boldsymbol{\omega}_{eff}^2 \boldsymbol{s}_t\right)}{1 + \frac{1}{4}(\Delta t)^2 \boldsymbol{\omega}_{eff}^2} \tag{2.1}$$

### 2.1.2 Algorithm for Finding the Lowest Energy State

We consider a spin system under the evolution of the LLG equation without the injection of energy from the external environment ( e.g. no external fields or STT). In this case, the effective torque $\boldsymbol{\omega}_\Sigma$ in Eq. 1.14 does not contain the damping-like torque, and does not explicitly contain time dependence. Such a system relaxes according to the LLG equation and should eventually relax to the lowest energy state in simple spin systems. To avoid unnecessary computation steps, it is possible to set the precession to be less significant and allow the spin to reach faster its local energy minimum. To achieve this, the simplest way is to set in Eq. 1.16 a large damping parameter $\alpha = 1$ during computation. To further accelerate the relaxation, we omit the first term $\boldsymbol{\omega}_\Sigma$ in Eq. 1.16 and leave only the second term. So we have

$$\boldsymbol{\omega}_{eff} = -\boldsymbol{\omega}_\Sigma \times \hat{\boldsymbol{s}} \tag{2.2}$$

in our computation.

The time step $dt$ is taken to be the proper value such that the spin only proceeds towards the local minimum but does not go over the minimum position. During testing, it was found that the algorithm can be unstable if the time step is set such that the spin rotates more than halfway towards its local minimum, so in our software, we set $dt$ to be smaller than the time it takes to rotate to the middle point towards the minimized position. $dt$ is evaluated in such a manner for each spin and set to be the minimal amongst all the spins in order that the whole spin system avoids instability.

In simple systems and especially ferromagnetic systems, such an algorithm usually could easily find the global energy minimum. However, in more complicated systems, especially those systems with topological structures and those with antiferromagnetic coupling or frustrations, the algorithm usually relaxes to one local energy minimum instead. Inducing some randomness in the initialized system and adding some noise could be useful to avoid saddle points, but still faces difficulties when the local energy minimum is protected by some topology and requires a rather large amplitude of perturbation or a certain collective perturbation. Thus in practice in our simulations, the topology of the end state is assumed and set in the initial system. We take several assumptions based on experimental observations and compare the energy of the relaxed state with the different topologies.

### 2.1.3 Algorithm for Calculating Dynamics

Besides Eq. 2.1 which conserves the spin norm, a straightforward implementation of the algorithm shown in the previous discussions still causes issues, especially in low-damping systems. If all the spins are computed for their effective field and then updated by Eq. 2.1, there will be an extra effective damping that decreases slowly when decreasing the $dt$, which is not intrinsic in the system but stemming from the algorithm. This is due to the fact that the energy is not conserved by this numerical implementation even if we set $\alpha = 0$. To conserve energy, it is necessary that the effective field is calculated for one spin, and the spin precesses (updated in the numerical computation), and then the same steps can be conducted for its neighbouring spins, illustrated by Fig. 2.1. For example, for a cubic lattice where only nearest neighbour and second nearest neighbour interactions are considered, the spins should be divided into at least 18 groups. Each group implements the precession alternatively. Our testing shows that there is no extra damping, and the algorithm is stable as long as $dt$ is kept at

a rather small value ( below 0.1fs for BFO simulation ).

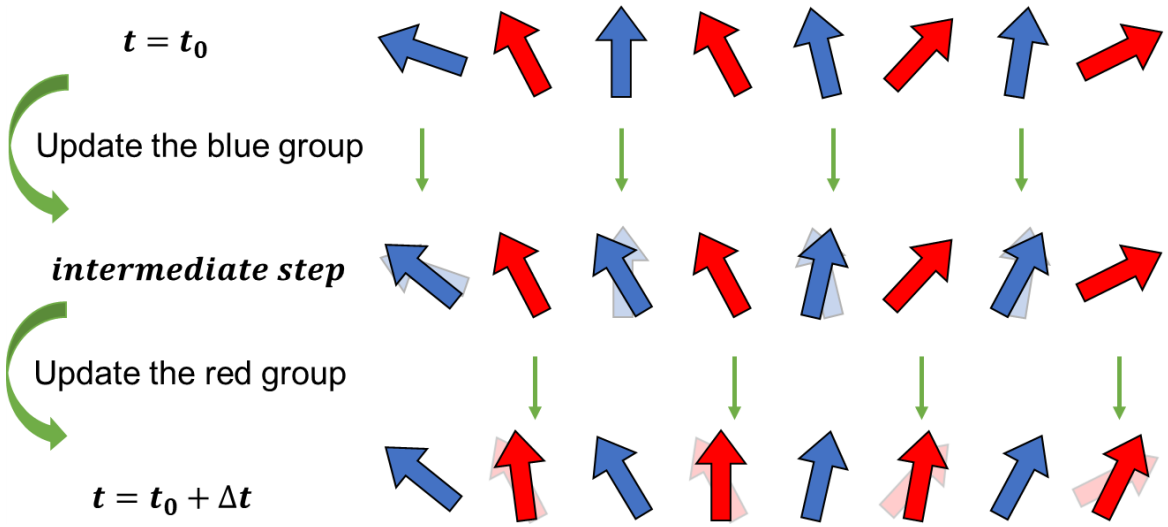


Figure 2.1: An illustration of the algorithm to update spins while preserving the energy. This is an example of a one-dimensional chain where only nearest-neighbour interaction is considered. The spins are divided into two groups, represented by blue and red colours. For each time increment, the update should be divided into two steps.

## 2.2 Parallel Computation and Concurrent Computation

When solving a differential equation numerically, the input quantity of a step is usually based on the result of the previous step of calculation. However, if the quantity is a high-dimensional vector or tensor, during each step it is possible that the scalars inside the vector or tensor do not compute in series, since the scalar's result is not dependent on other scalars' results of the same step. In such a case when the calculation is not serial, it is possible to execute the computation simultaneously on different processing units or cores. This is called parallel computing. Such a way of computing utilizes computing resources in exchange for time consumption. Parallel computing could boost the computation particularly when calculating large-scale systems and with multi-core processing units. Typical hardware used for this purpose is multi-processor computers, for example, a server equipped with a multi-core CPU ( such as Xeon CPU from Intel ), and GPU ( Nvidia RTX 3080 or Nvidia A100). In the thesis, both parallel computing on CPU and GPU are used. CPU parallel is implemented in the software of LAMMPS. GPU parallel is accomplished by a piece of code developed during the thesis.

Concurrent computing is a different concept from parallel computing. It is a form of computing in which several computing processes are executed simultaneously and independently. They do not necessarily synchronize their steps of computation and usually do not share their information with each other during computing. This method is also used to maximize the usage of the computing device in order to shorten the overall time. In the following subsections, we list and briefly introduce the packages and APIs used to obtain the results.

### 2.2.1 CPU Parallel Computing

Two computation APIs for CPU parallelism have been used in the thesis: MPI and Pytorch.

Message Passing Interface ( MPI ) is one of the most widely used models for parallel computing. [48] As the computation is divided into different processes, MPI is a message-passing application programming interface (API) that allows users to define the message to be passed between processes. MPI is the parallel model used in the spin package of LAMMPS.

PyTorch is an optimized tensor library for deep learning using CPUs ( and GPUs). It is featured with CPU (and GPU) parallelism for operations with tensors. It could easily calculate all the frequently used operations in physics, such as cross-product and Einstein summation of tensors. It also provides an advanced indexing feature to easily parallelize parts of a tensor.

### 2.2.2 CPU Concurrent Programming

The Multiprocessing package in Python is a package that allows for concurrent programming. It allows for launching a group of calculations simultaneously. The group of processes can be called by a function with a list of parameters as input. Thus, It can launch the same piece of simulation or analysis code with different parameters. This is useful when a single calculation process does not use up the computing resource, whereas a large number of repetitive calculations need to be launched with different inputs.

It can be especially useful when the calculation results are used to estimate the input of the next iteration of the calculation. Suppose calculation $A$ will produce the result of one data point, and a group of 10 data points is necessary to estimate the input parameters of the next iteration of calculations $A$. Assuming that in our computing task, we need at least three iterations to find the desired result of the data point. Using an automatic code to estimate the next iteration of input, the concurrent programming package could efficiently use the computing resource for each iteration and boost the search for the desired data point.

### 2.2.3 GPU Parallel Computing

Graphical processing units (GPUs) are specialized devices for parallel computing. They are delicately designed in their architecture to simplify the functionality of each core in exchange for the capacity on the chip for more cores that function synchronously. Scientific computations usually do not require the complicated instruction set of CPU so GPU can be the perfect calculation device for large-scale calculation. In our study, the GPU is the main device used for calculating systems with a large number of spins. Due to the constraints of Pytorch in its indexing, a more bottom-layer package called Numba which is based on CUDA is mainly used in our study.

CUDA® is a parallel computing platform and programming model developed by NVIDIA for general computing on GPUs. With CUDA, developers are able to dramatically speed up computing applications by harnessing the power of GPUs. Numba is an open-source JIT compiler and its CUDA feature could directly translate a subset of Python and NumPy code into CUDA kernels and device functions. The parallelism is written in the form of for-loop but executed in parallel by CUDA stream cores. The

main device we use at the moment is Geforce 30 series and it has approximately 10000 CUDA stream cores, so efficient programming would be expected to boost up a calculation by at least 1000 times.

## 2.3 Software

Two software are used to conduct our spin dynamics simulations: LAMMPS and our homemade code.

### 2.3.1 LAMMPS

LAMMPS is an open-source classical molecular dynamics code. It focuses on material modelling. Its name is an acronym for Large-scale Atomic/Molecular Massively Parallel Simulator. It could parallelize the computation by spatially decomposing the simulated system into smaller blocks and passing the information of the related blocks by a few message-passing techniques. The spin package of LAMMPS allows for atomic-scale simulation of spins [49]. It uses MPI as its message-passing system and can parallelize the computation on the CPU. The programming language is C++.

### 2.3.2 Home-made Code

During this thesis, I independently developed a code that parallelizes spin dynamic simulations on GPU. This code uses Python as its programming language. Nvidia GPU was used as the hardware for the parallelization.

The package Numba was the main package used for compiling on GPU. The choice of Numba instead of Pytorch is mainly based on that it provides an easier way to assign the location of the nearest neighbour in RAM. However, we are aware that it is possible to execute similar calculations with the GPU function of Pytorch as long as careful indexing of the tensor is chosen. Finding the nearest neighbour's location is essential for this code as it primarily aims to simulate spins in BFO. Unlike conventional micro-magnetic simulation codes, we are targeting atomic-scale simulations. The first goal is a 2D simulation of BFO at the atomic scale. Its lattice is taken to be cubic with a thin film growth direction along $[111]$. Such a lattice direction induces significant complications regarding mapping the system into a three-dimensional array, passing the information from nearest neighbour spins, and finding the neighbouring spins at the boundary in the case of periodic boundary conditions. With the flexibility of Numba, it is possible to assign a different neighbouring index to each atom and still parallelize the computing.

The code allows for simulating $[111]$ direction BFO and [001] BFO with a cubic geometry. The boundary in the three dimensions can be easily set to be free or periodic. The BFO system can be tuned or excited by any anisotropy, constant or dynamical external excitation including electric field, magnetic field or spin-transfer-torque, on any portion of the whole system. The code allows for initialization of the system with different topologies, including cycloids in any direction, skyrmions with some defined size, skyrmion lattice, or a simple co-linear state.

The evolution can be set to either a relaxation to find the lowest energy state or spin dynamics with a defined Gilbert damping parameter. The relaxation process is set to be several iterations.

Each iteration contains a period of adding random noises and a period of energy minimization as explained in Chapter 2.1.3. The minimization period can be accelerated by optimizing the $dt$. The minimization process stops when it reaches a set of calculation steps or the state stops evolving with a pre-set tolerance. If the energy between two final states of iterations is close enough, then the code jumps out of the loop and reports the minimized state found. The dynamical simulation mode can be set with a certain Gilbert damping parameter. It adopts the method described in Chapter 2.1.3 to avoid the error of extra damping. The dynamical mode could have dynamical stimulation including magnetic fields, electric fields that enter via the magneto-electric coupling, or STT. The dynamical field can typically be a sinusoidal, step, or rectangular function.

The output can be visualized by OVITO, a scientific data visualization and analysis software for molecular and other particle-based simulation models [50]. It can also be analyzed by other small codes that I wrote mainly based on the GPU feature of Pytorch. The analysis includes extracting the spin information along some direction, and calculating the radiated magnetic field at some height above the BFO surface (this is to compare with the results from NV center measurements).

### 2.3.3 Verification of the Software

Our homemade code has been calibrated and verified. The verification starts from calculating the correct energy of the system to each time step of the evolution of the spins with different damping. Each interaction has been individually verified: the exchange energy, Zeeman energy, the magneto-electric interaction, the DMI, the uniaxial anisotropy, the six-fold anisotropy, the spin-transfer torque, etc. Each verification of the interaction starts by calculating two spins, and then $2 \times 2 \times 2$ spins (or $2 \times 2 \times 6$ spins if the z direction is [111]), and then larger systems... The verification has been applied to both LAMMPS and our homemade code. For some processes that are not possible to obtain an analytical benchmark, the two software are cross-benchmarked. In the end, several more complicated cases such as a skyrmion motion under STT are cross-benchmarked. It is also tested that the $BiFeO_3$ spin texture we simulate in our code gives the correct result. The cycloid of BFO has a wavelength of 64 nm (a detailed introduction of $BiFeO_3$ can be found in Chapter 3). Our test result gives the correct texture, as shown in Fig. 2.2. The dynamical results have been verified by comparing them with LAMMPS. The thorough verification ensures that our newly developed software gives correct results.

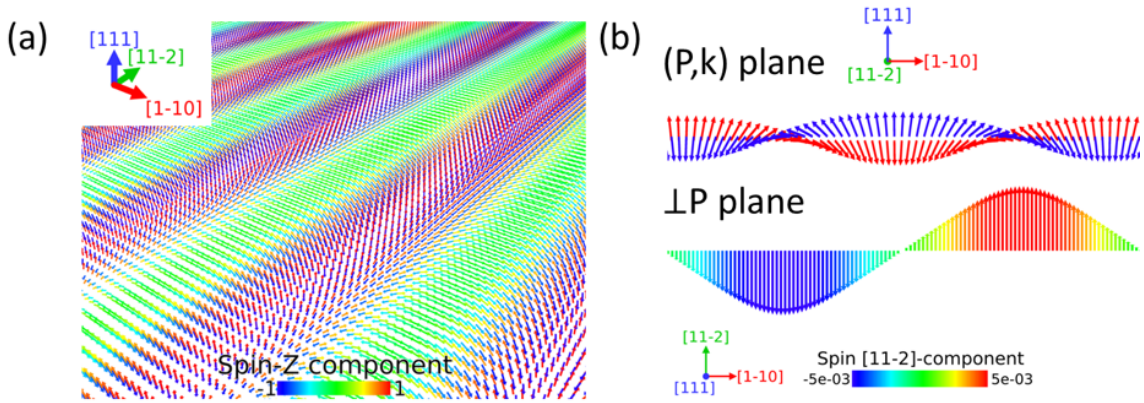


Figure 2.2: Test results of our homemade code. (a) The 64 nm period AF cycloid is obtained as the ground state of bulk BFO. (b) A small concomitant spin density wave is correctly obtained by the simulation in the perpendicular plane caused by the alternating DMI.

# Chapter 3

# NiO and BFO

Two materials, NiO and $BiFeO_3$, have been studied throughout this PhD. NiO was chosen for our study because it has been an archetypal insulating antiferromagnet, with its Neel temperature above room temperature. We chose to study $BiFeO_3$ because it is a room-temperature multiferroic antiferromagnet that couples the ferroelectric order and antiferromagnetic order, which provides an extra handle ( the electric polarization ) to manipulate the AF textures. The magnetoelectric interaction also induces a cycloidal order of the spins which opens the possibility to topological magnetic entities. Due to their importance to this dissertation, we present their properties, models, and histories in this chapter.

## 3.1 Antiferromagnetic NiO

NiO is of interest in several branches of solid-state physics [51, 52]. It has been one of the first studied antiferromagnets owing to its AF state at room temperature. We do not intend to give an overview of its history but only to present its magnetic properties that are related to our studies.

### 3.1.1 Microscopic Model of Spins in NiO

NiO is a 3d-transition metal oxide. It is antiferromagnetic at room temperature with a Néel temperature of $T_N = 523K$. Above $T_N$ NiO has NaCl-like fcc lattice where each sublattice is cubic, as shown in Fig. 3.1 (a) and (b). Below $T_N$ there is a small contraction along the $[111]$ direction. The spins are ferromagnetically coupled within [111] planes and antiferromagnetically coupled between (111) layers. There are four possible choices of (111) layers and six energy-favoured directions in the (111) plane as shown in Fig. 3.1 (c), corresponding to four so-called T-domains and six S-domains. The Hamiltonian of NiO is

$$\mathcal{H} = J_1 \sum_{<i,j>} \boldsymbol{s}_i \cdot \boldsymbol{s}_j + J_2 \sum_{<i,j>'} \boldsymbol{s}_{i'} \cdot \boldsymbol{s}_{j'} + K_1(\boldsymbol{s} \cdot \boldsymbol{a})^2 + K_3|\boldsymbol{s}|^6 \sin^6(\theta)\cos(6\phi) \tag{3.1}$$

where $< i, j >$ represent nearest neighbours, $< i, j >'$ represent next nearest neighbours. The corresponding exchange energies have values $J_1 = -1.37meV$ and $J_2 = 19.01meV$ taken from spin-wave dispersion measurements by inelastic neutron scattering [53]. The spin $|\boldsymbol{s}|$ is 1. $\boldsymbol{a}$ is a unit vector along the [111] direction. $\theta$ and $\phi$ are the polar and azimuthal angles, taking [111] to be the z-axis and $\phi$

is chosen such that [11-2] is a favoured direction in the (111)-plane. $K_1 = 0.038meV$ and $K_3 = 80neV$ are taken from [54], so that the resonance frequency fits the experimental measurements [55, 56]. The $\alpha$ Gilbert damping is taken to be 0.0002 in NiO.

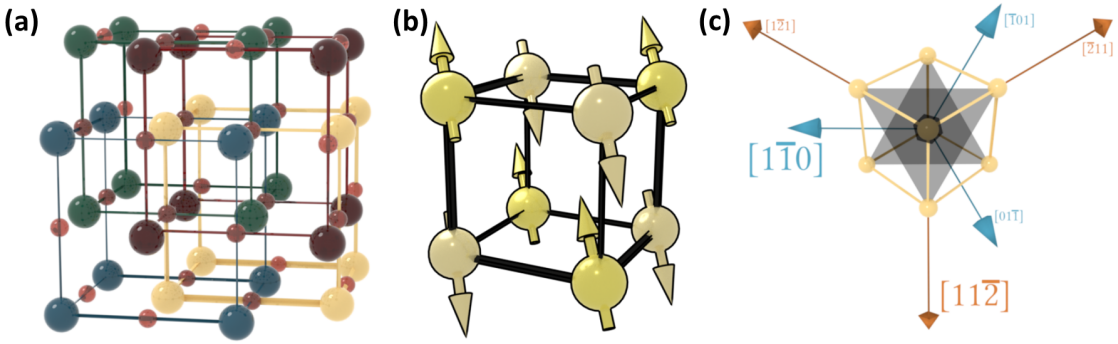


Figure 3.1: (a) NiO crystalline structure. The smaller sphere represents Oxygen; the larger sphere represents Nickel. (b) At room temperature, each sublattice has a G-type antiferromagnetic texture. (c) The easy axes are represented by the red arrows and the hard axes by the blue in the (111) plane. The figures are taken from [2].

## 3.2 Multiferroic $BiFeO_3$

### 3.2.1 A brief History of the Multiferroic $BiFeO_3$

Most ferroic materials show only one order, such as a magnetic order, an electric polarization or a distortion order. Among these materials, a few show two or more orders simultaneously. These materials are called multiferroic materials. An important feature of multiferroics is that often, the different ferroic orders interact. The multiferroics were first studied in Russia in the early 1960s [57, 58, 59]. Some of them are ferroelectric and (anti)ferromagnetic. Thus one could envision the control and manipulation of the magnetic order by an electric field, and the electric polarization by applying a magnetic field. However, most known multiferroics have low ordering temperatures and the only one that could function at room temperature was found to be $BiFeO_3$. In 1958 - 1960, $BiFeO_3$ (BFO) was first studied by Smolenskii's group in Leningrad, and at that time it was called a "ferroelectromagnet". Around the same years, based on symmetry arguments Dzyaloshinskii proposed the possibility of a magnetoelectric coupling term in the free energy of $Cr_2O_3$ [60], one of the first studied materials of this type. Later Moriya showed the possible mechanism based on Anderson's superexchange theory in the presence of spin-orbit coupling and deduced its strength from microscopic modeling [61]. This type of interaction, called today the Dzyaloshinskii–Moriya Interaction (DMI), has the form of Eq. 1.12 in the spin Hamiltonian. This Hamiltonian plays a crucial role in the properties of $BiFeO_3$. The early interest in multiferroics declined after the first Conference on Magnetoelectric Interaction Phenomena in Crystals ( MEIPIC - 1 ). The motivation for the functionality of $BiFeO_3$ was lost due to the high conductivity and the secondary phases of the samples at that time.

About 30 years later, the interest was brought up again. The revival was mainly due to newer experimental techniques, novel synthesis methods, and updated theoretical concepts. In 2003, strikingly large spontaneous polarization that is 10 times larger than measured before was found by Wang et al [62, 63, 64] in thin films. This large polarization was later found to be intrinsic instead of strain-induced, which is demonstrated by the measurement of single crystal $BiFeO_3$ by Lebeugle et al in 2007 [65, 66]. The single crystal platelet was high-quality $BiFeO_3$ fabricated by solid-state reaction and leaching with $HNO_3$. It was found that the fabrication of high-quality $BiFeO_3$ was crucial since the presence of oxygen vacancies could lead to some conductivity preventing an accurate measurement of the ferroelectricity; the presence of two impurities (Bi-poor phase) $Bi_2Fe_4O_9$ and (Bi-rich phase) $Bi_{25}FeO_{39}$ could also lead to measurement problems, such as inducing a ferromagnetic moment at low temperature. In thin films [67] and single crystals [31] electric control of antiferromagnetic domains was found. This property later became a crucial part of the design of magnetoelectric spin–orbit logic (MESO) [68] by Intel cooperation. As high-quality $BiFeO_3$ was more reliably fabricated and different experimental techniques were used for its measurements, the basic properties of $BiFeO_3$ became gradually clear.

### 3.2.2 Basic Properties of $BiFeO_3$

There are several theoretical models used to understand BFO. Ab initio methods in the framework of density functional theory (DFT) have been used to determine the ground state properties, including atomic and magnetic structures, and the origin of the polarization, as well as several metastable states. DFT calculations also help to calculate the parameters for an effective Hamiltonian depending on strain, polarization or magnetic moment. Besides DFT, Landau-Ginzburg theory is used to calculate phase transitions, where the phenomenological free energy is expanded into powers of different order parameters. Linear spin-wave theory is also used to determine the magnetic properties. One starts from an effective Hamiltonian related to spins and calculates the relaxation or dynamics based on the Landau-Lifshitz-Gilbert ( LLG ) equation, or from writing the Lagrangian of the system and solving the Euler–Lagrange equation. Linear spin-wave theory based on an effective Hamiltonian will be the main theory that we use in this study. In order to accurately model our system, it is crucial to determine the parameters in the effective Hamiltonian. Some of the parameters can be calculated by DFT, but DFT fails to obtain the correct sign for the uniaxial anisotropy and the correct rotation plane for the cycloid. The anisotropy is measured to be easy-axis whilst DFT gives easy-plane[69]. One possibility [58] is due to an overestimation of the energy of antiferrodistortive (AFD) rotation. It is in competition with a ferroelectric (FE) distortion. AFD favours easy-plane anisotropy while FE favours easy axis. Since the two energies are close in value, a slight overestimation could result in an anisotropy with the correct order of magnitude but the wrong sign. Since DFT calculations contradict some experiments, we decided to choose our parameters based on experimental measurements.

The crystalline structure of $BiFeO_3$ is pseudocubic with a perovskite structure $ABO_3$ and a rhombohedral distortion along the [111] direction (see Fig. 3.2 ). The lattice parameter is 3.96 Å[31] and the rhombohedral angle is 89.3-89.4 ° [70]. The Fe and Bi ions are displaced along the [111] direction by 0.13Åand 0.54Å. The oxygen has an alternative octahedral tilting which is called an antiferrodistortive (AFD) rotation. The rotation angle is 13.8 degrees around the [111] direction. The curie temperature

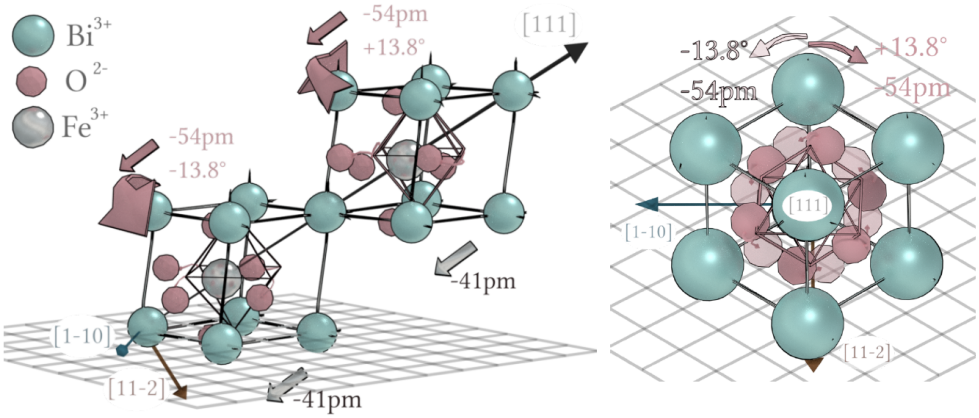


Figure 3.2: $BiFeO_3$ crystalline structure. Figure taken from [2]

of the ferroelectricity is 1103 K. The Néel temperature of the antiferromagnetism is 643 K [71]. Due to the Fe-O-Fe superexchange, the spins are G-type antiferromagnetically arranged. The electric polarization induces a spiral modulation of the antiferromagnetic vector by virtue of the magnetoelectric interaction. The plane of the spin cycloid is parallel to the [111] direction and its wavelength is measured to be 62 nm. Along with the cycloid, there is also a canting of the spins perpendicular to the cycloid plane, causing a spin density wave(SDW), which originates from the octahedral tilting.

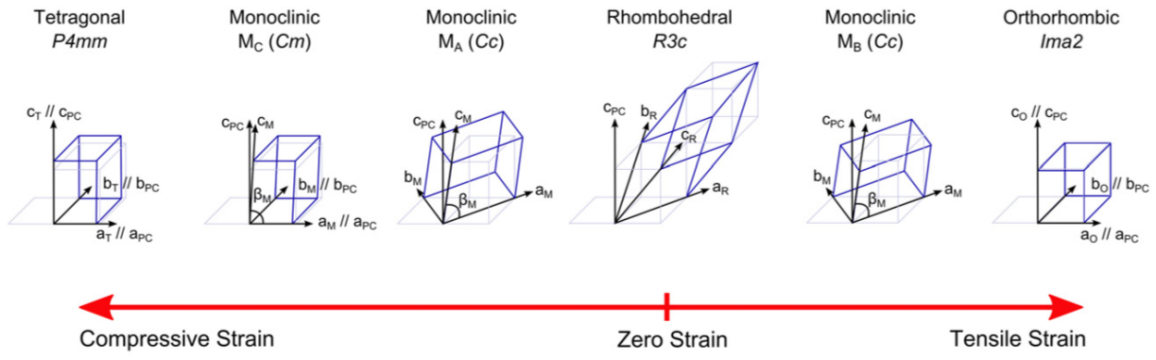


(a)

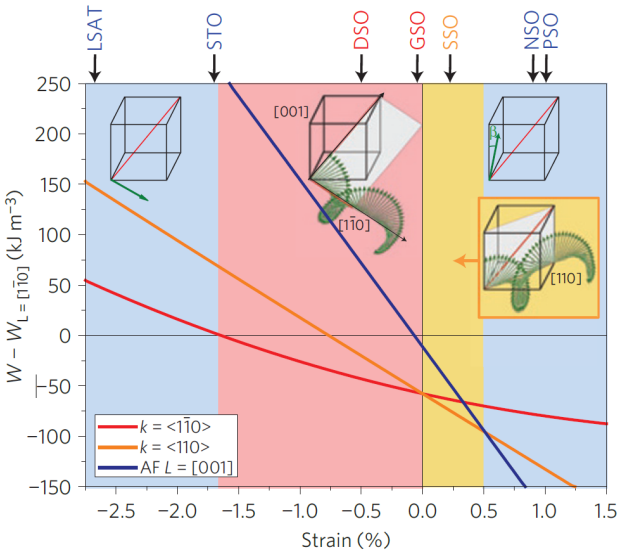


(b)

Figure 3.3: (a) An illustration of the crystalline structure of $BiFeO_3$ thin films under varied strain. (b) An illustration of the magnetic order under strain control. Figures taken from [72, 126].

The properties of $BiFeO_3$ could be tuned in thin films [72]. Thin film technologies have been considered to have similarities to hydrostatic pressure [73, 74]. This is due to the fact that by choosing the substrate, the mismatch of the lattice parameters could lead to a strain in the crystalline structure of the objective material, which is easier to control than applying pressure. The strain applied could be uniaxial or bi-axial; it could be tensile or compressive. $BiFeO_3$ thin film could belong to a different crystalline symmetry group than in a single crystal, as illustrated by Fig. 3.3 (a). The magnetic order could be tuned under varied strain; the cycloid structure could be eliminated when enough strain is applied, as illustrated by Fig. 3.3 (b). The strain induces an anisotropy in the magnetic system, which can be easy-axis or easy-plane. If it is over some threshold, BFO thin films could end up with a collinear state.

Several magnon modes exist in BiFeO3. The high energy magnons are probed by inelastic neutron scattering [75]. Since these high-energy modes depend only on the exchange interaction, they are used to measure the value of exchange. Low energy (k close to 0) modes of spin-waves are measured

by polarized Raman spectroscopy. They can be categorized into the cyclon ( where spins oscillate within the cycloid plane) mode and the extra-cyclon ( where spins oscillate out of the cycloid plane).

### 3.2.3 Microscopic Model of Spins in BFO

The Hamiltonian of BFO is taken to be [76] :

$$\begin{aligned}\mathcal{H} =& J_1 \sum_{<i,j>} \boldsymbol{s}_i \cdot \boldsymbol{s}_j + J_2 \sum_{<i,j>'} \boldsymbol{s}_i \cdot \boldsymbol{s}_j + D_1 \sum_{<i,j>} (\boldsymbol{z}' \times \frac{\boldsymbol{e}_{ij}}{a}) \cdot (\boldsymbol{s}_i \times \boldsymbol{s}_j) \\ &+ D_2 \sum_{<i,j>} (-1)^{h_i} \boldsymbol{z}' \cdot (\boldsymbol{s}_i \times \boldsymbol{s}_j) - K_1 \sum_i (\boldsymbol{z}' \cdot \boldsymbol{s}_i)^2 \\ &- K_3 |\boldsymbol{s}|^6 \sum_i \sin^6 \theta_i \cos 6\phi_i - 2\mu_B \sum_i \boldsymbol{s}_i \cdot \boldsymbol{B}\end{aligned} \tag{3.2}$$

where $\boldsymbol{z}'$ is taken to be along the [111] direction, and $\theta_i$ and $\phi_i$ the angles in the polar coordinate system. $< i, j >$ represents a summation over nearest neighbours; $< i, j >'$ represents next nearest neighbours. $J_1$ and $J_2$ are exchange energies; $D_1$ represents the magneto-electric interaction; $D_2$ represents DMI; $K_1$ and $K_3$ represent the uniaxial and six-fold anisotropies. We use the parameters from [76] which are mostly extracted from experiments and generally accepted. The parameters are given in Table 3.1. In our dynamical simulation, we take $\alpha$, the damping term in Eq. 1.13, to be $0.001$, a small value due to the fact that BFO is an insulator. For example, YIG is a ferromagnetic insulator with a low damping of $10^{-4}$.

Table 3.1: BFO parameters

| Parameter | $J_1$ | $J_2$ | $D_1$ | $D_2$ | $K_1$ | $K_3$ | $\alpha$ | $\lvert\boldsymbol{s}\rvert$ |
|---|---|---|---|---|---|---|---|---|
| Value in meV | -5.3 | -0.2 | 0.18 | 0.06 | 0.004 | 6 $\times 10^{-6}$ | 0.001 | 2.5 |

# Chapter 4

# NiO Spin Wave Control and Logic Gates

## 4.1 Background

Besides the current semiconductor electronics, transmission and processing of information by spins have been considered an alternative technique for information processing. Transmission of information by spin waves, especially in insulators [20], could achieve a lower dissipation time due to the absence of charge displacement. Information processors such as logic gates with a hybrid structure of spin waves and electronics have been demonstrated [77, 78] and those purely based on spin waves have been proposed [79]. However, the demonstration of these logic devices faces challenges due to the complexity of the manipulation of the propagation of spin waves [80]. In this background introduction, the difficulty of manipulating spin waves in ferromagnets for the purpose of computing will be discussed. Then, previous studies of the spin waves in antiferromagnets, especially in NiO will be summarized.

### 4.1.1 Spin Waves in Ferromagnets

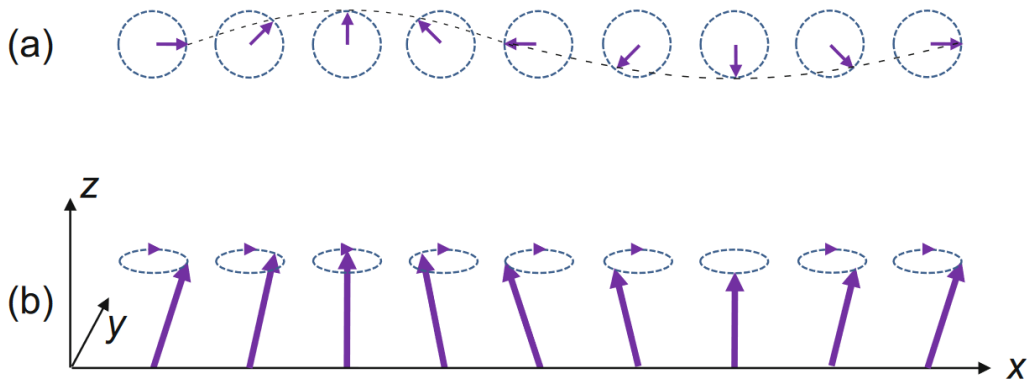


Figure 4.1: Illustration of a spin wave in a linear chain of classical spins propagating in the +x direction taken from [23]. The distance between the two spins at the ends corresponds to one wavelength. (a) Top view of the spins (b) Side view

Spin waves are the eigen-excitations of a magnetic system above its ground state, first proposed by Felix Bloch[81]. They were found to be able to propagate in ferromagnetic systems. An illustration of spin waves is shown in Fig. 4.1. The most studied spin waves are the ones whose wavelengths are much larger than the lattice constant. The property of the propagation of these low-wave-vector spin-waves is almost completely determined by dipole-dipole interactions [80]. It is important to note here that for ferromagnets, the internal field in the material, resulting from the external applied field and the demagnetization field from the internal dipole-dipole interaction, plays a crucial role in the behaviour of spin waves.

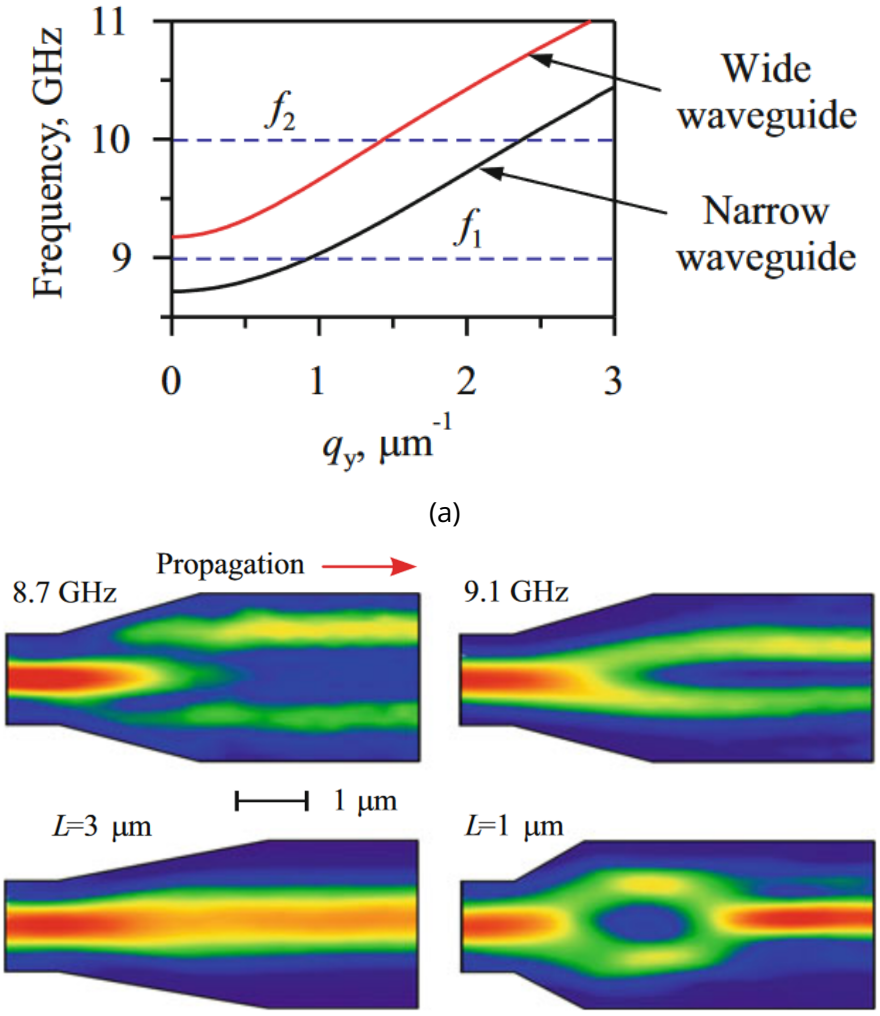


Figure 4.2: Spin waves propagating through a waveguide with varied width taken from [82, 80]. (a) shows the dispersion relation of the two widths. (b) shows maps of the spin-wave intensity measured at the excitation frequencies of 8.7 and 9.1 GHz, as labelled. The two maps on the left have longer transition areas ( 2 $\mu$m) whilst the two on the right have transition a area of 1$\mu$m.

For spin waves propagating in a 2D geometry, such as thin films, the dispersion relations are different for magnetization out-of-plane and in-plane. Even for magnetization in-plane, the dispersion relation is drastically different for spin waves propagating parallel or perpendicular to the magnetization direction(the demagnetization field depends on the direction of magnetization). Spin waves propagating in thin layers ( typically $100nm$ ) of narrow stripes ( typically $2\mu m$ ) are often studied for quasi-1D propagation [83]. As in the 2D case, the dispersion relation is different depending on the magnetization direction. Due to the constrained boundary, the internal field is inhomogeneous along the constrained dimension. Such inhomogeneity generally leads to the presence of edge modes [84].

The demagnetization field depends on the ratio between the width and the thickness, thus altering the dispersion relation. By simply varying the width of the stripe, spin-waves could either propagate through or split into two edge modes, as shown in Fig. 4.2. The inhomogeneity of the internal field and the anisotropy of spin wave propagation introduce some difficulties when waveguides need to be curved. Spin waves cannot propagate through a simple corner [85] and reflect in a complicated pattern[86]. This can be circumvented by applying a magnetic field that follows the waveguide which complicates matters. Such a magnetic field keeps the magnetization perpendicular to the waveguide direction by applying a strong current ( $10^7 A/cm^{-2}$ on a $50nm$ thick $2\mu m$ width gold wire ) below the curved waveguide. This way, spin waves propagate through the corner on some specific frequency range. This method consumes a rather high energy and could lead to extra damping or spin-wave attenuation. The phase of the propagating spin wave could be tuned by the magnetic field of an electric current. Such a tuned phase could build constructive or destructive interferences, which has been experimentally demonstrated. This can lead to the building of logic gates [77, 78] based on phase control and interference of spin waves as proposed theoretically [79], but not experimentally demonstrated yet. The main reason for the lack of a real-life demonstration is that even the simplest design requires the curvature of waveguides. Still, due to the difficulty of building a simple curved waveguide, as well as the complexity of building a spin wave coupler and decoupler, it eventually becomes complicated and difficult to experimentally achieve.

### 4.1.2 Spin Waves in Antiferromagnets

In contrast to ferromagnetic materials, which have complicated behaviour due to the effect of demagnetization fields, antiferromagnetic materials have anti-aligned moments at the atomic scale and show no magnetization. The spin waves in antiferromagnets are simpler as they are determined by the exchange interaction and magnetic anisotropy [23]. Antiferromagnetic spin-wave guides could vastly simplify the situation when one needs to consider the geometry. Antiferromagnetic spin waves also benefit from the high frequency of their magnetic resonance, typically at the THz level in contrast to ferromagnetic resonance in the GHz range. The ultrafast dynamics of spins in antiferromagnets allows for the possibility of information processing at the THz level. Since a vast majority of antiferromagnets are insulating oxides, the damping in these systems is expected to be one to two orders of magnitude lower than in ferromagnetic metals but similar as that in YIG, which permits lower dissipation and longer spin wave propagation [22].

Theoretical models have been studied for calculating antiferromagnetic spin waves. The most straightforward model is atomic-scale Hamiltonian and atomic-scale simulations based on the LLG equation[54]. Besides atomic-scale simulations, two types of analytical models have been elaborated in the literature. One model is based on the continuous approximation of two sublattices that are antiferromagnetically coupled. But many articles that adopt this model are actually calculating the spin dynamics of synthetic antiferromagnets (SAFs) [87, 88, 89]. The difference is in the coupling term, which will be mentioned in the following discussion. If not properly treated, the coupled two sublattices may not be generally the correct equation for real antiferromagnets. Another model is based on calculating the continuous approximation of magnetization and antiferromagnetic vector, which is called the Sigma Model [90, 91, 92, 30]. The dynamical equation of this model can be derived

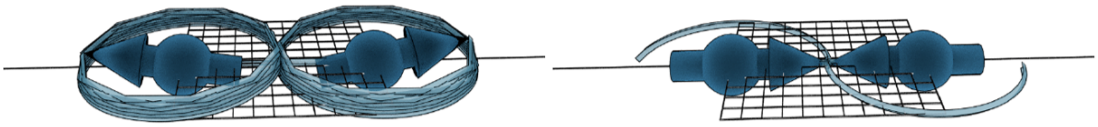

Figure 4.3: A short STT pulse cants the AF, which triggers precession around the net magnetization axis (vertical). Left: initial canting of 25° with its induced precession. Right: initial canting of 1.5° resulting in an orientation swap. The figure is taken from [2]

from the LLG equation of two sublattices with properly treated AF coupling. We will adopt this model when understanding the results of our atomic simulations.

The antiferromagnetic dynamics in NiO has been calculated in several studies. Besides the intrinsic resonance mode, NiO under homogeneous spin-transfer torque has been studied, including the S-domain switching [93, 94, 54, 95]. It has been shown that under sufficiently large constant STT, the spins in NiO will precess around the STT direction. A short pulse of STT cants the AF, which transfers some angular momentum to the system; the angular momentum will then be released by a switching of the S-domain of NiO, as shown in Fig. 4.3. The propagation of antiferromagnetic spin waves has also been demonstrated in experiments[22]. Manipulations of spin waves in easy-axis antiferromagnets [96, 97] and logic gate design based on easy-axis antiferromagnets [98] have been proposed in theory. However, in practice, the archetypal room temperature AF, such as NiO, is easy-plane. The manipulation of spin waves in NiO, or the propagations of domain walls (DWs) in waveguides, especially in waveguides with special geometries, have not been studied.

## 4.2 Theory – Wave Equations of the Spins in Easy-Plane Antiferromagnets

Assume a cubic lattice G-type antiferromagnet. The Hamiltonian is written as

$$\mathcal{H} = J \sum_{<i,j>} \hat{\boldsymbol{s}}_i \cdot \hat{\boldsymbol{s}}_j \tag{4.1}$$

where $< i, j >$ represents nearest neighbours. If we use two continuous vector fields $\boldsymbol{m_1}$ and $\boldsymbol{m_2}$ ( $|\boldsymbol{m_1}| = |\boldsymbol{m_2}| = 1$ ) to represent it, we have

$$\mathcal{H} = J \sum_{<i,j>} \boldsymbol{m_1}(\boldsymbol{r_i}) \cdot \boldsymbol{m_2}(\boldsymbol{r_j}) \tag{4.2}$$

where $\boldsymbol{r_i}$ and $\boldsymbol{r_j}$ are the position vectors of $i$ and $j$ sites. It can be expressed by a form taking the differentiation of the two vector fields

$$\mathcal{H} = J \sum_{\boldsymbol{a}} \sum_{i} \boldsymbol{m_1}(\boldsymbol{r_i}) \cdot [\boldsymbol{m_2}(\boldsymbol{r_i}) + \frac{1}{2} a^2 \partial_{\boldsymbol{a}}^2 \boldsymbol{m_2}(\boldsymbol{r_j})] \tag{4.3}$$

where the summation over $i$ is only over one of the two sublattices, $\boldsymbol{a}$ is the displacement vector of the nearest neighbour sites. For our cubic lattice, it becomes

$$\mathcal{H} = 6J \sum_i \boldsymbol{m_1}(\boldsymbol{r_i}) \cdot \boldsymbol{m_2}(\boldsymbol{r_i}) + J \sum_i \boldsymbol{m_1}(\boldsymbol{r_i}) \cdot a^2 \nabla^2 \boldsymbol{m_2} \tag{4.4}$$

Symmetrizing the expression by doing the same for the other sublattice for half of the exchange, we have

$$\begin{aligned} \mathcal{H} =& 3J \sum_i \boldsymbol{m_1}(\boldsymbol{r_i}) \cdot \boldsymbol{m_2}(\boldsymbol{r_i}) + 3J \sum_j \boldsymbol{m_1}(\boldsymbol{r_j}) \cdot \boldsymbol{m_2}(\boldsymbol{r_j}) + \frac{1}{2} J \sum_i \boldsymbol{m_1}(\boldsymbol{r_i}) \cdot a^2 \nabla^2 \boldsymbol{m_2}(\boldsymbol{r_i}) \\ &+ \frac{1}{2} J \sum_j \boldsymbol{m_2}(\boldsymbol{r_j}) \cdot a^2 \nabla^2 \boldsymbol{m_1}(\boldsymbol{r_j}) \end{aligned} \tag{4.5}$$

where summations over $i$ and $j$ are over one of the two sublattices respectively. Taking the limit $\lim_{a \to 0}$, we end up with integral expressions

$$\mathcal{H} = \frac{3J}{a^3} \int d^3\boldsymbol{r}\, \boldsymbol{m_1} \cdot \boldsymbol{m_2} + \frac{J}{4a} \int d^3\boldsymbol{r}\, (\boldsymbol{m_1} \cdot \nabla^2 \boldsymbol{m_2} + \boldsymbol{m_2} \cdot \nabla^2 \boldsymbol{m_1}) \tag{4.6}$$

This expression is different from the SAF expression. The first obvious difference is that the first term is much larger than the second one. The "antiferromagnetic coupling" is much larger than that in SAFs so a misalignment of the two sublattices is almost impossible. This leads to some fundamental differences, such as when AF skyrmions are moving they can never "disentangle" into two separate ferromagnetic ones as opposed to SAF skyrmions [89]. The second difference is the "ferromagnetic-like" exchange coupling term. In SAFs, each layer is a real ferromagnet, and the exchange coupling has the form $\boldsymbol{m_1} \cdot \nabla^2 \boldsymbol{m_1}$. For some common situations such as when we have STT applied in an area of our system, the $\nabla^2$ terms could be opposite for the two sublattices, and this different term in AFs and SAFs will lead to an opposite sign of the second part of the Hamiltonian (the part after the plus ).

The dynamical evolution of spins is approximated by the LLG equation Eq. 1.13. Taking the continuous limit of this equation (especially the effective field), we obtain

$$\frac{\partial \boldsymbol{m_i}}{\partial t} = \boldsymbol{\omega_i} \times \boldsymbol{m_i} - \alpha \frac{\partial \boldsymbol{m_i}}{\partial t} \times \boldsymbol{m_i} \tag{4.7}$$

where i = 1,2. $\omega_i$ here is a continuous vector field that comes from the atomic expression. The limit must be taken in the form of $\lim_{a \to 0} \frac{\partial \mathcal{H}}{\boldsymbol{s}}$ instead of $\partial \frac{\lim_{a \to 0} \mathcal{H}}{\boldsymbol{m_i}}$ where $a$ represents lattice constant. Otherwise, an error of factor 2 will appear.

The sigma model describes the AF with two other vector fields, defined as $\boldsymbol{m} = \frac{\boldsymbol{m_1} + \boldsymbol{m_2}}{2}$ , $\boldsymbol{l} = \frac{\boldsymbol{m_1} - \boldsymbol{m_2}}{2}$, which represents the magnetization and the antiferromagnetic vector. For most of the cases and throughout our study, we can have $m \ll l$ and $l \approx 1$. From their definition we have

$$\boldsymbol{m} \cdot \boldsymbol{l} = 0 \tag{4.8}$$

and

$$\boldsymbol{m}^2 - \boldsymbol{l}^2 = \boldsymbol{m_1} \cdot \boldsymbol{m_2} \tag{4.9}$$

The time derivative of these two vector fields can be derived from the LLG equation. For simplicity, we neglect the small terms due to $m \ll l$ and since we are dealing with insulating AFs where damping is small, we neglect the damping term in LLG and obtain

$$\partial_t \boldsymbol{m} = \frac{J}{\hbar} a^2 (\boldsymbol{l} \times \nabla^2 \boldsymbol{l}) \tag{4.10}$$

and

$$\partial_t \boldsymbol{l} = \frac{12J}{\hbar} (\boldsymbol{m} \times \boldsymbol{l}) \tag{4.11}$$

We can thus obtain a second-order differential equation only related to $\boldsymbol{l}$

$$\boldsymbol{l} \times \partial_t^2 \boldsymbol{l} = \frac{12J^2 a^2}{\hbar^2} (\boldsymbol{l} \times \nabla^2 \boldsymbol{l}) \tag{4.12}$$

Suppose our $\boldsymbol{l}$ rotates only in-plane due to an easy plane anisotropy, which is similar to the $\beta$ mode mentioned in Chapter 1.2.3 but easy-axis anisotropy is taken small which is indeed the case for NiO. Suppose the rotation angle is described by $\phi$. Then the dynamics of the $\boldsymbol{l}$ can be described by a wave equation

$$\partial_t^2 \phi = v_0^2 \nabla^2 \phi \tag{4.13}$$

with $v_0 = 2\sqrt{3} Ja/\hbar$. For NiO, $v_0$ is calculated to be 41.7 km/s. This is a simplified model of NiO since we have considered only one of the four cubic sublattices and the interactions are also simplified. We will see that in the following section, our numerical simulations give the same result.

Wave equations can be obtained in a similar way if one includes the easy-plane and the smaller easy-axis anisotropy in the Hamiltonian. It can be written in the form of

$$\partial_t^2 \phi = v_0^2 \nabla^2 \phi - \omega_0^2 (\phi - \phi_0) \tag{4.14}$$

where $\omega_0 = \frac{12\sqrt{3(-JK_3)}}{\hbar} = 2\pi \times 0.2$ THz is the eigen-frequency of the $\beta$ mode of the $k = 0$ case. We can thus obtain the dispersion relation

$$\omega = \sqrt{v_0^2 k^2 + \omega_0^2} \tag{4.15}$$

and the group velocity by taking $v_g = \frac{\partial \omega}{\partial k}$ to get

$$v_g = \frac{v_0}{\sqrt{1 + (\frac{k_0}{k})^2}} \tag{4.16}$$

We can see that at the high k limit, $v_g \approx v_0$, while at the low k limit $v_g \approx 0$.

Suppose we apply STT perpendicular to the easy plane. The time derivative of $\boldsymbol{m}$ will become

$$\partial_t \boldsymbol{m} = \frac{Ja^2}{\hbar} (\boldsymbol{l} \times \nabla^2 \boldsymbol{l}) + \boldsymbol{J}_{STT} \tag{4.17}$$

where $J_{STT}$ represents the STT stimuli. A very short pulse of STT can be approximated as a Dirac function that rapidly changes the magnetization.

## 4.3 Results

### 4.3.1 Propagation Properties along a Stripe

The spin dynamics of NiO under spin-transfer torque has already been studied [94, 93, 95, 54]. A pulse of STT applied along $[111]$ could trigger an in-plane oscillation or switching of the S-domain. Here we assume that a 100 fs short pulse of STT is applied along the [111] direction, on one end of a long stripe of NiO which serves as a waveguide, as shown in Fig. 4.4. Short pulses of STT could be applied by the ultrafast demagnetization from an adjacent ferromagnetic material. The process is induced by intense femtosecond laser pulses.

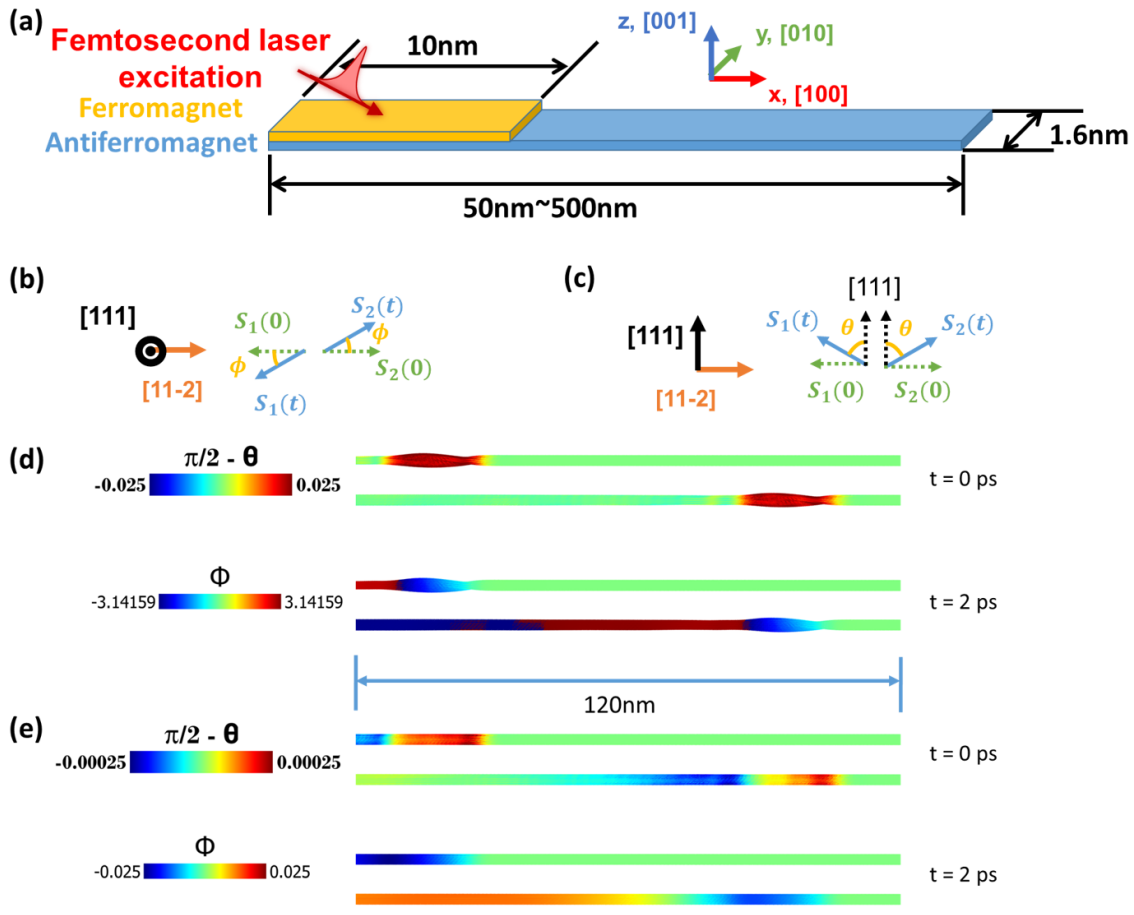


Figure 4.4: (a) shows the scenario to apply 100fs STT pulses on the end of a stripe. (b) and (c) show the definition of $\theta$ and $\phi$. The spins are initially along the [11-2] easy axis. $\phi$ is the angle of the precession of the two sublattice spins ($\boldsymbol{S}_1$ and $\boldsymbol{S}_2$ ), or equivalently the angle of $\boldsymbol{l}$ rotation in the (111) plane. $\theta$ is defined to be the canting angle towards [111] direction, which is approximately the $\boldsymbol{m}$ amplitude. The static directions of the spins are denoted $\boldsymbol{S}_1(0)$ and $\boldsymbol{S}_2(0)$ and their directions at time $t$ are $\boldsymbol{S}_1(t)$ and $\boldsymbol{S}_2(t)$. (d) is the propagation of an STT-induced domain wall. (e) shows the propagation of an oscillating spin wavefront.

The static spin direction is in the (111) plane along the [11-2] easy axis. The short pulse of STT cants the AF spins along the [111] direction with a very small angle (below 2° in this chapter ). The spins thereafter precess in the (111) plane. We extract two angles: $\theta$ which represents the canting along [111] and $\phi$ which represents the rotation of the $\boldsymbol{l}$ vector in the (111) plane with respect to its static direction, as illustrated by Fig. 4.4 (b) and (c). The wavefront can be visually seen in Fig. 4.4 (d) and (e). The envelope of the wavefront is more concentrated if the spin wave is a translating domain wall. This is understandable: since the spin precession finishes at another easy axis, the oscillations thereafter are around a new static position and the oscillation angles are smaller than the overall reorientation angle. This can also be seen in Fig. 4.5, where the envelope of the $\phi$ and $\theta$ are shown. If the STT is small enough such that the $\phi$ angle is small compared with 60°, the dynamics is an oscillation around the static direction, triggering an oscillating spin wave. The $\theta$ in this case also oscillates. If the STT is sufficient to switch the S-domain, the $\theta$ landscape is a uni-polar spike. The propagating domain wall has a smaller width ( 20nm ) compared with the static ones ( typically 200nm in the literature ). This is due to the relativistic-like wave equation of antiferromagnetic spins[27, 30]. The propagating domain has a shorter length due to the Lorentz contraction.

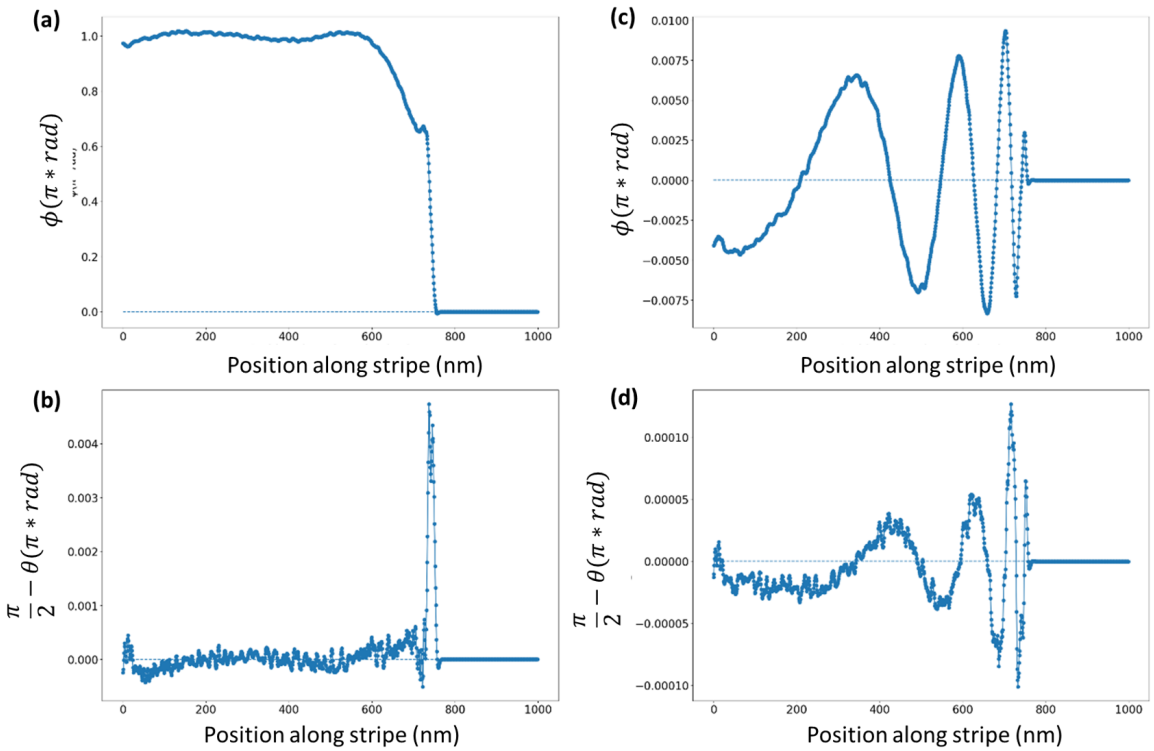


Figure 4.5: (a) and (b) show landscapes of the propagating domain wall. (c) and (d) show the oscillating spin wave. The amplitudes of the domain wall and spin wave are different from Fig. 4.4, but the landscapes are similar.

As shown in Fig. 4.6, the wave propagates at a velocity of about 41.7 km/s regardless of the STT amplitude, which agrees with theory. As shown in Fig. 4.7 (a) and (b), although the wavefront propagates

at about 41 km/s, the low k components travel at a lower velocity due to the non-linear dispersion relation induced by the anisotropy. They tend to cluster around the original point, causing the wavelength of the oscillation around the starting position to increase as the wave propagates. This can also be seen from the shifted peak of the Fourier spectrum in Fig. 4.7 (c).

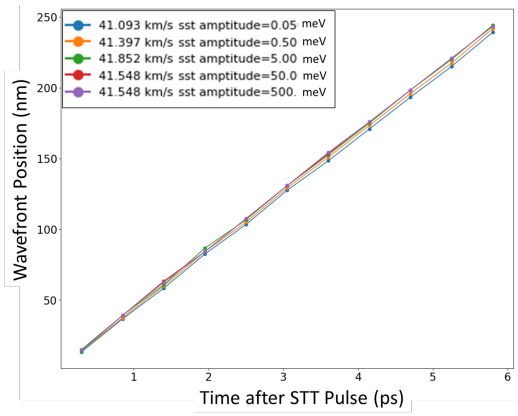


Figure 4.6: The wavefront position vs. time. The velocity of the wavefront is around 41.7 km/s regardless of the amplitude.

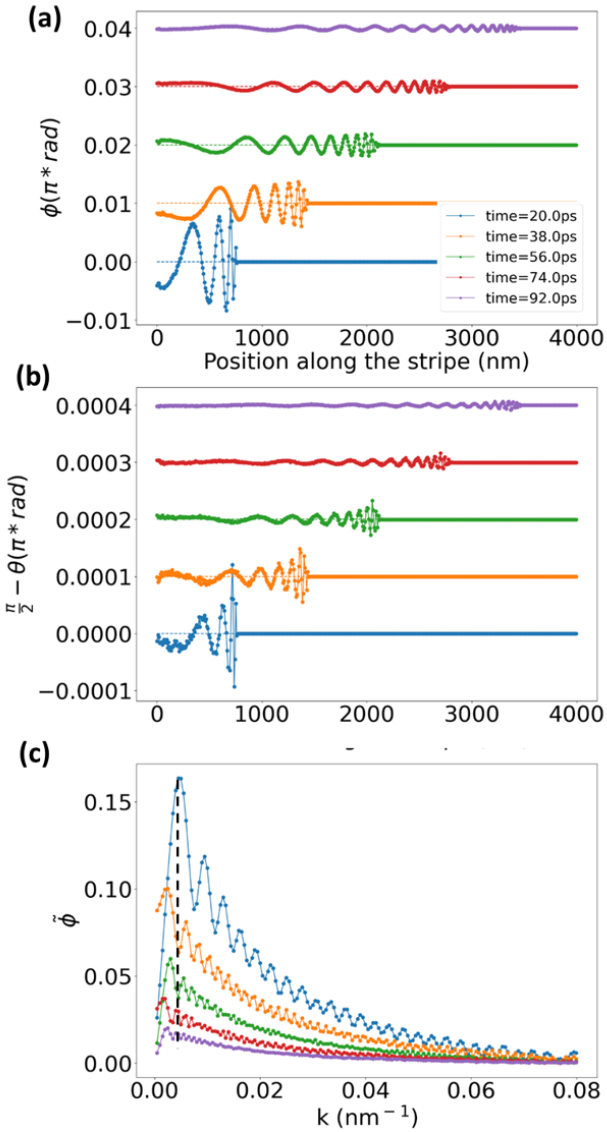


Figure 4.7: The landscape of spin wave. (a) and (b) are the $\phi$ and $\theta$ at different times after the end of the STT pulse. (c) is a Fourier transform of (a), with a dashed line denoting the peak position of the 20ps snapshot.

Similar effects exist for the propagating domain wall, shown in Fig. 4.8. As the 180° domain wall propagates, the $\theta$ amplitude decreases. At some point, it splits into a 60° domain wall and a 120°. The 120° continues to propagate, whilst the 60° domain wall slows down. The 120° domain wall also breaks into two 60° domain walls afterwards, with one propagating at 41.7 km/s and the other one slowing down. The majority of the $\boldsymbol{m}$ is carried by the one that propagates at a higher velocity. The breaking of the domain wall can be seen from both $\phi$ and $\theta$, indicating that the domain wall that breaks off and slows down also carries a small proportion of $\boldsymbol{m}$. The velocity of the wavefront remains constant, even after the last domain wall slows down. We can see from Fig. 4.8 (b) that an oscillation continues

to propagate over the domain wall which stops around 3000nm.

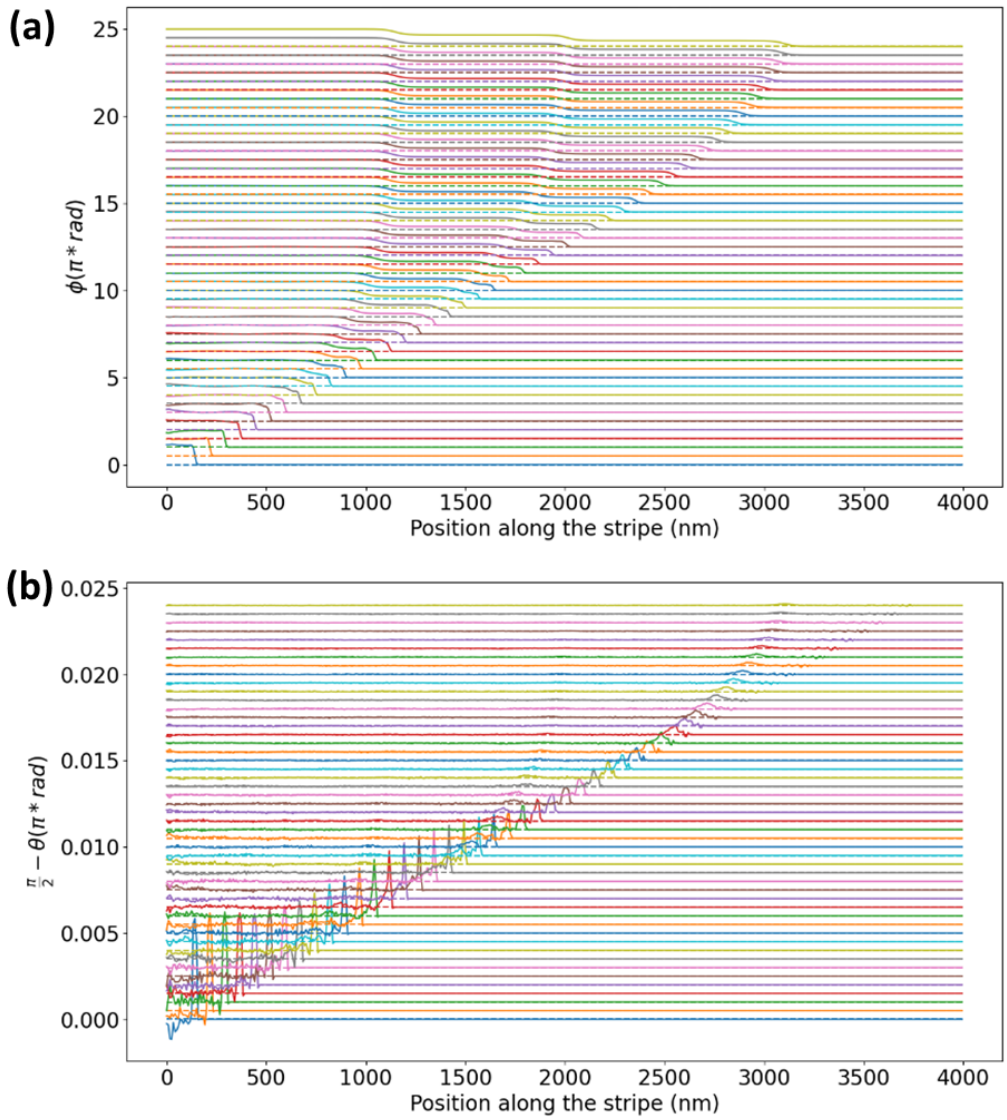


Figure 4.8: The domain wall propagation landscape, depicted by (a) $\phi$ and (b) $\theta$ in different snapshots. Each snapshot is taken 2ps after the previous one and shifted in order to visualize. The 180° domain wall breaks out a 60° DW at the positions of around 600nm and 1200nm.

### 4.3.2 Propagation Properties over Complicated Geometries

We next launch a spin wave and let it propagate through more complicated geometries. In Fig. 4.9, we show that the wave propagates through a straight corner without changing its velocity and with an amplitude not visibly influenced. This is true for all spin wave amplitudes studied. This behaviour of antiferromagnetic spin waves is significantly different from the ferromagnetic case, and this is mainly

due to the absence of stray field. We further study the propagation of spin waves through waveguides with varied widths. The amplitude of rotation of $l$ increases when the waveguide narrows, and the amplitude decreases when the waveguide widens. In particular, a very interesting behaviour is shown in Fig. 4.9 where a spin wave can be transformed into a domain wall by focusing. The reverse behaviour is obtained by de-focusing where a domain wall can be transformed into a spin wave. These components could be useful in designs when one needs to amplify or attenuate the wave and when rectification is required. The simplicity of manipulation using these components lies in the nature of antiferromagnetic spin waves. Since the wave is mainly mediated by exchange, the geometry matters less and the width of the waveguide plays a main but simpler role in the propagation.

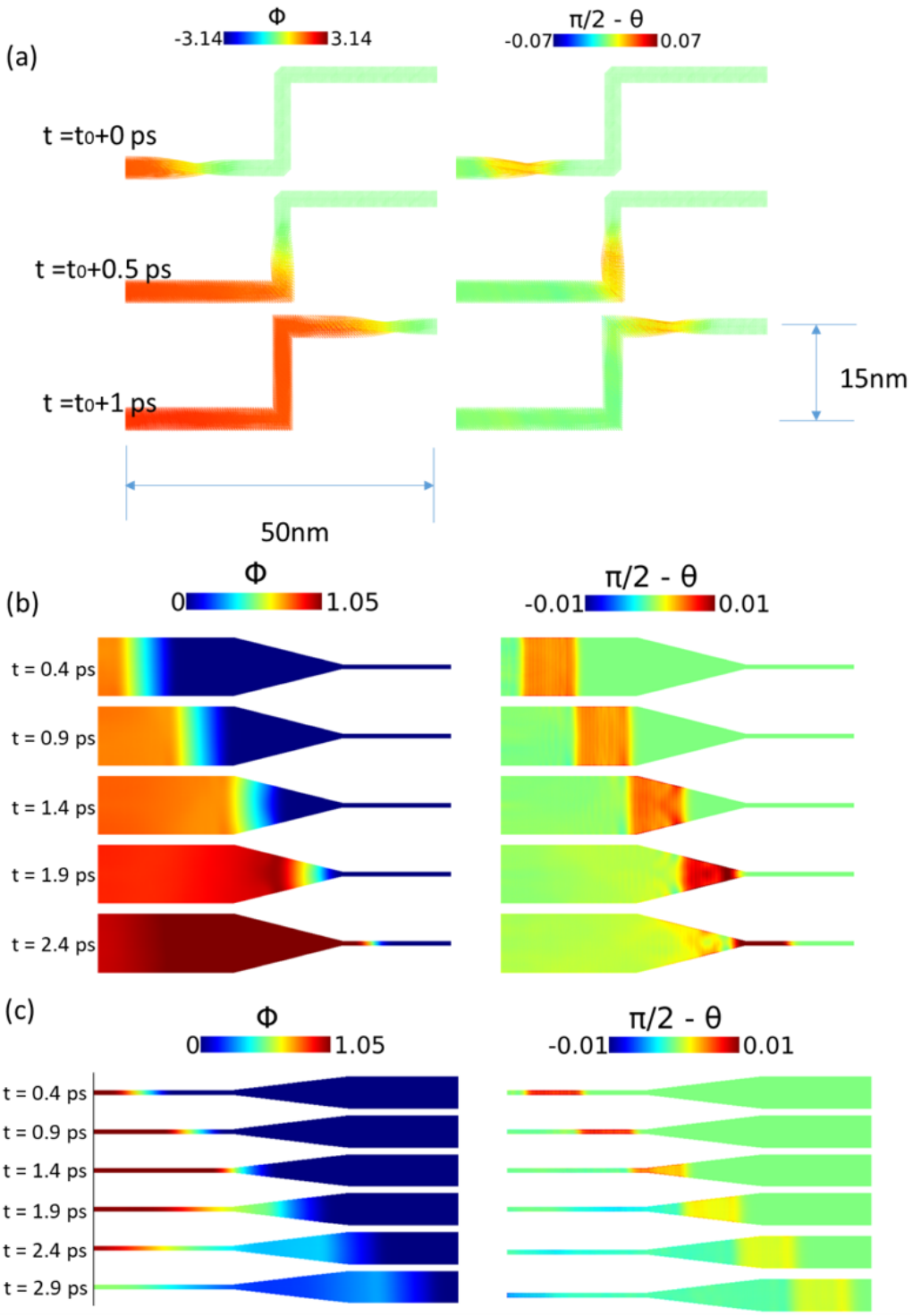


Figure 4.9: (a) shows a domain wall that propagates through a straight corner. (b) shows a spin wave propagating through a narrowing waveguide. The spin wave is amplified ( can also be viewed as being focused). If the spin wave is just below the threshold for a domain wall switching as in the case shown here, the rotation of $\boldsymbol{l}$ will be amplified over the threshold and create a domain wall. The domain wall propagates both forward and backward. (c) is the reverse process of (b).

Fig. 4.10 shows a four-end geometry where two domain walls of the same amplitude simultaneously reach a cross. If the rotation of the antiferromagnetic vector $\boldsymbol{l}$ is in the same direction, the domain wall propagates through the cross without any visible disturbance. If the rotation is opposite, the DWs bounce back acquiring an opposite rotation shown from the change of $\frac{\pi}{2} - \theta$. The wave is bounced back by the spins in the center of the cross, which are fixed due to symmetry. Such a behaviour allows one to design a logic gate, such as an AND gate or a majority gate. The state of the antiferromagnetic domain could then be read by the exchange-bias effect or magneto-resistance. The writing of the polarization of the STT can be achieved by a spin-valve structure, where the ferromagnetic state could be electrically controlled. Note that this process would be slow and impede the fast actuation of the AFs.

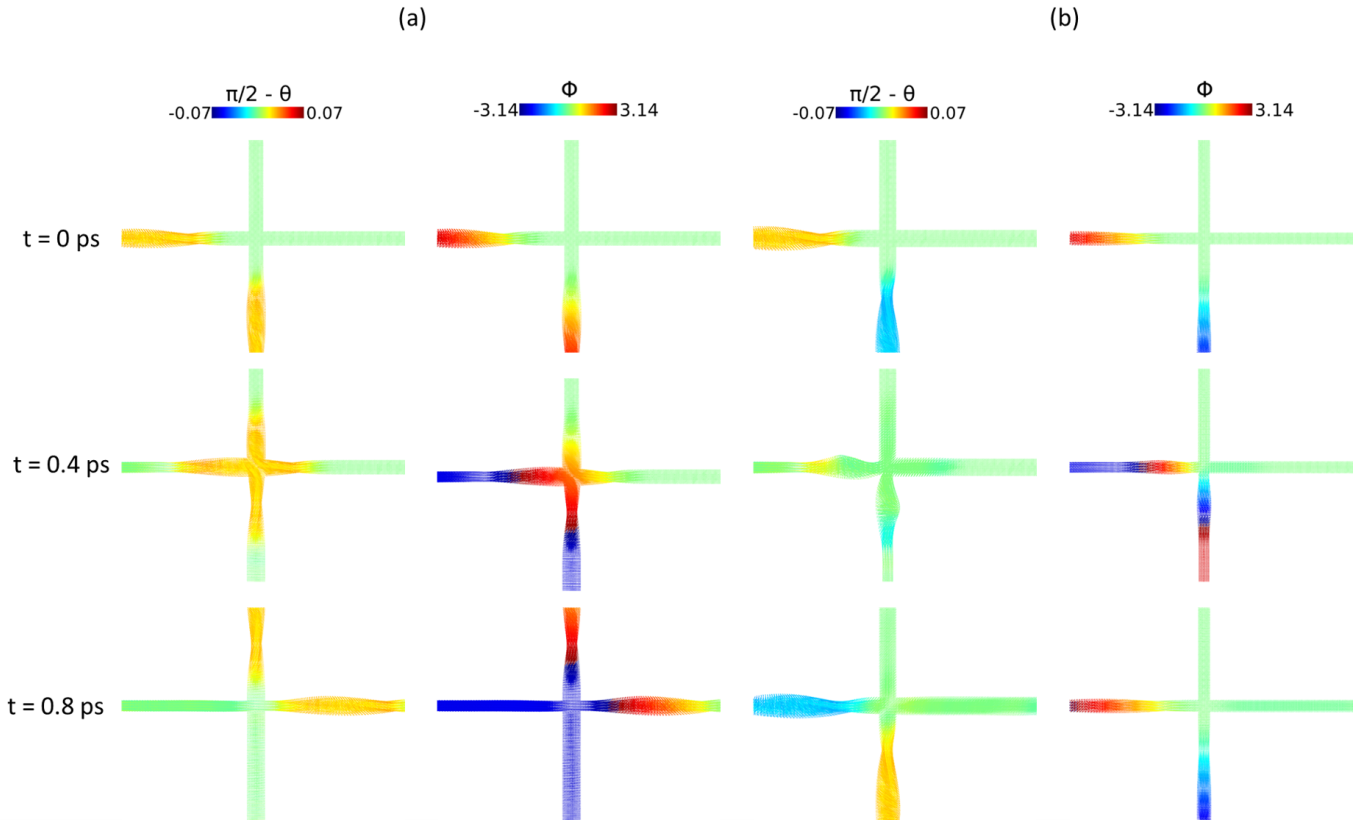


Figure 4.10: Propagating domain walls meeting in a cross geometry. (a) shows when the STTs have the same direction, the domain wall propagates through the cross without any perturbation. (b) shows when the STTs have opposite directions, the domain wall bounces back from the junction.

## 4.4 Conclusion

We have deduced the wave equation from linear spin wave theory and obtained the spin wave velocity and dispersion relation in NiO. From the microscopic model of spin state in NiO, we numerically simulated the propagation of spin waves with the same velocity deduced by the theory. We further

found that such a spin wave could propagate through a straight corner without disturbance. It can be focused or de-focused when the width of the waveguide varies. And we proposed a possible way of realizing logic gates based on a crossing geometry. Our study will inspire the experiments towards the manipulation of the spin waves in NiO, and logic gates based on spin waves that function at the THz frequency.

# Chapter 5

# BFO in Strong Magnetic Fields

## 5.1 Background

The chiral spin structure in $BiFeO_3$ is induced by the electric polarization. The mechanism responsible for this is called the magnetoelectric interaction. Inversely, the spiral spin texture induces an electric polarization [99]. This is called the spin-current mechanism or the inverse Dzyaloshinskii–Moriya effect [100]. The chiral spin texture can be associated with an invariant $\boldsymbol{V}$ which is proportional to the induced polarization $\boldsymbol{P}$:

$$\boldsymbol{P}_{ind} \propto \boldsymbol{V} = \sum_{ij} \boldsymbol{e}_{ij} \times (\boldsymbol{s}_i \times \boldsymbol{s}_j) \tag{5.1}$$

where i and j are the nearest neighbour sites and $\boldsymbol{e}_{ij}$ is the unit vector connecting these sites. This polarization can be removed by applying a strong magnetic field. This is due to the fact that a strong field of about 20T [101] could destabilize the cycloid and cause a transition of the magnetic order from the cycloid to a canted antiferromagnetic state. The invariant endures a sudden drop, which is the "flop" of the cycloidal structure in BFO. The destruction of the modulation in BFO allows for the existence of the linear and quadratic magnetoelectric effects, which are described by

$$P_i = \sum_k \alpha_{ik} H_k + \sum_{jk} \beta_{ijk} H_j H_k \tag{5.2}$$

where i,j,k are coordinate indices ( i, j, k = x, y, or z) and $P_i$ is the i component of the polarization; $H_k$ and $H_j$ are the k and j components of the applied field. Experimentally, the polarization and the magnetization of BFO under varied fields have been measured, but its spin structures have not been fully uncovered. To understand the orientation dependence of the critical field and reveal the spin texture, we use our code developed during the thesis to simulate the spin structure under a strong field in $BiFeO_3$.

## 5.2 Method

The simulation is conducted by our homemade code described in Chapter 2. It has been verified that it correctly calculates the relaxed state of $BiFeO_3$ when a cycloid state is initialized. It is required to find the critical field in which this system goes through a topological transition. When finding such a critical point, the following aspects should be considered.

The change in the structure of spins usually requires the system to go over an energy barrier. Since the relaxation process based on LLG is usually along a path which lowers the energy, it does not automatically climb over an energy barrier. The system should be excited above the energy barrier for the topological transition to happen. For an antiferromagnetic spin structure, especially such systems as $BiFeO_3$ with the winding of the $\boldsymbol{l}$ vector, the energy barrier is usually high and difficult to overcome with trivial noise or randomness (it could be topologically protected). Thus if one wants to consider a phase transition of the spin structure and find the critical condition ( the critical magnetic field in this case ), all possible topology and structure of the relaxed state should be considered and set to be the initial condition for relaxation.

In this section, the coordinate system is shown as Fig. 5.1 where $\boldsymbol{k}$ is along the [1-10] direction, defined as the x direction, y is defined to be the [11-2] direction, and P is along [111], which is also the z direction. Hence, the cycloid is rigidly taken to lie along these fixed directions while the magnetic field can be applied along any axis. Here, we have studied the cases where a magnetic field is applied in three different directions: $x$, $y$ and $z$.

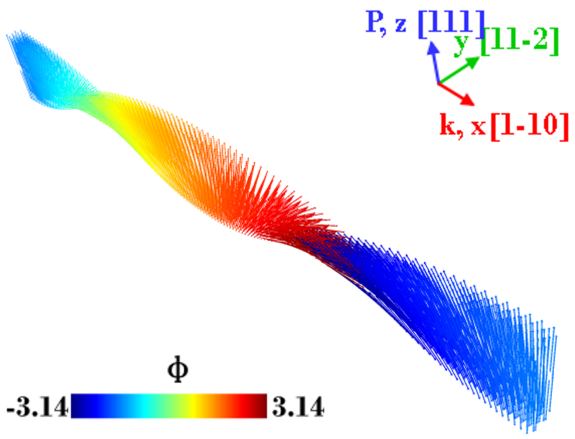


Figure 5.1: Illustration of the coordinate.

In our simulation, we have considered three kinds of boundary conditions. Periodic boundary condition in all three directions is the cheapest to simulate and it represents a large single domain of cycloid. We set the initialization to be either a cycloidal state , or a flopped state . The drawback of this model lies in the topology due to the forced periodicity. Any transition that breaks the periodicity is not allowed. Also, it assumes that the relaxed state has a certain periodicity, fixed by the size of the box. In order to avoid these drawbacks, two other boundary conditions are considered: periodic in x

and y while free boundary in z, and periodic in z while free in x and y. Initialization is still set to be the cycloidal state and flopped state for these two situations.

## 5.3 Results

The energy of the two states for the field applied along x, y and z is shown in Fig. 5.2. The critical field along z can be extracted to be around 25T and the system is flopped above. When the field is below 25T, the system is in a cycloid state. It flops at a field above 26T. When the field is applied in the x-y plane, the energy should be compared together since in real life the cycloid direction could rotate in the (111) plane [102]. The lowest energy state below 23T is the $\boldsymbol{k}$ perpendicular to $\boldsymbol{H}$ state. The state flops when the field is above 23T. The chirality shown in Fig. 5.3 verifies that indeed these fields are the critical fields for phase transition.

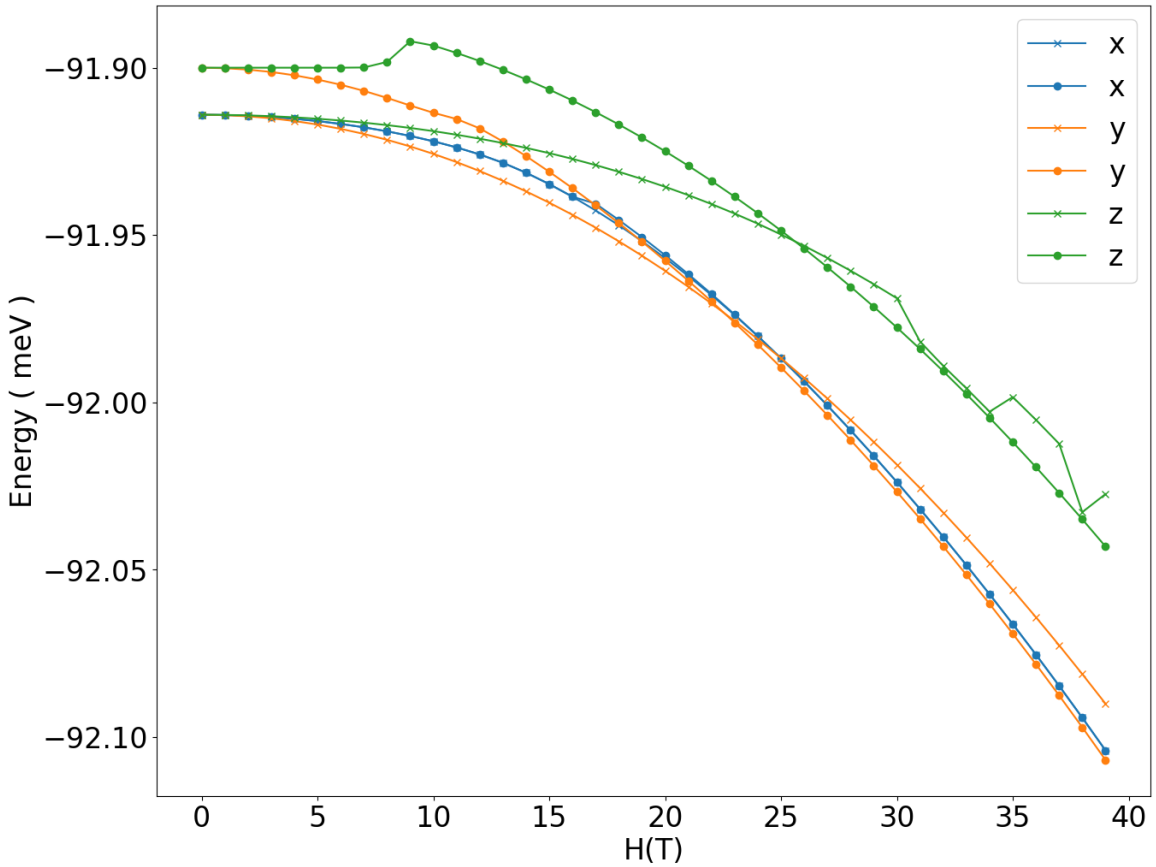


Figure 5.2: The average energy per site with magnetic fields applied along the three respective directions. Crosses are for states with the cycloid initialization, whereas filled circles represent the flopped initialization. The cycloid state with the field along y always has a lower energy than the cycloid state with the field along x in the range of 1 to 25T. The six-fold anisotropy energy per atom is at the $10^{-3}$ meV order, which is responsible for the energy difference of the two flopped states at high fields in the x and y directions. At fields below 17T, the flopped initialized state also relaxes into a cycloidal state for the field applied along x. At fields above 30T applied along z, the initial cycloid state could lose its structure and relax to a flopped state, so the energy difference could drop suddenly in the plot. At low fields below 9T applied along z, the flopped initial states relax to some spiral structure, with its energy showing a sudden drop.

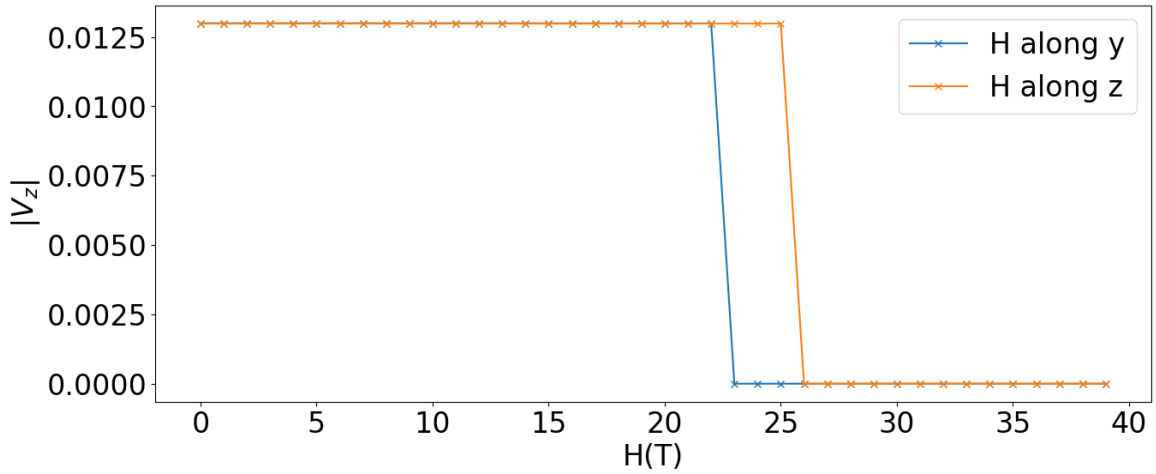


Figure 5.3: The absolute value of the invariant $\boldsymbol{V}$ z component under different applied magnetic fields. The invariant is calculated by Eq. 5.1 for each site and averaged among all sites. Both initializations (cycloid and flopped) are calculated, and what is plotted is only the one among the two that ends up with lower energy.

These results are qualitatively consistent with those obtained by Fishman [103] who calculated semi-analytically the full angular dependence. Since we show here that the field perpendicular to the cycloidal plane is the lowest energy configuration, it is likely that in a real sample, cycloids may rotate, or at least distort, before the flop field is reached. As this could not be studied here, we focus now on the most stable configuration where the field is perpendicular to the cycloidal plane. In this case, the cycloid becomes anharmonic before it flops. When the field is applied along y, the half period elongates where the spin density wave is favoured; the other half period contracts, as shown in Fig. 5.4. This is a very important aspect of the action of a large field: the SDW is essential in the cycloid evolution. Moreover, it can be said here that if one forgets the DMI interaction responsible for the SDW, the cycloid does not flop when the field is applied along y (perpendicular to its plane of rotation). The ratio between the length of the longer half and the shorter half increases linearly with the field, and the overall period of the cycloid remains the same. This has been verified to be the same case when the x and y directions are set to be free boundary conditions, and thus is not induced by the imposed periodicity (See Fig. B.3 in the Appendix). When the system flops, it becomes a canted collinear state with $\boldsymbol{l}$ along the x direction ( which is different from the assumption in [101] ), because the $D_2$ DMI term and the canting result in an effective in-(111)-plane anisotropy that overcomes the easy-axis $K_{1u}$.

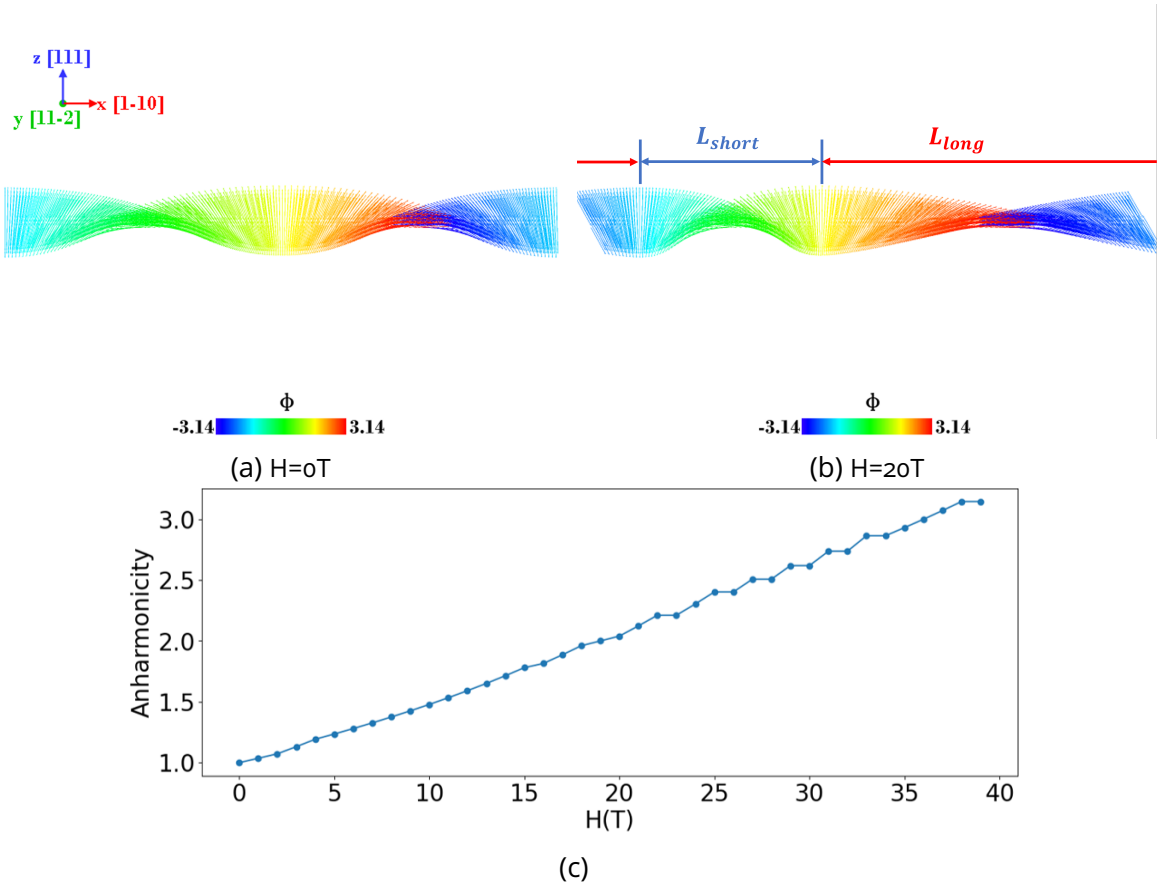


Figure 5.4: The Cycloid initialized state relaxes and becomes anharmonic as the field increases. The anharmonicity shown in (c) is defined to be $L_{long}/L_{short}$. $L_{long}$ and $L_{short}$ are defined to be the longer and shorter distance between the spins that are along the z direction, as denoted in (b).

In contrast to the previous case, the spins favour in-(111)-plane merely due to the Zeeman energy when the field is applied along z. As a result, the spins in the cycloid tend to be more aligned along the x and -x directions, as shown in Fig. 5.5. The $\boldsymbol{l}$ vector rotates anharmonically, with more components along $\boldsymbol{k}$. The spin density wave also becomes anharmonic, but since this is an auxiliary effect, the SDW is not shifted and its maximum amplitude remains unchanged. Above the critical field, the structure flops into a state where $\boldsymbol{l}$ is along the x direction. Besides the magnetization along z, it also possesses a net magnetization along the y direction which does not depend on the amplitude of the field, as shown in Fig. 5.6. The consequence of $\boldsymbol{m}$ y component pointing towards the y direction instead of -y is partially induced by spontaneous symmetry breaking; if the two sublattices swap directions, $m_y$ should flip its sign. For a specific arrangement of the directions of spin in the two sublattices, the sign of the $m_y$ is determined by the sign of the $D_2$ term in the Hamiltonian. If the sign of the $D_2$ term is changed, such as in the case of a $D_2$ domain wall ( which will be addressed in Chapter 7 ), the sign of $m_y$ will flip, which in reverse provide a useful method to detect the $D_2$ domain. More detailed discussions related to the $D_2$ domain and domain wall that we predict could be found in Chapter 7.

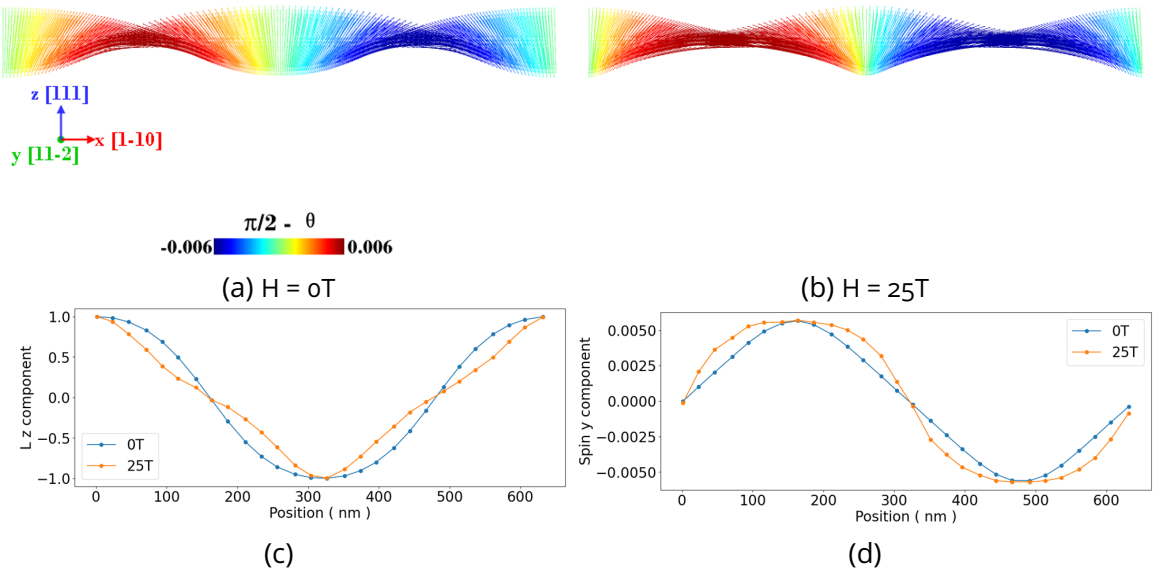


Figure 5.5: The relaxed state of cycloid initialized state. From (a) 0T to (b) 25T, the spins favour the x and -x directions, leading to an anharmonicity of the cycloid. (c) the cycloid $\boldsymbol{l}$ rotation becomes anharmonic and as a result (d) the spin density wave is not shifted but anharmonic.

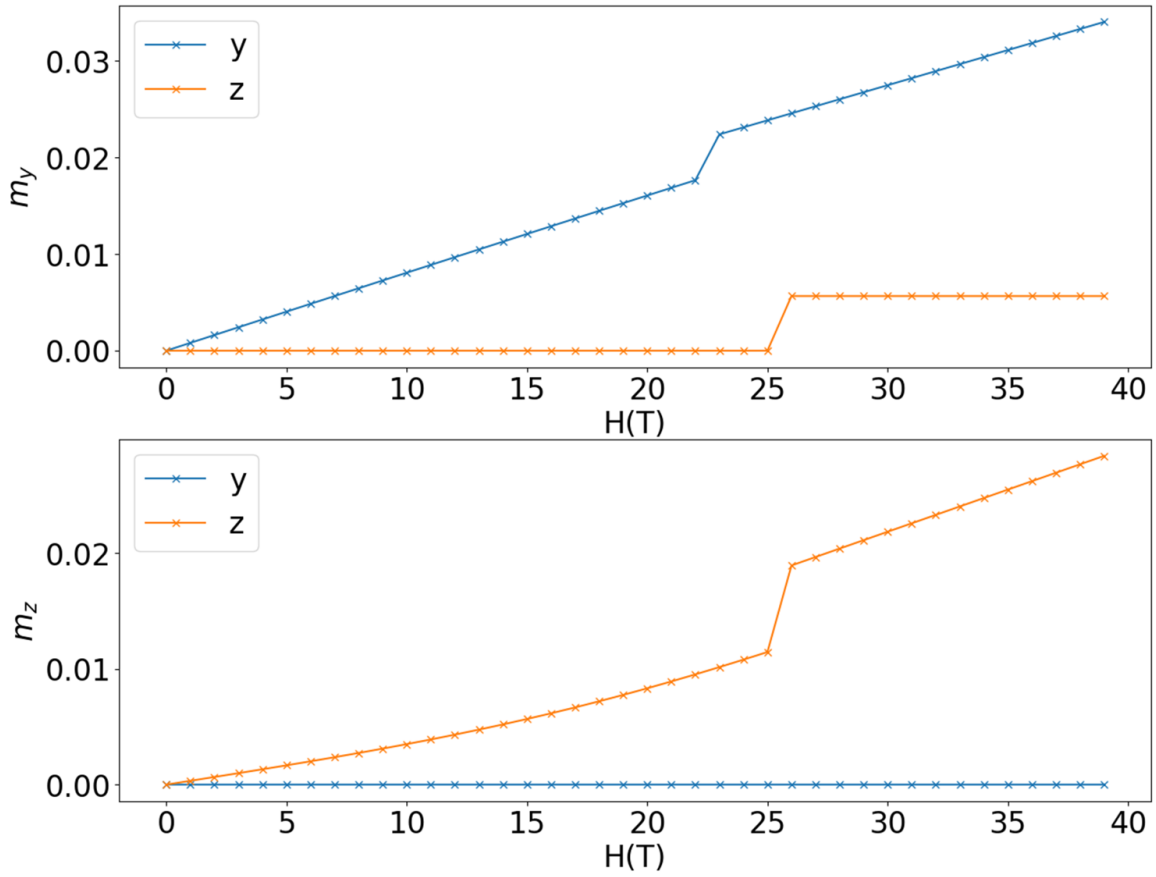


Figure 5.6: The magnetization under different magnetic fields applied. The magnetization is calculated to be the minus of the spin vector averaged among all the spins in the simulation.

## 5.4 Conclusion

The critical field is dependent on the direction of the field applied. The model we have chosen shows the critical field to be 23T for $\boldsymbol{H}$ applied in the plane perpendicular to $\boldsymbol{P}$ and 25T for $\boldsymbol{H}$ along $\boldsymbol{P}$. When $\boldsymbol{H}$ is applied perpendicular to $\boldsymbol{P}$, $\boldsymbol{H}$ perpendicular to $\boldsymbol{k}$ has a lower energy than $\boldsymbol{H}$ parallel to $\boldsymbol{k}$. The anharmonicity of the cycloid induced by the field has been discussed. The SDW ( or the $D_2$ DMI term in the Hamiltonian ) plays a crucial role in the transition to the flopped state, as well as the anharmonicity.

# Chapter 6

# Effect of a Pulse of Spin-transfer Torque on the BFO Cycloid

## 6.1 Background

In Chapter 4, we have discussed the spin dynamics of NiO under an excitation by spin-transfer torque. We have seen how the STT could trigger dynamics and how the spin waves propagate. In contrast to NiO, the spins in $BiFeO_3$ are non-collinear. The antiferromagnetic texture of $BiFeO_3$ has broken isotropic symmetry in the (111) plane (Fig. 6.1). A picosecond spin torque injected into $BiFeO_3$ should induce different dynamics if the spin torque direction is varied outside the cycloidal plane. It is interesting to see how $BiFeO_3$ reacts to these STT pulses. In this chapter, we will present our numerical study of the responses of BFO cycloids under STT pulses.

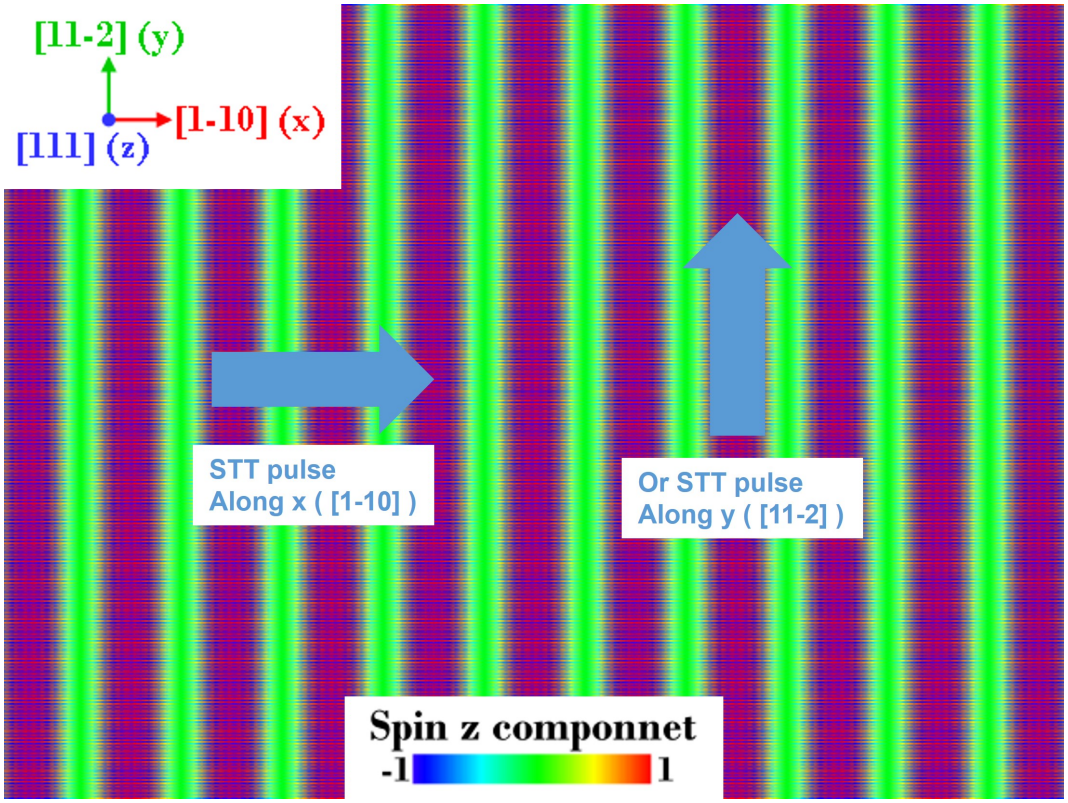


Figure 6.1: BFO cycloid breaks the isotropic symmetry in the (111) plane. The response of the STT pulse in different directions should not be the same. In particular, the STT pulse along the x or y directions should induce different spin dynamics.

## 6.2 Method

The simulation applies STT for a short pulse of 100 fs. The amplitude of STT varies from an estimation of the strongest pulse of an ultrafast demagnetization experiment ( 0.01meV ) to a small torque ( $10^{-5}$ meV) which equals the one induced by the SOT from the adjacent Pt layer. We have tuned the STT in such a large range since the strength of the torque can be tuned by attenuating the pump beam in the experiment. The simulation considers three scenarios shown in Fig. 6.2 corresponding to three different regions of the experimental situations. In the ultra-fast demagnetization experiment in our lab, the STT is applied on an area typically 100 $\mu$m in size, much larger than the cycloid wavelength. Therefore, the amplitude of the STT remains approximately constant on the scale of one period of cycloid. We consider this scenario as shown in Fig. 6.2 (a), where we simulate a box of BFO with periodic boundary conditions and spatially homogeneous STT pulse over the whole area. On the other hand, in order to study how the induced spin-wave and spin dynamics propagate, we considered a large box of BFO and an STT applied only on a smaller area in the middle, as shown in Fig. 6.2 (b). This geometry allows us to study the propagation along the cycloid direction $\boldsymbol{k}$. In order to study the propagation in the other direction ( perpendicular to $\boldsymbol{k}$), we simulated a wide area of cycloid and

applied STT only on a smaller area in the middle, as illustrated in Fig. 6.2 (c). The results are shown in the following section.

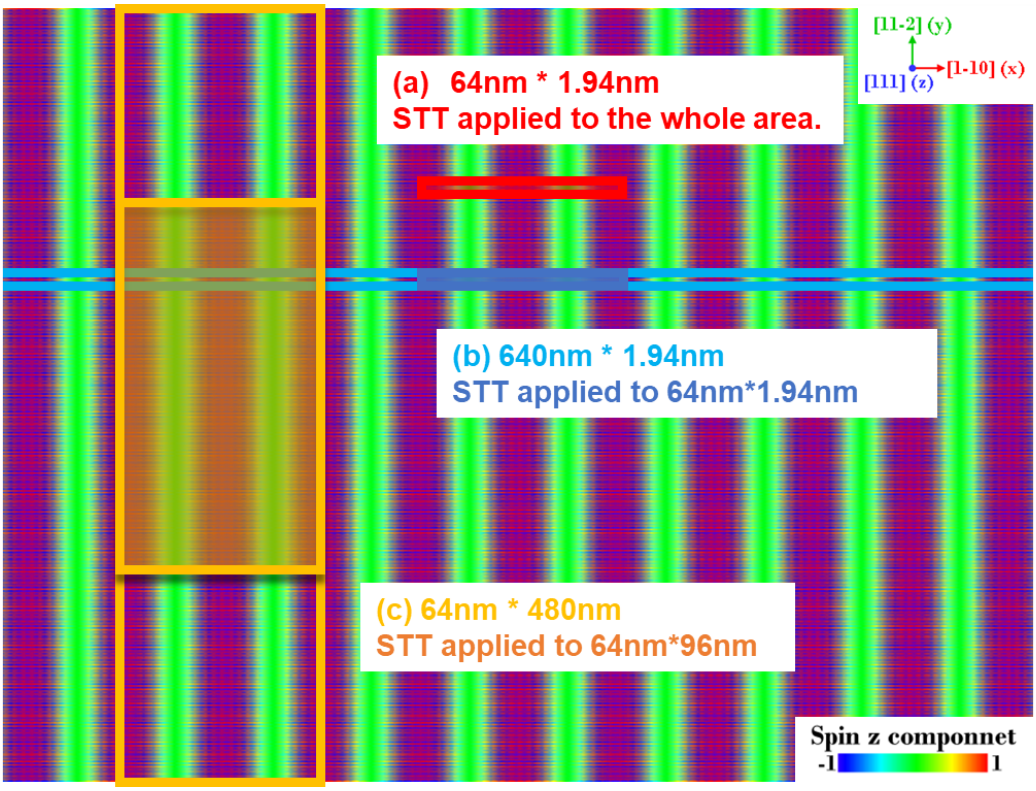


Figure 6.2: An illustration of the simulation box size. In order to study the different properties of the dynamics, we define three different box sizes for the simulations, illustrated by the red, blue and orange rectangles. The z-direction is always 1.38nm in size and with periodic boundary conditions. The red box (a) shows the simulation where we confine the BFO cycloid in a necessarily large periodic box which is 64 nm $\times$ 1.94nm in size. An STT pulse of 100 fs is applied to the whole region in the red box. In order to simulate the propagation of the spin dynamics, we consider, as shown in (b)) and (c), a longer or wider cycloid also in a box with periodic boundary conditions, whereas STT is applied on only a small region.

## 6.3 Result

### 6.3.1 STT Applied along $k$ —- Oscillations

We define, as in the previous chapter, the x direction along [1-10], y along [11-2], and z along [111]. Besides this overall coordinate, for each spin, we build up a coordinate (indicated as x',y',z' and x'',y'',z'',...) in the frame of its static direction. We define its original direction to be the x'-axis, and [11-2] to be the y'-axis, so that $\phi$ is taken to be its rotation in the plane defined by the antiferromagnetic vector $\boldsymbol{l}$ and the [11-2] direction. $\theta$ is defined to be the out-of-plane angle, taking the z-axis direction to be $\theta$ = 0 (

such as the x',y',z' and x'', y'', z'' coordinates in Fig. 6.3 for the two spins at different positions ).

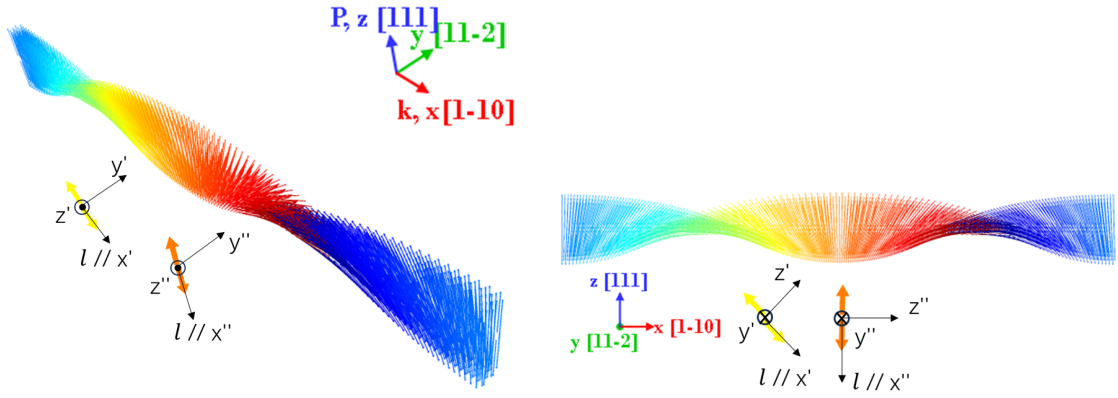


(a) (b)

Figure 6.3: For each spin, we define a spherical coordinate system. The yellow and red spins are taken from the cycloid, as illustrations.

If the STT is applied along $\boldsymbol{k}$, then the main dynamics will be a rotation inside the $\boldsymbol{l}$-[11-2] plane (out of the cycloidal plane), as shown in Fig. 6.4. We can see from the plots that the resonance frequency is 0.68 THz. Further comparison between the amplitude of the spins in the different positions of the cycloid shows that this resonance mode has different amplitude along the cycloid. The reason is illustrated in Fig. 6.5. Indeed, an STT pulse applied along the $\boldsymbol{k}$ direction applies a torque on the spins. This torque is proportional to the spin component perpendicular to the STT direction. So the tilting of the dark blue spins in Fig. 6.5 is larger than the tilting of the light blue spins, and the tilting of the light green spins is zero. After the pulse, the spins rotate and oscillate around the magnetization direction, as discussed in the NiO case in Chapter 4. However, as the antiferromagnetic vector $\boldsymbol{l}$ changes to an opposite direction after half a wavelength of the cycloid, the spins that are aligned with $\boldsymbol{k}$ —- such as the light green spins in Fig. 6.5 —- undergo opposite torque from their two sides. After cancelling, their dynamics is more than one order of magnitude smaller than that of the other spins. These amplitude-modulated dynamics happen coherently along the cycloid, as shown by Fig. 6.6, which is mainly a snapshot of the spin displacements [11-2] components. The amplitude of the dynamics is indeed different along the cycloid, distributing as a sinusoidal function.

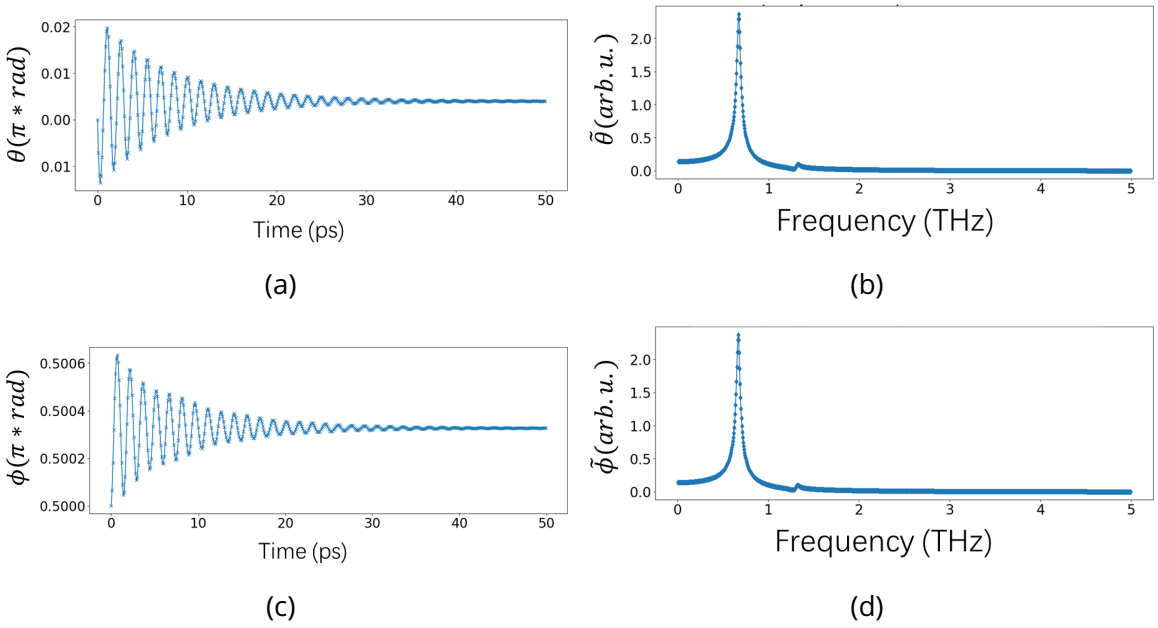


Figure 6.4: The dynamics of the spins that are aligned along the 45° of x and y direction. (a) time-dependent oscillations of the $\phi$ angle. (b) is the Fourier transform of the oscillation. The resonance frequency is around 0.67 THz. (c) is time-dependent oscillations of $\theta$ angle. (d) is the Fourier transform of the (c). The main dynamics are oscillations of $\phi$.

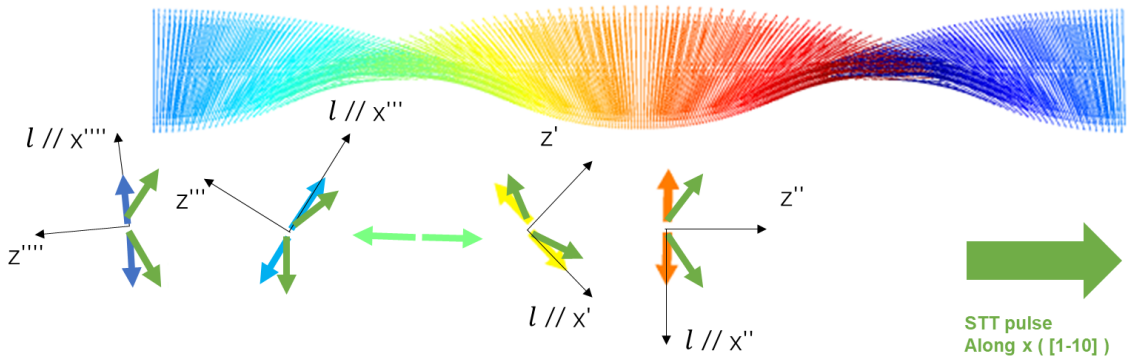


Figure 6.5: After STT is applied, the spins are tilted perpendicular to the $\boldsymbol{l}$-[11-2] plane. The tilt directions with respect to the z' (or z'', z''', z'''',...) directions are opposite on the two half-segments of the cycloid. The oscillations are thus opposite on these two segments in the coordinates that follow the spins ( e.g. x', y', z' ).

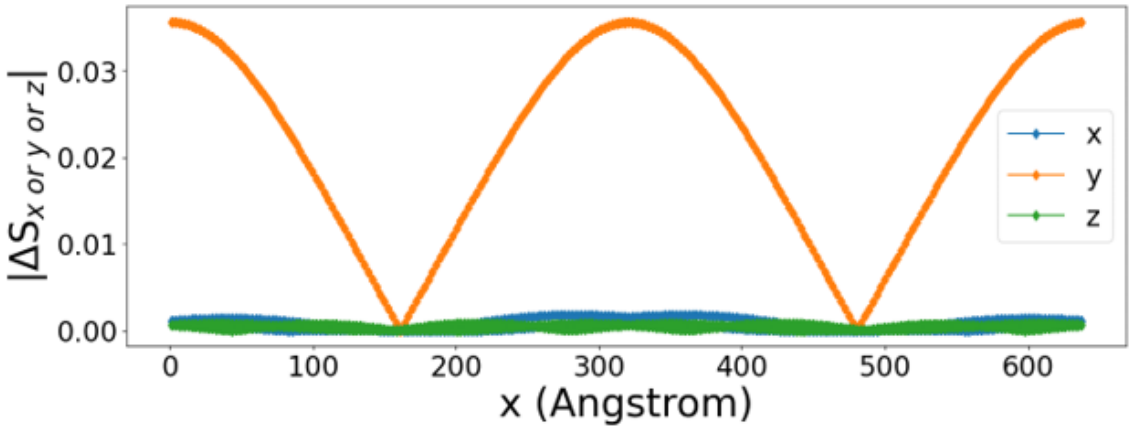


Figure 6.6: The main dynamics of the oscillation of the $\boldsymbol{l}$ vector is in its y direction. In this figure, the absolute value of the difference of the spin x, y and z components compared with their initial direction at 0.6ps after the end of the STT=1 $\times$ $10^{-2}$ meV pulse is shown.

Since the dynamics is highly elliptical, it can be seen as a resonance oscillation of $\boldsymbol{l}$ perpendicular to the plane of the cycloid (the y or [11-2] direction). Along this direction, the spin component intrinsically has a small canting induced by the $D_2$ term DMI interaction in the Hamiltonian. Since the canting is modulated by the cycloid, it appears as a sinusoidal function, known as the spin density wave of $BiFeO_3$ ( shown in Fig. 6.7 (a) ). The amplitude of the spin density wave is 0.006 (and along the [11-2] direction). Depending on the strength of the STT, the dynamics can be viewed as either an oscillating spin density wave ( Fig. 6.7 (c) ), or an oscillating modulation upon the spin density wave ( Fig. 6.7 (b) ). Besides the oscillation of the $\boldsymbol{l}$ vector along the [11-2] direction, the magnetization oscillates mainly along the [1-10] direction (the cycloid $\boldsymbol{k}$ direction), as shown in Fig. 6.8. The oscillation amplitude scales linearly with the applied torque and should be detectable even for small applied STT.

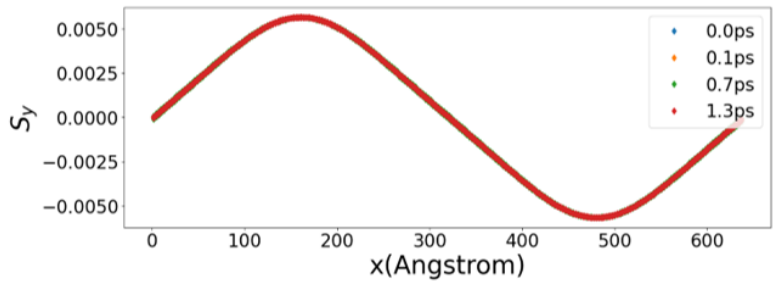


(a) STT =1e-5 meV.

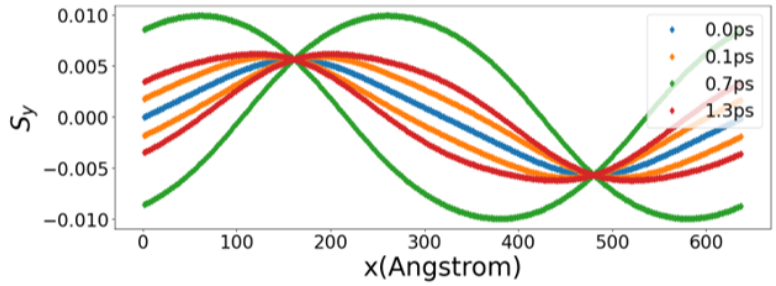


(b) STT =1e-3 meV.

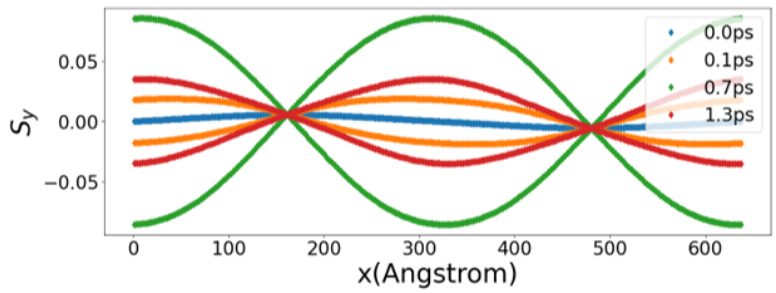


(c) STT =1e-2 meV.

Figure 6.7: The Spin y component. The STT pulse is applied in the first 0.1 ps. In (a), the STT is small so that the intrinsic spin density wave dominates. In (b), the STT-induced dynamics is comparable to the intrinsic amplitude, resulting in a modulation. The two separate lines of the same colour represent the two sublattices. In (c), the STT overwhelms the intrinsic structure.

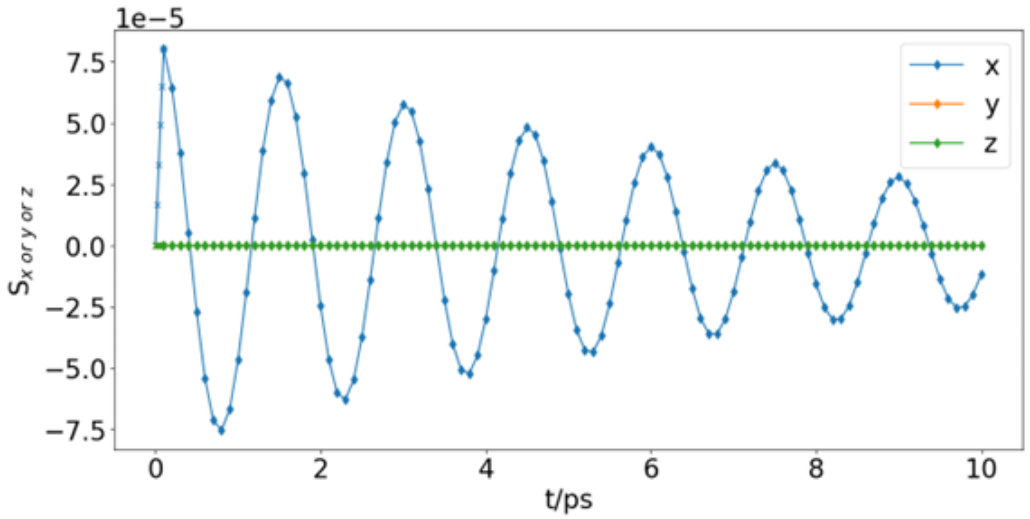


Figure 6.8: Spin x, y and z component for STT = $1\times10^{-3}$ meV on average. The crosses are during the STT pulse and the filled dots are after the STT pulse. The magnetization oscillates mainly along the x direction ($\boldsymbol{k}$ direction). For more details, including the oscillations of the spin y component, check Fig. C.1 in the Appendix.

### 6.3.2 STT Applied Perpendicular to $k$ — Driven Motion of the Cycloid

The dynamics is very different when the STT is applied perpendicular to $\boldsymbol{k}$. Since the projection of the spins along the STT in this case is negligible, the angular momentum stored in the system during the pulse is homogeneous along y. That is, after the pulse, the spin y component (the spin density wave) is shifted along the injected angular momentum, as shown in Fig. 6.9. After the pulse, the stored magnetization is released as a "velocity" of the cycloid, which is the same process as the pushed skyrmion in Chapter 8 and the switched domain wall in Chapter 4. The motion of the cycloidal domain is then damped, as shown in Fig. 6.10. The shifted spin y component attenuates as the cycloid moves, which can be viewed in Fig. 6.11.

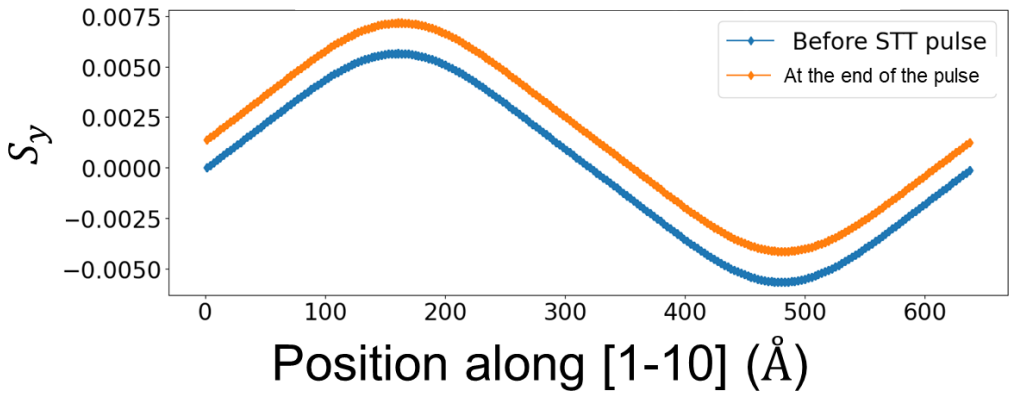


Figure 6.9: The Spin component along the y direction is shifted after the STT pulse. In this plot, STT = 1e-2 meV is taken as an example for illustration.

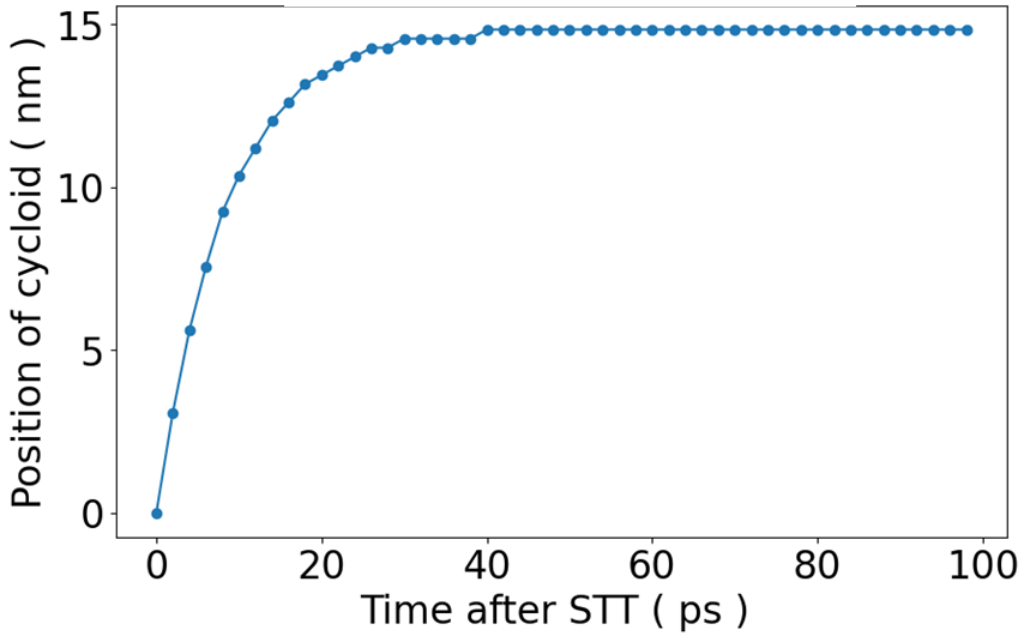


Figure 6.10: Position of cycloid for STT = 1e-2 meV. The translation distance scales linearly with the total angular momentum injected, similar to the behaviour of skyrmion motion. For STT = $10^{-3}$meV check Fig. C.2 in the Appendix.

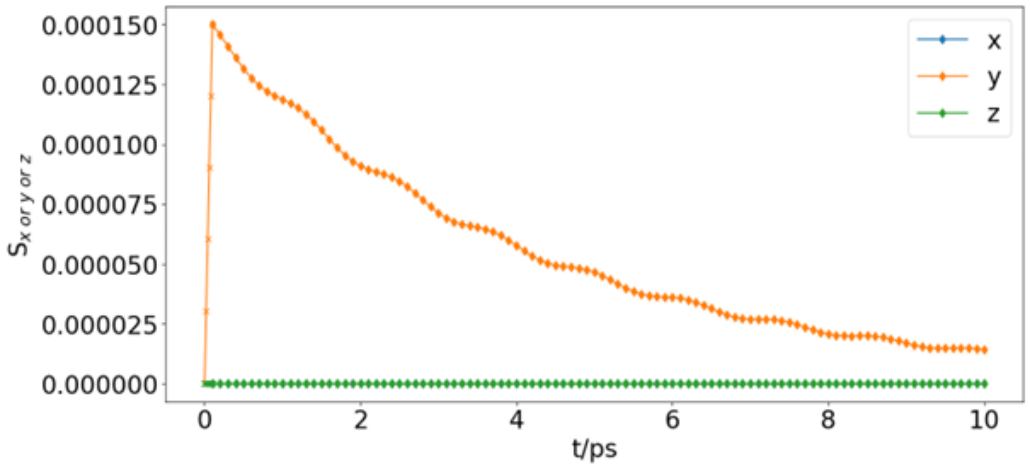


Figure 6.11: Attenuation with time of the spin x, y and z components for STT = $1\times10^{-3}$ meV. The crosses are during the STT pulse and the filled dots are after the pulse. For $S_x$ and $S_y$ with STT = $1\times10^{-2}$meV and $1\times10^{-5}$meV, check Fig. C.3 in the Appendix.

As shown in Fig. 6.1 (c). An STT pulse with a duration of 100fs is applied on a segment of the long cycloid structure, after which the excited spin dynamics is analyzed to extract the propagation velocity. Our simulations show that the two modes, induced by the STT along $\boldsymbol{k}$ and perpendicular to $\boldsymbol{k}$, propagate at the same velocity of 25km/s ( 25 nm/ps ) in both parallel to $\boldsymbol{k}$ direction and perpendicular to $\boldsymbol{k}$, shown by the wavefront vs time in Fig. 6.12.

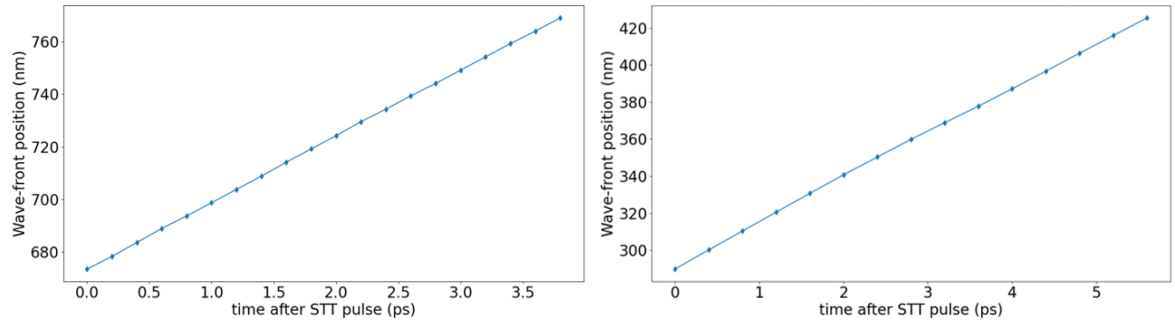


(a) (b)

Figure 6.12: (a) shows the wavefront of the modes propagating along the $\boldsymbol{k}$ direction. (b) shows the propagation perpendicular to the $\boldsymbol{k}$ direction. The velocity of the wavefront is about 25 km/s.

## 6.4 Conclusion

STT pulses applied parallel and perpendicular to $\boldsymbol{k}$ induce different dynamics modes. While STT parallel to $\boldsymbol{k}$ induces oscillations of $\boldsymbol{m}$ and $\boldsymbol{l}$, the other direction does not and instead pushes the cycloid towards $\boldsymbol{k}$. The propagation of these two dynamical modes have the same velocities at about 25km/s and the velocities are also the same for propagating along $\boldsymbol{k}$ and perpendicular to $\boldsymbol{k}$ and $\boldsymbol{P}$. These

results will be useful for the experimental study on the effect of an STT pulse on BFO. In our lab, optical experiments have been conducted to study the spin dynamics of BFO adjacent to a ferromagnet with an ultrafast demagnetization process. The difference in the dynamical modes concluded from our study will be a useful reference to understand the response signal.

# Chapter 7

# Multi-P domain in $BiFeO_3$

## 7.1 Background

Our discussion so far has been focused on the magnetic structure of BFO with a single ferroelectric domain. Different from a single crystal, pristine BFO thin films appear to have stripy P domains, as shown in Fig. 7.1. The P domain wall is usually of the order of a few atom layers, which is much shorter than the wavelength of the cycloid. The cycloid propagation vector $\boldsymbol{k}$ in these P domains can point in different directions and the stitching pattern of the spin texture at the P domain wall is interesting. Measurements together with atomistic simulations show that the stray fields at the interface of these P domains are enhanced along one domain wall out of two[104], as shown in Fig. 7.2. The peculiar texture at the interface has been proposed to be possible topological entities such as skyrmions, but it was not observed from the simulation.

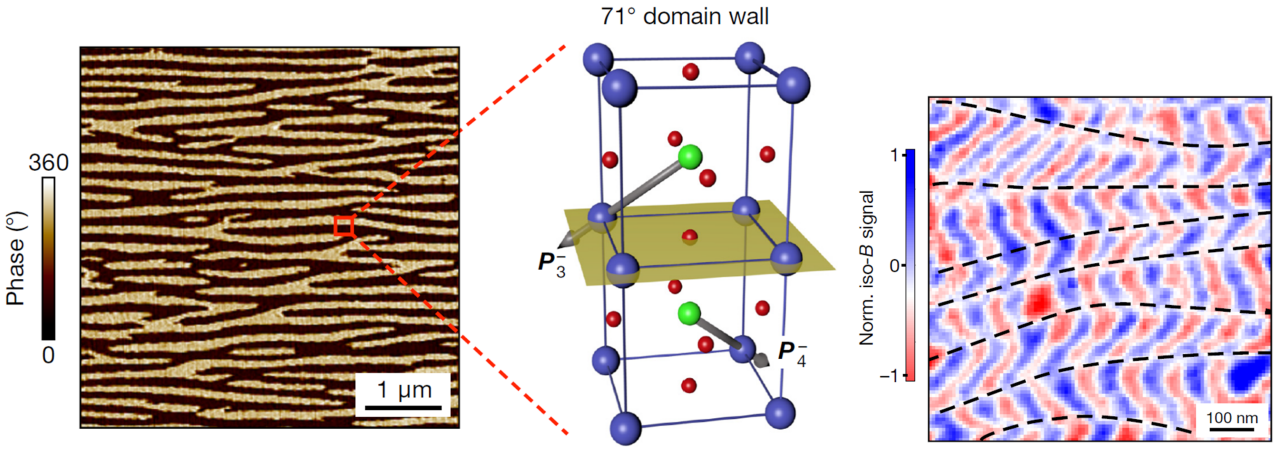


Figure 7.1: Left pannel: striped pattern of the P domains in the BFO thin film probed by piezoresponse force microscopy (PFM). The middle panel sketches the two variants of P domains separated by 71° domain walls located in the boxed area. Right pannel: the magnetic field image recorded above the BFO. The P domain walls are denoted by dashed lines. The figures are taken from [105].

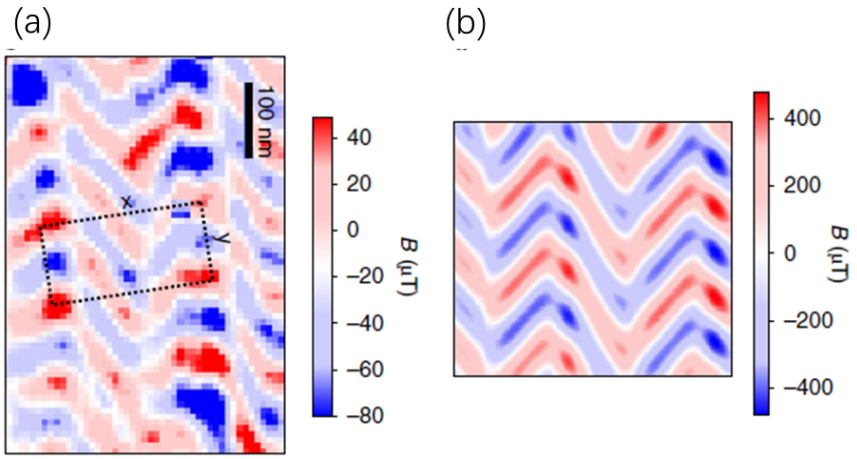


Figure 7.2: (a) Scanning NV magnetometry image of the stray field 60 nm above the sample. There is stitching of the pattern at the P domain walls and enhancement of the field in one out of two domain walls. (b) The stray field extracted from the atomistic simulations which shows excellent agreement with the NV magnetometry. This figure is taken from [104].

Recent advancement in experiments has allowed more complicated P domain structures to be written. By applying a pulse of electric field via a tip, it is possible to craft a four-quadrants-like P domains as shown in Fig. 7.3. The exotic magnetic structure, which is induced by the rather abrupt change in the domain wall of the 4 P domains at the center, has been proposed to be possibly topological objects. Such an object may not be fully revealed by the NV images due to the complex relation between the stray field and the AF texture in $BiFeO_3$. Here, the determination of the magnetic order below the scale of cycloid wavelength is crucial.

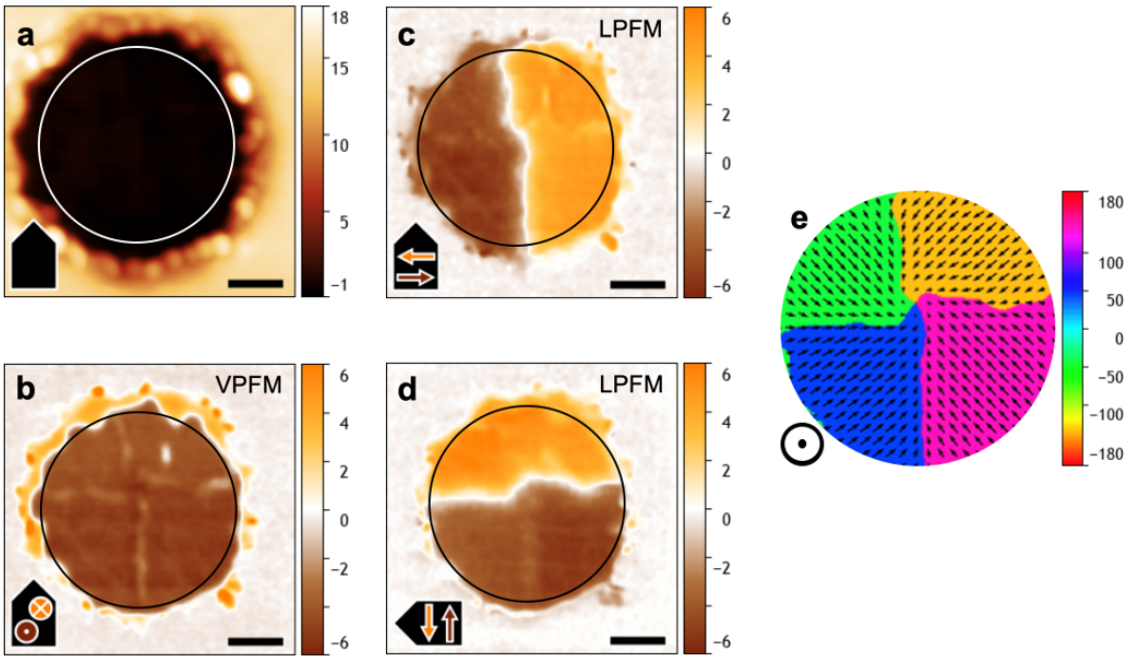


Figure 7.3: Ferroelectric polar maps extracted from piezoresponse force microscopy, taken from [106]. The P domains point upwards, forming a center-convergent ferroelectric texture, which is written by a +60 V pulse. a, Topography measured (colour bar in nm). b, Vertical piezoresponse (colour bar in arbitrary units). c-d, Lateral piezoresponse. e, 2D in-plane vector map of the piezoresponse, which shows the P domain texture.

## 7.2 Method

The cycloid structure, which could be depicted by a rotation of the $\boldsymbol{l}$ vector, could not be easily measured on the scale of its wavelength. One possible method is to detect indirectly its stray field by Nitrogen-vacancy (NV) centers in diamonds. The NV center is a type of impurity in diamond. The impurities endow colours to the originally colourless and transparent diamond, as they are named the colour centers[107]. The NV center is special amongst these impurities in that it is magnetic and its luminescence is coupled to the spin state. This allows for the NV center to be used as a tool to measure magnetic fields. An NV center embedded at the apex of a very sharp tip ( < 10 nm in radius ) can be used to map the field over the sample of interest. This is called the Scanning NV Magnetometry. Its spatial resolution could reach below 10 nm and the field sensitivity could be lower than 10 $\mu$T. Scanning NV Magnetometry is thus a very powerful tool to detect weak magnetic field patterns on a very small scale.

As seen previously, besides its antiferromagnetic nature, BFO possesses a weak oscillating stray field at the scale of its cycloid wavelength, averaging to zero on the macroscopic scale. It is induced by the spin density wave as introduced in previous chapters, which originates from the $D_2$ DMI term. Microscopically, the $D_2$ term results from the octahedral tilting of the oxygen atoms. Its direction,

which is represented by $z'$ in the Hamiltonian in Eq. 3.2, should follow $\boldsymbol{P}$. However, the sign of this term i.e. the phase of the spin density wave, shown by the $(-1)^{h_i}$ in the Hamiltonian, could be an independent parameter from $\boldsymbol{P}$. Despite the importance of this $D_2$ term (since it is what is actually measured), the possibility of the independent $D_2$ domains and domain walls has not been addressed yet. This becomes crucial if one wants to understand the four-P-quadrants domain walls: depending on the sign of the $D_2$ in these four P domains, there could be $2^4$=16 different patterns of stray field with the same $\boldsymbol{l}$ structure! Whether there exist some constraints on the $D_2$ domains and whether it is possible to observe all these 16 possibilities are questions to be answered.

It is challenging to determine both the cycloid structure and the $D_2$ order at the same time, particularly in the four quadrants. The stray field is averaged by the neighbouring magnetic moments due to the distance between the sample and the tip, so NV center measurements could not detect the atomic-scale spin structure. Numerical simulations are crucial to understand the measurements and to determine the spin structure. In this chapter, we will present the results obtained from numerical simulations and predict the image pattern measured from the NV center. We simulate simple cases for $D_2$ domains as well as four quadrants. In the end, we compare our obtained results with the NV measurements.

With the homemade code introduced in Chapter 2, it is possible to carry out sufficiently large-scale simulations to tackle the question. The simplest case is a single P domain with a straight $D_2$ domain wall. We then simulate the domain wall between 2 P domains. Then, four-quadrant P domains are simulated. In the end, we extract the polarization from experimental measurements, simulate the cycloid structure, and then compare it with the NV measurements.

The simulation is carried out based on the model mentioned in Chapter 8. Since the system is too large for our simulation power, we approximately take the magnetoelectric interaction and DMI 10 times larger, and the anisotropy 100 times larger. So our results are not quantitative; instead, the field pattern can be compared with experimental results. We simulate the system with periodic boundary conditions along the [001] direction. The magnetic field above the surface can be calculated by repeating the same structure infinitely below the surface. It has been tested and found that the fields below 100Å depth are negligible.

## 7.3 Result

### 7.3.1 $D_2$ Domain Wall in a Single P Domain

We simulate the spin system in a box with size 120nm $\times$ 120nm $\times$ 7.92 Å, as shown in Fig. 7.4. The cycloid structure is initialized and relaxed to a stable state. The cycloid direction is set to be [1-10] at initialization and we position a $D_2$ domain wall in the middle. On the left, $D_2$ has one sign and on the right $D_2$ the opposite sign. The cycloid structure of the $\boldsymbol{l}$ vector shows no difference as $D_2$ changes but the magnetization $\boldsymbol{m}$ acquires a 180° phase shift. In the simulation, dipole-dipole interactions are neglected. The cycloid is determined by the stronger exchange and magneto-electric interactions, but the spin density wave, which is an auxiliary effect, is determined by the cycloid structure and the sign of $D_2$. Hence, the weak magnetization $\boldsymbol{m}$ appears with a sharp change at the domain wall.

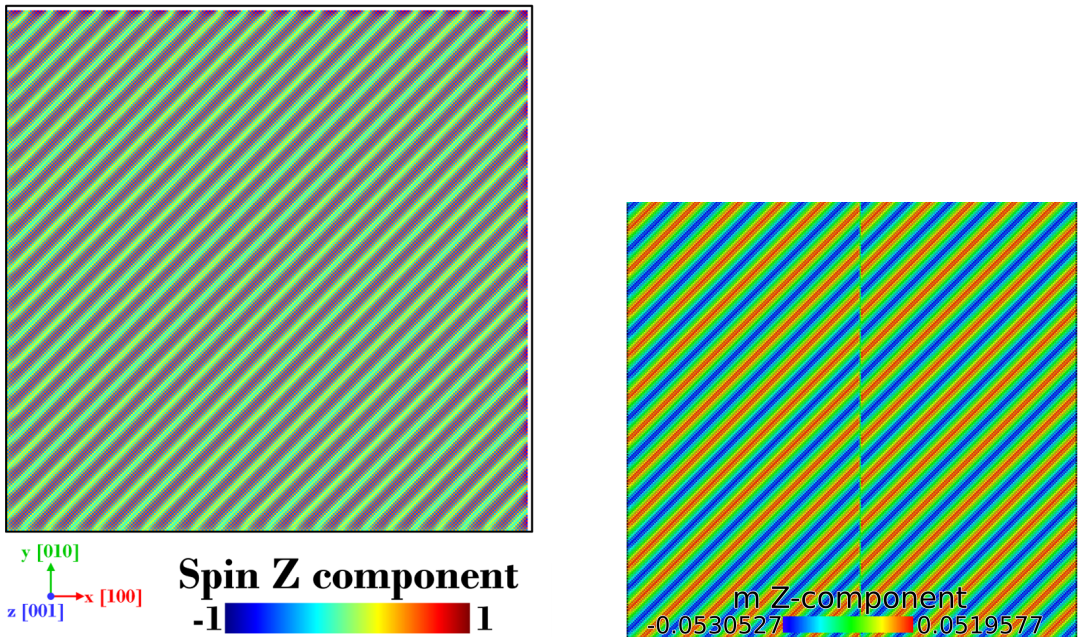


(a) (b)

Figure 7.4: (a) Spin cycloid texture of BFO in the simulation. The simulation size is 120nm $\times$ 120nm in x and y and periodic in z. Since the magneto-electric is amplified 10 times, this corresponds to a 1.2 $\mu$m size square of (almost) real BFO. (b) The corresponding magnetization vector $\boldsymbol{m}$ resulting from the canting. More images of other angles domain wall are in Fig. D.1 in the Appendix.

The stray magnetic field is calculated (with GPU acceleration) from the radiation of the magnetic dipoles. The discontinuous change of $\boldsymbol{m}$ induces a domain wall pattern. If the domain wall is perpendicular to $\boldsymbol{k}$, the stray field appears to be a mismatch of the cycloid, as shown in Fig. 7.5 (a). The shown magnetic field is assumed to be measured at 50A above the surface (roughly equivalent to 50nm for a real cycloid). If the domain wall has an angle less than 45 degrees with respect to $\boldsymbol{k}$, the alternating magnetic field is enhanced and larger in period, as shown in Fig. 7.5 (b) and (c).

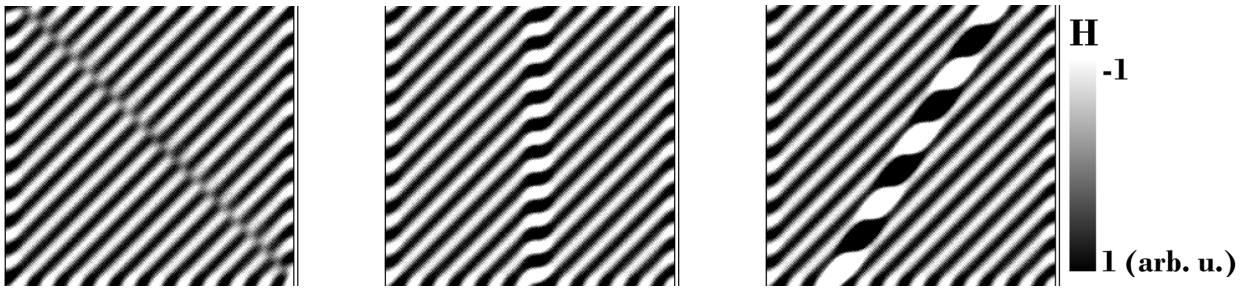


(a) (b) (c)

Figure 7.5: Stray field maps at 50 Angstrom above the BFO surface. The field is measured at 54.7° angle with respect to the z axis along the y direction. (a) -45 degree domain wall. (b) 0 degree. (c) 30 degree.

The apparent width of the domain wall may vary depending on the measurement height above the surface, as shown in Fig. 7.6. The closer the tip, the sharper the contrast is obtained, and the thinner the wall.

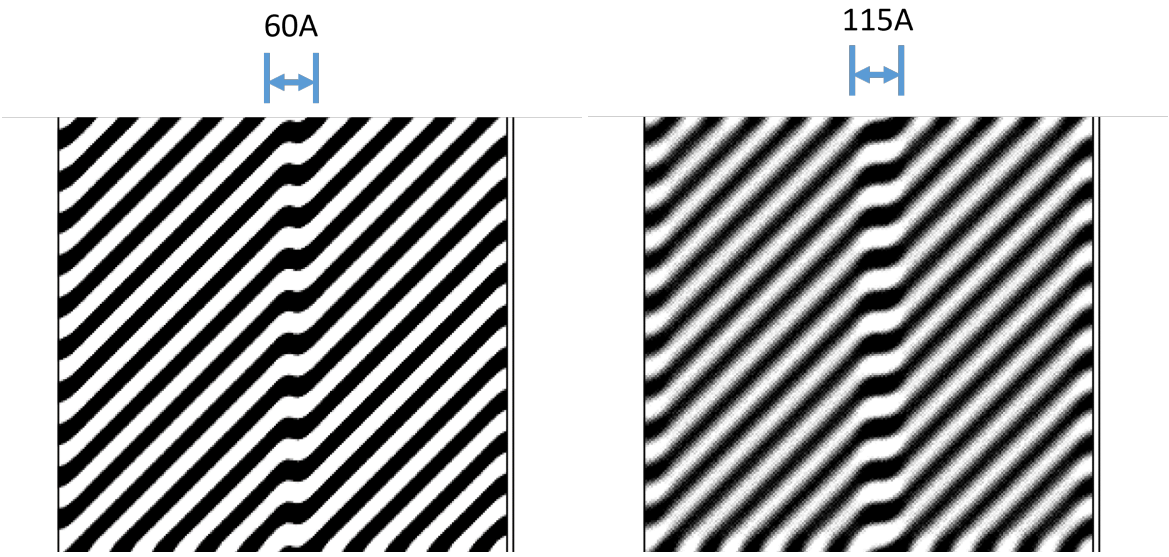


(a) 30A above surface (b) 50A above surface

Figure 7.6: Magnetic field measured at 30A and 50A above surface.

The pattern is about the same for most of the angles calculated. But for some specific angles shown in Fig. 7.7, the pattern shows some apparent differences depending on the angle of the NV tip.

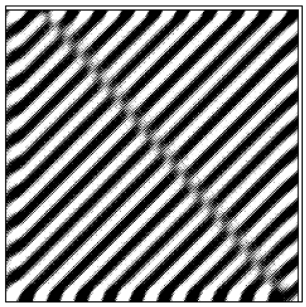

(a) X direction field

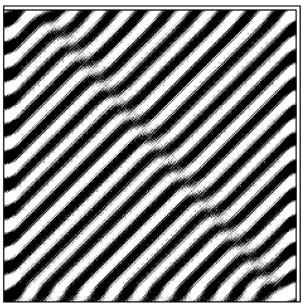

(b) Y direction field

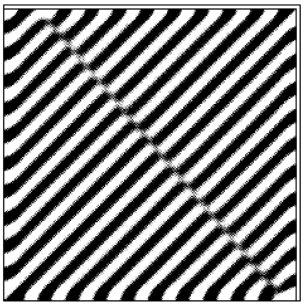

(c) Z direction field

Figure 7.7: Domain wall with a -40 ° angle with respect to the y direction. Magnetic field component along x, y and z directions. The pattern of the x and z field is more similar to discontinuity and the y field is more continuous.

These patterns agree perfectly with what has been measured, as shown in Fig. 7.8. In this pattern, there is a quarter circle $D_2$ domain in the upper left. The angle varies along the domain wall and we can see how the pattern varies with the angle, as predicted.

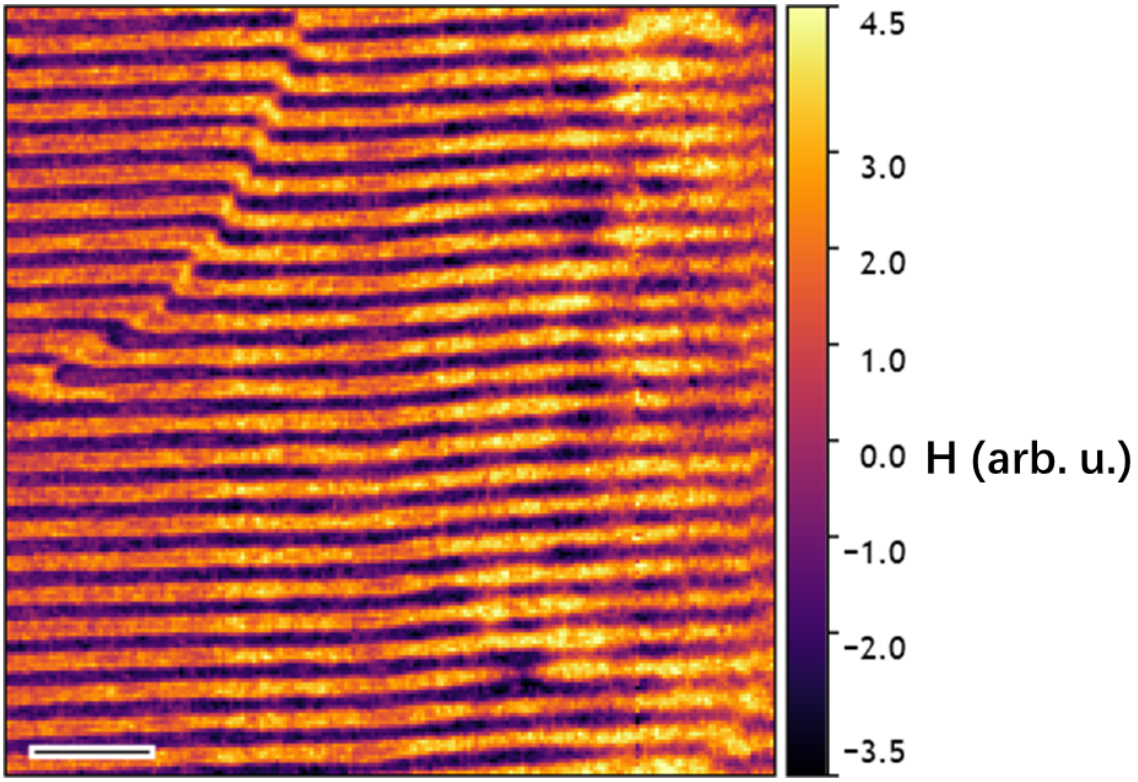


Figure 7.8: NV center measurements of a $D_2$ domain wall.

### 7.3.2 2P Domain

We discuss in this section the situation where the $D_2$ domain wall coincides with a P domain wall. This question arises more naturally than in the previous section, since the sign of the $D_2$ term is unknown for the oxygen distortion right next to the P domain wall. Furthermore, we are aware that discussing the "sign" of the $D_2$ term starts to become ambiguous in its meaning, since what is happening in reality at the interface is whether we end up with the clockwise octahedral rotation of the oxygen or counterclockwise from both sides of the domain wall. According to our result, the "same sign" or "different sign" of the $D_2$ term results in a different pattern. Thus they should each correspond to one or another of the two cases — the oxygen rotations of both sides of the domain wall end up with both clockwise or one clockwise and one counterclockwise. For simplicity, we will still stick to the "sign" of the $D_2$ terms in our following discussions and leave the determination of the oxygen rotation — which sign combination of the $D_2$ terms corresponds to which one of the two rotation cases — for further discussions in the future. The polarization and cycloid direction are illustrated by Fig. 7.9 as an example for 0 degree with respect to the y direction and as in the previous section, we will vary the angle of the domain wall. The magnetic field pattern of this configuration is shown in Fig. 7.10 (a) and (b). We can see a "V" shape at the $D_2$ and $\boldsymbol{P}$ domain wall. The "V" shape is symmetric if the $D_2$ have the same signs, and asymmetric if $D_2$ have opposite signs. If the domain wall is rotated by an angle, due to the mismatch of the cycloid period at the interface, there will be some “dangling”

cycloids at the interface as clearly indicated by Fig. 7.10 (c). This dangling should happen periodically. If the domain wall is with a larger angle, the period of the cycloid can be squeezed on one side and stretched on the other side, resulting in a blur or clear boundaries for the cycloid's stray field image, as indicated by Fig. 7.10 (d).

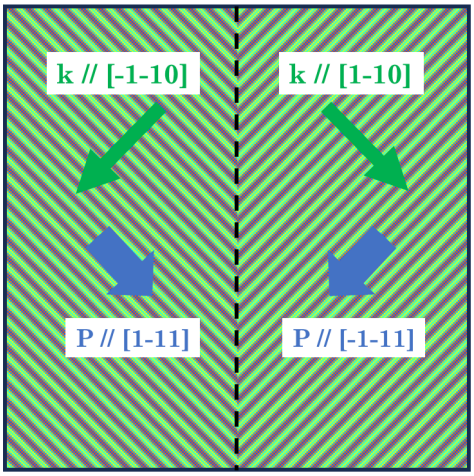


Figure 7.9: Illustration of the $\boldsymbol{P}$ and $\boldsymbol{k}$ configuration. Two P domains are simulated. The $\boldsymbol{k}$ directions are chosen to be the one in the (001) plane.

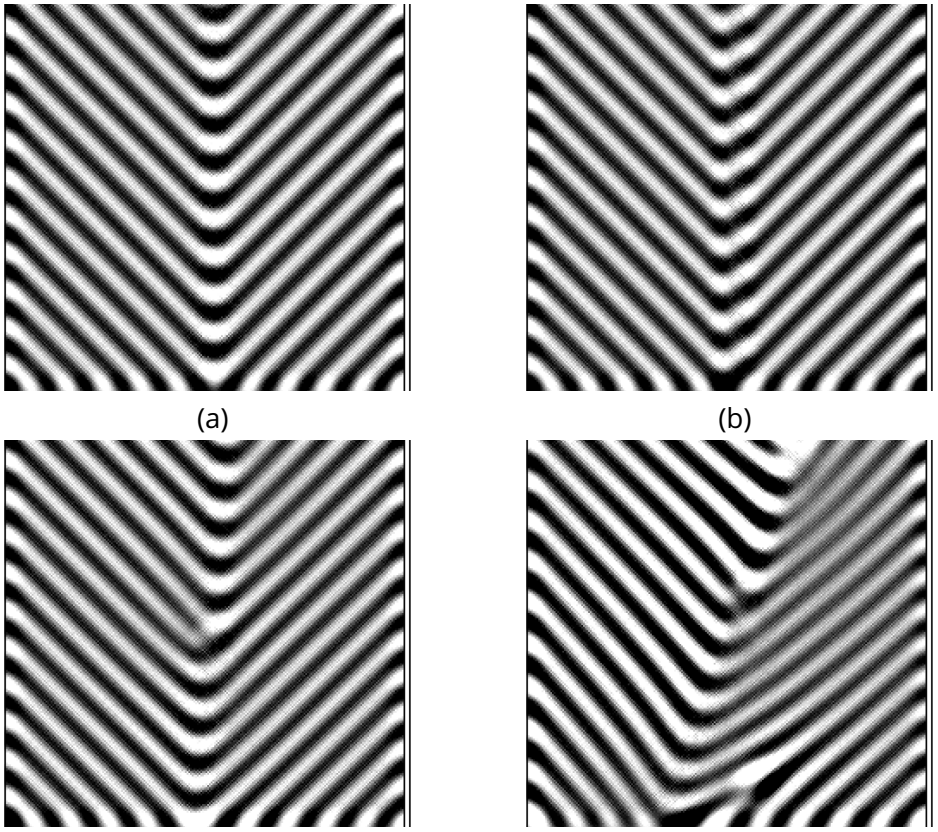


Figure 7.10: The stray field pattern of a common P and $D_2$ domain wall. (a) and (b) are domain walls along y. The $D_2$ are the same sign in (a) and different signs in (b). (c) and (d) have the same sign for $D_2$ with domain walls inclined by 5 and 20° from the y direction. For more details check Fig. D.5 and Fig. D.6 in the Appendix.

### 7.3.3 4P domain

The latest technique allows us to fabricate 4 P domains in the arrangement like that of Fig. 7.3. In this section, we will first discuss the results in a simplified case, as shown in Fig. 7.11. The four $\boldsymbol{P}$ point to the center. We will then set the P domains to be closer to what is measured in real life and use reverse engineering to deduce the spin structure.

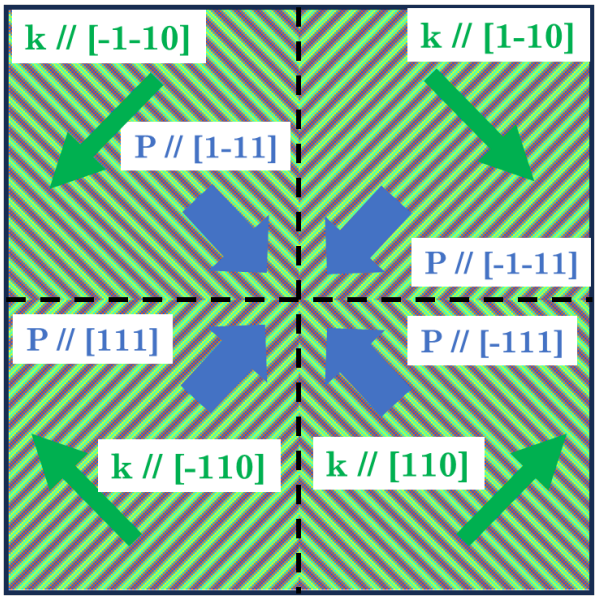


Figure 7.11: Illustration of the $\boldsymbol{P}$ and $\boldsymbol{k}$ configuration. There are four P domains that are pointing to the center.

This simple model of the four quadrants P domaind shows the main feature of the magnetic field pattern. We first initialized the system according to Fig. 7.12 (a). It relaxes to Fig. 7.12 (c). The magnetic moment vector $\boldsymbol{m}$ and the stray field are shown in Fig. 7.12 (f) and (e). The pattern is similar to what is simulated for two P domains. The main difference is that now $D_2$ can have 16 different configurations. The stray field patterns vary with the $D_2$ combination, as shown in Fig. 7.13. Depending on the $D_2$ sign, there could be a pattern enhancing the field at the interface or at the center. Similar results could be obtained for P pointing out. Since they are the same in principle, we present these results in Appendix D.1.3.

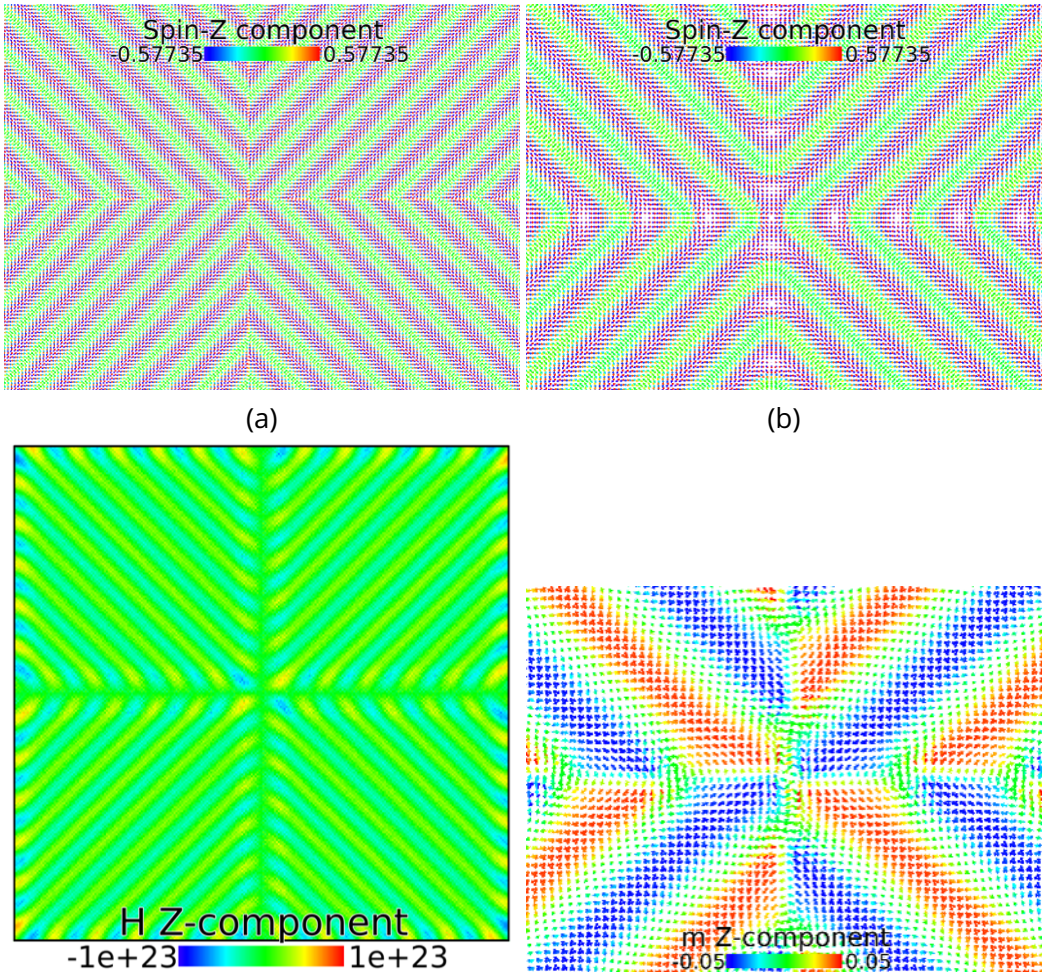


Figure 7.12: The initialized and relaxed spin textures. (a) is the initialized spin state and (b) is the relaxed state. (c) shows the stray field taken along z at 50A above the surface. (d) shows the magnetic moment in the center. The $m$ interface is sharp.

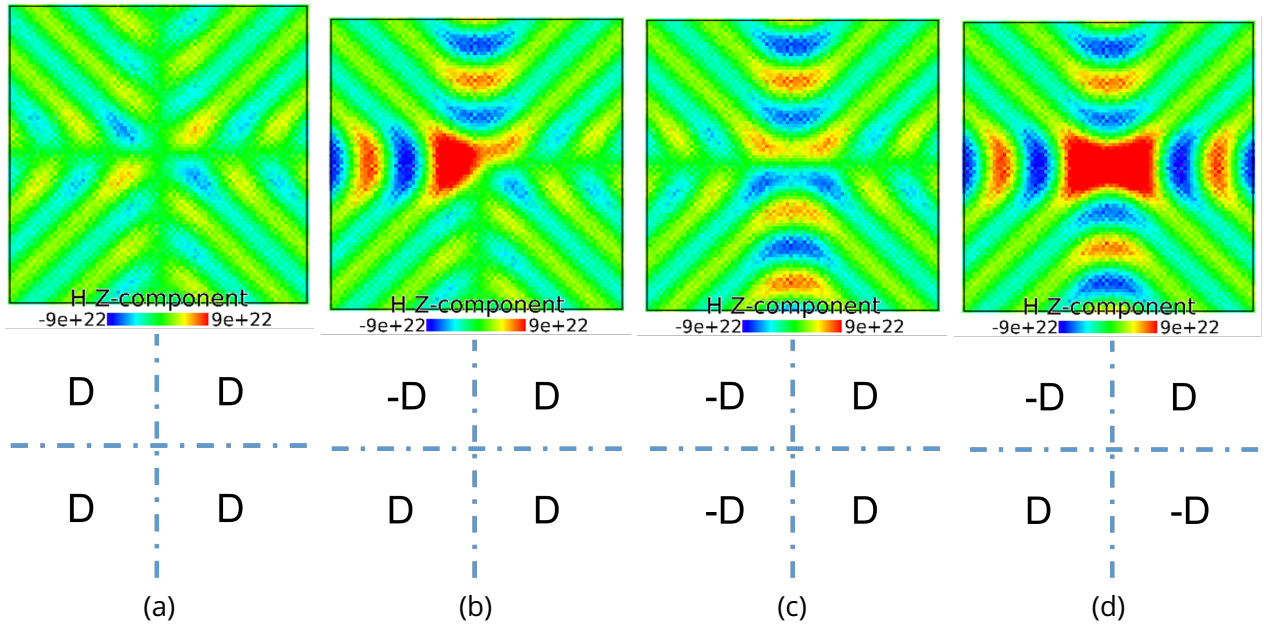


Figure 7.13: The stray field above the relaxed state shown in Fig. 7.12 with different $D_2$ configurations. Since the magnetic field normally cancels, it is enhanced if the magnetic moment has the same direction at the interface.

Interestingly, a simple asymmetry in the initialization brings asymmetry in the relaxed state. This is shown in Fig. 7.14 (a) and Fig. 7.14 c. The cycloid state becomes very different at the interface, with many cycloids winding back into the same P domain instead of merging with the other cycloid structures from other domains. The magnetic moment shows asymmetry and the magnetic field also shows an asymmetric "V" shape as shown in Fig. 7.14 (e). In reality, although the system favours the lower energy state, it is hard to go over the energy barrier so these states that are not the lowest energy state could be metastable. This is particularly the case when the system includes a lot of windings and possesses topological protection. We believe that these states are robust, so they can exist in real life depending on the history of the system. There could be different but possible spin states under the same $\boldsymbol{P}$ and $D_2$ conditions, which is an important message for our following study. We could not rely on a simple initialization and relaxation process to obtain the spin state even if we use the P-domain texture from measurements.

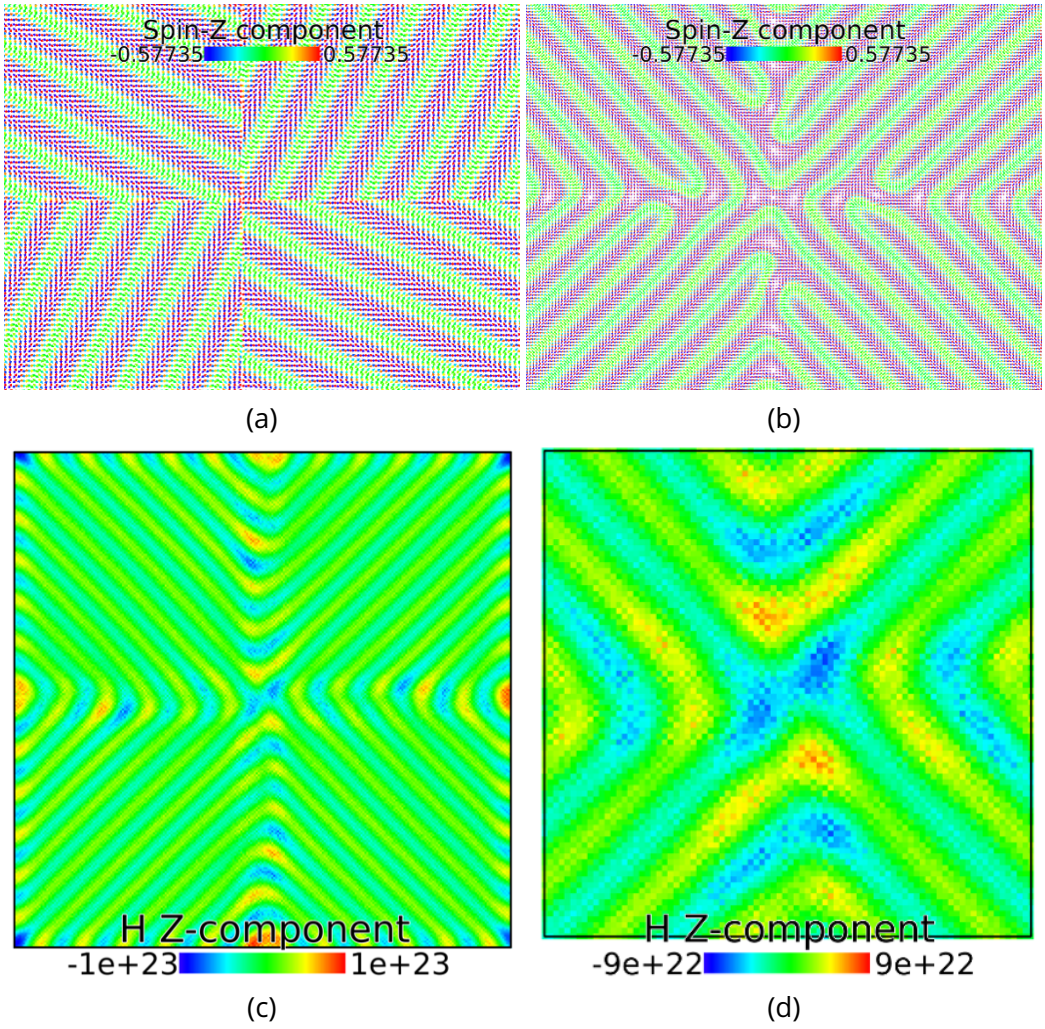


Figure 7.14: The initialized and relaxed spin texture. (a) is the initialized spin state and (b) is a relaxed state. The cycloids are rotated by a small angle compared with in Fig. 7.12. (c) is the stray field taken along z at 50A above the surface. (d) shows the magnetic moment in the center.

### 7.3.4 Reverse Engineering for the Spin Structure

The P domain of a sample that we denote No.103 is measured as shown in Fig. 7.15 (a). Since the P states at the outer boundary are unknown, we extract only the shape of the domain wall at the center of the four quadrants, and simplify the rest into a bigger four-quadrant pattern with straight interfaces, as shown in Fig. 7.15 (b). By doing this, we are neglecting the effect of the spin states from outside of the measured P zone. We attempted the same procedure as the simple cases of the previous section. The initialized system is the same as shown in Fig. 7.12 (a). At this time, we set the magneto-electric contribution as given by the P domain measured by PFM. The relaxed spin state is shown in Fig. 7.16. The magnetic field that we choose to be the best match among the 16 $D_2$ configurations is shown in Fig. 7.17 (a). The real-world measurement is compared with the simulated

results in Fig. 7.17. They coincide surprisingly well.

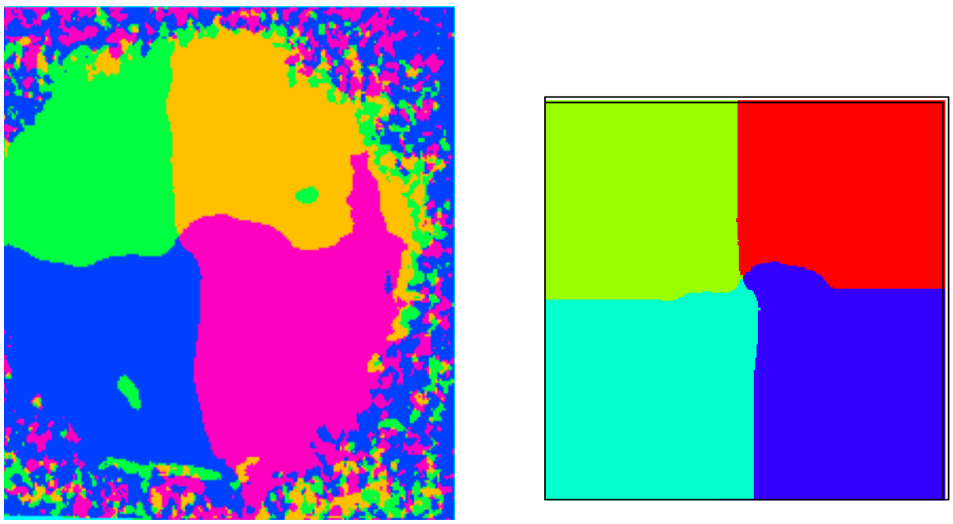

(a) (b)

Figure 7.15: (a) the measured P domain. (b) the simplified model.

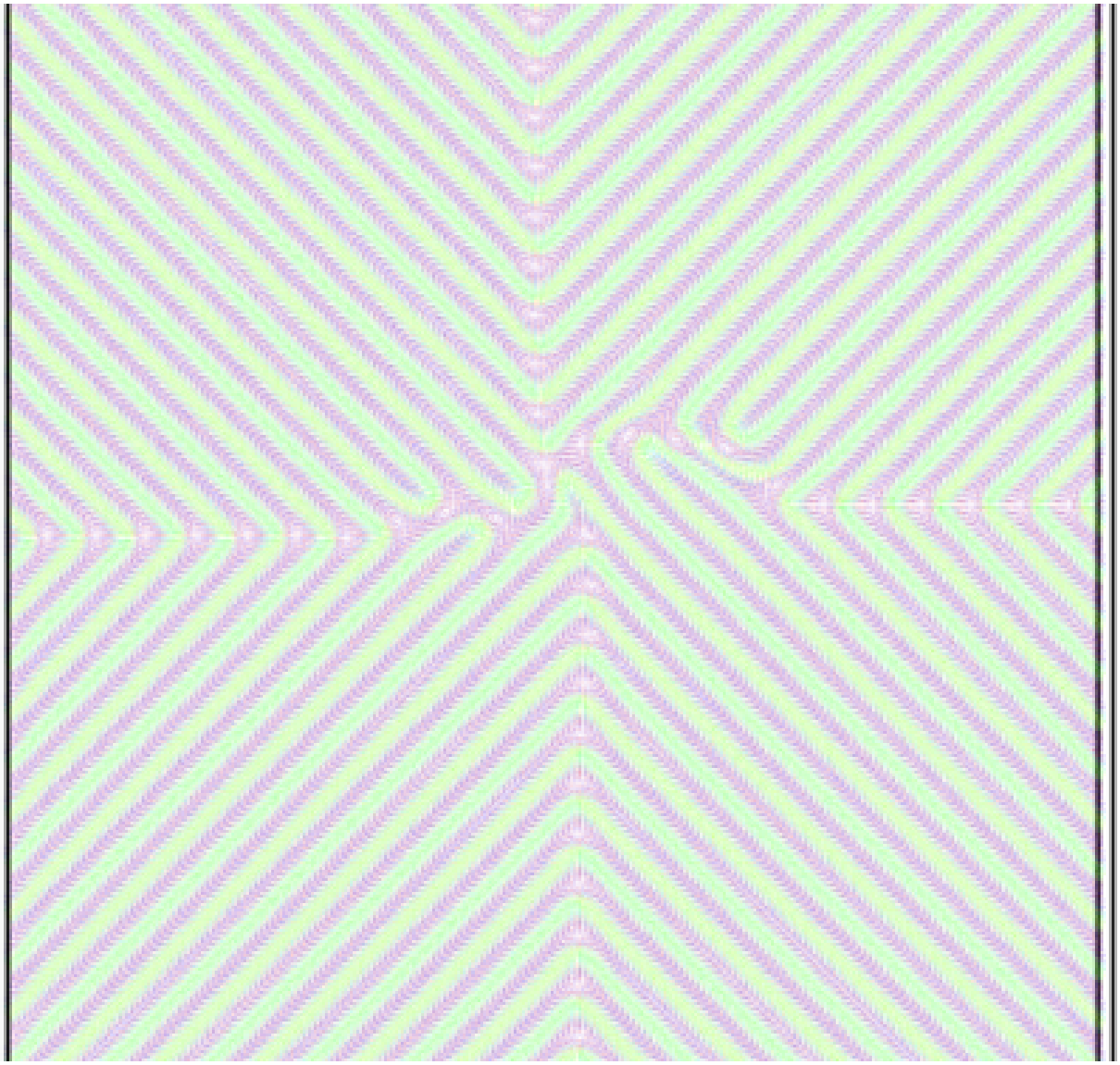

(a)

Figure 7.16: The spin texture after relaxation.

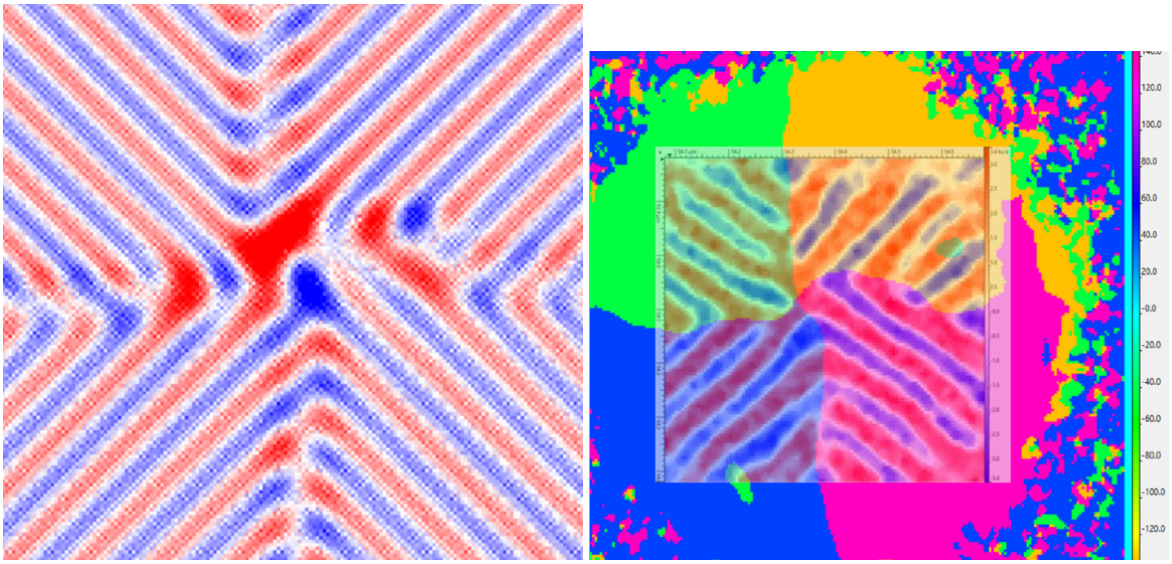

(a) (b)

Figure 7.17: (a) the simulated stray field. (b) the NV center measurement result.

## 7.4 Conclusion

In this chapter, we have predicted the existence of the $D_2$ domains, their $\boldsymbol{m}$ textures and their NV-center images. By fitting with the NV-center images, we obtained the spin textures of 4 P-domain BFO thin films and their $D_2$ domains. The reverse engineering technique that we developed will be useful for probing the underlying sub-wavelength spin textures. The $D_2$ domains that we predict could open a new independent parameter for the control of the magnetic structure of $BiFeO_3$.

# Chapter 8

# Antiferromagnetic Skyrmions in BFO

## 8.1 Background

Topology is a prominent concept from which new materials and properties are emerging [108]. In magnetic materials, it often arises as a consequence of the spin-orbit interaction, which couples the electrons' motion to their spin. Broken inversion symmetry can generate a chiral exchange interaction (Dzyaloshinskii-Moriya interaction or DMI) that curls spins into non-collinear textures carrying a finite topological charge, such as skyrmions [109]. These concepts applied to the field of spintronics pertain to a new research area coined spin-orbitronics [110]. Ferromagnetic skyrmions obtained in metallic multilayers can be used as ultra-small bits of magnetic information for mass data storage [111] and logic operations. However, their application is hindered by several problems: (i) a spin-polarized current pushes the chiral spin texture of skyrmions sideways and the entities eventually get trapped or annihilate on the track edges [112, 113] ; (ii) the power consumption required to displace them by current pulses is too large [114, 115] ; (iii) their displacement speed is limited to about 100 m/s [116]. These drawbacks could be alleviated by working with antiferromagnetic (AF) skyrmions [117] that can operate up to 2 orders of magnitude faster than their ferromagnetic counterparts [116, 47]. Moreover, using insulators, power consumption could be dramatically reduced, which is the aim of a new field called spin-insulatronics [20].

Usually, magnetic skyrmions are obtained by engineering the interfaces of artificial heterostructures [110, 118]. The basic relevant interaction is the DMI that stems from the coupling between magnetic atoms in the interface electrical built-in field. It is of the same nature as the more general Magneto-electric (ME) interaction expressing the gain in energy in presence of an internal electric field, or polarization, when magnetism is non-collinear [99, 119, 120]:

$$E_{ME} = \gamma_{ME} \sum \boldsymbol{P} \cdot [\boldsymbol{e}_{ij} \times (\boldsymbol{s}_i \times \boldsymbol{s}_j)] \tag{8.1}$$

with $\gamma_{ME}$ the inhomogeneous ME constant, $\boldsymbol{P}$ the polarization, $\boldsymbol{e}_{ij}$ the vector linking nearest neighbours and $\boldsymbol{s}_i \times \boldsymbol{s}_j$ the cross product of neighbouring spins. Therefore, magneto-electric materials intrinsically possess the possible interaction for generating skyrmions with the extra functionality that unlike interfaces, it can be toggled by switching the polarization. Among the relevant materials, $BiFeO_3$ is archetypal as it is an antiferromagnetic ferroelectric with both ordering temperatures well

above room temperature.

As such, it has been at the center of the huge revival of so-called 'multiferroics' since the early 2000s [121]. A vast literature has emerged to understand their nature [122], the coupling between antiferromagnetism and ferroelectricity [123, 124, 31, 125] as well as ways to engineer their properties, e.g. by epitaxial strain [126, 72, 127]. In BiFeO3, the significant coupling between electrical polarization P and AF order [123, 124, 125] forces the existence of a single AF T-domain (of constant AF staggering order) in a single polarization domain. This simplifies the domain structure of the AF order, leaving only 3 possible cycloids or 3 possible AF S-domains (when cycloids are destabilized by strain) [25]. The possibilities offered by thin film technologies and strain engineering are exciting, but it is thus far unclear what internal parameters should be tailored to produce and control individual skyrmions. The goal of the present chapter is to pave the way to experimentally achieve this, based on realistic modelling of $BiFeO_3$[128].

## 8.2 Modelling Method

The simulation is based on the classical model of spin dynamics with the LLG equation as introduced in Chapter 2. In BFO, the cycloid has a wavelength of 64 nm, equivalent to more than 100 atoms (the lattice parameter of BFO is $3.96$ Å). If one wants to calculate any 2-dimensional structures with skyrmions, the number of atoms in the simulation could easily reach half a million, which is rather heavy for the CPU. We thus use the code we developed as described in Chapter 2 to calculate on GPUs. We use the Hamiltonian as Eq. 3.2 and the parameters as described in Chapter 3.2.3.

## 8.3 Result

### 8.3.1 Stability

The stability (or meta-stability) of the topological entities is a crucial parameter to obtain experimentally achievable skyrmions. Therefore, the first part of this study is to find whether a skyrmion can be stable or metastable in BFO and our 'handle' is the uniaxial anisotropy $K_{1u}$. We find that when K1 is increased up to 0.012meV and we numerically initialize a skyrmionic state in a box of spins with periodic boundary conditions ( the box size is 120 nm), the skyrmion state survives after the relaxation process, as shown in Fig. 8.1. This parameter is just above the threshold anisotropy as will be explained in the following studies and will be the default parameter of skyrmion states in this chapter if not otherwise mentioned. The size of the relaxed skyrmion size is 28 nm in $BiFeO_3$ (close to the half period of the bulk cycloid), shown in Fig. 8.2 (a). Interestingly, in a magneto-electric medium the skyrmion is of hybrid nature as the spin winding generates an extra polarization in virtue of the spin current model: $\boldsymbol{P}_{ME} = \boldsymbol{e}_{ij} \times (\boldsymbol{S}_i \times \boldsymbol{S}_j)$. Note that this electrical part of the skyrmion is not chiral as it is generated by the spin chirality in a direction parallel to $\boldsymbol{P}$, hence purely along [111] ( Fig. 8.2 (b) ).

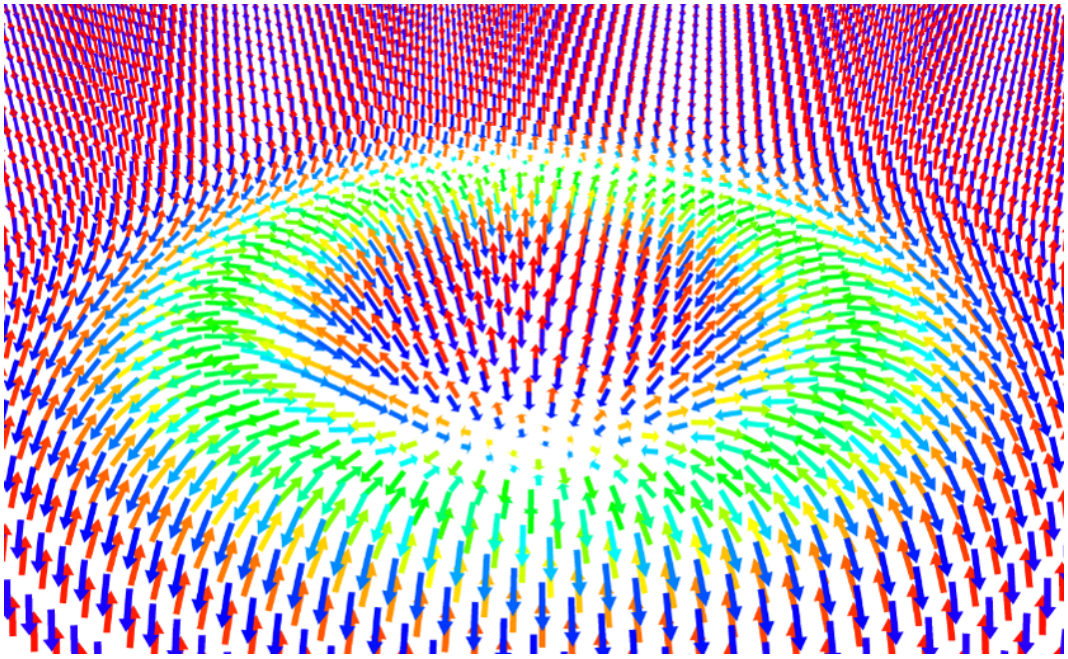

Figure 8.1: The spin texture of a skyrmion state with $K_{1u}$ tuned to be 0.012meV. (only 1 out of 24 spin vectors are represented in this figure)

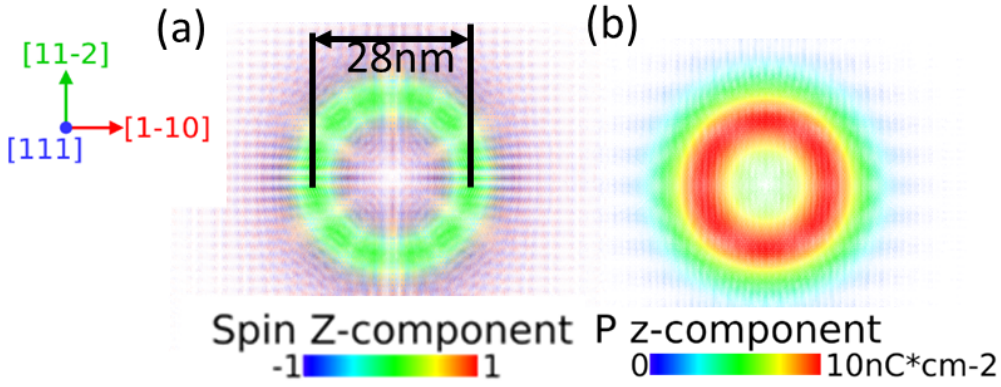


Figure 8.2: (a) shows the size of the skyrmion to be 28 nm when $K_{1u}$ = 0.012meV. (b) shows the magnetic chirality-induced electric polarization. The polarization is mainly along the [111] direction (z-direction).

To find the full region where skyrmions are stable, we tune the $K_{1u}$ in a larger range. We set the systems to relax starting from different initial conditions including a collinear AF state along [111], cycloidal states with different wavelengths, and skyrmion states. The energy per atom of these systems is compared and summarized in the phase diagram in Fig. 8.3. We find that there is a critical anisotropy $K_c$ indicated by the red dotted line that is at $0.01$meV. Above this threshold, all of the non-trivial states have higher energy than the collinear state, indicating that the system should be stable if

it is "flopped" along [111]. Below the threshold, the lowest energy state is the cycloid state, and the optimal period is close to $64$nm. Skyrmion states are simulated using the technique mentioned above. We find that from just above the threshold to a wide range of $K_{1u}$ up to $0.032$meV, the skyrmions survive and keep their topology under the relaxation process. Below the threshold, the skyrmions expand and become cycloid-like or so-called worm-like (as shown in Fig. 8.4), and keep their topology mainly due to the forced periodic boundary condition. From these results, we can conclude that the critical anisotropy $K_c$=0.01meV is the threshold of the flop state as well as the threshold for the metastability of the skyrmion. The size of the skyrmion also varies with the anisotropy, as shown in Fig. 8.5. The larger $K_{1u}$, the more the energy gained for spins to align along the [111] direction, the larger unbalanced torques induced by $K_{1u}$ from the outside and inside of the skyrmion's in-(111)-plane spins (as a result of the different density of [111]-aligned spins between the internal and external verge of the in-(111)-plane spins), and therefore the smaller the skyrmion.

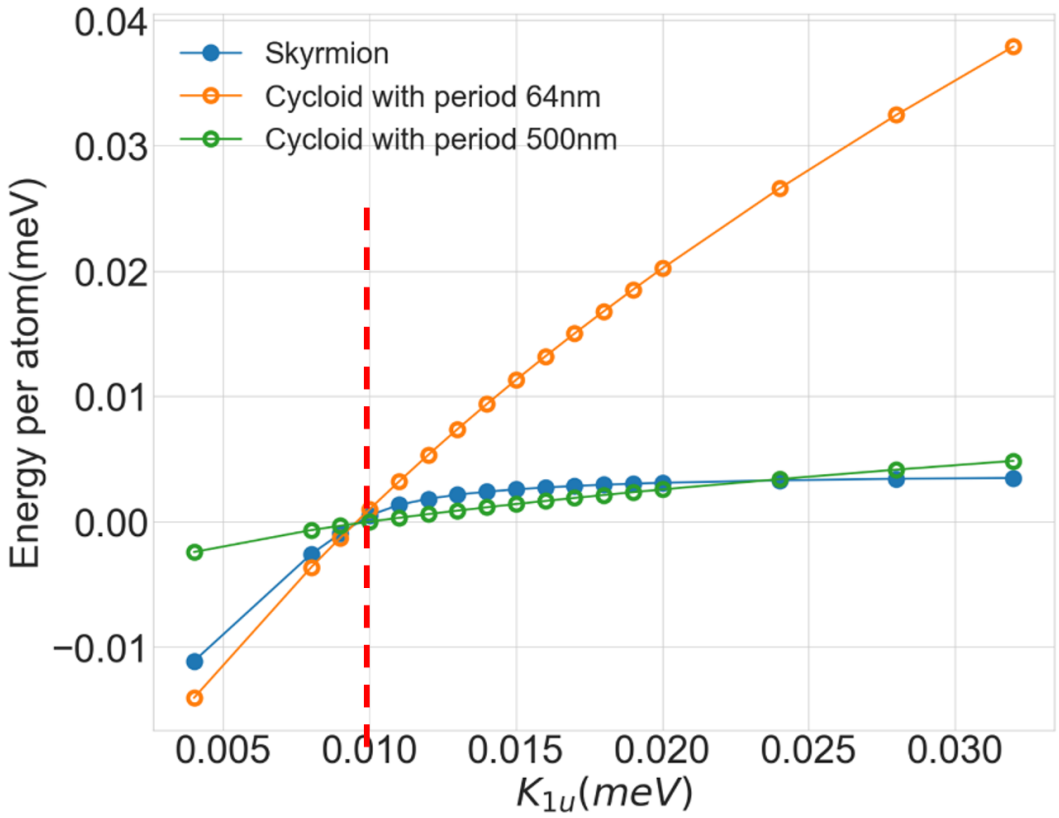


Figure 8.3: Phase diagram (energy vs anisotropy) where the zero is defined by the collinear AF state. Obtained ground states are the 64 nm cycloid below K = 0.010 meV and the collinear AF state above.

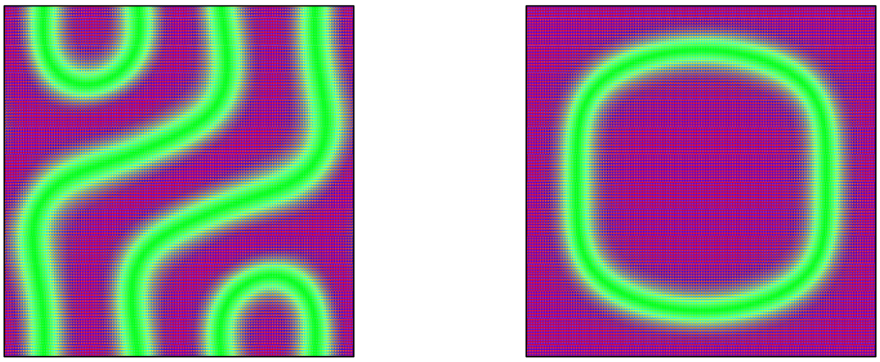

(a) K=$0.004$meV (b) K=$0.008$meV

Figure 8.4: The relaxed states with skyrmion initialized below $K_c$. They either keep a skyrmion-like shape due to the period boundary, or become a cycloid-like worm state.

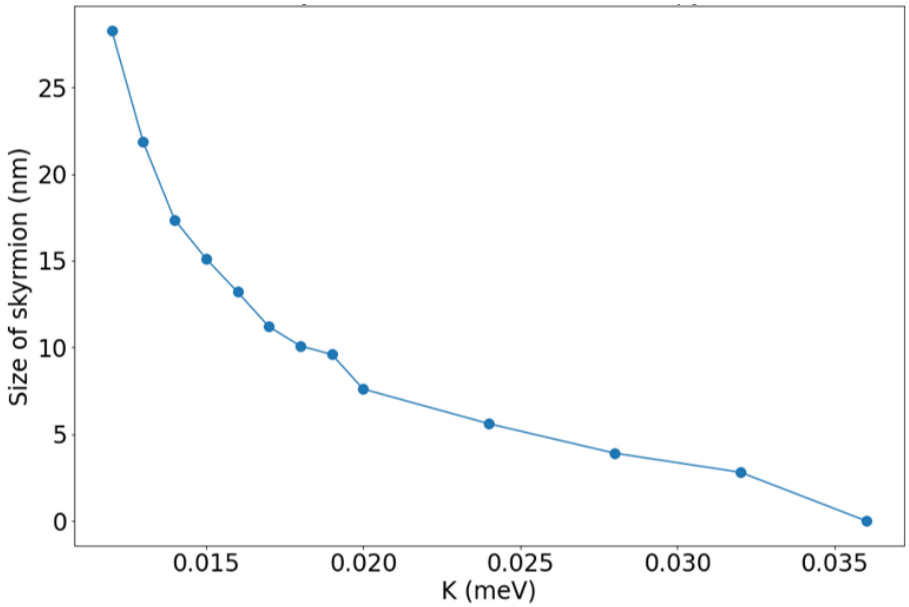


Figure 8.5: Skyrmion size vs. anisotropy.

Since the boundary condition is periodic, what is actually being simulated is a square lattice of skyrmion pillars. To prove that the stability is unaffected by the periodic boundary, we have varied the box size and observed that the energy of a skyrmion converges for a box size of 120 nm, as shown in Fig. 8.6. We also observed that the size of the skyrmions stays constant as the box size increases up to 120nm (not shown here). Therefore, It is certain that what has been simulated is actually equivalent to a single skyrmion since the interaction is negligible between the skyrmions ( i.e. itself reflected by the periodic boundary). Regarding the [111] periodic direction, we also simulated a finite thickness of 4nm instead of an infinite thickness and obtained a similar structure as shown in Fig. 8.7. Its size is

slightly smaller because of the missing exchange bonds induced by the free boundary condition. The average anisotropy per atom is thus larger than the periodic case, which leads to a smaller size of the skyrmion. Even if skyrmion lattice states exist in the two-dimensional plane, it should be in the form of a hexagonal lattice. We further tested skyrmion lattices by imposing a hexagonal skyrmion lattice and calculating the energy with varied super-lattice constants. We found that skyrmion lattices always possess a higher energy than that of a single skyrmion in any region of the anisotropy (result not shown). We thus conclude that the single skyrmion state will be the more stable skyrmion state under such conditions.

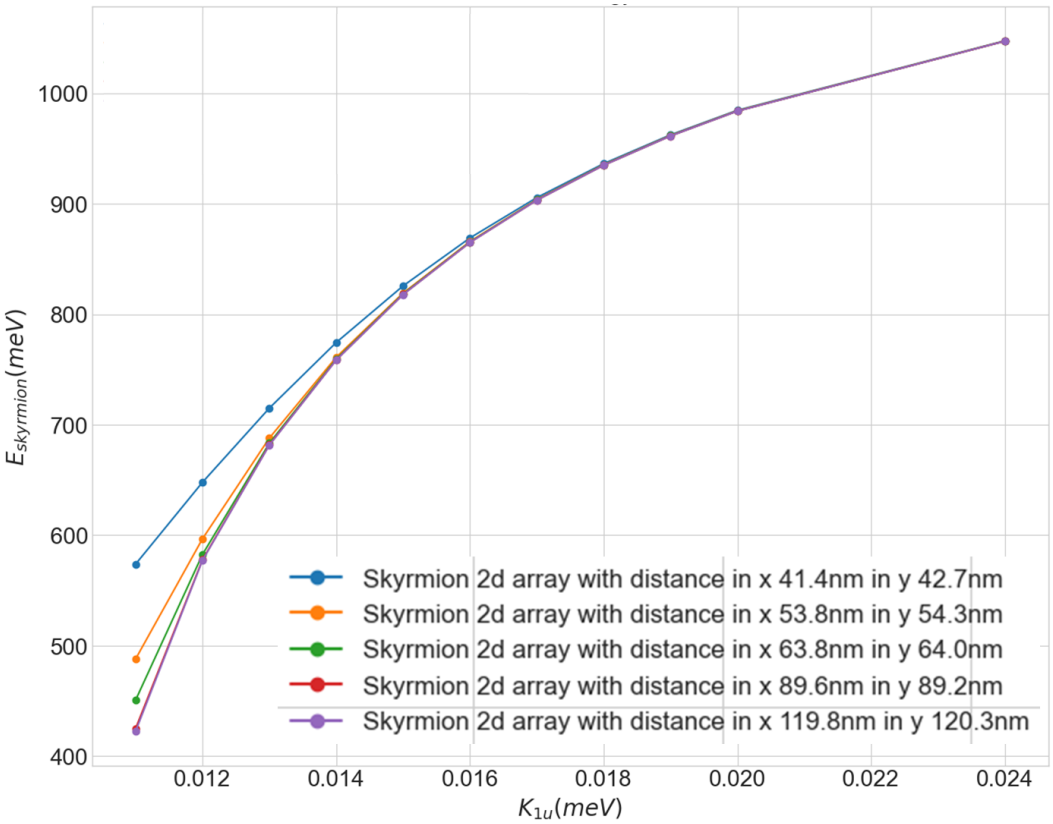


Figure 8.6: Skyrmion energy vs. distance. Here the skyrmion energy is defined to be the energy difference between skyrmion states and flop states of the whole system. The energy converges as the distance between skyrmions reaches 120 nm.

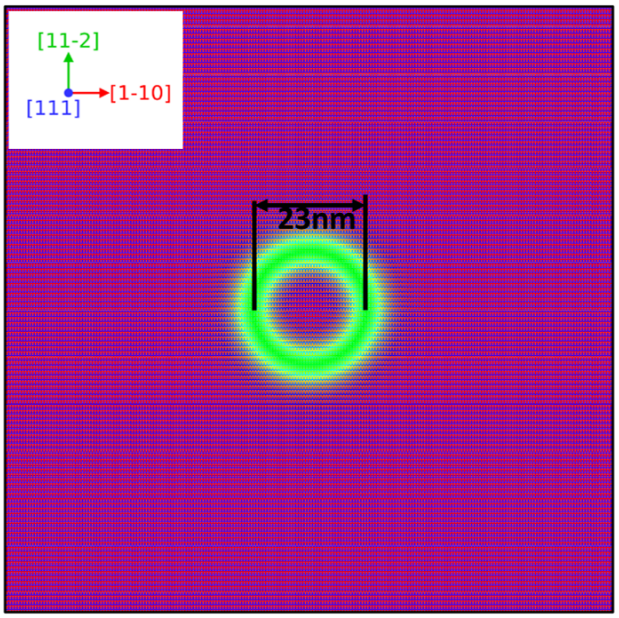


Figure 8.7: Skyrmion state of a 4nm thick thin film. The [111] direction has a free boundary condition.

A simple relaxation procedure using the LLG could not quantify the stability of the entity. Since thermal stability is crucial for real-life applications, we further conducted a GNEB calculation to verify the meta-stability quantitatively. GNEB calculations are conducted by the software LAMMPS. It can numerically find the lowest energy path to transform the topological to the trivial states. The calculation result is shown in Fig. 8.8. It can be seen that the energy barrier is about 0.7 eV for the simulated layers ( 6 (111)-layers, about 1.4nm ). Taking 4nm, which is the thickness of ultrathin BFO films proposed for an experiment, the energy barrier should be around 2eV. Such an energy barrier is high enough to resist thermal fluctuations at room temperature. Hence, we can conclude that if we are able to nucleate such a skyrmion structure in real life, it should survive for a sufficiently long time. Again, the main requirement here is that the uniaxial anisotropy has to be increased (by at least a factor of three) compared to that of bulk samples. Epitaxial strain is probably the right strategy to achieve this enhanced anisotropy, as it was already shown that different antiferromagnetic ground states ( collinear AF and different cycloid types ) can be reached when $BiFeO_3$ are grown on different substrates with different orientations.

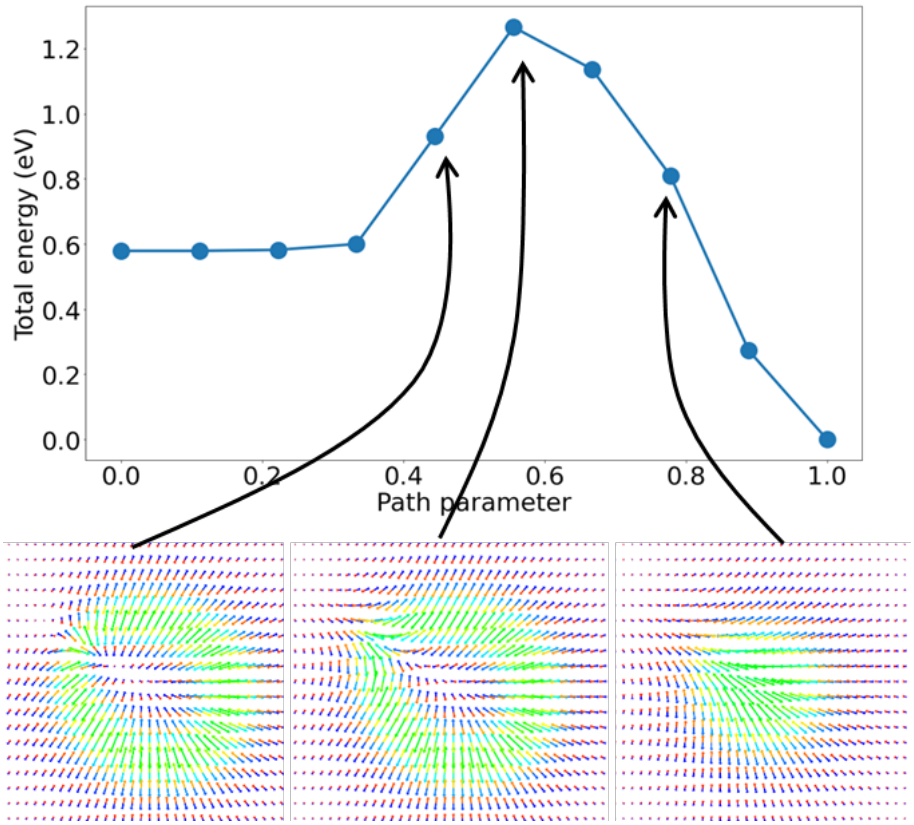


Figure 8.8: GNEB calcuation to verify the stability of the skyrmion. The starting state is a skyrmion state for $K_{1u}$ = 0.12meV. The end state is a flop state along [111]. The skyrmion goes through a Chimera-type annihilation. Therefore, the skyrmion is metastable but once nucleated, it is protected by a large energy barrier of 0.7eV of topological nature.

### 8.3.2 Dynamics

In order to go beyond the mere stability arguments, it is essential to find the right stimulus to control the AF skyrmionic texture either to nucleate or move the entities. The prime candidate for this is spin-transfer torque (STT). Since our material is insulating, out-of-equilibrium angular momentum has to be injected from another layer through an interface. This can be done using an adjacent conducting Pt layer where spin-orbit torque can be generated by passing a large current. Experimentally, it appears that this has never been achieved because the required current densities are so large that Joule heating has more effect than injected angular momentum. Another way of injecting the required spin densities with a limited Joule effect relies on the ultra-fast demagnetization of an adjacent ferromagnetic layer using a femtosecond optical laser pulse. This is the most efficient mechanism envisioned in the present chapter, taking reasonable spin bursts as measured experimentally. Alternatively, photoconductive switches may be used to generate longer pulses of spin currents. For computational purposes, the damping-like Slonczewski spin-transfer torque is introduced in the equation of motion

as:

$$\omega_\tau \approx \frac{G}{l}\frac{a^3}{n_s} j_s \tag{8.2}$$

with $G$ the spin transparency at the interface, $a$ the lattice constant, $n_s$ the number of magnetic atoms per unit cell, $l$ the thickness of the layer, and $j_s$ the spin current expressed in $\mu_B \cdot m^{-2} \cdot s^{-1}$ . $\omega_\tau$ has the dimension of a frequency. Here we take $G = 0.1$, $a = 0.396nm$, $n_s = 5$ per unit cell, $l = 5nm$ and $js = 6 \times 10^{31}$ , which leads to $\omega_\tau = 14.9GHz$, corresponding to $9.8 \times 10^{-3}meV$ in energy per atom.

As introduced in Chapter 1.3 and discussed in Chapter 4, in the case of a homogeneous AF domain, different behaviours can occur depending on the orientation and strength of the STT with respect to the Néel vector [54, 95]. In particular, during a sub-picosecond STT pulse applied perpendicular to it, the spins tilt towards the STT direction, accumulating energy and gaining magnetization; then they relax by gyrating along the generated magnetization direction on picosecond time scales. If the torque overcomes the anisotropy energy barrier, and the total angular momentum injected is sufficient, the spins eventually relax to another stable direction. We find that this is especially efficient in triggering the dynamics of pre-existing skyrmions in a BiFeO3 layer. Here, our atomistic simulations are essential because as the angle of angular momentum accumulation and local spins vary in space, it is hard to simply predict the possible distortion and motion of a topological entity. As shown in Fig. 8.9, an STT pulse along the -x direction in plane could store some angular momentum in the system (equivalent to transmitting some velocity to the skyrmion as revealed by the Eq. 4.17 in Chapter 4 ) and trigger a motion of the skyrmion along y. This is not constrained to the x or y direction. For an arbitrary direction of STT applied in the (111)-plane, the skyrmion will be set in motion with a velocity perpendicular to the STT direction ( it is isotropic in the plane due to the symmetry of the skyrmion ). The direction of motion is thus controlled in experiments by the magnetization direction of the adjacent ferromagnet. The final position of the skyrmion is proportional to the total angular momentum injected. There is no intrinsic constraint on the minimum torque that should be applied, as indicated by the torque modelled by SOT injection from Pt. The small torque pushes the skyrmion, reaching an equilibrium state with the friction that arises from the damping term in the LLG equation, such that the skyrmion moves at a constant velocity.

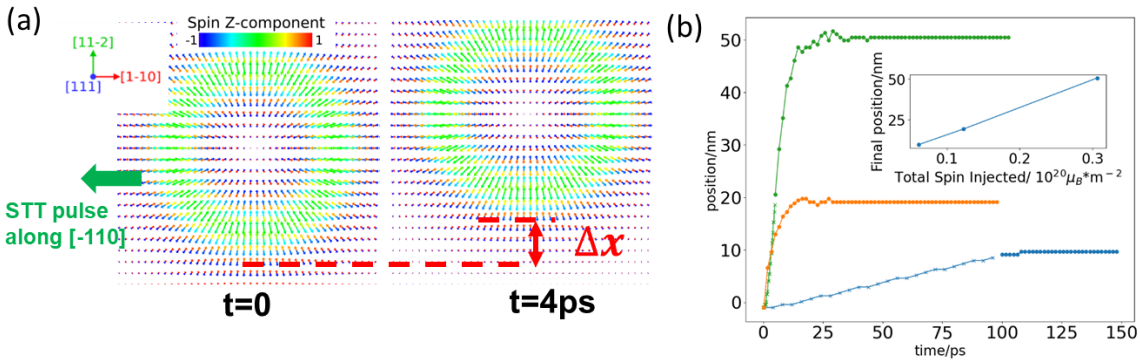


Figure 8.9: STT applied in-plane could trigger the dynamics of the skyrmion. (a) shows the motion resulting from a [-110] pulse with 200 fs duration. A maximum initial velocity over 10 km/s can be reached in a direction perpendicular to the injected spins without destroying the skyrmion. (b) shows the skyrmion motion for parameters mimicking three different experiments: a 100 ps long spin injection from Pt with $j_s = 0.06 \times 10^{30}\mu_B \cdot m^{(-2)} \cdot s^{(-1)}$ (blue line), STT generated from ultra-fast demagnetization of a ferromagnetic adjacent layer applied for 0.2 ps with $j_s = 61 \times 10^{30}\mu_B \cdot m^{-2} \cdot s^{-1}$ (orange line) and a 5ps long STT delivered by an electrical pulse from a photoconductive switch with $j_s = 6 \times 10^{30}\mu_B \cdot m^{-2} \cdot s^{-1}$ (green line). Crosses and filled circles represent positions respectively during and after the STT pulses. The inset shows that the final position scales linearly with the total amount of spins injected.

Furthermore, STT applied perpendicular to the (111) plane could trigger an interesting twisting mode of the skyrmion. The main motion of the spins is to oscillate in the (111) plane coherently around the skyrmion, as shown in Fig. 8.10. The frequency is extracted to be about 0.7 THz as plotted in Fig. 8.11.

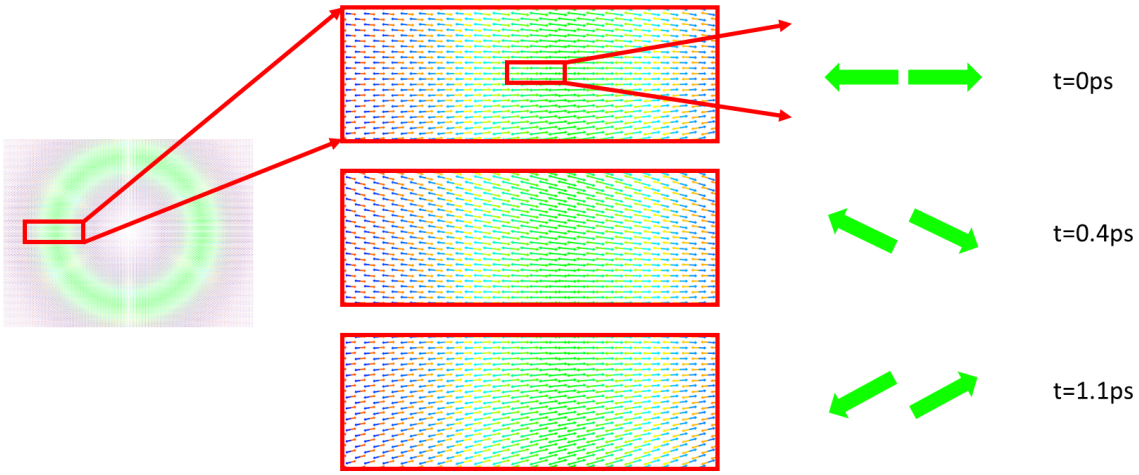


Figure 8.10: Illustration of the twisting mode. The spins oscillate coherently due to the symmetry of the skyrmion and the torque injected from STT.

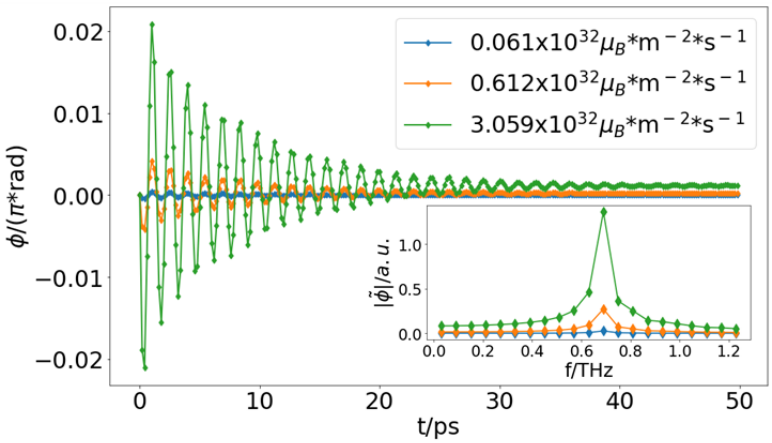


Figure 8.11: The twisting mode frequency is 0.7 THz. $\phi$ is the in-plane deviation angle of the in-(111)-plane spins from their original direction.

Since $BiFeO_3$ is multiferroic, it is natural to expect electric control of the antiferromagnetic skyrmion. Indeed, applying an electric field can in principle add or subtract to/from the magnetoelectric coefficient. This should transiently change the natural size of the skyrmion. Therefore, we simulated pulses of electric fields in different directions and found that a pulse along the [111] direction could induce a breathing mode as shown in Fig. 8.12. When applied along in-plane directions electric pulses trigger a complicated response of the skyrmion as shown in Fig. 8.13.

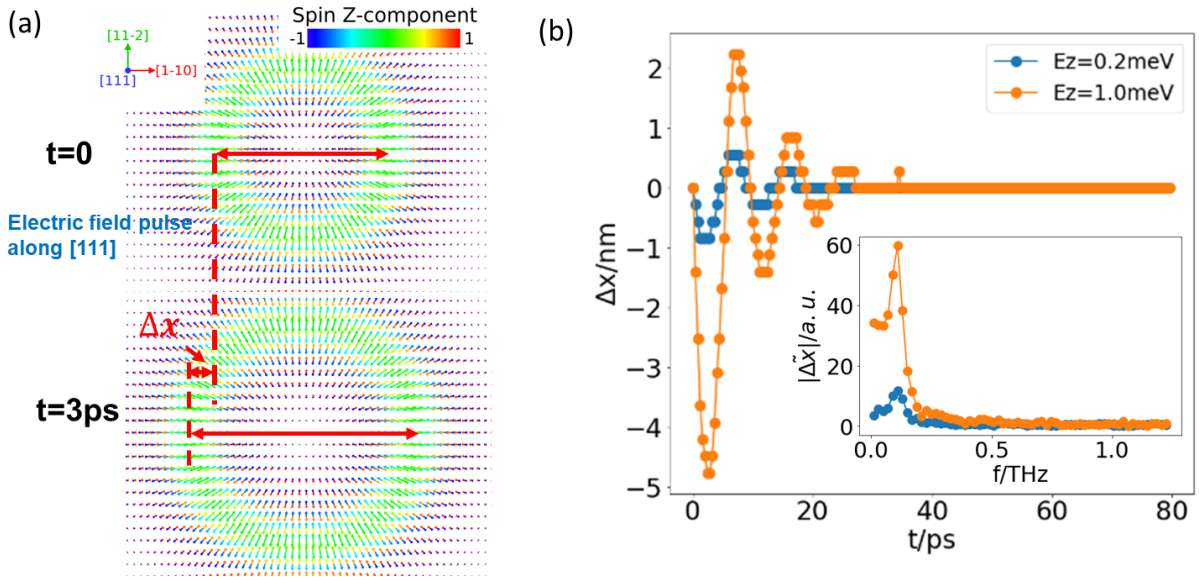


Figure 8.12: (a) Breathing mode induced by a [111] electric pulse where the mode frequency (b) is obtained at 0.11 THz (the FFT is in inset). The applied field is overly large (500 MV/cm) in order to better visually see the effect on the figure, but a smaller field gives the same qualitative result.

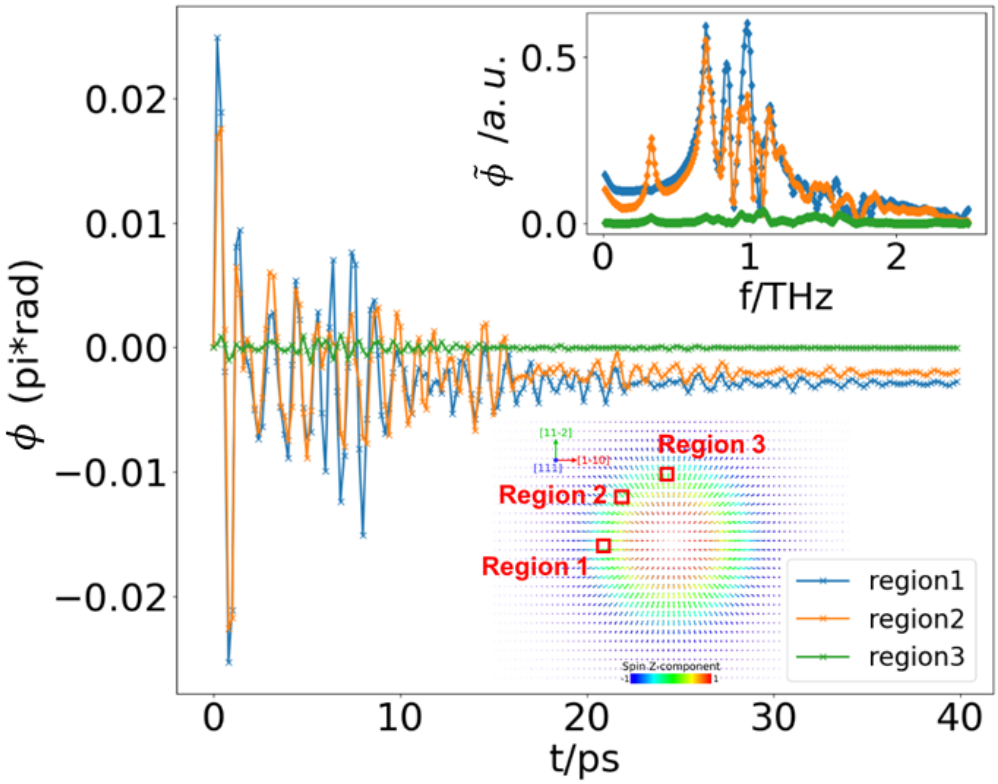


Figure 8.13: Response of the skyrmion in different regions after an electric field pulse in-plane. The skyrmion endures an inhomogeneous torque and results in a non-coherent oscillation.

### 8.3.3 Nucleation

The most stable state with our chosen parameters for $BiFeO_3$ is the collinear state along [111]. This configuration is the stable state on which we want to write a skyrmion. The energy barrier applies for both sides of the curve in Fig. 8.8. This indicates that an excitation of at least 1.2 eV per 6 (111)-layers is required to transform the system from trivial topology. The optimal strategy to overcome this huge energy barrier would be: (i) to apply stimuli that transform the topology close to the minimum energy path (ii) to apply the stimuli on larger areas and craft the right topology on larger scales in order to reduced the excitation energy per atom (iii) to accumulate the excitation over time.

STT has been shown in Chapter 4 to be a useful tool to switch AF domains. Creating the proper topology has to involve switching part of the AF domain from the trivial [111] state. So we first attempt to nucleate a skyrmion with STT. To apply strategy (ii), the manipulation with the cheapest per-atom energy cost to flip the AF state would be assumed to be applying STT on a very large area. Nevertheless, this is not true as we find that the threshold is lower if we apply only to a finite area, which will be discussed in the next paragraph. To find the threshold STT that could overcome the uniaxial anisotropy, we create a box of spins with a trivial collinear state along [111] with periodic boundary conditions. A step function in time of STT is applied. We find that the threshold is between 0.07 meV to 0.08 meV, which is close to the anisotropy but lower. Interested readers could check the snapshots

of the states shown in Fig. E.1 and Fig. E.2 in the Appendix.

The next to be simulated is STT applied on a 200nm$\times$200nm square, as illustrated by Fig. 8.14 (a). Although an analysis from strategy (ii) would indicate that the threshold should be higher in the square case, the numerical simulation shows the opposite. The threshold is found to be between 0.065meV and 0.066meV. The nucleation process is shown in Fig. 8.15 ( Fig. E.3 and Fig. E.4 in the appendix show a failed process and a successful process with higher STT). The $\boldsymbol{l}$ vector is successfully flipped even below the previous threshold in the homogeneous case. The reason is the accumulation of energy from the interference of the spin waves and the cycloid-like texture of the spin waves, which is favoured by the magneto-electric coupling. Despite these gains of energy, the threshold is not so much lowered compared with the homogeneous case ( only about 15% ).

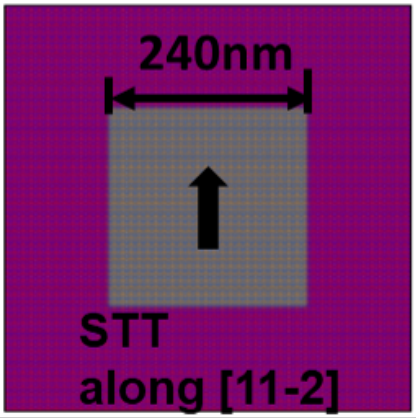


(a) STT along y direction

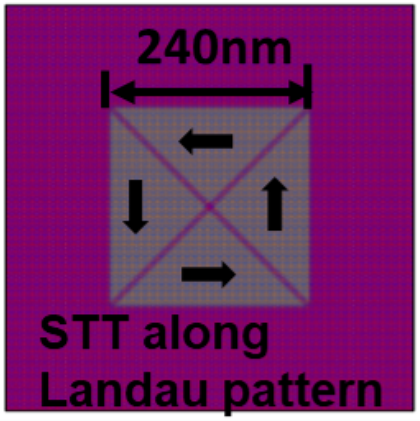


(b) STT along Landau pattern (clockwise)

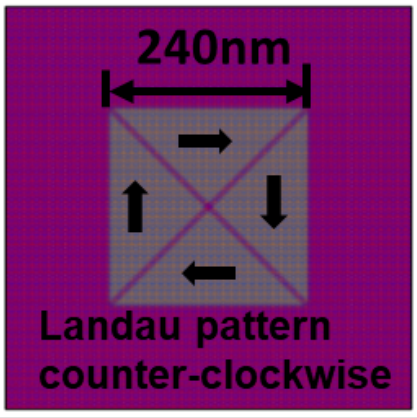


(c) Landau pattern (counter-clockwise)

Figure 8.14: Illustration of STT applied on a square area with 200nm size.

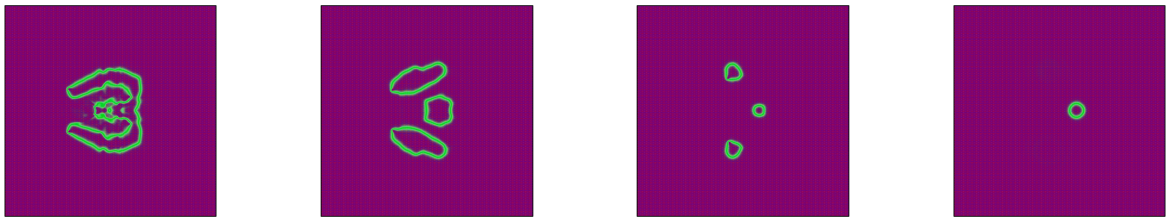

(a) t=6.2ps (b) t=12.6ps (c) t=20.2ps (d) t=24.2ps

Figure 8.15: A successful attempt to nucleate skyrmion for STT applied along y. STT=0.066meV. Two entities with topological defects annihilate while the third one survives as a skyrmion.

To adopt strategy (i), STT forming a Landau pattern is applied to the same initial state, as illustrated by Fig. 8.14 (b) and (c). The threshold is found to be slightly smaller (about 10%), as shown in Fig. 8.16. Interestingly, due to the intrinsic chirality of this magnetic configuration, there is a favoured direction which is the clockwise Landau pattern of STT. However, the inverse STT has the same threshold for creating a skyrmion ( as shown in Fig. E.5 in the appendix). This indicates that the skyrmions can be created by the sharp interface between different STT directions or the overlap of the spin waves generated by the different directions of STT. The advantage of using a Landau pattern with the preferred chirality is better revealed when the STT is slightly higher than the threshold ( as shown in Fig. E.6 in the appendix). Under this STT, the counter-clockwise creates two skyrmions in a similar process as in Fig. E.5 ( figures not shown ), but clockwise STT creates a target skyrmion, during the process where the Landau pattern collectively flips the spins twice with the right topology. Demagnetizing vortex states should achieve similar results and may be a good idea to nucleate skyrmion.

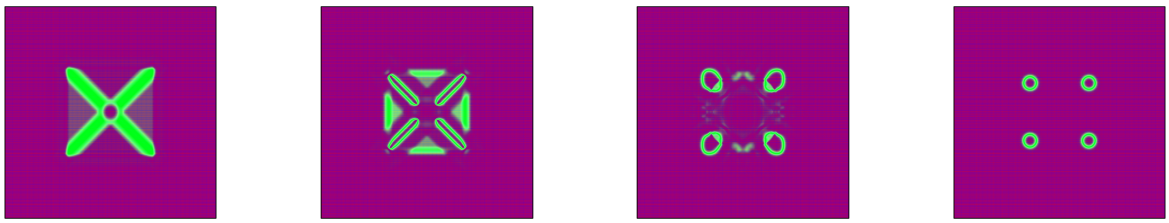

(a) t=1ps (b) t=1.8ps (c) t=4.2ps (d) t=14.2ps

Figure 8.16: Clockwise STT=0.062meV. Four skyrmions are formed at the corners. Due to symmetry, they have the proper topology.

We also tried to nucleate skyrmion with electric fields. However, we find that this does not generate the appropriate skyrmion for any reasonable field value applied on a 100nm spot. Attempting a periodic resonant excitation (adopting the strategy (iii) ), we also failed to nucleate a skyrmion even for a field amplitude of 100 MV/cm. Therefore, an electric field alone is not adequate for nucleation. The details can be found in the Appendix E.

## 8.4 Conclusion

To conclude, we have explored the conditions that drive $BiFeO_3$ towards a topological transition. We find that with a slightly enhanced uniaxial anisotropy that could be induced using strain, individual antiferromagnetic skyrmions are protected by a large topological barrier. Using spin-transfer torque alone, nucleation is hard to achieve with experimentally available intensities (at least within our simple model), but perhaps not impossible with the help of temperature to reduce the energy barrier. In any case, STT is adequate to excite and even push pre-existing skyrmions with speeds faster than 10 km/s. Therefore, our simulation work should trigger experimental studies to reach the conditions to produce skyrmions in BiFeO3 and use these entities as advantageous alternatives to their ferromagnetic counterparts regarding their faster dynamics and simpler linear motion.

# Chapter 9

# Conclusion

In this dissertation, we presented the results of our theoretical and numerical studies of the spin textures and dynamics in archetypical antiferromagnetic insulator NiO and multiferroic antiferromagnet $BiFeO_3$. Our numerical tools obtained crucial results based on atomistic models. In particular, the new high-performance code that we developed has made possible a series of studies in $BiFeO_3$. The antiferromagnets, due to their high resonance frequencies and low energy dissipation, have the potential for the ultrafast manipulation of magnetic textures. The magnetoelectric interaction in $BiFeO_3$ has endowed the possibilities for the existence of topological magnetic entities. Our studies could be useful for future theoretical and experimental studies.

# Appendix A

# NiO Spin Wave Control and Logic Gates

Discussions of the results in Chapter 4 are in this appendix.

## A.1 Discussion

### A.1.1 Attenuation of the Domain Wall motion

The $\theta$ attenuates as the domain wall propagates, which is induced by two effects: damping and the energy distribution along its propagation path (such as another domain wall that breaks off). The attenuation of the $\theta$ appears to be linear along the propagation, but its rate is two-fold linear, as shown by Fig. A.1.

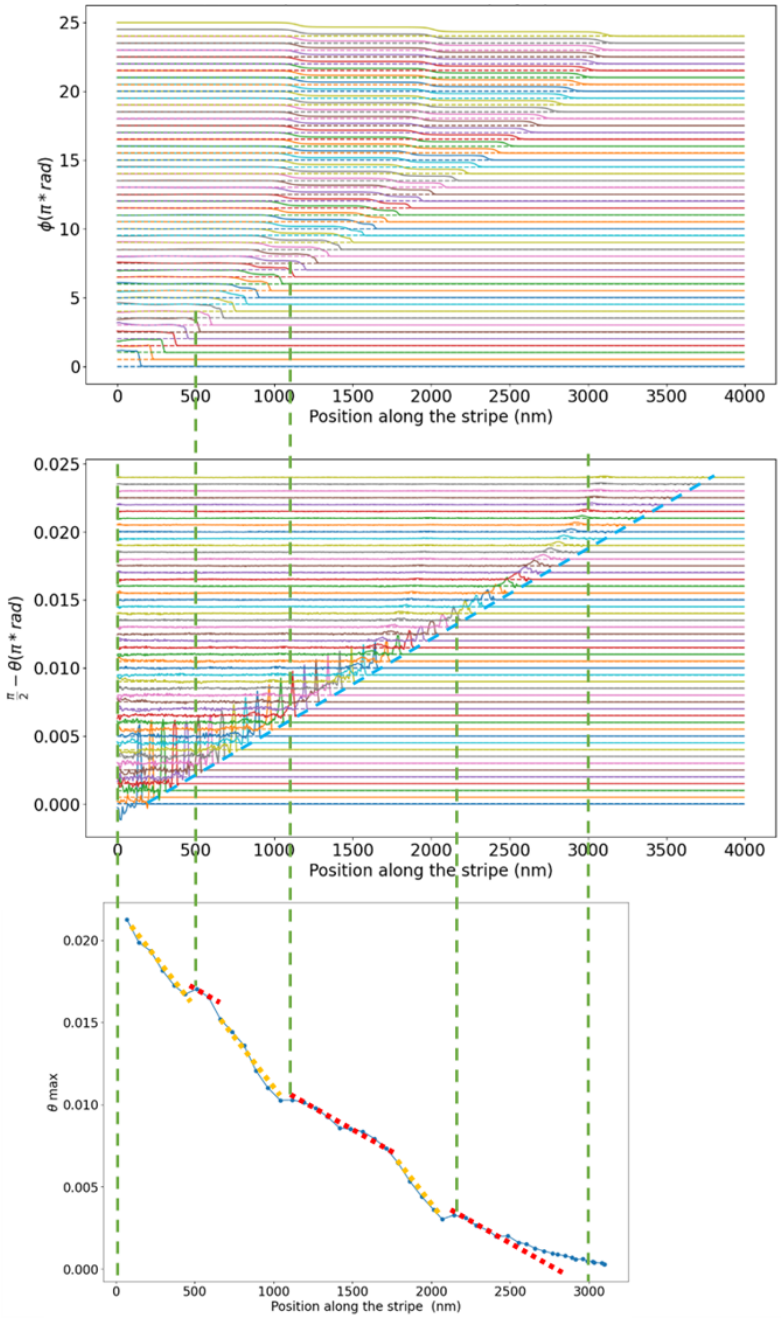


Figure A.1: The attenuation of $\theta$ in comparison with Fig. 4.8. "$\theta$ max" represents the maximum amplitude of $\theta$ and its position when the domain wall propagates. The blue dashed line represents the wavefront that propagates at 41.7km/s. The green dashed lines indicate the onm position, the beginning of the first breakdown of the domain wall, the beginning of the second breakdown, the beginning of the slow down of the last domain wall, and the 3000nm position, respectively. The yellow dashed lines are all parallel, indicating that the phases when the domain has broken down have the same velocity, which differs from the other phases indicated by the parallel red dashed line.

# Appendix B

# BFO in Strong Magnetic Fields

## B.1 Periodic Boundary in x, y and z

The invariant defined in Eq. 5.1 is a vector, but the main component of the vector is along [111] direction. The $\boldsymbol{V}$ along z per atom is plotted in Fig. B.1 .

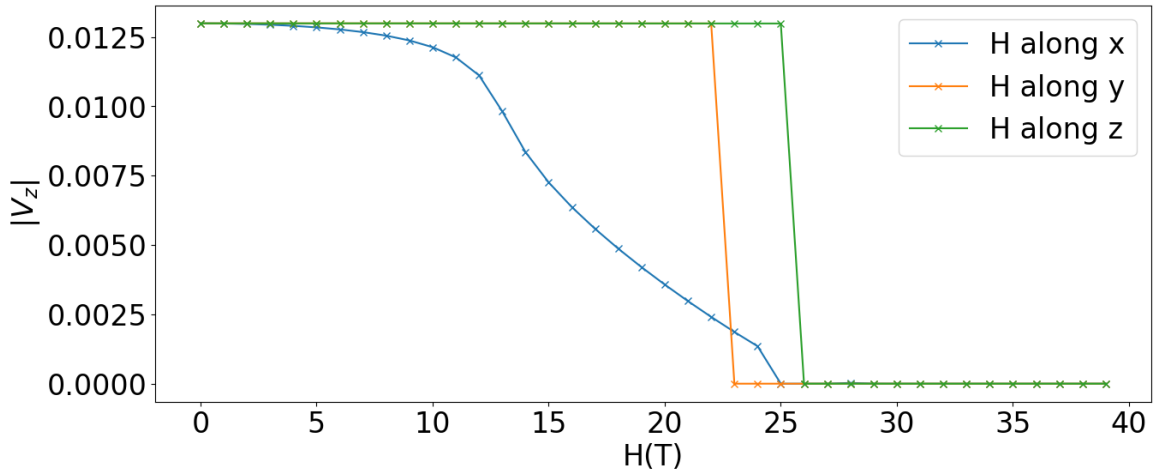


Figure B.1: The absolute value of the invariant $\boldsymbol{V}$ z component under different magnetic fields applied. The invariant is calculated by Eq. 5.1 for each site and taken as average among all sites. Both initializations (cycloid and flopped) are calculated, and what is plotted is only the one among the two that ends up with lower energy.

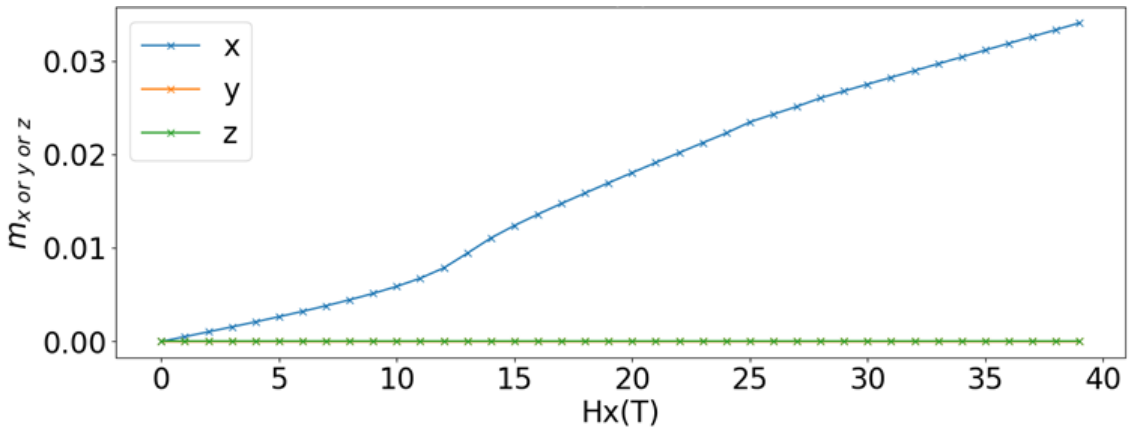


Figure B.2: The three direction components of the magnetization with magnetic fields applied along x. The magnetization is calculated as the minus of the mean value among all the spin unit vectors in the simulation. Similar to Fig. B.1, the magnetization of the lower energy state is plotted.

With the field applied along y, the anharmonicity scales linearly, which is verified for free boundary conditions in the x and y directions, as shown in Fig. B.3. When the field is applied along z, the period is also verified to be constant ( plot not shown ).

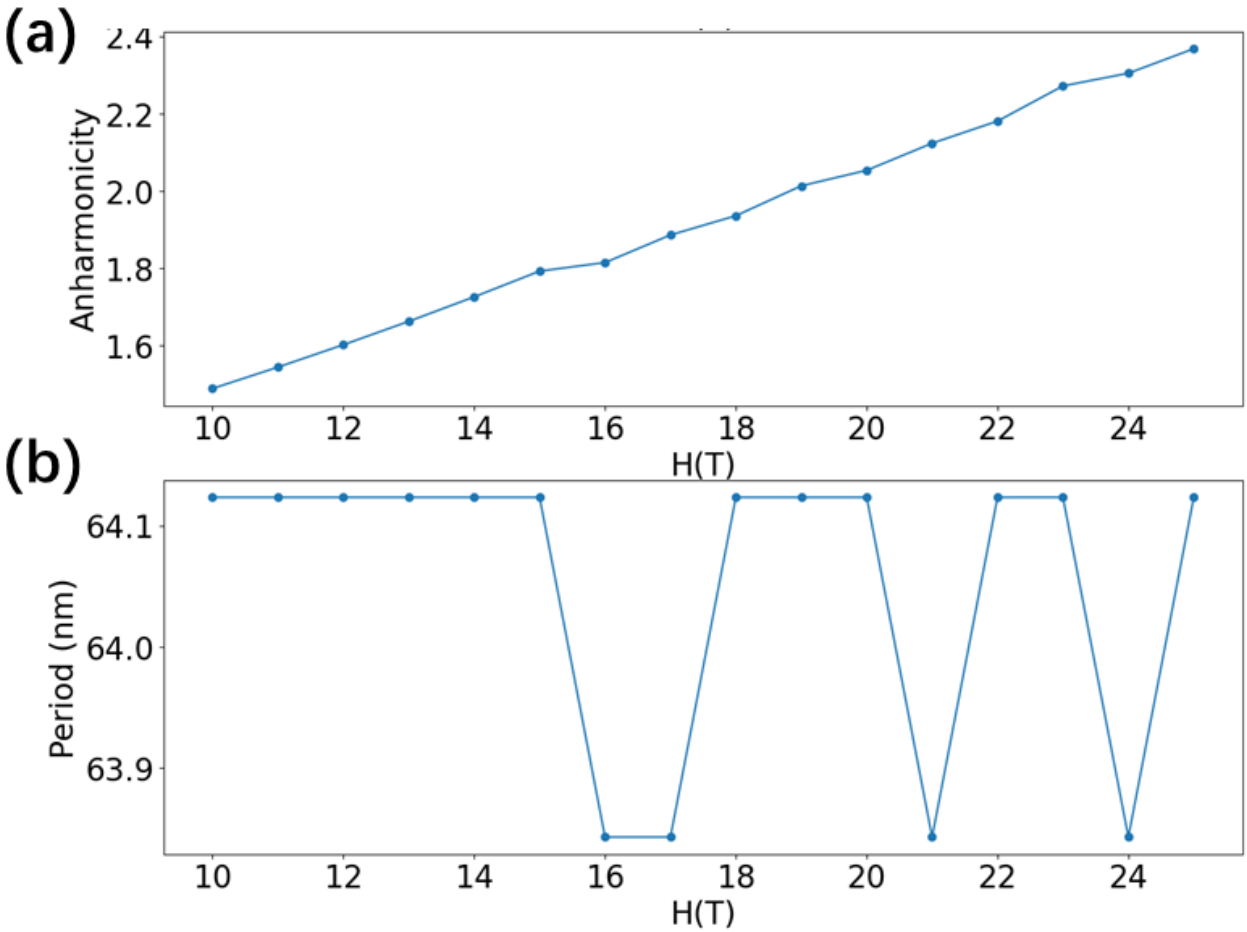


Figure B.3: With magnetic fields applied along y, (a) the anharmonicity and (b) the period of the cycloid are verified for free boundary conditions in the x and y directions. As the field increases, the period does not change, whereas the anharmonicity changes.

# Appendix C

# Effect of a Pulse of Spin-transfer Torque on the BFO Cycloid

Some details of the spin dynamics in NiO and some discussions are recorded in this appendix.

## C.1 Results

### C.1.1 Homogeneous STT along $k$ Applied on the Whole Area

In this model, the STT is applied homogeneously on the cycloid. We simulate a box with periodic boundary conditions in all three directions, as shown in Fig. 6.2 (b).

#### C.1.1.1 STT Applied Parallel to $k$

The magnetization oscillates mainly along the x direction (the cycloid direction), as shown in Fig. C.1.

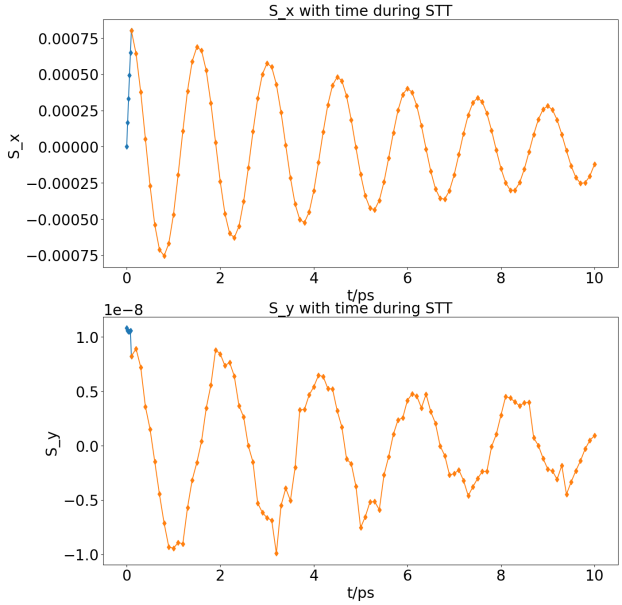


(a) Spin x and y component for STT = 1e-2 meV

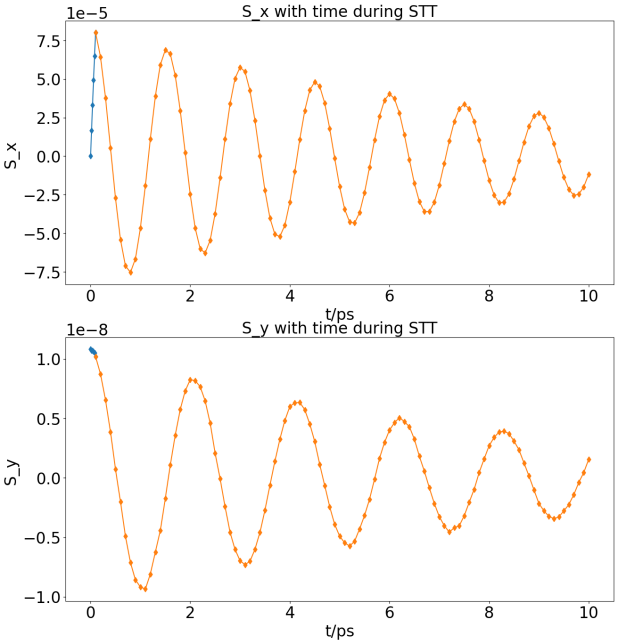


(b) Spin x and y component for STT = 1e-3 meV

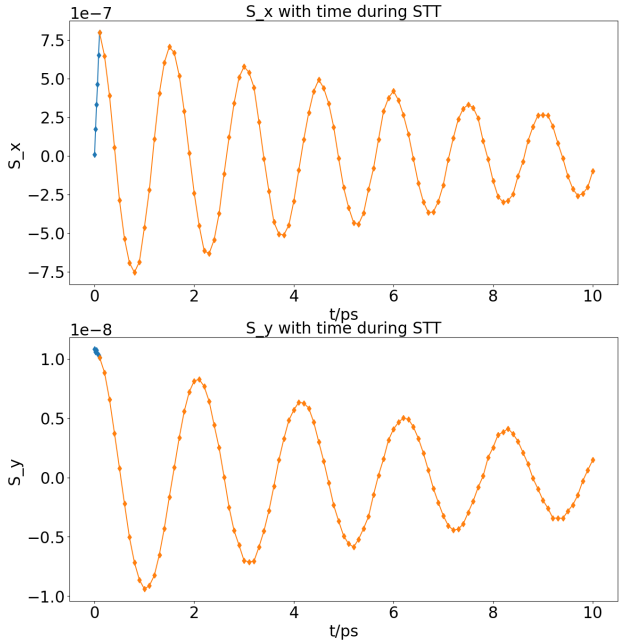


(c) Spin x and y component for STT = 1e-5 meV

Figure C.1: Spin x and y components on average. The blue dots are during the STT pulse and the orange ones are after the STT. The magnetization oscillates along the x direction ($\boldsymbol{k}$ direction). It is interesting that despite the magnetization oscillation along y being at least two orders weaker than along x, its frequency is not the same: it is about 1THz.

#### C.1.1.2 STT Applied Perpendicular to $k$

The motion of the cycloidal domain wall is damped similar to a friction model, as shown in Fig. C.2.

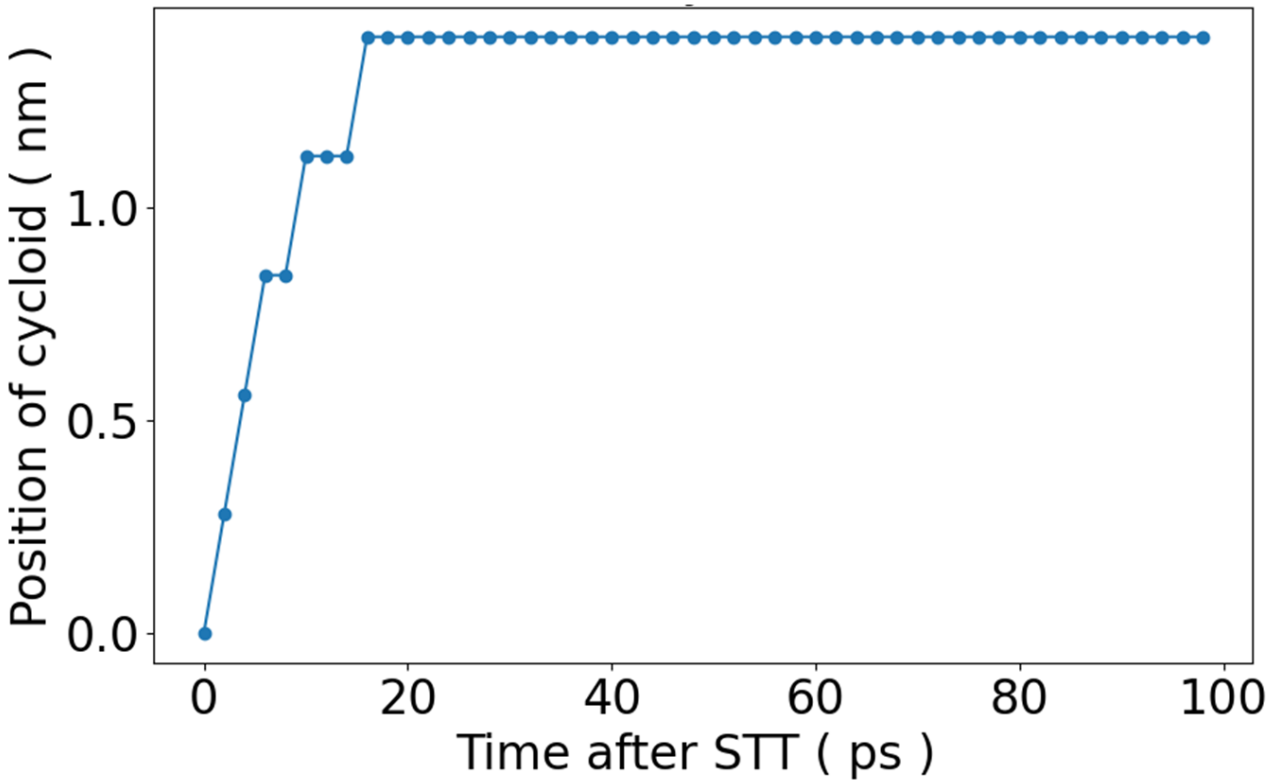


Figure C.2: Translation of the cycloid for STT = 1e-3 meV.

The spin density wave is at the same order of magnitude of the STT-induced shift, or orders of magnitude larger. The translation of the cycloid is accompanied by a second-order effect of oscillation. The nonlinearity is probably induced by the presence of the $D_2$ DMI term, the anharmonicity of the cycloid which is induced by the $K_{1u}$ term, and the rotation of the $\boldsymbol{l}$ vector in the $\boldsymbol{l}$-[11-2] plane instead of rotation around [1-10]. This self-oscillation of the cycloid can be viewed in Fig. C.3, where the average spin y component along the cycloid is plotted for different STT amplitude.

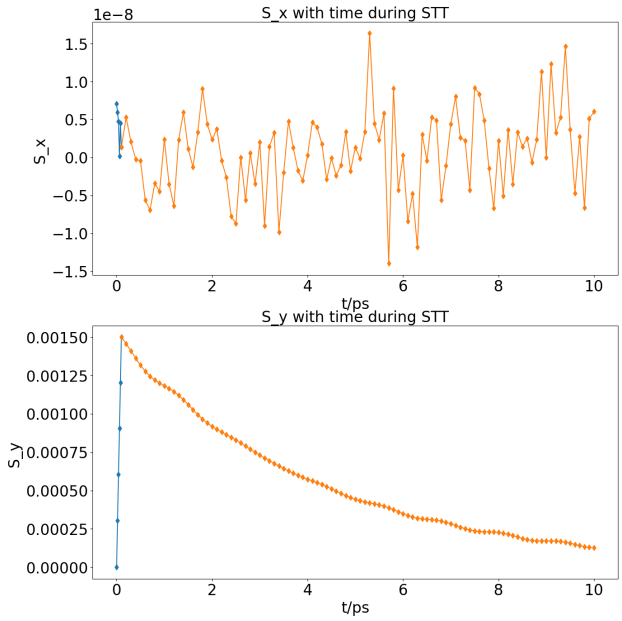


(a) Spin x and y component for STT = 1e-2 meV

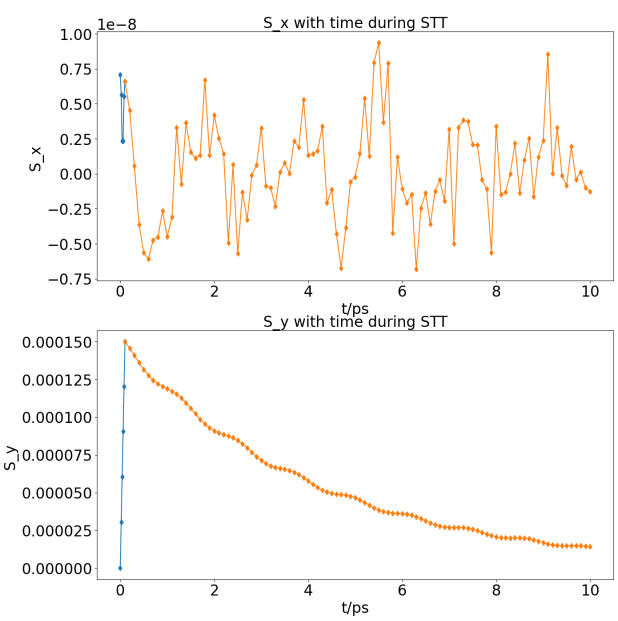


(b) Spin x and y component for STT = 1e-3 meV

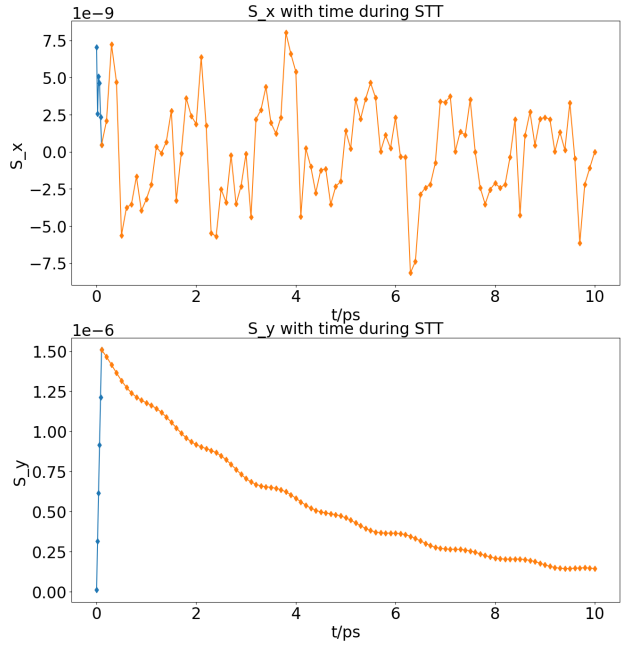


(c) Spin x and y component for STT = 1e-5 meV

Figure C.3: Spin x and y component on average.

### C.1.2 STT Applied on a Fragment of Long Multi-period Cycloid

The result discussed in this section is obtained from simulation as shown in Fig. 6.1 (c). STT pulse with a duration of 100fs is applied on a segment of the long cycloid structure, after which the excited

spin dynamics are analyzed. How these dynamics propagate, and in particular, in what velocity and whether in the same velocity for different propagation directions is the main concern in this and the following section.

To simplify and focus on the main feature, we show the absolute value of the variation of $s$. The landscapes of the difference between $s$ and their directions at initial time (before the STT pulse) are shown in Fig. C.4 and Fig. C.5. As shown by the data (not shown), the dynamical modes are the same as in the previous section. The velocities for the two modes are the same at 25km/s, which is shown in Fig. C.6.

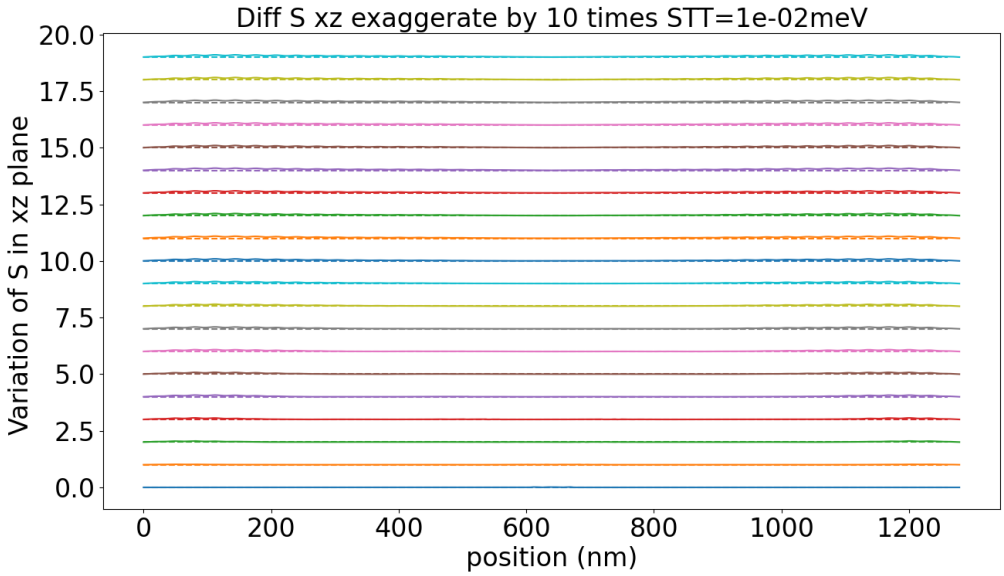


(a) The landscape of variation in the xz plane. The variation is amplified by 10 times.

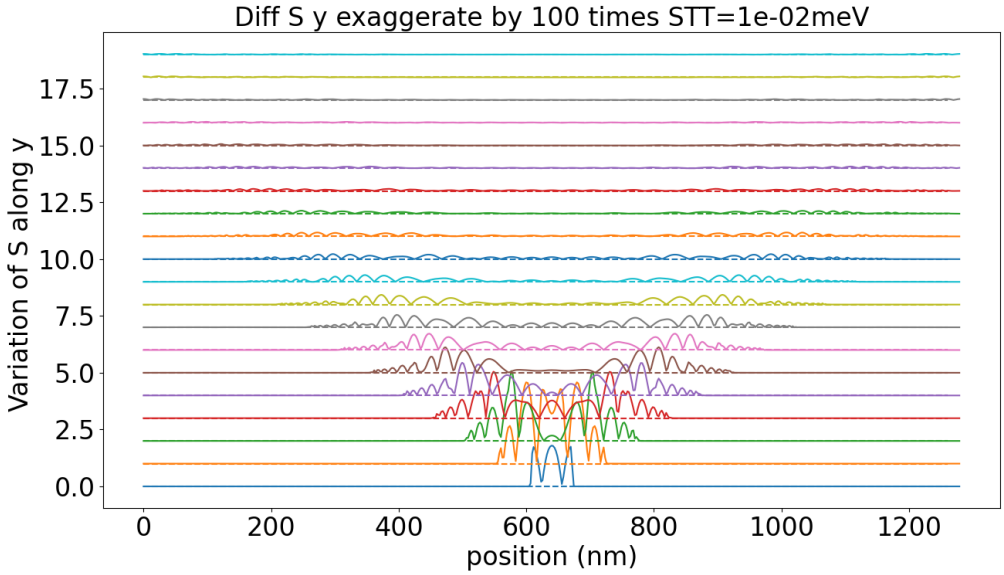


(b) The landscape of variation along y. The variation is amplified by 100 times.

Figure C.4: The landscape of the spin dynamics with time for STT pulse ( 0.01meV strength and 100fs duration ) applied along x. The y-scale in the plot is the norm of the variation of $s$. Different colours represent the different times after the pulse of STT. The bottom line is the snapshot taken at the end of the STT pulse. The data is shifted by 1 along y for every following snapshot. Each snapshot is taken at 2 ps after the previous one. The dashed lines are the baselines that show the zero value for each snapshot. The variation is shown by the solid lines with some amplification to visualize.

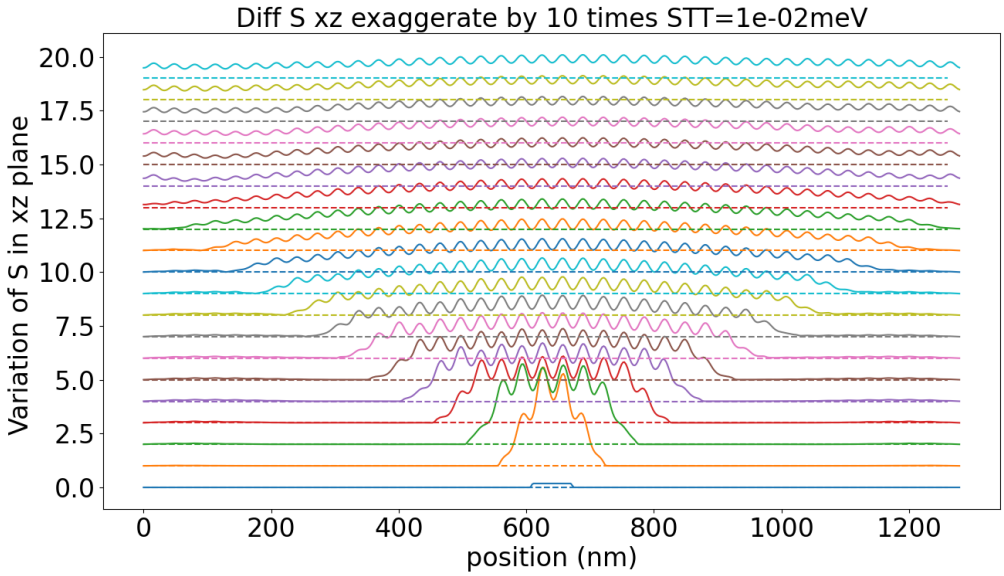


(a) The landscape of variation in the xz plane. The variation is amplified by 10 times.

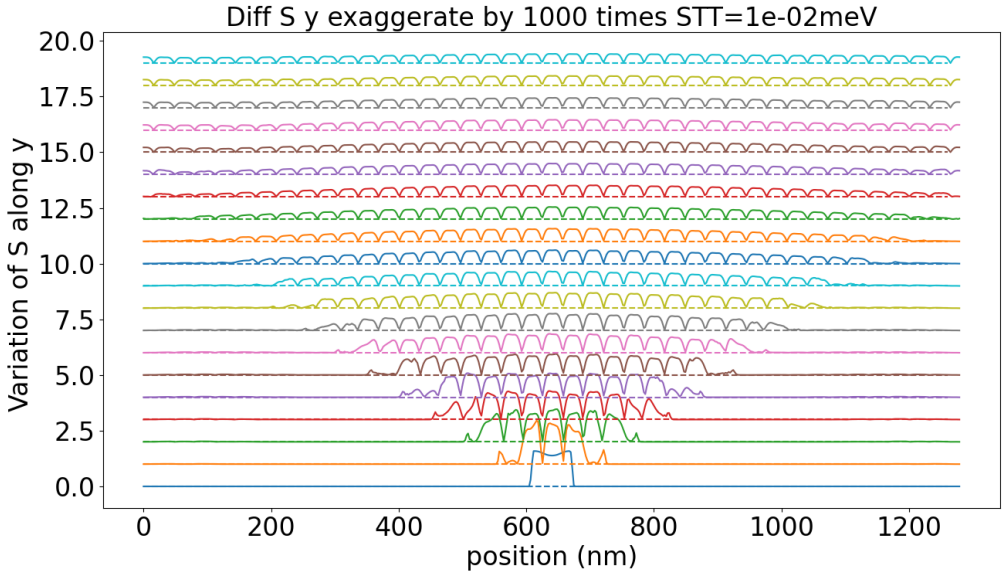


(b) The landscape of variation along y. The variation is amplified by 1000 times.

Figure C.5: The landscape of the spin dynamics with time for STT pulse ( 0.01meV strength and 100fs duration ) applied along y. The figure is in the same format as Fig. C.4.

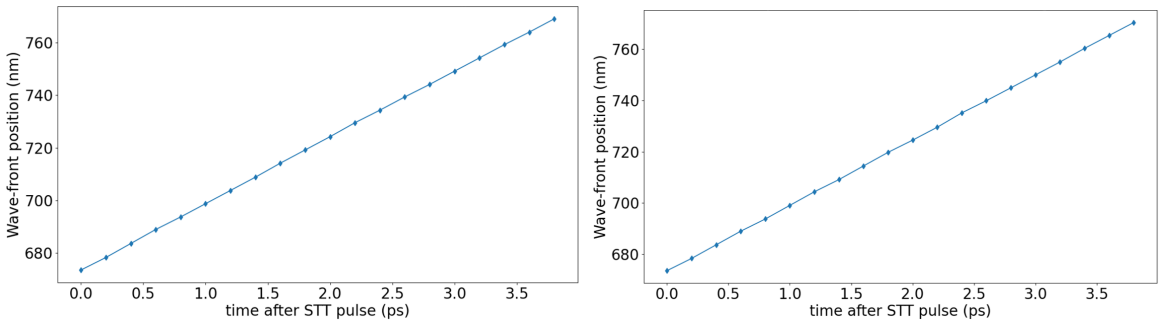


(a) STT applied along the x direction.

(b) STT applied along the y direction.

Figure C.6: The position of wavefront vs time after the pulse. STT is applied along the x and y directions. The velocity of the wavefront is about 25 km/s.

### C.1.3 STT Applied on a Small Area of a Wide Cycloid

The result discussed in this section is obtained from the simulation as shown in Fig. 6.1 (d). STT pulse with a duration of 100fs is applied on a segment of the wide cycloid structure. It is unknown a priori if the propagation velocity is the same along $\boldsymbol{k}$ and perpendicular to $\boldsymbol{k}$. The landscapes of the variations are shown in Fig. C.7 and Fig. C.8. The velocities for the two modes are the same at 25km/s, which is shown in Fig. C.9.

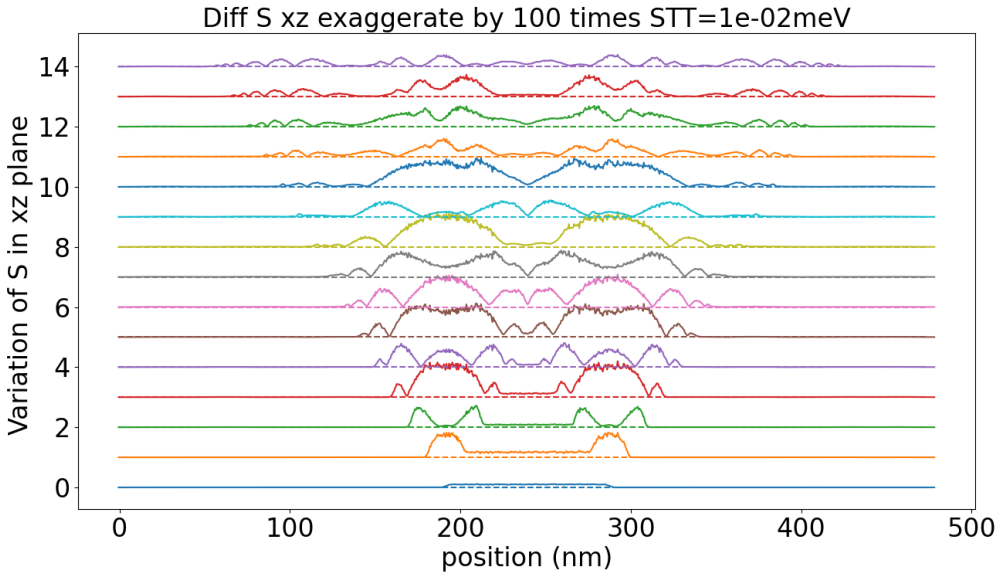


(a) The landscape of Sxz for STT along x. The variation is amplified by 100 times.

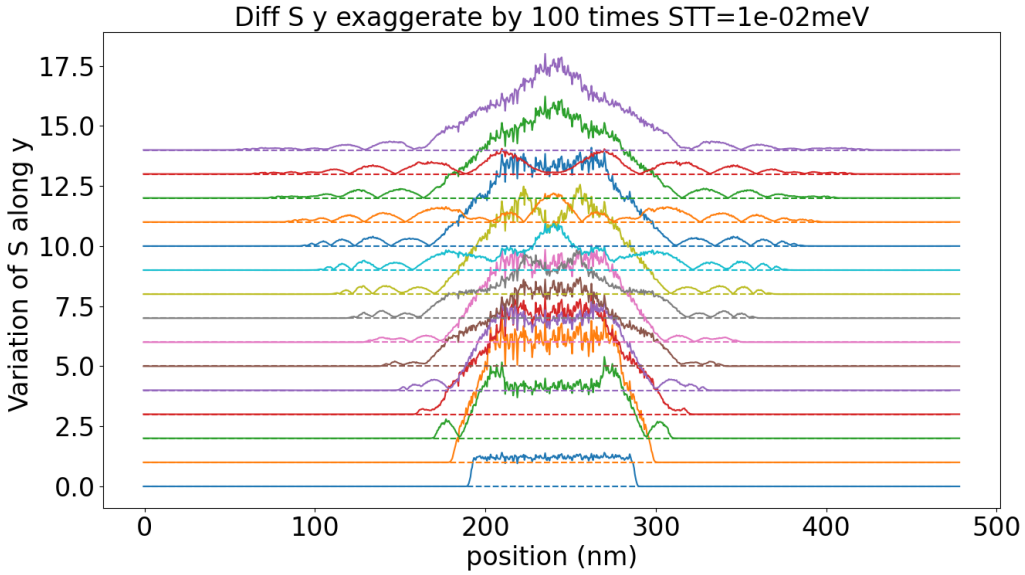


(b) The landscape of Sy for STT along x. The variation is amplified by 100 times.

Figure C.7: The landscape of the spin dynamics with time for STT pulse ( 0.01meV strength and 100fs duration ) applied along x. The figure is in a similar format as Fig. C.4, but each snapshot is taken 0.2 ps after the previous one.

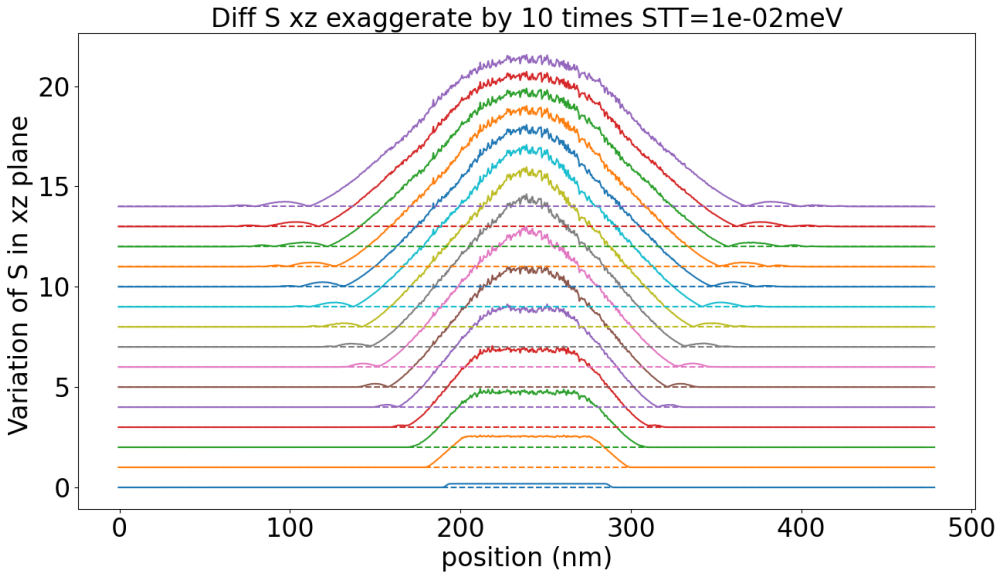


(a) The landscape of Sxz for STT along y. The variation is amplified by 10 times.

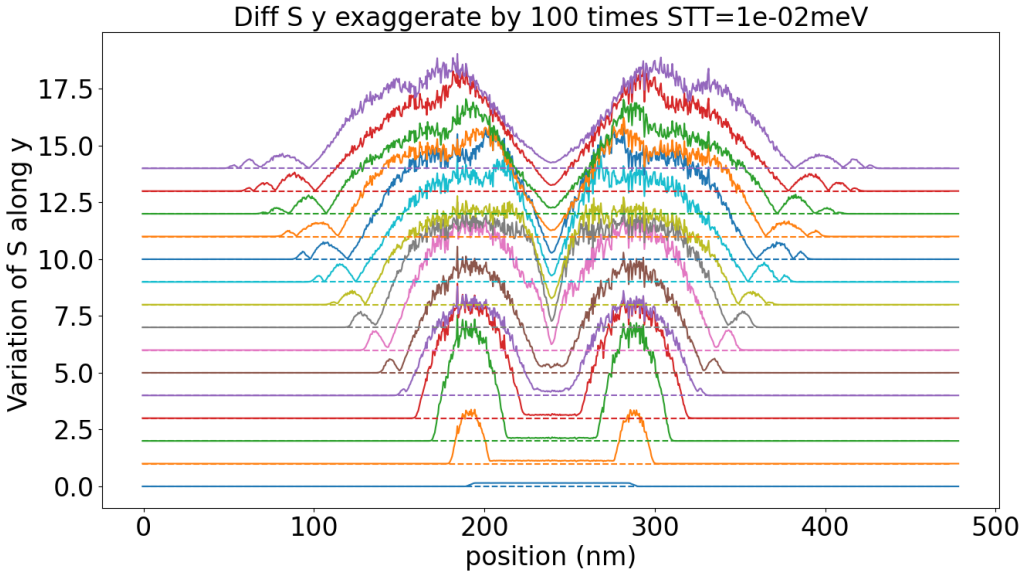


(b) The landscape of Sy for STT along y. The variation is amplified by 100 times.

Figure C.8: The landscape of the spin dynamics with time for STT pulse ( 0.01meV strength and 100fs duration ) applied along y. The figure is in the same format as Fig. C.7.

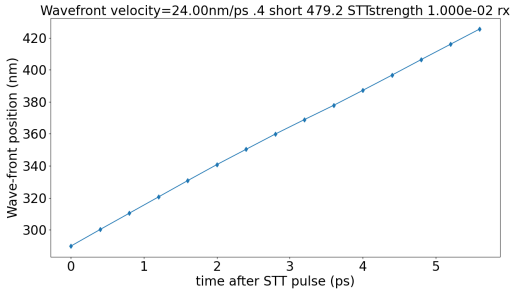


(a) STT applied along the x direction.


(b) STT applied along the y direction.

Figure C.9: The position of wavefront vs time after the pulse. STT is applied along the x and y directions. The velocity of the wavefront is about 25 km/s.

## C.2 Discussion

### C.2.1 Constant STT Applied

The previous simulation mainly concerned STT pulses. In Fig. C.10, the spin x and y components after 100 ps of STT are shown. It can be seen that the oscillation is mainly induced by the pulse or the sharp increase (decrease) of STT. For constant STT applied along y, the scenario is similar to the skyrmion constant velocity motion, where the cycloid motion becomes a constant velocity due to the equilibrium between driving and friction.

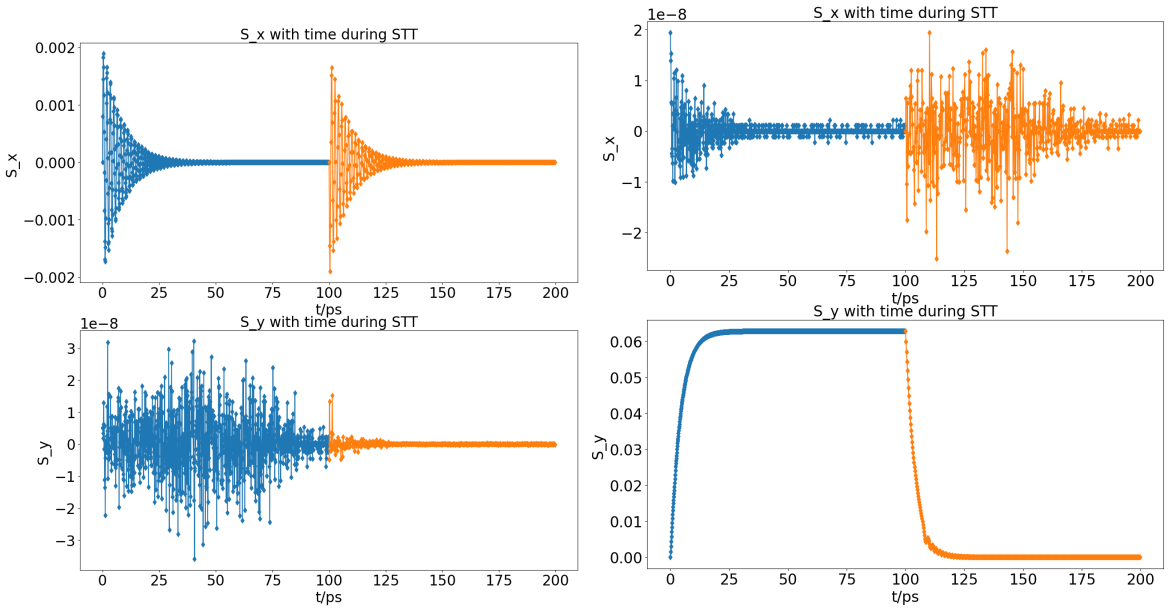


(a) STT applied along x

(b) STT applied along y

Figure C.10: STT = 1e-2 meV applied for 100 ps (blue lines) then paused for 100 ps ( orange lines ). It can be seen that oscillation comes from the sharp raising or dropping of the torque.

# Appendix D

# Multi-P domain in $BiFeO_3$

## D.1 Results

### D.1.1 $D_2$ Domain wall in a Single P Domain

The $\boldsymbol{m}$ map for different angles of the domain wall is shown in Fig. D.1.

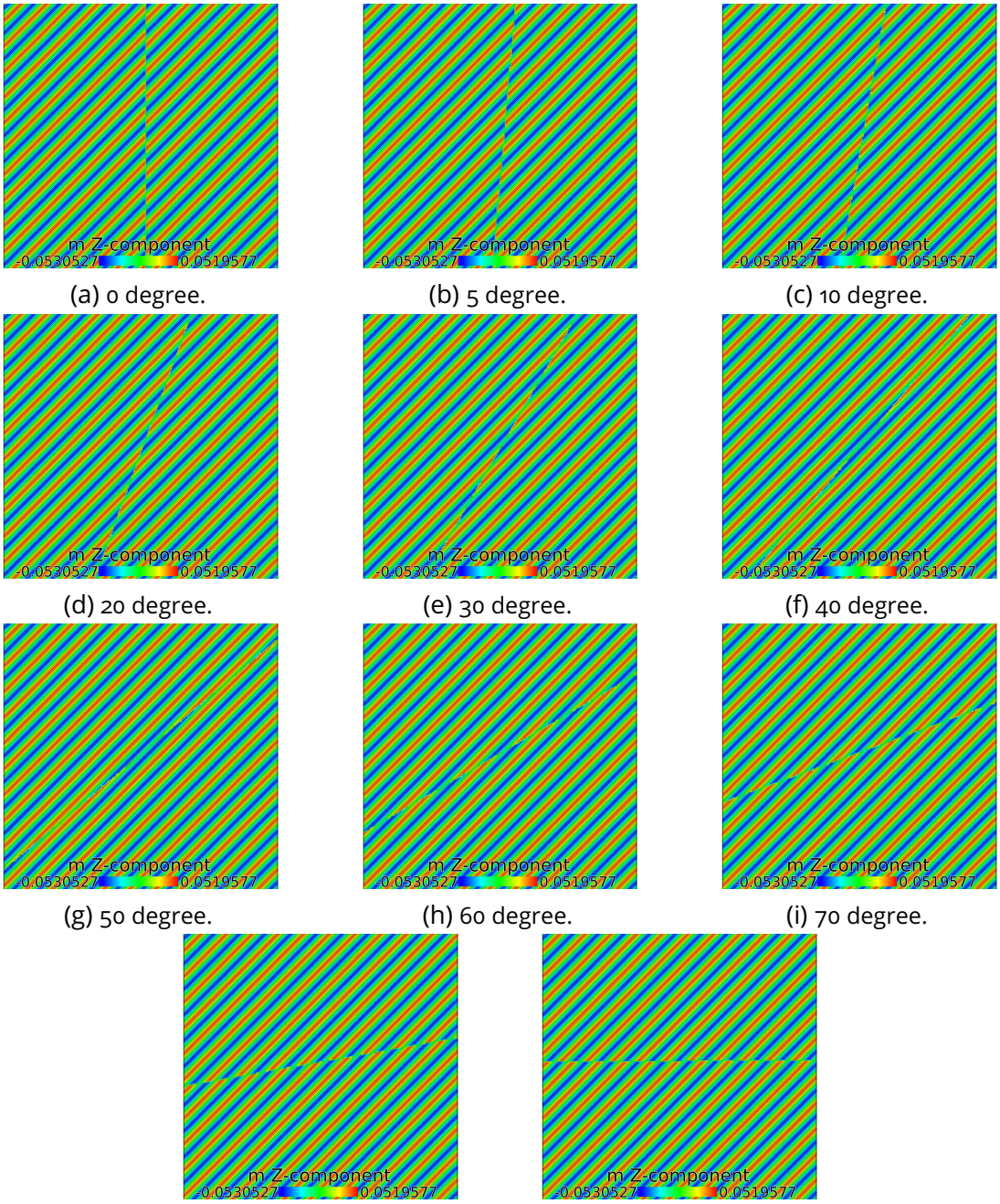


(a) 0 degree. (b) 5 degree. (c) 10 degree.

(d) 20 degree. (e) 30 degree. (f) 40 degree.

(g) 50 degree. (h) 60 degree. (i) 70 degree.

(j) 80 degree. (k) 90 degree.

Figure D.1: Magnetization vector $\boldsymbol{m}$ in a single P domain with $D_2$ domain wall.

The stray magnetic field is calculated and shown in Fig. D.2 and Fig. D.3. The shown magnetic field is assumed to be measured at 50A above the surface. The discontinuous change of $\boldsymbol{m}$ induces a domain wall pattern. Depending on the angle with respect to the cycloid, the domain wall either shows a mismatch of the cycloid, or an enhancement of the magnetic field.

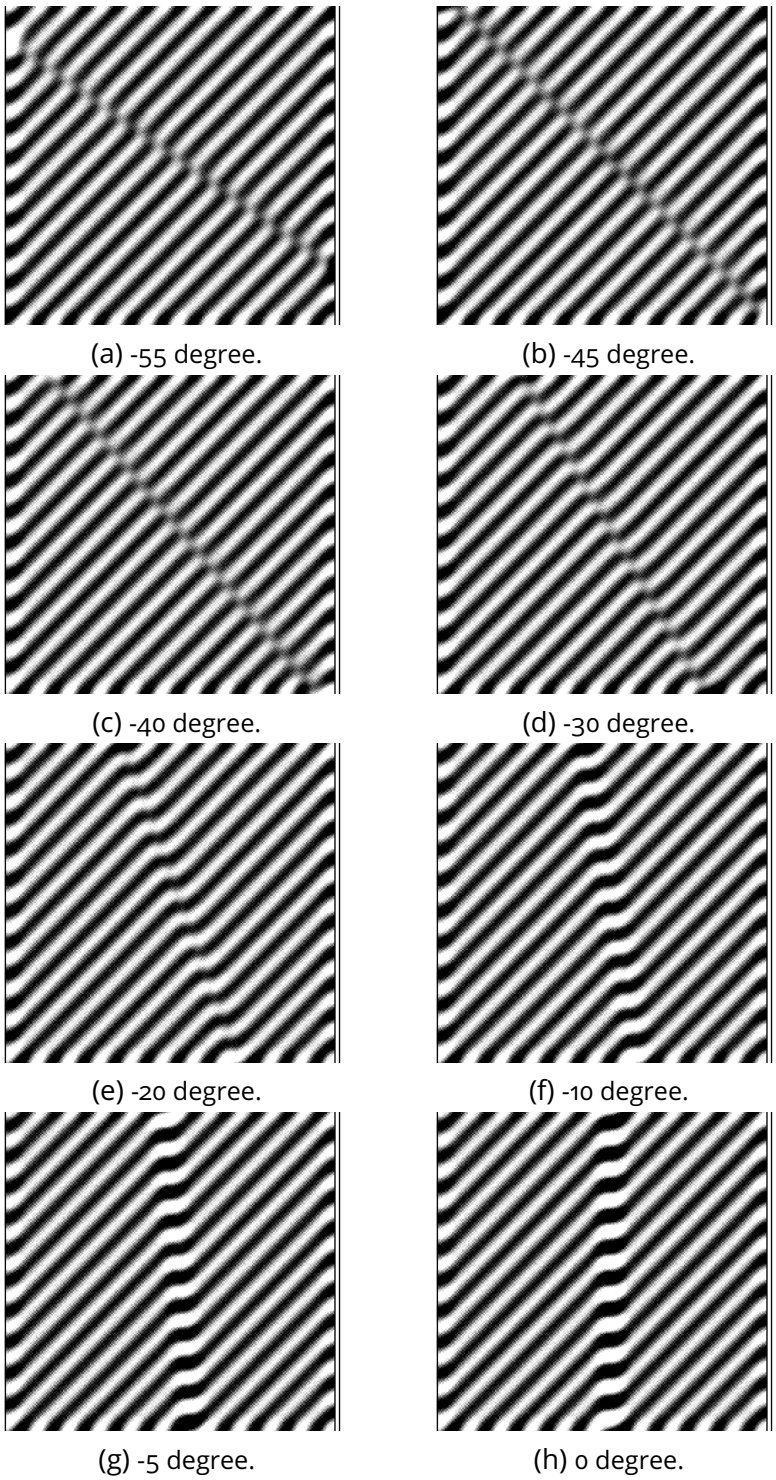

(a) -55 degree. (b) -45 degree.

(c) -40 degree. (d) -30 degree.

(e) -20 degree. (f) -10 degree.

(g) -5 degree. (h) 0 degree.

Figure D.2: Stray field measured at 50 Angstrom above the BFO surface. The field is measured at 54.7 degree angle with respect to z axis along y direction.

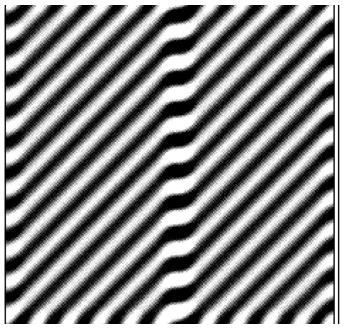

(a) 0 degree.

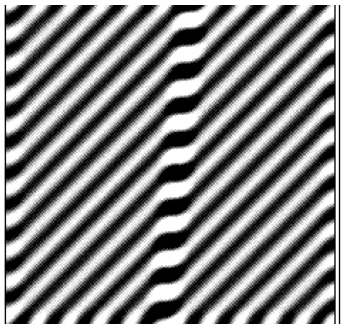

(b) 5 degree.

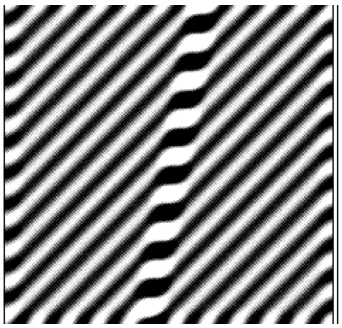

(c) 10 degree.

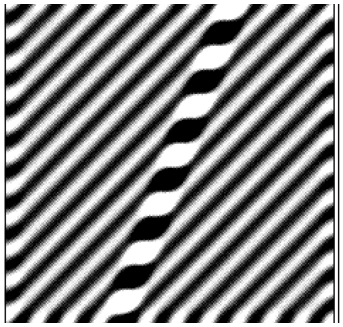

(d) 20 degree.

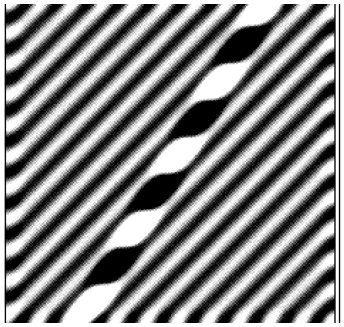

(e) 30 degree.

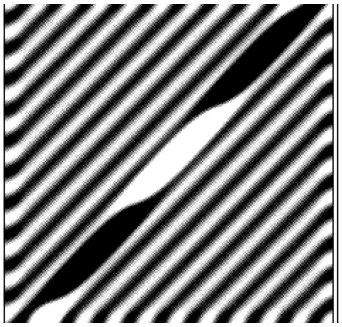

(f) 40 degree.

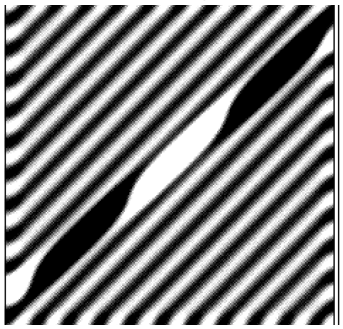

(g) 50 degree.

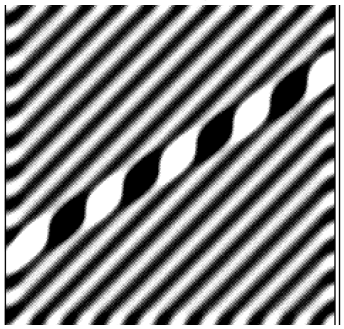

(h) 60 degree.

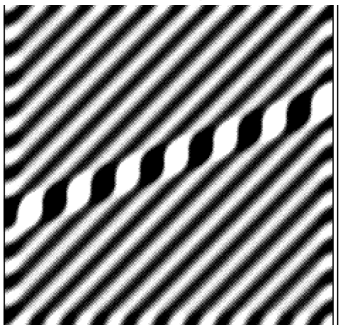

(i) 70 degree.

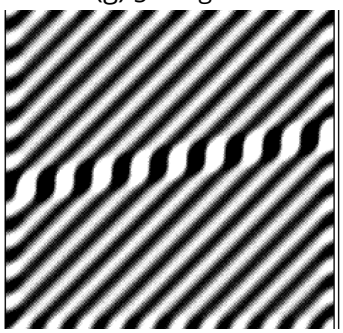

(j) 80 degree.

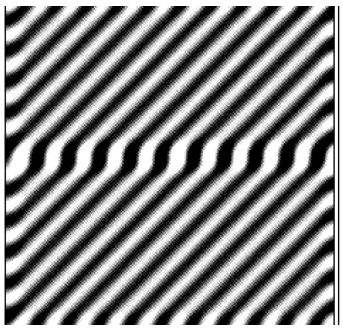

(k) 90 degree.

Figure D.3: The stray field measured at 50 Angstrom above the BFO surface. The field is measured at a 54.7-degree angle with respect to the z-axis along y direction.

### D.1.2 2P Domain

In the following, in order to view the spin texture and the magnetic field at the same time, the cycloid structure is represented by green dots. The extraction of the green dotted lines globally follows the in-plane spins in the cycloid. The magnetic stray field together with the cycloid structures is shown in Fig. D.4 (c) where it can be seen that for the same sign of $D_2$, even though the stray field looks symmetric on the two D2 domains, the spin structure is not completely symmetric.

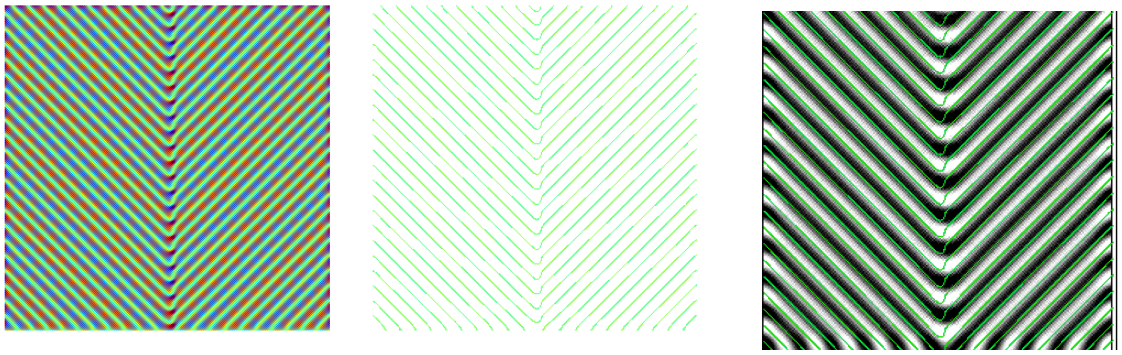

(a) 0 degree. (b) 0 degree. (c) 0 degree.

Figure D.4: The spin texture of a symmetric field pattern could be asymmetric. (a) is the spin texture. (b) extracts only those spins that are in the (001) plane (the green dots). (c) overlaps the green dots on the field image.

The magnetic fields are shown in Fig. D.5 and Fig. D.6. There are two different types of domain walls, where the $D_2$ in the left and right domains are either the same sign or different sign. It can be seen that the domain wall patterns are either symmetric or asymmetric depending on the sign or $D_2$. If the D2 has an opposite sign, then the center of the "V" shape in the field pattern is shifted with respect to the D2 domain wall.

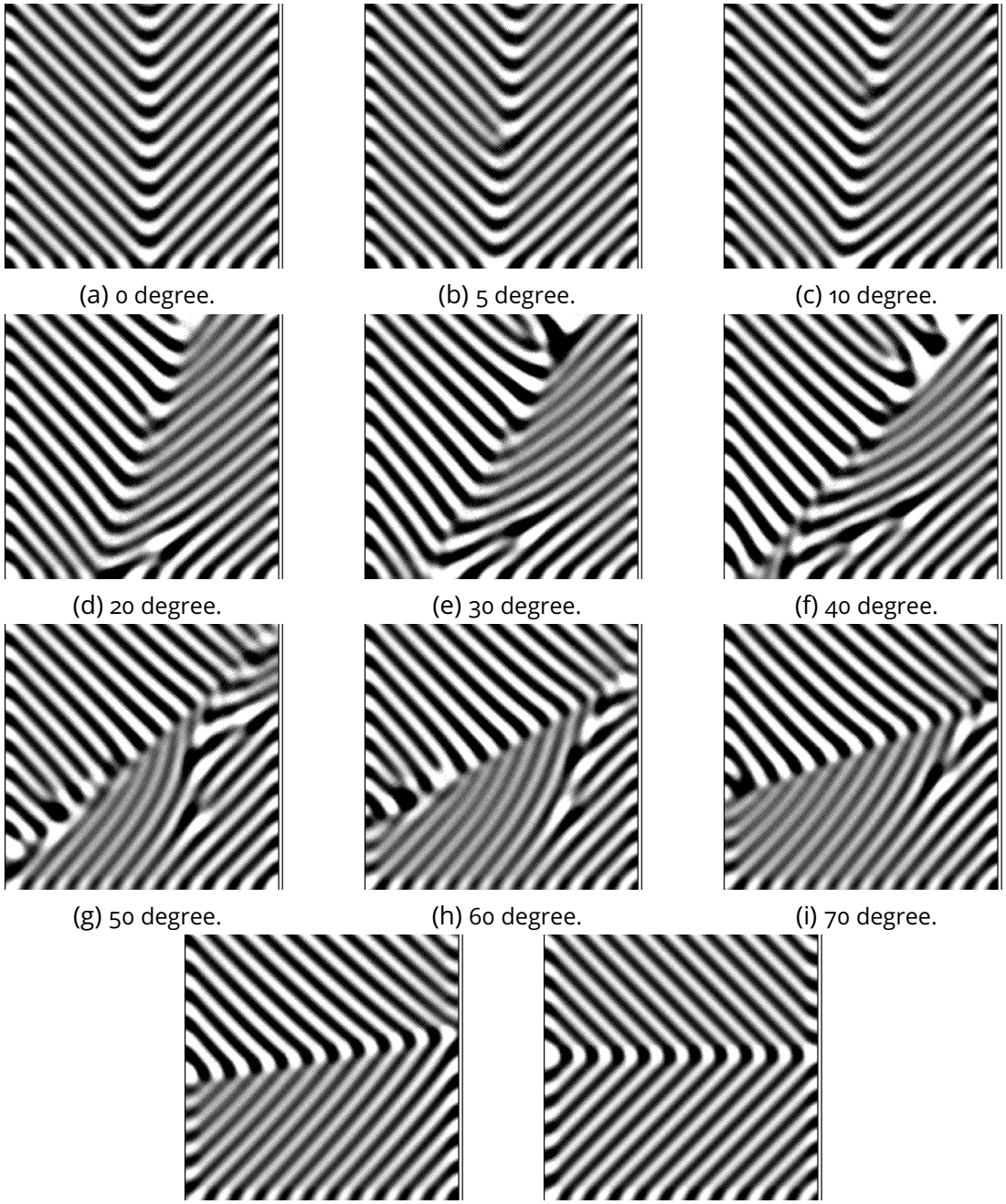

(a) 0 degree. (b) 5 degree. (c) 10 degree.

(d) 20 degree. (e) 30 degree. (f) 40 degree.

(g) 50 degree. (h) 60 degree. (i) 70 degree.

(j) 80 degree. (k) 90 degree.

Figure D.5: P Domain wall -40 degree. The $D_2$ of the two domains have the same sign.

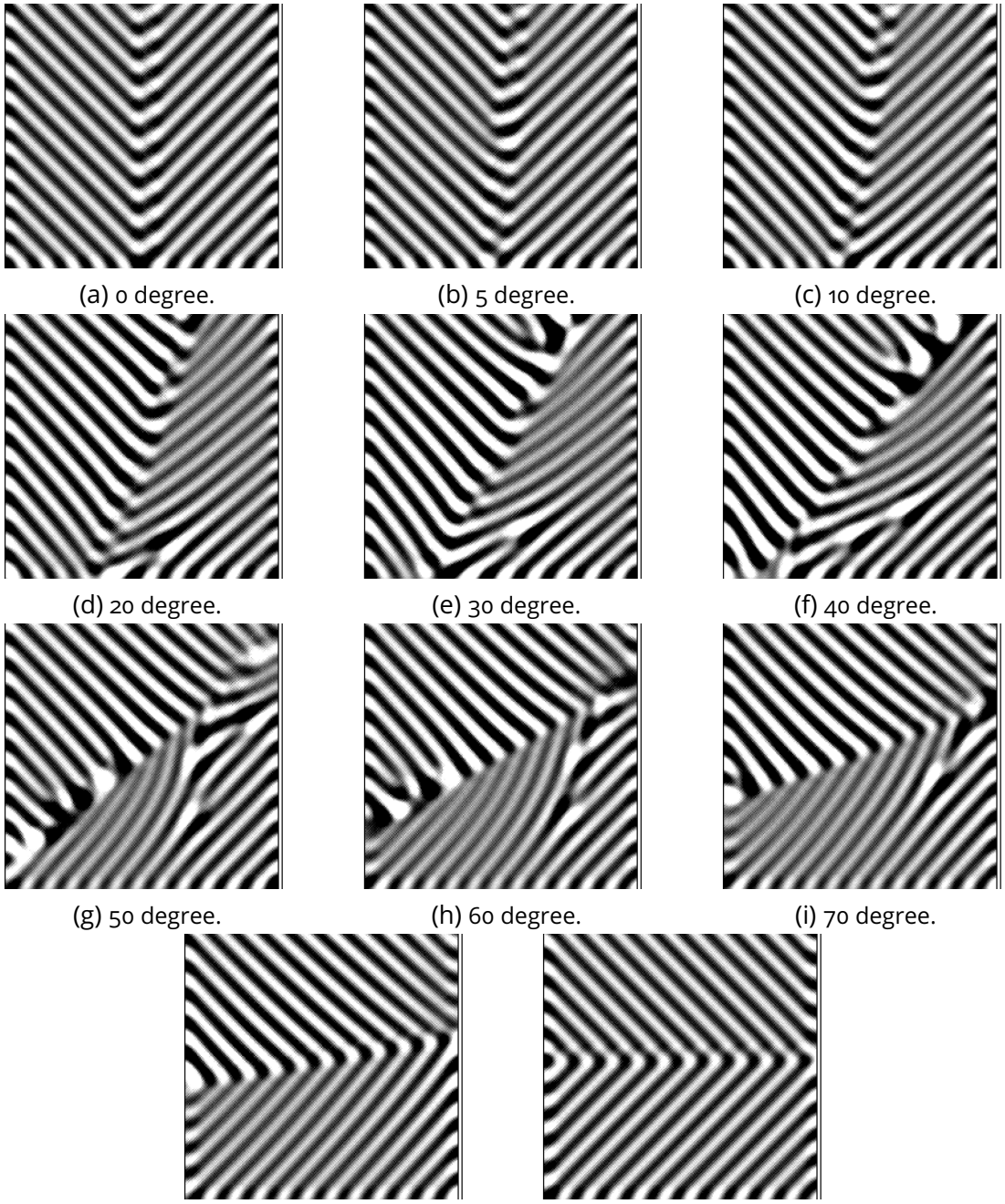

(a) 0 degree. (b) 5 degree. (c) 10 degree.

(d) 20 degree. (e) 30 degree. (f) 40 degree.

(g) 50 degree. (h) 60 degree. (i) 70 degree.

(j) 80 degree. (k) 90 degree.

Figure D.6: P Domain wall -40 degrees. The $D_2$ of the two domains have the opposite sign.

The magnetic field together with the cycloid structures are shown in Fig. D.7 and Fig. D.8. D2 was turned off to test if this asymmetry is induced by a bad-defined D2. The texture of the cycloid is the same. In order to see if our domain wall model is influencing this, A P domain wall was created for 1-2 atomic layers. The asymmetry still exists. It was found that this asymmetry is induced by initialization. We varied two parameters for this initialization: the relative phase and the position of

the interface. We find that both factors influence the relaxed state. But the position is responsible for this asymmetry. The results are shown in Fig. D.9 and Fig. D.10.

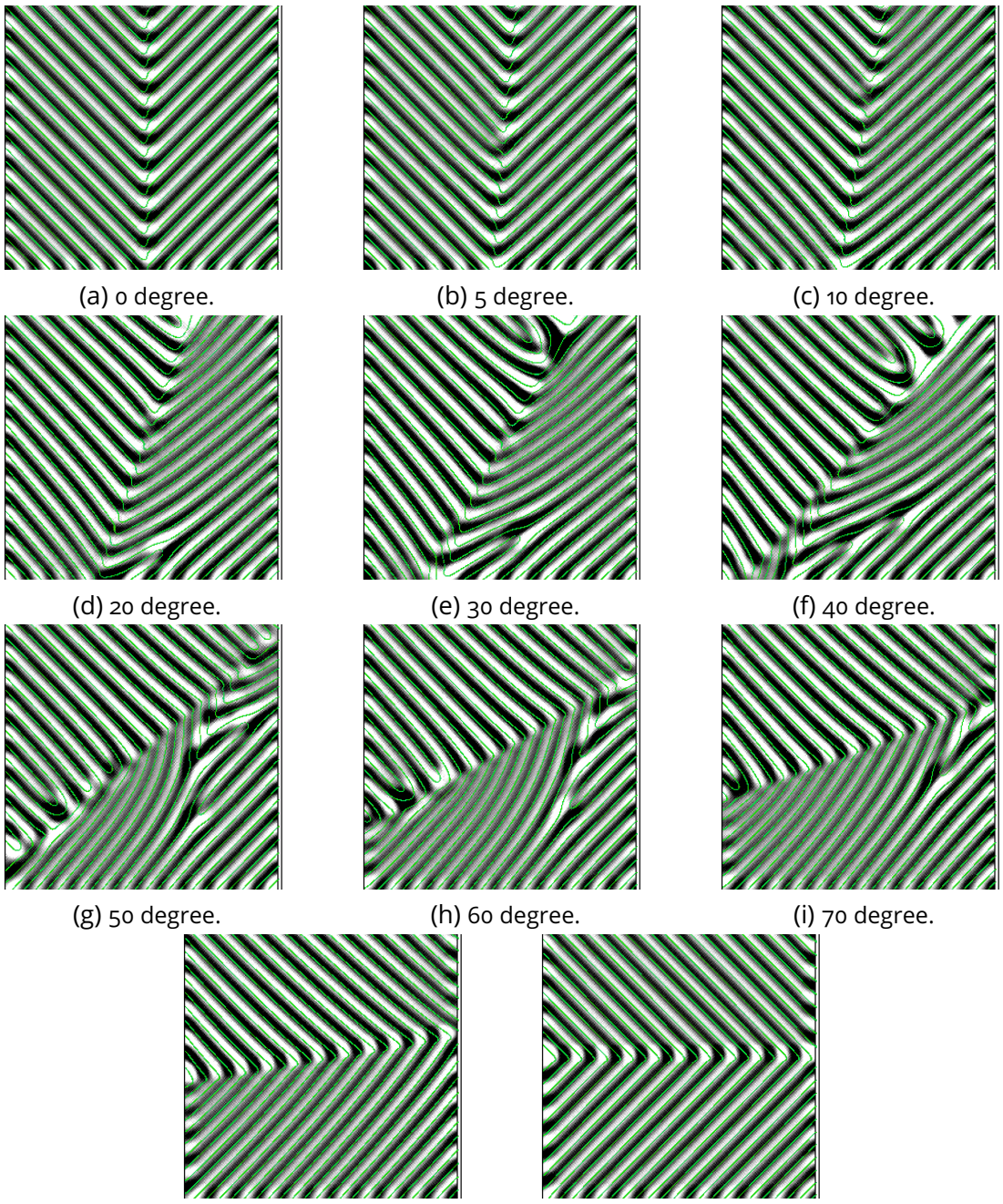

(a) 0 degree. (b) 5 degree. (c) 10 degree.

(d) 20 degree. (e) 30 degree. (f) 40 degree.

(g) 50 degree. (h) 60 degree. (i) 70 degree.

(j) 80 degree. (k) 90 degree.

Figure D.7: P Domain wall -40 degree. The $D_2$ of the two domain have the same sign.

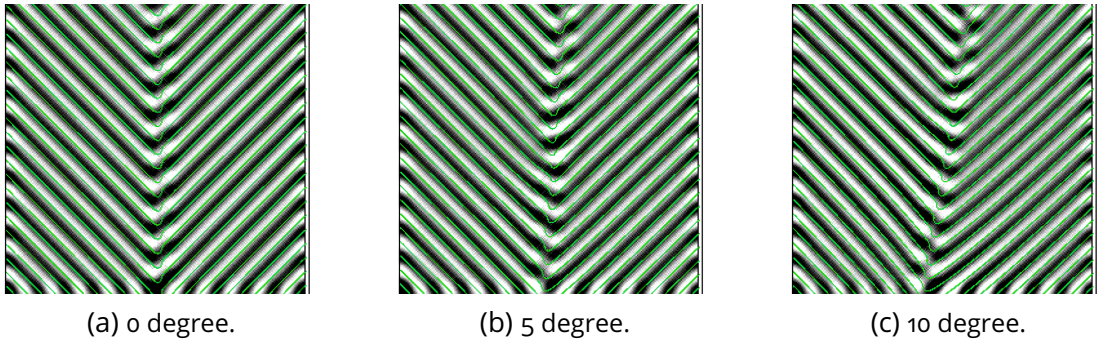

(a) 0 degree. (b) 5 degree. (c) 10 degree.

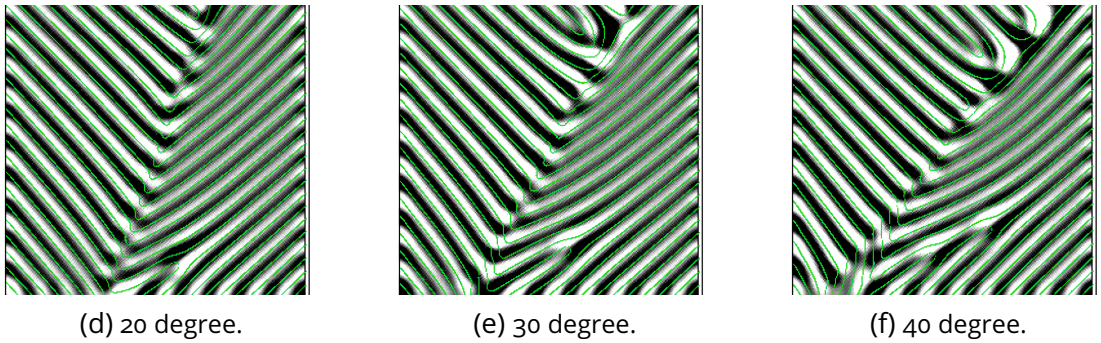

(d) 20 degree. (e) 30 degree. (f) 40 degree.

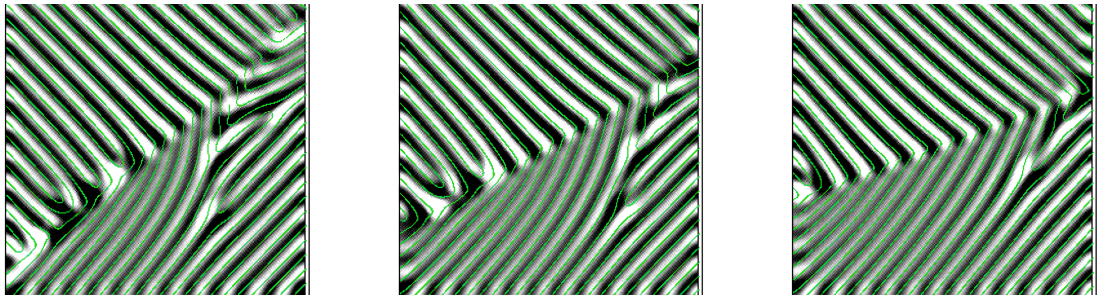

(g) 50 degree. (h) 60 degree. (i) 70 degree.

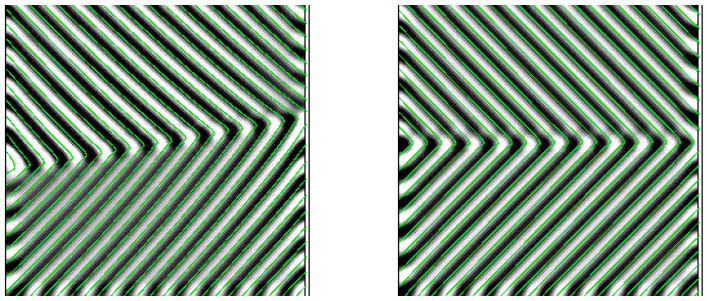

(j) 80 degree. (k) 90 degree.

Figure D.8: The stray field and the cycloid structure of P domain wall -40 degrees. The $D_2$ of the two domains have the opposite sign.

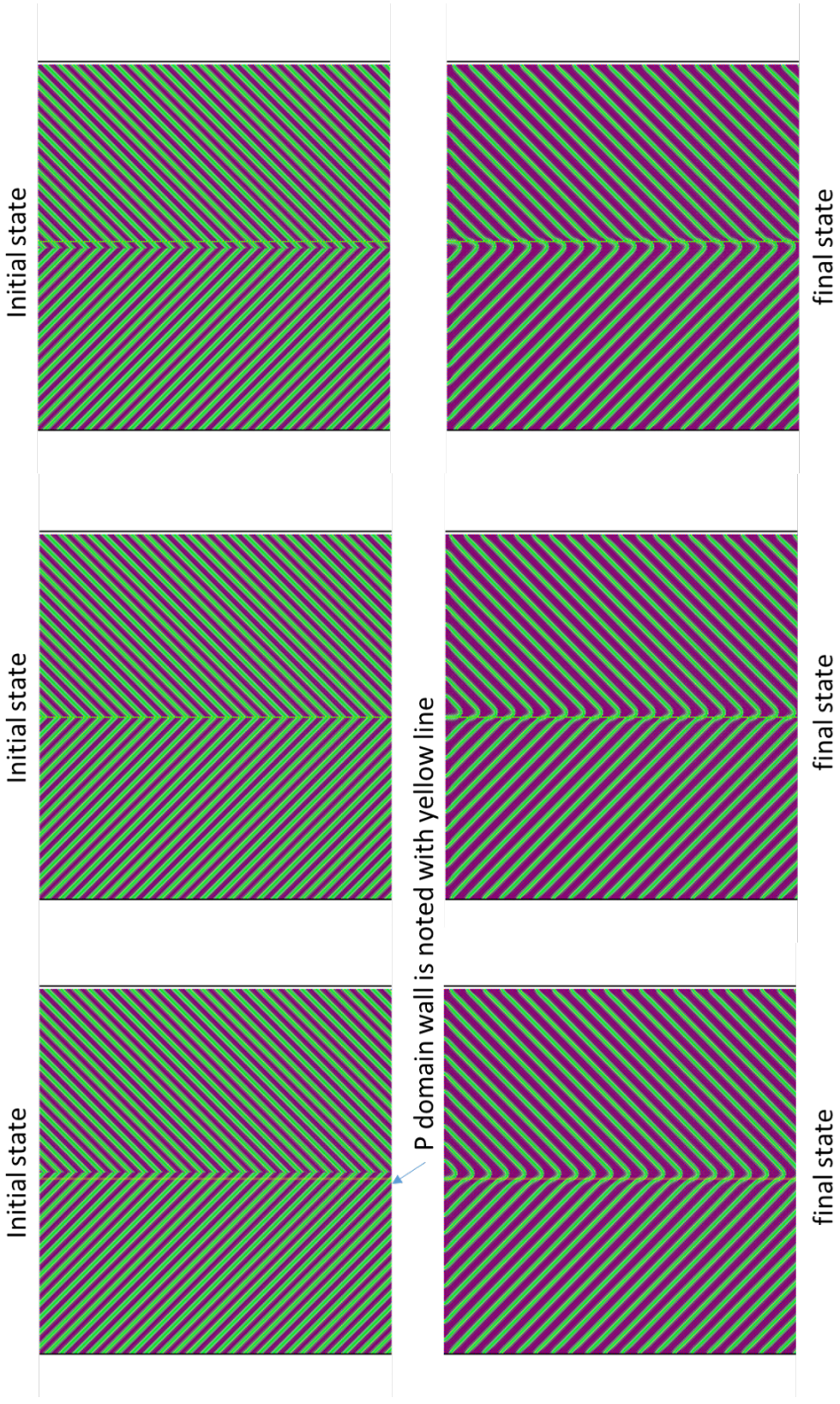


Figure D.9: Changing the position of the initialized interface influences the relaxed state.

Figure D.10: Changing the phase of the cycloids influences the relaxed state.

### D.1.3 4P Domain

Similar results as in the main text could be obtained for P pointing out, as shown in Fig. D.11.

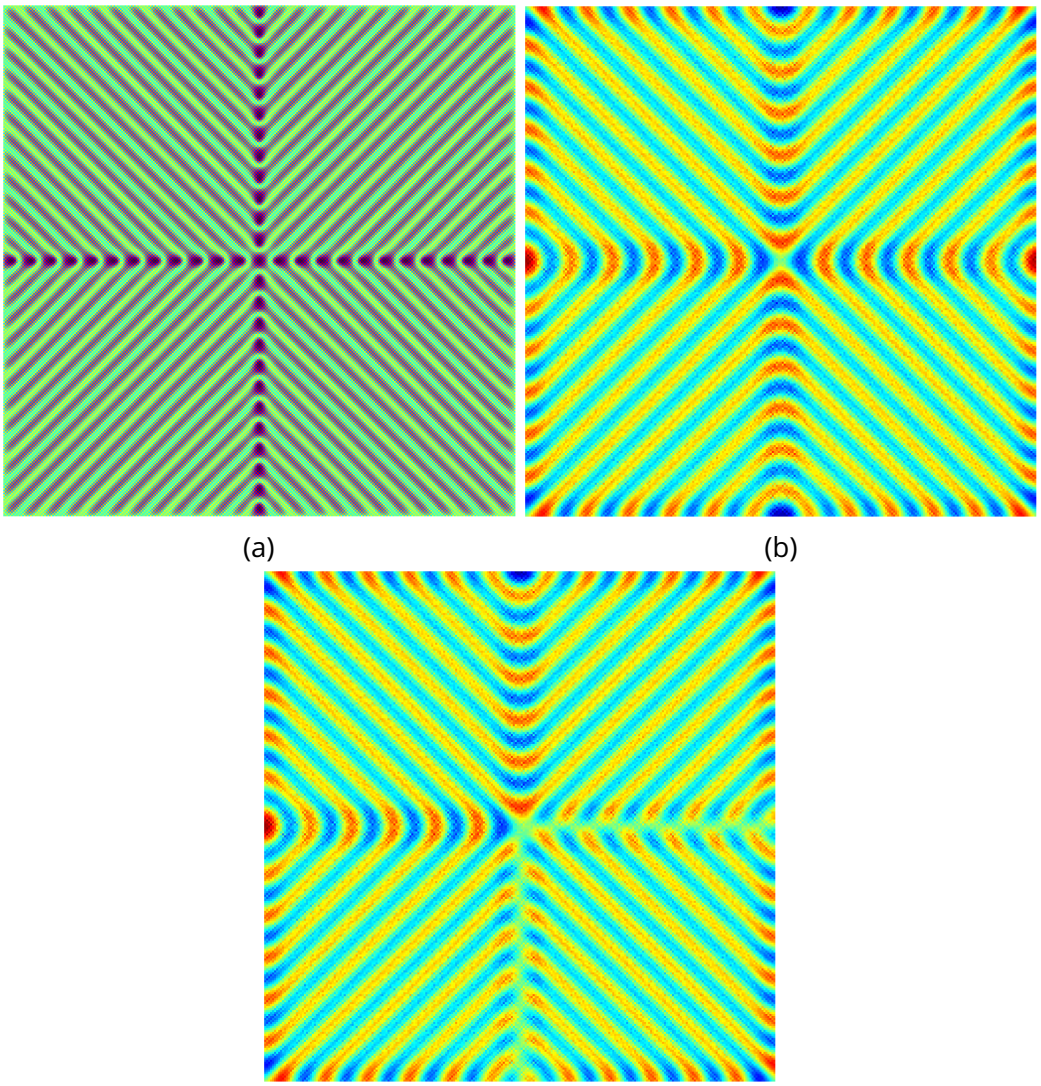

(a) (b)

(c)

Figure D.11: (a) the spin texture. (b) the field image. (c) the field image with the lower-right domain flipping the $D_2$ sign.

# Appendix E

# Antiferromagnetic skyrmion in BFO

Some results and discussions related to Chapter 8 are in this appendix.

## E.1 Results

### E.1.1 Nucleation

Homogenous STT is applied on [111] flop BFO with $K_{1u}$ tuned to 0.01meV. The spin dynamics are shown in Fig. E.1 and Fig. E.2.

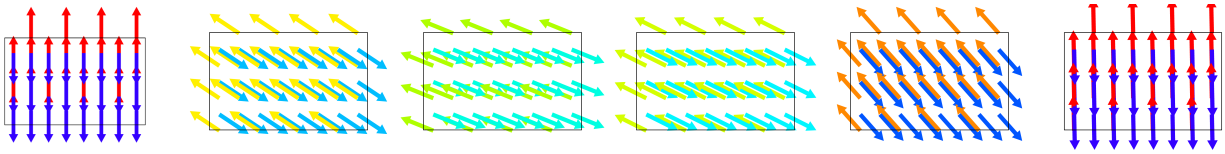

(a) t=0ps (b) t=4.2ps (c) t=8.2ps (d) t=12.2ps (e) t=16.2ps (f) t=20.2ps

Figure E.1: Homogeneous STT of 0.07meV applied perpendicular to [111] direction. The STT is applied in a step function in time. The spins are not flipped by the STT and returns back to be along [111].

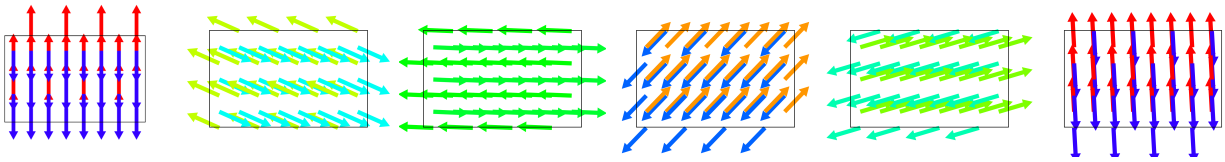

(a) t=0ps (b) t=4.2ps (c) t=8.2ps (d) t=12.2ps (e) t=16.2ps (f) t=20.2ps

Figure E.2: Homogeneous STT of 0.08meV applied perpendicular to [111] direction. The STT is applied in a step function in time. The spins are flipped by the STT.

The STT below the threshold applied on a 200nm$\times$200nm square, as illustrated by Fig. 8.14 (a), could create some entities that are topologically faulty, as shown in Fig. E.3.

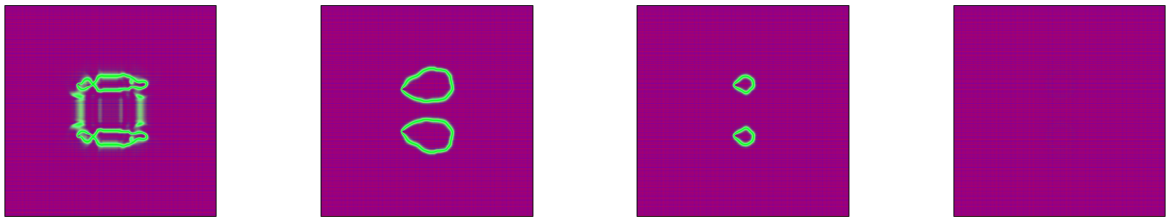

(a) t=4.2ps (b) t=14.2ps (c) t=20.2ps (d) t=24.2ps

Figure E.3: Failed attempt to nucleate skyrmion for STT applied along y. STT=0.065meV. The two entities nucleated annihilate due to the imperfect topology. The topology is broken in the same way as shown in the GNEB calculation. The asymmetry (the broken topology) arises from the favoured chirality of magneto-electric coupling.

Different from what is shown in Fig. 8.15, the STT over the threshold could create a skyrmion from flipping the whole region, as shown in Fig. E.4.

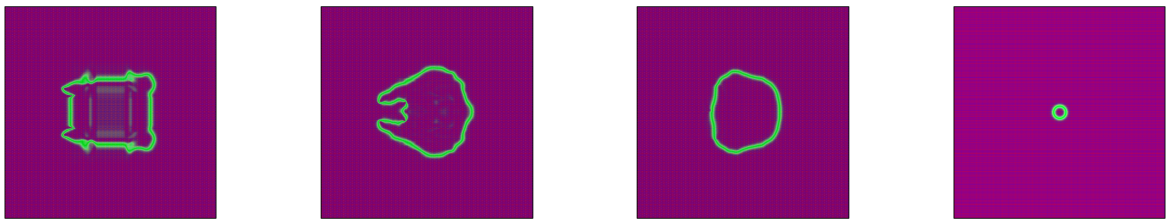

(a) t=3.6ps (b) t=9ps (c) t=16.6ps (d) t=66ps

Figure E.4: A successful attempt to nucleate skyrmion for STT applied along y. STT=0.067meV. The whole region is flipped under this torque and relaxes to the right topology. The relaxation time is longer than the STT=0.066 meV case because the large skyrmion takes time to shrink and dampen its breathing mode.

The STT forming a counter-clockwise Landau pattern also creates skyrmions at the same threshold as the clockwise Landau pattern, as shown in Fig. E.5.

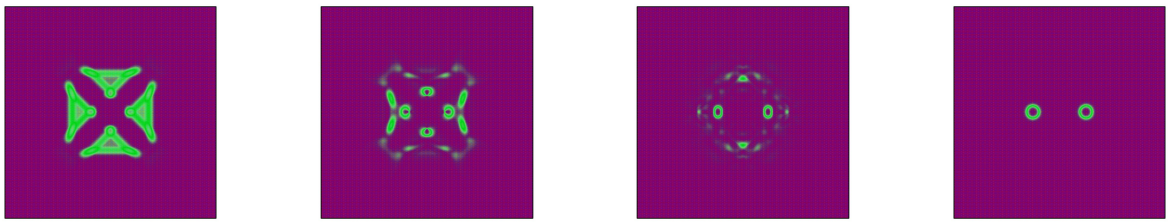

(a) t=1.8ps (b) t=2.2ps (c) t=4.2ps (d) t=14.2ps

Figure E.5: Counter-clockwise STT=0.062meV. The skyrmion is formed at the center.

The STT forming a clockwise Landau pattern with its amplitude higher than the threshold creates a target skyrmion, as shown in Fig. E.6.

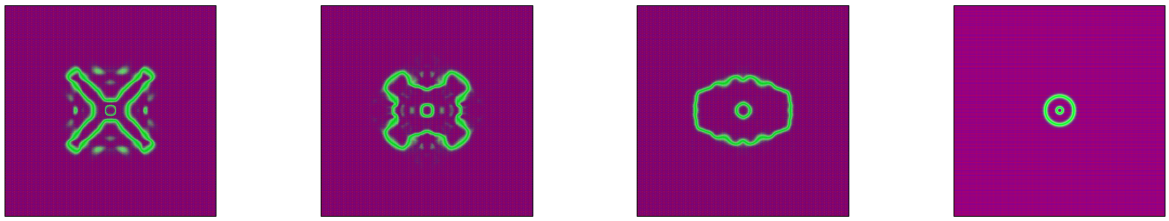

(a) t=2.4ps (b) t=5ps (c) t=10.6ps (d) t=66ps

Figure E.6: Clockwise STT=0.064meV. The whole applied region flips coherently.

## E.2 Discussion

### E.2.1 Stability

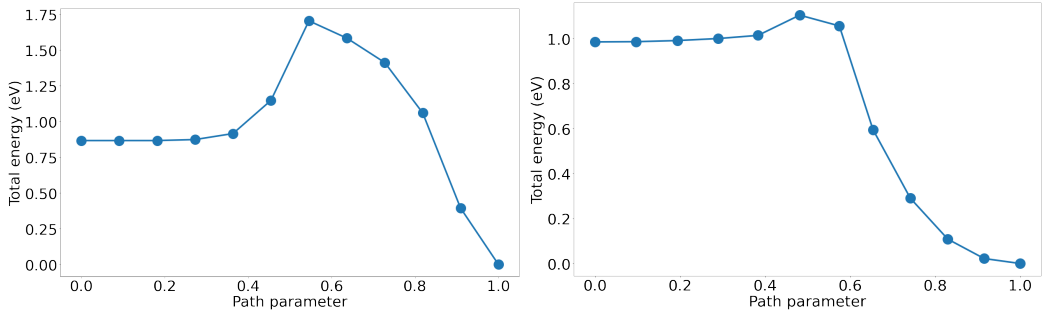


(a) GNEB calculation for K=$0.016$meV. (b) GNEB calculation for K=$0.020$meV.

Figure E.7: GNEB calculation for $K_{1u}$ above 0.012 meV

In the result section, we conducted a GNEB calculation for $K_{1u} = 0.012$meV. The stability of skyrmion states for other anisotropy is also verified as shown in Fig. E.7. The energy barrier increases up to about 0.8 eV as $K_{1u}$ increases to 0.016meV, then drops down to about 0.1 eV as $K_{1u}$ reaches 0.02meV. The increase in the energy barrier could be caused by the increase in anisotropy. The decrease of the barrier could be induced by the shrinkage of the skyrmion size. As indicated by Fig. 8.5, skyrmion size reaches about 7 nm at 0.02meV anisotropy.

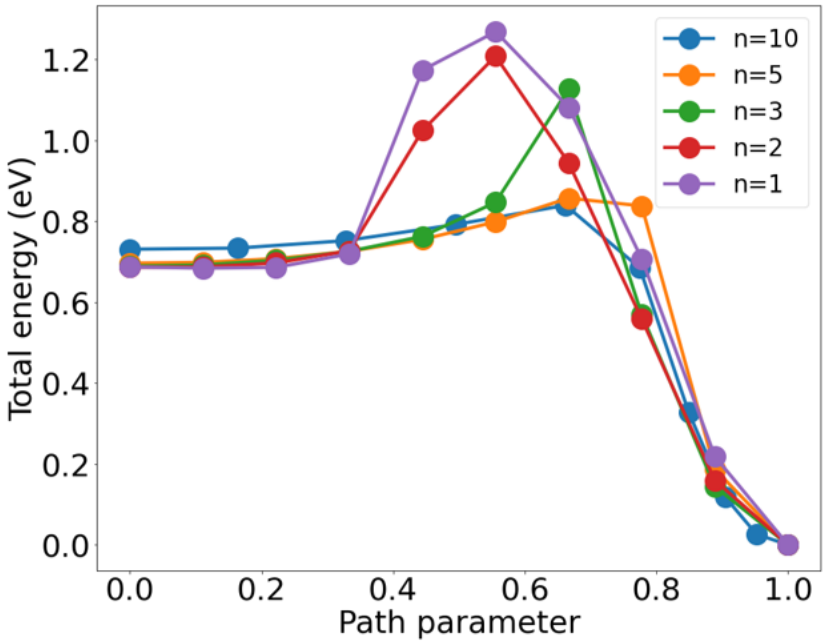


Figure E.8: GNEB calculations to find the stability of different sizes of skyrmion ( or different coarse grain simulations )

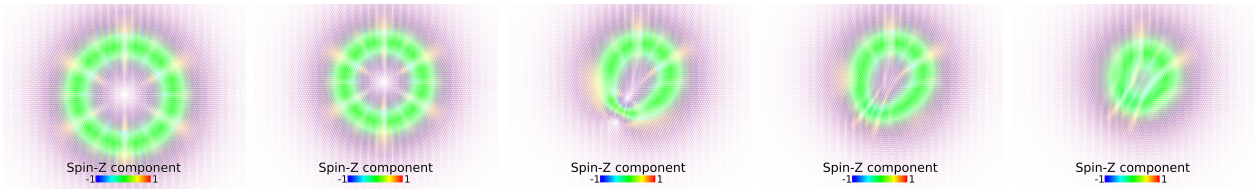


(a) (b) (c) (d) (e)

Figure E.9: The skyrmions along the minimum energy path. The parameter of the system is bulk BFO with $K_{1u}$ tuned to 0.012meV. The skyrmion size is 28 nm.

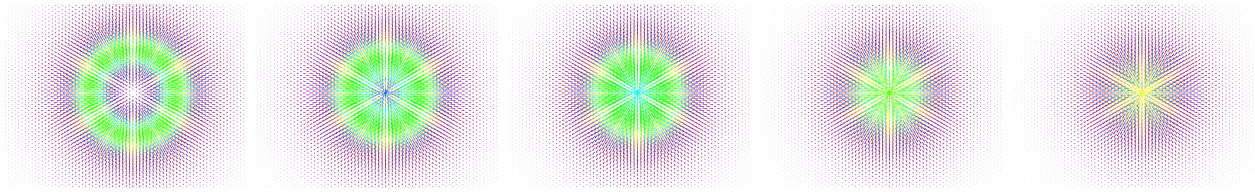

(a) (b) (c) (d) (e)

Figure E.10: The skyrmions along the minimum energy path. The system is tuned by factor $n = 3$ so the skyrmion size is 7nm.

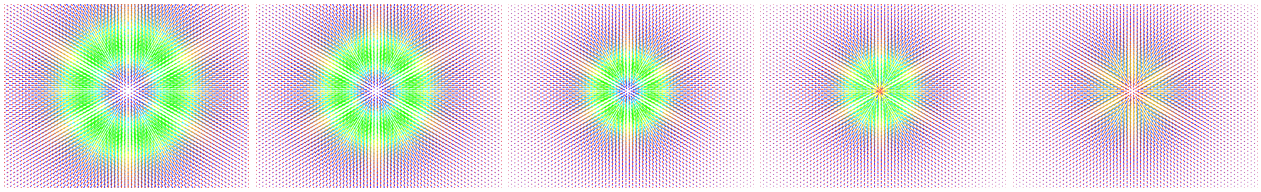

(a) (b) (c) (d) (e)

Figure E.11: The skyrmions with bulk BFO and $K_{1u}$=0.02meV along the minimum energy path. The skyrmion size is 6nm.

In general, the relation between the energy barrier and skyrmion size is a complicated issue [129]. It is essentially the same problem of how coarse grain the numerical implementation of the continuous approximation can be allowed for appropriate GNEB calculation. We tuned the magneto-electric and anisotropy by n and $n^2$ times respectively, corresponding to the case of the "n-times" coarse grain or n-times smaller skyrmion. We conducted GNEB calculations to obtain the energy barrier of these cases. The results are shown in Fig. E.8. For large skyrmions, the For n=2 and n=1, the energy barrier has similar behaviour as the case for $K_{1u}$=0.020 meV shown in Fig. E.7b. The detailed topological transition of skyrmions of the case of BFO with $K_{1u}$=0.012meV, BFO with $K_{1u}$=0.02meV, and n=3 factor of BFO with originally $K_{1u}$=0.012meV are shown in Fig. E.9, Fig. E.11 and Fig. E.10 respectively. The critical size appears to be above 7 nm and below 11 nm (skyrmion size of n=2 case). The annihilation path for skyrmions larger than the critical size is the Chimera type, where the topology is broken at some position that is center-asymmetric. This is preferred rather than the symmetric annihilation for skyrmions smaller than the critical size, probably because the energy barrier is higher for shrinkage of skyrmion as revealed by the sharp increase of energy barrier of $n = 3$ case in Fig. E.8.

### E.2.2 Nucleation

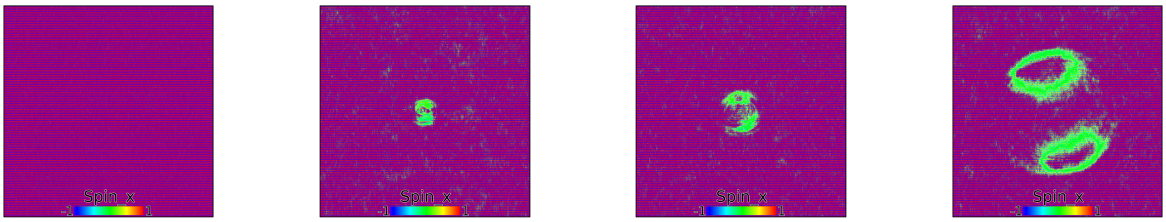


(a) t=0ps (b) t=10ps (c) t=20ps (d) t=60ps

Figure E.12: Electric field 2ps pulse with an amplitude of ≈ 10000MV/cm applied to a flopped state with very large noise (spin tilting at an angle up to 10 degrees).

A very strong pulse of electric field could nucleate a skyrmion with the help of some noise in the system, as shown in Fig. E.12. Although this is working in the simulation, the electric field applied is way above the feasible value.

# Résumé en Français

## Introduction

Les matériaux magnétiques ont été explorés et utilisés depuis longtemps dans l'histoire de l'humanité. Il s'agit de matériaux qui peuvent interagir avec les champs magnétiques. Historiquement, les boussoles fabriquées à partir de pierres de « lodestones » magnétiques ont été utilisées pour la navigation via leur intéraction avec le champ magnétique terrestre. Aujourd'hui, malgré notre connaissance approfondie des matériaux magnétiques, nous cherchons encore des méthodes pour manipuler les minuscules "boussoles" - les moments magnétiques de spin et orbitaux -, en utilisant la fonctionnalité de leur "navigation" pour enregistrer et traiter l'information à l'échelle du micromètre ou du nanomètre par leur direction d'aimantation. En particulier, l'utilisation des moments magnétiques de spin a été intensivement étudiée dans le domaine de la spintronique. Les matériaux magnétiques fonctionnels et leurs manipulations sont la clé de cette recherche.

Les matériaux magnétiques typiques tels que les métaux de transition Fe, Co, Ni et leurs alliages ont été les matériaux magnétiques les plus étudiés. Il s'agit de matériaux ferromagnétiques, dans lesquels les spins sont alignés par les interactions d'échange. Ces interactions sont étroitement liées à leur conduction électrique : elles sont induites par la délocalisation des électrons des bandes 3d. Leurs moments magnétiques peuvent être facilement manipulés par des champs magnétiques externes. En appliquant un champ magnétique oscillant, on peut exciter une résonance de la dynamique de spin connue sous le nom de résonance ferromagnétique. Leurs fréquences caractéristiques se situent généralement dans la gamme des GHz. Contrairement à ce qui se passe dans les ferromagnétiques métalliques, dans certains oxydes, les interactions d'échange sont médiées par les atomes d'oxygène, ce qui entraîne un désalignement des spins des atomes magnétiques par rapport à leurs sites voisins. Les matériaux présentant ces arrangements de spins anti-alignés sont des matériaux antiferromagnétiques.

Ces matériaux antiferromagnétiques possèdent des fréquences de résonance atteignant la gamme du THz, soit deux ordres de grandeur plus élevés que ceux des ferromagnétiques. De nombreux antiferromagnétiques, tels que l'oxyde de nickel NiO, sont des oxydes isolants dans lesquels la dissipation d'énergie de la dynamique des spins est faible en raison de la nature localisée des électrons. Leur fréquence de résonance élevée et leur faible dissipation d'énergie ont suscité un intérêt considérable, car l'industrie électronique moderne se heurte a des limites en rapidité et dissipation de chaleur, et atteint des limites de taille. En outre, en raison de leur disposition antiparallèle, les structures de spin dans les AF sont robustes, ne sont pas facilement affectées par des champs externes et ne produisent pas de champs parasites à l'extérieur de l'échantillon. Cette propriété peut être con-

sidérée comme un avantage en termes de robustesse, mais elle pose également des défis en termes de sondage et de manipulation. Par conséquent, la modélisation et les simulations numériques de leur dynamique de spin sont cruciales pour comprendre les processus microscopiques pertinents à l'échelle de temps de la picoseconde et pour prédire les conditions critiques de certains phénomènes physiques intéressants.

# Méthodes

La dynamique du spin peut être approximée par l'équation de Landau-Lifshitz-Gilbert (LLG), sur laquelle est basée notre simulation de la relaxation et de la dynamique. Nous avons utilisé deux logiciels pour notre étude : LAMMPS ainsi qu'un code maison que nous avons développé. LAMMPS peut être utilisé comme code de simulation de la dynamique de spin pour n'importe quel matériau. Comme il ne peut être parallélisé sur des CPU, nous n'avons pu l'utiliser que pour simuler des textures de spin plus petites à l'échelle atomique (quelques dizaines de milliers d'atomes). Nous l'avons utilisé exclusivement dans notre étude sur le NiO. Sur les ordinateurs ordinaires, LAMMPS prendrait un temps inacceptable pour simuler des systèmes de spin plus importants, tels que les textures de skyrmions bidimensionnels dans $BiFeO_3$, où des millions d'atomes sont requis. Afin de simuler ces textures de spin sans l'aide de superordinateurs, nous avons choisi de développer un nouveau code qui parallélise le calcul sur des GPU. Ce code maison a été conçu sur mesure pour optimiser les performances sur les GPU et son algorithme est spécialement conçu pour simuler les textures de spin avec la structure du réseau de $BiFeO_3$. Avec l'aide des GPU les plus récents, ses performances sont plus de 100 fois supérieures à celles de LAMMPS, ce qui a permis notre étude du BFO. Notre code maison a été calibré et vérifié, en commençant par chaque type d'interaction sur quelques atomes, jusqu'à considérer toutes les interactions incluses dans l'hamiltonien sur des dizaines de milliers d'atomes. Cette vérification approfondie garantit que notre nouveau logiciel donne des résultats corrects.

# NiO et BFO

Deux matériaux, NiO et $BiFeO_3$, ont été étudiés tout au long de cette thèse. Le NiO a été l'un des premiers antiferromagnétiques étudiés en raison de son état AF à température ambiante avec une température de Néel de TN = 523K. Au-dessus de TN, le NiO a un réseau fcc de type NaCl où chaque sous-réseau est cubique. En dessous de TN, une petite contraction le long de la direction [111] apparait. Les spins sont couplés ferromagnétiquement dans les plans [111] et antiferromagnétiquement entre ces plans. Il existe quatre choix possibles de couches (111) et six directions énergétiques dans le plan (111), ce qui correspond à quatre domaines T et six domaines S. Nous avons choisi le NiO pour étudier la propagation et le contrôle des ondes de spin antiferromagnétiques. La ferrite de bismuth $BiFeO_3$ (BFO) est l'archétype du matériau multiferroïque, c'est-à-dire un type de matériau qui possède simultanément plus d'un ordre ferroïque. Dans les conditions ambiantes, il s'agit d'un antiferromagnétique ferroélectrique, avec une interaction magnétoélectrique qui couple les ordres magnétique et ferroélectrique, fournissant une possibilité supplémentaire pour manipuler la structure de spin. L'orientation du spin AF dans le BFO est modulée par un ordre cycloïdal incommensurable, induit

par l'interaction magnéto-électrique, ce qui permet de créer des entités topologiques. Le plan de la cycloïde de spin est parallèle à la direction [111] (la direction de la cycloïde k est donc perpendiculaire à [111]) et sa longueur d'onde est mesurée à 62 nm. Parallèlement à la cycloïde, il y a également une inclinaison des spins perpendiculaire au plan de la cycloïde, ce qui induit une onde de densité de spin (SDW), qui provient de l'inclinaison de l'octaèdre. Nous avons étudié la texture magnétique dans le BFO sous l'effet de champs magnétiques intenses et de couples de transfert de spin (STT), dans de multiples domaines ferroélectriques, et prédit l'existence d'entités topologiques telles que des skyrmions dans certaines conditions susceptibles d'être induites par une distorsion de la maille.

## Contrôle des ondes de spin et portes logiques en NiO

La transmission et le traitement de l'information par les ondes de spin ont été considérés comme une méthode alternative à l'électronique semi-conductrice actuelle. Cette technique, en particulier dans les isolants, pourrait permettre de réduire le temps de dissipation en raison de l'absence de déplacement de charge. Les ondes de spin sont les excitations propres d'un système magnétique au-dessus de son état fondamental qui se sont avérées capables de se propager. Les ondes de spin les plus étudiées jusqu'à présent ont été celles des ferromagnétiques et leurs longueurs d'onde associées sont beaucoup plus grandes que la constante de réseau. La propriété de propagation de ces ondes de spin à faible vecteur d'onde est presque entièrement déterminée par les interactions dipôle-dipôle, qui dépendent largement de la géométrie du matériau magnétique. Par conséquent, le contrôle des ondes de spin dans les guides d'ondes est difficile : une onde de spin ne peut pas traverser un angle droit; la largeur du guide d'ondes peut conduire à la division des ondes de spin en modes de bord. Cette difficulté a empêché l'application de dispositifs basés sur les ondes de spin tels que les portes logiques même avec une structure hybride ondes de spin / électronique. Contrairement aux matériaux ferromagnétiques, qui ont un comportement compliqué en raison de l'effet des champs de désaimantation, les matériaux antiferromagnétiques ont des moments anti-alignés à l'échelle atomique et ne présentent pas d'aimantation. Les ondes de spin dans les antiferromagnétiques sont plus simples car elles sont déterminées par l'interaction d'échange et l'anisotropie magnétique. Les guides d'ondes de spin antiferromagnétiques pourraient simplifier considérablement la situation si l'on tient compte de la géométrie. Les ondes de spin antiferromagnétiques bénéficient également de la haute fréquence de leur résonance magnétique, ce qui permet d'envisager le traitement de l'information au niveau des fréquences THz. L'amortissement plus faible de ces systèmes permet aussi de réduire la dissipation et de prolonger la propagation des ondes de spin. Malgré tous ces avantages, la propagation et le contrôle des ondes de spin dans les antiferromagnétiques n'ont pas été étudiés en profondeur, même en théorie. Dans cette partie de la thèse, nous avons étudié la dynamique de spin de NiO induite par une impulsion de couple de transfert de spin sur la base de valeurs expérimentales. Nous avons déduit l'équation d'onde de la théorie de l'onde de spin linéaire et obtenu la vitesse de l'onde de spin et sa relation de dispersion. À partir du modèle microscopique des états de spin dans le NiO, nous avons simulé numériquement la propagation des ondes de spin et trouvé la même vitesse que celle déduite de la théorie. Nous avons également constaté qu'une telle onde de spin pouvait se propager dans un angle droit sans perturbation. Elle peut être focalisée ou défocalisée lorsque la largeur du guide d'ondes varie. Nous avons proposé une façon possible de réaliser

des portes logiques basées sur une géométrie en croix. Notre étude devrait inspirer les expériences de manipulation des ondes de spin dans le NiO et les portes logiques basées sur des ondes de spin fonctionnant aux fréquences THz.

## BFO dans les champs magnétiques intenses

La structure chirale du spin dans le $BiFeO_3$ est induite par la polarisation électrique. Le mécanisme responsable de ce phénomène est appelé interaction magnétoélectrique. Inversement, la texture de spin en spirale induit une petite polarisation électrique. C'est ce qu'on appelle le mécanisme de courant de spin ou l'effet Dzyaloshinskii-Moriya inverse. Cette polarisation peut être supprimée par l'application d'un champ magnétique puissant. En effet, un champ fort d'environ 20T est à même de déstabiliser la cycloïde et provoquer une transition de l'ordre magnétique de la cycloïde vers un état antiferromagnétique incliné. Expérimentalement, la polarisation et l'aimantation du BFO sous différents champs ont été mesurées, mais ses structures de spin n'ont pas été entièrement mises à jour. Pour comprendre la dépendance en orientation du champ critique et révéler la texture de spin, nous utilisons notre code développé pendant la thèse pour simuler la structure de spin sous un champ fort dans $BiFeO_3$. Nous avons trouvé dans notre simulation que les champs critiques dépendent de la direction du champ appliqué. La valeur des champs critiques est en accord avec les mesures expérimentales. L'anharmonicité de la cycloïde induite par le champ a été discutée. Nous avons constaté que la SDW (ou le terme $D_2$ DMI dans l'hamiltonien) joue un rôle crucial dans la transition vers l'état « floppé », ainsi que dans l'anharmonicité.

## Effet d'une impulsion de couple de transfert de spin sur le cycloïde BFO

La texture antiferromagnétique du $BiFeO_3$ présente une symétrie isotrope brisée dans le plan (111) en raison de la cycloïde, de sorte qu'un couple de spin picoseconde injecté dans $BiFeO_3$ devrait induire une dynamique dépendant de la direction du couple de spin. Pour étudier comment $BiFeO_3$ réagit à ces impulsions STT, nous avons mené des études numériques des réponses des cycloïdes BFO sous des impulsions STT. Nous avons constaté que les impulsions STT appliquées parallèlement et perpendiculairement à k induisent des modes dynamiques différents. Alors que le STT parallèle à k induit des oscillations, l'autre direction ne le fait pas et pousse plutôt la cycloïde. La propagation de ces deux modes dynamiques a les mêmes vitesses à environ 25km/s. Ces résultats seront utiles pour les études expérimentales sur l'effet d'une impulsion STT sur le BFO ; en particulier, ils aideront à comprendre le signal de réponse du BFO adjacent à un ferromagnétique subissant un processus de démagnétisation ultrarapide, qui est une expérience en cours dans notre laboratoire.

## Domaine multi-P dans $BiFeO_3$

A la différence d'un monocristal, les films minces de BFO vierges semblent avoir des domaines P en bandes. Le vecteur de propagation cycloïdal k dans ces domaines P peut pointer dans différentes directions et le motif de continuité de la texture de spin au niveau de la paroi du domaine P est intéressant. Les progrès récents dans les expériences ont permis d'écrire des structures de domaines P plus complexes. En appliquant une impulsion de champ électrique via une pointe, il est possible de créer des domaines P de type quatre quadrants, avec un changement assez brusque de la polarisation des 4 domaines P au centre, où des objets topologiques peuvent éventuellement exister. Un tel objet peut ne pas être entièrement révélé par les images NV en raison de la relation complexe entre le champ parasite et la texture AF dans $BiFeO_3$. Ici, la détermination de l'ordre magnétique en dessous de l'échelle de longueur de l'onde cycloïdale est cruciale. En utilisant nos outils de simulation pour étudier cette texture, nous avons prédit l'existence des domaines $D_2$ indépendamment des domaines P, donnant lieu potentiellement à différentes images NV. En ajustant par rapport aux images expérimentales de microscopie NV, nous avons obtenu les textures de spin des films minces BFO à 4 domaines P ainsi que leurs domaines $D_2$. Cette technique d'ingénierie inverse que nous avons développée pourrait être utile pour sonder les textures de spin sous-jacentes. Les domaines $D_2$ que nous avons prédits et étudiés pourraient ouvrir la voie à un nouveau paramètre indépendant pour le contrôle de la structure magnétique de $BiFeO_3$.

## Skyrmions antiferromagnétiques dans le BFO

Les skyrmions sont des textures magnétiques topologiquement protégées. Les skyrmions ferromagnétiques, obtenus dans des multicouches métalliques, peuvent être utilisés comme de très petits bits d'information magnétique pour le stockage de masse des données et les opérations logiques. Cependant, leur application est entravée par plusieurs problèmes : (i) un courant polarisé en spin pousse latéralement la texture de spin chirale des skyrmions et les entités finissent par être piégées ou par s'annihiler sur les bords de la piste ; (ii) la consommation d'énergie nécessaire pour les déplacer par des impulsions de courant est trop importante ; (iii) leur vitesse de déplacement est limitée à environ 100 m/s. Ces inconvénients pourraient être atténués en travaillant avec des skyrmions antiferromagnétiques qui peuvent fonctionner jusqu'à deux ordres de grandeur plus rapidement que leurs homologues ferromagnétiques, avec une consommation d'énergie considérablement réduite si l'on utilise des isolants. En général, les skyrmions magnétiques sont obtenus par une ingénierie d'interfaces d'hétérostructures artificielles. L'interaction de base est l'interaction Dzyaloshinskii-Moriya (DMI), qui découle du couplage entre les atomes magnétiques dans le champ électrique effectif de l'interface. Elle est de même nature que l'interaction magnéto-électrique plus générale, qui exprime le gain d'énergie en présence d'un champ électrique interne, ou d'une polarisation, lorsque le magnétisme n'est pas colinéaire. Par conséquent, les matériaux magnéto-électriques possèdent intrinsèquement l'interaction nécessaire à la génération de skyrmions et parmi les matériaux concernés, $BiFeO_3$ en est l'archétype. Dans cette partie de la thèse, nous ouvrons la voie à des conditions expérimentalement accessibles pour obtenir les skyrmions AF, basées sur une modélisation réaliste de $BiFeO_3$. Nous avons exploré les conditions qui conduisent $BiFeO_3$ à une transition topologique. Avec les technolo-

gies d'ingénierie de couches minces, il a été démontré que la texture cycloïdale peut être déstabilisée en un état antiferromagnétique colinéaire, qui est le résultat d'une anisotropie effective induite par la contrainte. Nous avons constaté qu'avec une anisotropie uniaxiale légèrement accrue dans la limite de la faisabilité expérimentale, les skyrmions antiferromagnétiques individuels sont stabilisés et protégés par une grande barrière énergétique d'origine topologique. La nucléation peut être obtenue par STT au niveau de la plus grande valeur rapportée dans les expériences. Les impulsions courtes de STT sont suffisantes pour exciter les modes de résonance et pourraient pousser les skyrmions préexistants à des vitesses supérieures à 10 km/s. Notre travail de simulation devrait stimuler des études expérimentales pour atteindre les conditions nécessaires à la production de skyrmions dans le $BiFeO_3$ et utiliser ces entités comme des alternatives avantageuses à leurs homologues ferromagnétiques.

# Conclusion

Dans cette thèse, nous avons concentré notre étude sur NiO et $BiFeO_3$. Nous avons basé notre modélisation de la dynamique de spin sur les paramètres mesurés expérimentalement et avons mené des études théoriques et numériques. Nous avons étudié la propagation des ondes de spin dans le NiO à partir de géométries triviales jusqu'à des géométries plus complexes, ainsi que l'interaction entre les ondes de spin dans une jonction. Afin de modéliser le BFO, nous avons développé un nouveau code à partir de zéro pour simuler efficacement sa dynamique de spin avec l'accélération GPU. Ce code a considérablement augmenté la vitesse de calcul et a rendu possible une série d'études. Nous avons ensuite abordé la transition de phase de sa texture de spin sous un champ magnétique intense de différentes orientations. Nous avons simulé sa dynamique de spin sous l'effet d'une impulsion de couple de transfert de spin. Nous avons également modélisé des textures de spin dans des parois de domaine ferroélectriques et des configurations de polarisation plus exotiques. Finalement, nous avons découvert les conditions critiques pour l'existence et la stabilité des skyrmions AF dans le BFO, étudié leurs propriétés dynamiques et les conditions possibles pour leur nucléation. Ce travail vise à fournir une référence utile pour les futures études expérimentales dans ce nouveau domaine de la spintronique antiferromagnétique.

# Bibliography


[1] Joachim Stöhr and Hans Christoph Siegmann. Magnetism. *Solid-State Sciences. Springer, Berlin, Heidelberg*, 5:236, 2006.

[2] Theophile Chirac. *New spintronic components based on antiferromagnetic materials*. PhD thesis, Universite Paris Saclay (COmUE), 2019.

[3] Walter R Johnson. *Atomic structure theory*. Springer, 2007.

[4] Tai L Chow. *Introduction to electromagnetic theory: a modern perspective*. Jones & Bartlett Learning, 2006.

[5] Ramamurti Shankar. *Principles of quantum mechanics*. Springer Science & Business Media, 2012.

[6] John David Jackson. Classical electrodynamics, 1999.

[7] Werner Heisenberg and Pascual Jordan. Anwendung der Quantenmechanik auf das Problem der anomalen Zeemaneffekte. *Zeitschrift für Physik*, 37(4-5):263–277, 1926.

[8] Werner Heisenberg. Über die Spektra von Atomsystemen mit zwei Elektronen. *Zeitschrift für Physik*, 39(7-8):499–518, 1926.

[9] Walter Heitler and Fritz London. Wechselwirkung neutraler Atome und homöopolare Bindung nach der Quantenmechanik. *Zeitschrift für Physik*, 44(6-7):455–472, 1927.

[10] John Norman Murrell, Sidney Francis Alan Kettle, and John Michael Tedder. *The chemical bond*. Wiley New York, 1985.

[11] H.A Kramers. L'interaction entre les atomes magnétogènes dans un cristal paramagnétique. *Physica*, 1(1):182–192, 1934. ISSN 0031-8914. doi: https://doi.org/10.1016/S0031-8914(34)90023-9. URL https://www.sciencedirect.com/science/article/pii/S0031891434900239.

[12] Po W Anderson. Antiferromagnetism. theory of superexchange interaction. *Physical Review*, 79 (2):350, 1950.

[13] J Mathon and A Umerski. Physics of low dimensional systems, 2001.

[14] Charles Kittel. Interpretation of anomalous larmor frequencies in ferromagnetic resonance experiment. *Physical Review*, 71(4):270, 1947.

[15] James HE Griffiths. Anomalous high-frequency resistance of ferromagnetic metals. *Nature*, 158 (4019):670–671, 1946.

[16] F. Keffer and C. Kittel. Theory of antiferromagnetic resonance. *Phys. Rev.*, 85:329–337, Jan 1952. doi: 10.1103/PhysRev.85.329. URL https://link.aps.org/doi/10.1103/PhysRev.85.329.

[17] LR Maxwell and TR McGuire. Antiferromagnetic resonance. *Reviews of modern physics*, 25(1):279, 1953.

[18] Zongxia Guo, Jialiang Yin, Yue Bai, Daoqian Zhu, Kewen Shi, Gefei Wang, Kaihua Cao, and Weisheng Zhao. Spintronics for energy-efficient computing: An overview and outlook. *Proceedings of the IEEE*, 109(8):1398–1417, 2021.

[19] Wang Kang, Yue Zhang, Zhaohao Wang, Jacques-Olivier Klein, Claude Chappert, Dafiné Ravelosona, Gefei Wang, Youguang Zhang, and Weisheng Zhao. Spintronics: Emerging ultra-low-power circuits and systems beyond mos technology. *ACM Journal on Emerging Technologies in Computing Systems (JETC)*, 12(2):1–42, 2015.

[20] Arne Brataas, Bart van Wees, Olivier Klein, Grégoire de Loubens, and Michel Viret. Spin insulatronics. *Physics Reports*, 885:1–27, 2020. ISSN 0370-1573. doi: https://doi.org/10.1016/j.physrep.2020.08.006. URL https://www.sciencedirect.com/science/article/pii/S0370157320302933. Spin Insulatronics.

[21] EV Gomonay and VM Loktev. Spintronics of antiferromagnetic systems. *Low Temperature Physics*, 40(1):17–35, 2014.

[22] Romain Lebrun, Andrew Ross, Olena Gomonay, Vincent Baltz, Ursula Ebels, A-L Barra, Alireza Qaiumzadeh, Arne Brataas, Jairo Sinova, and Mathias Kläui. Long-distance spin-transport across the morin phase transition up to room temperature in ultra-low damping single crystals of the antiferromagnet $\alpha$-fe203. *Nature communications*, 11(1):6332, 2020.

[23] Sergio M Rezende. *Fundamentals of magnonics*, volume 969. Springer, 2020.

[24] Manfred Fiebig, D Fröhlich, Th Lottermoser, VV Pavlov, RV Pisarev, and H-J Weber. Second harmonic generation in the centrosymmetric antiferromagnet nio. *Physical review letters*, 87(13): 137202, 2001.

[25] J-Y Chauleau, Eloi Haltz, C Carrétéro, S Fusil, and Michel Viret. Multi-stimuli manipulation of antiferromagnetic domains assessed by second-harmonic imaging. *Nature materials*, 16(8):803–807, 2017.

[26] AV Kimel, BA Ivanov, RV Pisarev, PA Usachev, A Kirilyuk, and Th Rasing. Inertia-driven spin switching in antiferromagnets. *Nature Physics*, 5(10):727–731, 2009.

[27] Vincent Baltz, Aurelien Manchon, M Tsoi, Takahiro Moriyama, T Ono, and Y Tserkovnyak. Antiferromagnetic spintronics. *Reviews of Modern Physics*, 90(1):015005, 2018.

[28] IS Jacobs. Spin-flopping in mnf 2 by high magnetic fields. *Journal of Applied Physics*, 32(3):S61–S62, 1961.

[29] IS Jacobs and PE Lawrence. Metamagnetic phase transitions and hysteresis in fecl 2. *Physical Review*, 164(2):866, 1967.

[30] Victor G Bar'yakhtar, Mikhail V Chetkin, Boris A Ivanov, and Sergei N Gadetskii. *Dynamics of topological magnetic solitons: experiment and theory*, volume 129. Springer, 2006.

[31] Delphine Lebeugle, Dorothée Colson, A Forget, Michel Viret, AM Bataille, and A Gukasov. Electric-field-induced spin flop in bifeo 3 single crystals at room temperature. *Physical review letters*, 100 (22):227602, 2008.

[32] Nguyen Phuc Duong, Takuya Satoh, and Manfred Fiebig. Ultrafast manipulation of antiferromagnetism of nio. *Physical review letters*, 93(11):117402, 2004.

[33] AV Kimel, Andrei Kirilyuk, Artem Tsvetkov, RV Pisarev, and Th Rasing. Laser-induced ultrafast spin reorientation in the antiferromagnet tmfeo3. *Nature*, 429(6994):850–853, 2004.

[34] AV Kimel, A Kirilyuk, PA Usachev, RV Pisarev, AM Balbashov, and Th Rasing. Ultrafast non-thermal control of magnetization by instantaneous photomagnetic pulses. *Nature*, 435(7042): 655–657, 2005.

[35] Cheng Song, Ruiqi Zhang, Liyang Liao, Yongjian Zhou, Xiaofeng Zhou, Ruyi Chen, Yunfeng You, Xianzhe Chen, and Feng Pan. Spin-orbit torques: Materials, mechanisms, performances, and potential applications. *Progress in Materials Science*, 118:100761, 2021.

[36] Tobias Kampfrath, Marco Battiato, Pablo Maldonado, Gerrit Eilers, J Nötzold, Sebastian Mährlein, Vladyslav Zbarsky, Frank Freimuth, Yuriy Mokrousov, Stefan Blügel, et al. Terahertz spin current pulses controlled by magnetic heterostructures. *Nature nanotechnology*, 8(4):256–260, 2013.

[37] Yoshinori Tokura and Naoya Kanazawa. Magnetic skyrmion materials. *Chemical Reviews*, 121(5): 2857–2897, 2020.

[38] Tony Hilton Royle Skyrme. A non-linear field theory. *Proceedings of the Royal Society of London. Series A. Mathematical and Physical Sciences*, 260(1300):127–138, 1961.

[39] Tony Hilton Royle Skyrme. A unified field theory of mesons and baryons. *Nuclear Physics*, 31: 556–569, 1962.

[40] Alexei N Bogdanov and DA Yablonskii. Thermodynamically stable "vortices" in magnetically ordered crystals. the mixed state of magnets. *Zh. Eksp. Teor. Fiz*, 95(1):178, 1989.

[41] Sebastian Muuhlbauer, Benedikt Binz, F Jonietz, Christian Pfleiderer, Achim Rosch, Anja Neubauer, Robert Georgii, and Peter Boni. Skyrmion lattice in a chiral magnet. *Science*, 323 (5916):915–919, 2009.

[42] XZ Yu, Yoshinori Onose, Naoya Kanazawa, Joung Hwan Park, JH Han, Yoshio Matsui, Naoto Nagaosa, and Yoshinori Tokura. Real-space observation of a two-dimensional skyrmion crystal. *Nature*, 465(7300):901–904, 2010.

[43] Naoto Nagaosa and Yoshinori Tokura. Topological properties and dynamics of magnetic skyrmions. *Nature nanotechnology*, 8(12):899–911, 2013.

[44] Michael Victor Berry. Quantal phase factors accompanying adiabatic changes. *Proceedings of the Royal Society of London. A. Mathematical and Physical Sciences*, 392(1802):45–57, 1984.

[45] Naoto Nagaosa and Yoshinori Tokura. Emergent electromagnetism in solids. *Physica Scripta*, 2012(T146):014020, 2012.

[46] João Sampaio, Vincent Cros, Stanislas Rohart, André Thiaville, and Albert Fert. Nucleation, stability and current-induced motion of isolated magnetic skyrmions in nanostructures. *Nature nanotechnology*, 8(11):839–844, 2013.

[47] Xichao Zhang, Yan Zhou, and Motohiko Ezawa. Antiferromagnetic skyrmion: stability, creation and manipulation. *Scientific reports*, 6(1):24795, 2016.

[48] Sayantan Sur, Matthew J. Koop, and Dhabaleswar K. Panda. High-performance and scalable mpi over infiniband with reduced memory usage: An in-depth performance analysis. In *Proceedings of the 2006 ACM/IEEE Conference on Supercomputing*, SC '06, page 105–es, New York, NY, USA, 2006. Association for Computing Machinery. ISBN 0769527000. doi: 10.1145/1188455.1188565. URL https://doi.org/10.1145/1188455.1188565.

[49] Julien Tranchida, Steven J Plimpton, Pascal Thibaudeau, and Aidan P Thompson. Massively parallel symplectic algorithm for coupled magnetic spin dynamics and molecular dynamics. *Journal of Computational Physics*, 372:406–425, 2018.

[50] Alexander Stukowski. Visualization and analysis of atomistic simulation data with ovito–the open visualization tool. *Modelling and simulation in materials science and engineering*, 18(1):015012, 2009.

[51] H. Sato, T. Minami, S. Takata, and T. Yamada. Transparent conducting p-type nio thin films prepared by magnetron sputtering. *Thin Solid Films*, 236(1):27–31, 1993. ISSN 0040-6090. doi: https://doi.org/10.1016/0040-6090(93)90636-4. URL https://www.sciencedirect.com/science/article/pii/0040609093906364.

[52] R Newman and RM Chrenko. Optical properties of nickel oxide. *Physical Review*, 114(6):1507, 1959.

[53] M. T. Hutchings and E. J. Samuelsen. Measurement of spin-wave dispersion in nio by inelastic neutron scattering and its relation to magnetic properties. *Phys. Rev. B*, 6:3447–3461, Nov 1972. doi: 10.1103/PhysRevB.6.3447. URL https://link.aps.org/doi/10.1103/PhysRevB.6.3447.

[54] Théophile Chirac, Jean-Yves Chauleau, Pascal Thibaudeau, Olena Gomonay, and Michel Viret. Ultrafast antiferromagnetic switching in nio induced by spin transfer torques. *Physical Review B*, 102(13):134415, 2020.

[55] A. J. Sievers and M. Tinkham. Far infrared antiferromagnetic resonance in mno and nio. *Phys. Rev.*, 129:1566–1571, Feb 1963. doi: 10.1103/PhysRev.129.1566. URL https://link.aps.org/doi/10.1103/PhysRev.129.1566.

[56] Tobias Kampfrath, Alexander Sell, Gregor Klatt, Alexej Pashkin, Sebastian Mährlein, Thomas Dekorsy, Martin Wolf, Manfred Fiebig, Alfred Leitenstorfer, and Rupert Huber. Coherent terahertz control of antiferromagnetic spin waves. *Nature Photonics*, 5(1):31–34, 2011.

[57] AM Kadomtseva, Yu F Popov, AP Pyatakov, GP Vorob'Ev, AK Zvezdin, and D Viehland. Phase transitions in multiferroic bifeo3 crystals, thin-layers, and ceramics: enduring potential for a single phase, room-temperature magnetoelectric 'holy grail'. *Phase Transitions*, 79(12):1019–1042, 2006.

[58] Je-Geun Park, Manh Duc Le, Jaehong Jeong, and Sanghyun Lee. Structure and spin dynamics of multiferroic bifeo3. *Journal of Physics: Condensed Matter*, 26(43):433202, 2014.

[59] Srihari NV, KB Vinayakumar, and KK Nagaraja. Magnetoelectric coupling in bismuth ferrite—challenges and perspectives. *Coatings*, 10(12):1221, 2020.

[60] Ie E Dzyaloshinskii. On the magneto-electrical effects in antiferromagnets. *Soviet Physics JETP*, 10:628–629, 1960.

[61] Tôru Moriya. Anisotropic superexchange interaction and weak ferromagnetism. *Physical review*, 120(1):91, 1960.

[62] JBNJ Wang, JB Neaton, H Zheng, V Nagarajan, SB Ogale, B Liu, D Viehland, V Vaithyanathan, DG Schlom, UV Waghmare, et al. Epitaxial bifeo3 multiferroic thin film heterostructures. *science*, 299(5613):1719–1722, 2003.

[63] W. Eerenstein, F. D. Morrison, J. Dho, M. G. Blamire, J. F. Scott, and N. D. Mathur. Comment on "epitaxial bifeo<sub>3</sub> multiferroic thin film heterostructures". *Science*, 307(5713):1203–1203, 2005. doi: 10.1126/science.1105422. URL https://www.science.org/doi/abs/10.1126/science.1105422.

[64] J Wang, A Scholl, H Zheng, SB Ogale, D Viehland, DG Schlom, NA Spaldin, KM Rabe, M Wuttig, L Mohaddes, et al. Response to comment on. *Epitaxial BiFeO3 multiferroic thin film heterostructures"", Science*, 307, 2005.

[65] Delphine Lebeugle, Dorothée Colson, Anne Forget, Michel Viret, Pierre Bonville, Jean-Francis Marucco, and Stephane Fusil. Room-temperature coexistence of large electric polarization and magnetic order in bi fe o 3 single crystals. *Physical Review B*, 76(2):024116, 2007.

[66] Delphine Lebeugle, Dorothée Colson, A Forget, and Michel Viret. Very large spontaneous electric polarization in bifeo3 single crystals at room temperature and its evolution under cycling fields. *Applied Physics Letters*, 91(2), 2007.

[67] T Zhao, A Scholl, F Zavaliche, K Lee, M Barry, A Doran, MP Cruz, YH Chu, C Ederer, NA Spaldin, et al. Electrical control of antiferromagnetic domains in multiferroic bifeo3 films at room temperature. *Nature materials*, 5(10):823–829, 2006.

[68] Sasikanth Manipatruni, Dmitri E Nikonov, Chia-Ching Lin, Tanay A Gosavi, Huichu Liu, Bhagwati Prasad, Yen-Lin Huang, Everton Bonturim, Ramamoorthy Ramesh, and Ian A Young. Scalable energy-efficient magnetoelectric spin–orbit logic. *Nature*, 565(7737):35–42, 2019.

[69] Bin Xu, Sebastian Meyer, Matthieu J Verstraete, Laurent Bellaiche, and Bertrand Dupé. First-principles study of spin spirals in the multiferroic bifeo 3. *Physical Review B*, 103(21):214423, 2021.

[70] J.M. Moreau, C. Michel, R. Gerson, and W.J. James. Ferroelectric bifeo3 x-ray and neutron diffraction study. *Journal of Physics and Chemistry of Solids*, 32(6):1315–1320, 1971. ISSN 0022-3697. doi: https://doi.org/10.1016/S0022-3697(71)80189-0. URL https://www.sciencedirect.com/science/article/pii/S0022369771801890.

[71] W. Kaczmarek, Z. Pajak, and M. Polomska. Differential thermal analysis of phase transitions in (bi1-xlax)feo3 solid solution. *Solid State Communications*, 17(7):807–810, 1975. ISSN 0038-1098. doi: https://doi.org/10.1016/0038-1098(75)90726-7. URL https://www.sciencedirect.com/science/article/pii/0038109875907267.

[72] Daniel Sando, A Barthélémy, and M Bibes. Bifeo3 epitaxial thin films and devices: past, present and future. *Journal of Physics: Condensed Matter*, 26(47):473201, 2014.

[73] Darrell G Schlom, Long-Qing Chen, Chang-Beom Eom, Karin M Rabe, Stephen K Streiffer, and Jean-Marc Triscone. Strain tuning of ferroelectric thin films. *Annu. Rev. Mater. Res.*, 37:589–626, 2007.

[74] Darrell G Schlom, Long-Qing Chen, Craig J Fennie, Venkatraman Gopalan, David A Muller, Xiaoqing Pan, Ramamoorthy Ramesh, and Reinhard Uecker. Elastic strain engineering of ferroic oxides. *Mrs Bulletin*, 39(2):118–130, 2014.

[75] Jaehong Jeong, EA Goremychkin, T Guidi, K Nakajima, Gun Sang Jeon, Shin-Ae Kim, S Furukawa, Yong Baek Kim, Seongsu Lee, V Kiryukhin, et al. Spin wave measurements over the full brillouin zone of multiferroic bifeo 3. *Physical review letters*, 108(7):077202, 2012.

[76] Randy S Fishman. The microscopic model of bifeo3. *Physica B: Condensed Matter*, 536:115–117, 2018.

[77] MP Kostylev, AA Serga, T Schneider, B Leven, and B Hillebrands. Spin-wave logical gates. *Applied Physics Letters*, 87(15):153501, 2005.

[78] Thomas Schneider, Alexander A Serga, Britta Leven, Burkard Hillebrands, Robert L Stamps, and Mikhail P Kostylev. Realization of spin-wave logic gates. *Applied Physics Letters*, 92(2):022505, 2008.

[79] Ki-Suk Lee and Sang-Koog Kim. Conceptual design of spin wave logic gates based on a mach–zehnder-type spin wave interferometer for universal logic functions. *Journal of Applied Physics*, 104(5):053909, 2008.

[80] Sergej O Demokritov and Andrei N Slavin. Spin waves. In *Handbook of Magnetism and Magnetic Materials*, pages 281–346. Springer, 2021.

[81] Felix Bloch. Zur Theorie des Ferromagnetismus. *Zeitschrift für Physik*, 61(3-4):206–219, 1930.

[82] Vladislav E Demidov and Sergej O Demokritov. Magnonic waveguides studied by microfocus brillouin light scattering. *IEEE Transactions on Magnetics*, 51(4):1–15, 2015.

[83] Burkard Hillebrands. Brillouin light scattering from quantized spin waves in micron-size magnetic wires. 1999.

[84] Vladislav E Demidov and Sergej O Demokritov. Magnonic waveguides studied by microfocus brillouin light scattering. *IEEE Transactions on Magnetics*, 51(4):1–15, 2015.

[85] K Vogt, H Schultheiss, S Jain, JE Pearson, A Hoffmann, SD Bader, and B Hillebrands. Spin waves turning a corner. *Applied Physics Letters*, 101(4):042410, 2012.

[86] A. V. Sadovnikov, C. S. Davies, V. V. Kruglyak, D. V. Romanenko, S. V. Grishin, E. N. Beginin, Y. P. Sharaevskii, and S. A. Nikitov. Spin wave propagation in a uniformly biased curved magnonic waveguide. *Phys. Rev. B*, 96:060401, Aug 2017. doi: $10.1103/\mathrm{PhysRevB.96.060401}$. URL https://link.aps.org/doi/10.1103/PhysRevB.96.060401.

[87] RA Duine, Kyung-Jin Lee, Stuart SP Parkin, and Mark D Stiles. Synthetic antiferromagnetic spintronics. *Nature physics*, 14(3):217–219, 2018.

[88] William Legrand, Davide Maccariello, Fernando Ajejas, Sophie Collin, Aymeric Vecchiola, Karim Bouzehouane, Nicolas Reyren, Vincent Cros, and Albert Fert. Room-temperature stabilization of antiferromagnetic skyrmions in synthetic antiferromagnets. *Nature materials*, 19(1):34–42, 2020.

[89] Sujit Panigrahy, Sougata Mallick, João Sampaio, and Stanislas Rohart. Skyrmion inertia in synthetic antiferromagnets. *Physical Review B*, 106(14):144405, 2022.

[90] EG Galkina and BA Ivanov. Dynamic solitons in antiferromagnets. *Low Temperature Physics*, 44 (7):618–633, 2018.

[91] BA Ivanov. Spin dynamics of antiferromagnets under action of femtosecond laser pulses. *Low Temperature Physics*, 40(2):91–105, 2014.

[92] Viktor Grigorievich Bar'yakhtar, Boris Alekseevich Ivanov, and Mikhail V Chetkin. Dynamics of domain walls in weak ferromagnets. *Soviet Physics Uspekhi*, 28(7):563, 1985.

[93] Roman Khymyn, Ivan Lisenkov, Vasyl Tiberkevich, Boris A Ivanov, and Andrei Slavin. Antiferromagnetic thz-frequency josephson-like oscillator driven by spin current. *Scientific reports*, 7(1): 43705, 2017.

[94] Helen V Gomonay and Vadim M Loktev. Spin transfer and current-induced switching in antiferromagnets. *Physical Review B*, 81(14):144427, 2010.

[95] Ran Cheng, Matthew W Daniels, Jian-Gang Zhu, and Di Xiao. Ultrafast switching of antiferromagnets via spin-transfer torque. *Physical Review B*, 91(6):064423, 2015.

[96] Ran Cheng, Matthew W Daniels, Jian-Gang Zhu, and Di Xiao. Antiferromagnetic spin wave field-effect transistor. *Scientific reports*, 6(1):24223, 2016.

[97] Jin Lan, Weichao Yu, and Jiang Xiao. Antiferromagnetic domain wall as spin wave polarizer and retarder. *Nature communications*, 8(1):178, 2017.

[98] Weichao Yu, Jin Lan, Jiang Xiao, et al. Magnetic logic gate based on polarized spin waves. *Physical Review Applied*, 13(2):024055, 2020.

[99] Hosho Katsura, Naoto Nagaosa, and Alexander V Balatsky. Spin current and magnetoelectric effect in noncollinear magnets. *Physical review letters*, 95(5):057205, 2005.

[100] M Tokunaga, M Akaki, T Ito, S Miyahara, A Miyake, H Kuwahara, and N Furukawa. Magnetic control of transverse electric polarization in bifeo3. *Nature communications*, 6(1):5878, 2015.

[101] Yu F Popov, AM Kadomtseva, SS Krotov, DV Belov, GP Vorob'ev, PN Makhov, and AK Zvezdin. Features of the magnetoelectric properties of bifeo 3 in high magnetic fields. *Low Temperature Physics*, 27(6):478–479, 2001.

[102] Sándor Bordács, DG Farkas, JS White, R Cubitt, L DeBeer-Schmitt, T Ito, and István Kézsmárki. Magnetic field control of cycloidal domains and electric polarization in multiferroic bifeo 3. *Physical review letters*, 120(14):147203, 2018.

[103] Randy S Fishman. Orientation dependence of the critical magnetic field for multiferroic bifeo 3. *Physical Review B*, 88(10):104419, 2013.

[104] J-Y Chauleau, T Chirac, S Fusil, Vincent Garcia, W Akhtar, J Tranchida, P Thibaudeau, I Gross, C Blouzon, A ea Finco, et al. Electric and antiferromagnetic chiral textures at multiferroic domain walls. *Nature materials*, 19(4):386–390, 2020.

[105] Isabell Gross, W Akhtar, V Garcia, LJ Martínez, Saddem Chouaieb, K Garcia, C Carrétéro, A Barthélémy, P Appel, P Maletinsky, et al. Real-space imaging of non-collinear antiferromagnetic order with a single-spin magnetometer. *Nature*, 549(7671):252–256, 2017.

[106] Arthur Chaudron, Zixin Li, Finco Aurore, Pavel Marton, Pauline Dufour, Amr Abdelsamie, Sophie Collin, Jirka Hlinka, Vincent Jacques, Jean-Yves Chauleau, Michel Viret, Karim Bouzehouane, Stéphane Fusil, and Vincent Garcia. Electric-field induced multiferroic topological solitons. *To be published*.

[107] Romana Schirhagl, Kevin Chang, Michael Loretz, and Christian L Degen. Nitrogen-vacancy centers in diamond: nanoscale sensors for physics and biology. *Annual review of physical chemistry*, 65:83–105, 2014.

[108] F Duncan M Haldane. Nobel lecture: Topological quantum matter. *Reviews of Modern Physics*, 89(4):040502, 2017.

[109] Albert Fert, Nicolas Reyren, and Vincent Cros. Magnetic skyrmions: advances in physics and potential applications. *Nature Reviews Materials*, 2(7):1–15, 2017.

[110] Anjan Soumyanarayanan, Nicolas Reyren, Albert Fert, and Christos Panagopoulos. Emergent phenomena induced by spin–orbit coupling at surfaces and interfaces. *Nature*, 539(7630):509–517, 2016.

[111] Albert Fert, Vincent Cros, and Joao Sampaio. Skyrmions on the track. *Nature nanotechnology*, 8 (3):152–156, 2013.

[112] Wanjun Jiang, Xichao Zhang, Guoqiang Yu, Wei Zhang, Xiao Wang, M Benjamin Jungfleisch, John E Pearson, Xuemei Cheng, Olle Heinonen, Kang L Wang, et al. Direct observation of the skyrmion hall effect. *Nature Physics*, 13(2):162–169, 2017.

[113] Kai Litzius, Ivan Lemesh, Benjamin Krüger, Pedram Bassirian, Lucas Caretta, Kornel Richter, Felix Büttner, Koji Sato, Oleg A Tretiakov, Johannes Förster, et al. Skyrmion hall effect revealed by direct time-resolved x-ray microscopy. *Nature Physics*, 13(2):170–175, 2017.

[114] Yizheng Liu, Na Lei, Chengxiang Wang, Xichao Zhang, Wang Kang, Daoqian Zhu, Yan Zhou, Xiaoxi Liu, Youguang Zhang, and Weisheng Zhao. Voltage-driven high-speed skyrmion motion in a skyrmion-shift device. *Physical Review Applied*, 11(1):014004, 2019.

[115] Seonghoon Woo, Kai Litzius, Benjamin Krüger, Mi-Young Im, Lucas Caretta, Kornel Richter, Maxwell Mann, Andrea Krone, Robert M Reeve, Markus Weigand, et al. Observation of room-temperature magnetic skyrmions and their current-driven dynamics in ultrathin metallic ferromagnets. *Nature materials*, 15(5):501–506, 2016.

[116] Chendong Jin, Chengkun Song, Jianbo Wang, and Qingfang Liu. Dynamics of antiferromagnetic skyrmion driven by the spin hall effect. *Applied Physics Letters*, 109(18), 2016.

[117] Joseph Barker and Oleg A Tretiakov. Static and dynamical properties of antiferromagnetic skyrmions in the presence of applied current and temperature. *Physical review letters*, 116(14): 147203, 2016.

[118] Albert Fert and Peter M Levy. Role of anisotropic exchange interactions in determining the properties of spin-glasses. *Physical Review Letters*, 44(23):1538, 1980.

[119] Maxim Mostovoy. Ferroelectricity in spiral magnets. *Physical review letters*, 96(6):067601, 2006.

[120] Antonina Mikhailovna Kadomtseva, Anatolii Konstantinovich Zvezdin, Yu F Popov, Aleksandr Pavlovich Pyatakov, and Gennadii Petrovich Vorob'ev. Space-time parity violation and magnetoelectric interactions in antiferromagnets. *Journal of Experimental and Theoretical Physics Letters*, 79:571–581, 2004.

[121] Manfred Fiebig. Revival of the magnetoelectric effect. *Journal of physics D: applied physics*, 38(8): R123, 2005.

[122] Gustau Catalan and James F Scott. Physics and applications of bismuth ferrite. *Advanced materials*, 21(24):2463–2485, 2009.

[123] Izabela Sosnowska, T Peterlin Neumaier, and E Steichele. Spiral magnetic ordering in bismuth ferrite. *Journal of Physics C: Solid State Physics*, 15(23):4835, 1982.

[124] I Sosnowska and AK Zvezdin. Origin of the long period magnetic ordering in bifeo3. *Journal of magnetism and magnetic materials*, 140:167–168, 1995.

[125] A Haykal, J Fischer, W Akhtar, J-Y Chauleau, D Sando, A Finco, F Godel, YA Birkhölzer, C Carrétéro, N Jaouen, et al. Antiferromagnetic textures in bifeo3 controlled by strain and electric field. *Nature communications*, 11(1):1704, 2020.

[126] D Sando, A Agbelele, D Rahmedov, J Liu, P Rovillain, C Toulouse, IC Infante, AP Pyatakov, S Fusil, E Jacquet, et al. Crafting the magnonic and spintronic response of bifeo3 films by epitaxial strain. *Nature materials*, 12(7):641–646, 2013.

[127] Zuhuang Chen, Zhanghui Chen, Chang-Yang Kuo, Yunlong Tang, Liv R Dedon, Qian Li, Lei Zhang, Christoph Klewe, Yen-Lin Huang, Bhagwati Prasad, et al. Complex strain evolution of polar and magnetic order in multiferroic bifeo3 thin films. *Nature communications*, 9(1):3764, 2018.

[128] Z Li, T Chirac, J Tranchida, V Garcia, S Fusil, V Jacques, J-Y Chauleau, and M Viret. Multiferroic skyrmions in bifeo 3. *Physical Review Research*, 5(4):043109, 2023.

[129] AS Varentsova, Maria N Potkina, Stephan Von Malottki, Stefan Heinze, and Pavel F Bessarab. Interplay between size and stability of magnetic skyrmions. *Nanosystems: Physics, Chemistry, Mathematics*, 9(3):356–363, 2018.